

Investigation of Robust Surface Architectures under Ultra-High Vacuum

Christian R. Larrea



University of
St Andrews

This thesis is submitted in partial fulfilment for the degree of PhD
at the
University of St Andrews

November, 2017

I, Christian R. Larrea, hereby certify that this thesis, which is approximately 60 000 words in length, has been written by me, and that it is the record of work carried out by me, or principally by myself in collaboration with others as acknowledged, and that it has not been submitted in any previous application for a higher degree.

(If you received assistance in writing from anyone other than your supervisor/s):

Date _____ signature of candidate

Date _____ signature of supervisor

PRINTED COPY

- Supporting statement for printed embargo request if greater than 2 years:**

Supporting statement for electronic embargo request if greater than 2 years:

ABSTRACT AND TITLE EMBARGOES

An embargo on the full text copy of your thesis in the electronic and printed formats will be granted automatically in the first instance. This embargo includes the abstract and title except that the title will be used in the graduation booklet.

If you have selected an embargo option indicate below if you wish to allow the thesis abstract and/or title to be published. If you do not complete the section below the title and abstract will remain embargoed along with the text of the thesis.

- | | | |
|----|---|-----|
| a) | I agree to the title and abstract being published | NO |
| b) | I require an embargo on abstract | YES |
| c) | I require an embargo on title | YES |

Date

signature of candidate

signature of supervisor

Please note initial embargos can be requested for a maximum of five years. An embargo on a thesis submitted to the Faculty of Science or Medicine is rarely granted for more than two years in the first instance, without good justification. The Library will not lift an embargo before confirming with the student and supervisor that they do not intend to request a continuation. In the absence of an agreed response from both student and supervisor, the Head of School will be consulted. Please note that the total period of an embargo, including any continuation, is not expected to exceed ten years. Where part of a thesis is to be embargoed, please specify the part and the reason.

To David, of course.

Abstract

Robust surface architectures are desirable for extended durability in many applications. Novel surface modification methods have recently emerged that permit the synthesis of complex interfaces of high thermal and chemical stability. In this thesis, these chemical modification methods are exploited in UHV in two separate themes. In the first part, the challenges surrounding the direct synthesis of sCOFs on catalytically active metals are presented. A protocol based on metal alloys was developed to circumvent the reduced mobility of monomers on palladium. This protocol permits 2D polymerisation of halogenated precursors and the formation of a porous sCOF on a catalytically relevant surface. This protocol is transferable to sCOF synthesis from the self-condensation of boronic acids. However, the quality of the framework is compromised.

The second part of this thesis focuses on NHC-based SAM fabrication, which offers many advantages over traditional organosulfur SAMs such as superior stability against oxidation. Vapour deposition of NHCs in UHV from the thermolysis of NHC bicarbonate adducts is demonstrated. The effect of substituent groups at the *N, N* position impacts dramatically on the binding geometry and behaviour of the SAM. The SAM of *flat-lying* NHC transforms into a surface-bound (NHC)₂Cu complex by incorporation of copper adatoms. In addition, the experimentally derived chemisorption energy of an *upright*-bound NHC onto Au(111) and Cu(111) is the same within error. Last, the results of exploratory experiments are presented where the role of NHC SAMs as passivators against copper oxidation and as oxide etchants is assessed. NHCs reduce a model copper oxide to metallic copper and some degree of passivation was qualitatively derived from thermal desorption spectroscopy. The substituents at the *N, N* have a tangible effect on the degree of passivation.

Contents

1	Methods	5
1.1	Ultra High Vacuum (UHV)	5
1.2	Vibrational Spectroscopy	7
1.3	Temperature Programmed Desorption (TPD)	13
1.4	Low Energy Electron Diffraction (LEED)	17
1.5	Scanning Tunnelling Microscopy (STM)	24
1.6	General Considerations	28
1.7	References	36
2	sCOF Synthesis on a Reactive Metal Surface	39
2.1	Introduction	39
2.2	Surface Confined Covalent Organic Frameworks (sCOFs)	44
2.3	Direct Synthesis of sCOFs on Pd(111)	49
2.4	sCOF Synthesis on AuPd(111) Thin-film Alloys	60
2.5	sCOF Synthesis from Boronic Acid Precursors on AuPd(111)	83
2.6	Summary and Outlook	93
2.7	References	96
2.8	Appendix A	113
3	N-Heterocyclic Carbenes: A New Class of Surface Ligand	117
3.1	Introduction	117
3.2	NHC Monolayers on Au(111)	125
3.3	NHC Monolayers on Cu(111)	137
3.4	Summary and Outlook	151
3.5	References	153

3.6	Appendix B	162
4	NHC interaction with $\text{Cu}_x\text{O}/\text{Cu}(111)$	165
4.1	Introduction	165
4.2	$\text{Cu}_x\text{O}/\text{Cu}(111)$: A Model Copper Oxide	166
4.3	Adsorption of NHCs on $\text{Cu}_x\text{O}/\text{Cu}(111)$	173
4.4	NHC SAMs as Inhibitors against Oxidation	181
4.5	Summary and Outlook	186
4.6	References	189
5	Conclusion	193

Chapter 1

Methods

1.1 Ultra High Vacuum (UHV)

Many surface science studies involving single crystals are conducted under ultra-high vacuum (UHV) conditions ($P < 1 \times 10^{-9}$ mbar). The need, or sometimes choice, of UHV is justified mainly by the following reasons. Firstly, with the purpose of maintaining a controlled and contamination free environment, the number of adventitious species adsorbing onto the surface must be kept to a minimum. The rate of species impinging onto a surface (F) with a sticking probability of $S = 1$, can be derived from the kinetic theory of gases (Equation 1.4), where n : molecular gas density, \bar{v} : average molecular speed, N : number of molecules, V : volume, P : pressure, K_b Boltzmann's constant, T : temperature, m : molecular mass.^{1,2}

$$F = \frac{1}{4} n \bar{v} \quad (1.1)$$

$$n = \frac{N}{V} = \frac{P}{k_b T} \quad (1.2)$$

$$\bar{v} = \sqrt{\frac{8k_b T}{\pi m}} \quad (1.3)$$

$$F = \frac{P}{\sqrt{2k_b T \pi m}} (\text{molecules} \cdot \text{m}^{-2} \cdot \text{s}^{-1}) \quad (1.4)$$

It follows from this expression that, to maintain a contamination-free surface for an experimental time scale of hours, pressures of the order of 1×10^{-10} mbar are required. A clean surface is usually defined as the lowest detection limit of current surface spectroscopic techniques (0.1–1 %), which translates into a surface coverage of $\leq 1 \times 10^{13} \text{ atoms} \cdot \text{cm}^{-2}$.

A second reason for conducting experiments under UHV is that these conditions allow for investigation in a solvent-free environment. Solubility issues are eliminated, as well as issues concerning the preferential adsorption of solvent molecules over the molecule of interest. Additionally, reaction temperatures are not limited by the solvent, and a wide range of temperatures can be employed that range from a few to hundreds of K. However, there are certain restrictions on the type of molecules that can be deposited. Most gases can be easily dosed, but liquids and solid compounds are limited by their vapour pressure and sublimation temperature, respectively. Besides, the undesired decomposition or side reactions of the compounds may occur in the doser.

Thirdly, certain characterisation techniques demand UHV conditions, such as electron spectroscopies. Photoelectrons ejected from the sample will experience multiple inelastic scattering with gas molecules before arriving at the detector, losing any spectroscopic information associated with the sample. This fact also imposes some restrictions on the experiment set-up, as *in-situ* experiments under real conditions are generally not accessible.

1.2 Vibrational Spectroscopy

Vibrational spectroscopy is a non-destructive analytical technique routinely used in the characterisation of compounds, which can also be implemented in the characterisation of adsorbates on solid surfaces. The number of normal vibrational modes of a polyatomic molecule containing N -atoms is $3N - 6$, or $3N - 5$ for a linear molecule. Upon adsorption, translational and rotational degrees of freedom are lost and converted into *frustrated* vibrational modes. Most often, surface vibrational spectroscopy is used to probe the fundamental transition $\nu_0 \rightarrow \nu_1$, which can be described to a first approximation using a harmonic oscillator. In this model, the separation between vibrational energy levels is constant for all values of ν , where ν is the vibrational quantum number, ν_0 the fundamental frequency of the harmonic oscillator, k the force constant of the bond, and μ the reduced mass of atoms of mass m_1 and m_2 (Equation 1.5).³

$$\begin{aligned} E_\nu &= (\nu + 1/2)h\nu_0 \\ \nu_0 &= \frac{1}{2\pi} \sqrt{\frac{k}{\mu}} \\ \mu &= \frac{m_1 m_2}{m_1 + m_2} \end{aligned} \tag{1.5}$$

However, the harmonic model is unsuitable for describing higher vibrational level transition, molecular dissociation, low-frequency energy modes, overtones, or combinations bands, which are best described by a Morse potential (Figure 1.1). The vibrational energy for the Morse potential can be described by a high order polynomial that contains anharmonicity constants (x_e, y_e, etc) (Equation 1.6). The spacing between vibrational energy levels for a Morse potential is no longer constant as in the harmonic approximation and becomes virtually continuous for high values of ν .

$$E_\nu = (\nu + 1/2)h\nu_0 + (\nu + 1/2)^2 h\nu_0 x_e + (\nu + 1/2)^3 h\nu_0 y_e + \dots \tag{1.6}$$

Overall, vibrational spectra provide information about the type of chemical

bonds present in the sample. It is a definitive means in the identification of surface species formed from adsorption, as well as their on-surface reaction products. A variety of techniques are capable of providing vibrational data, and in this project, RAIRS and HREELS were employed.

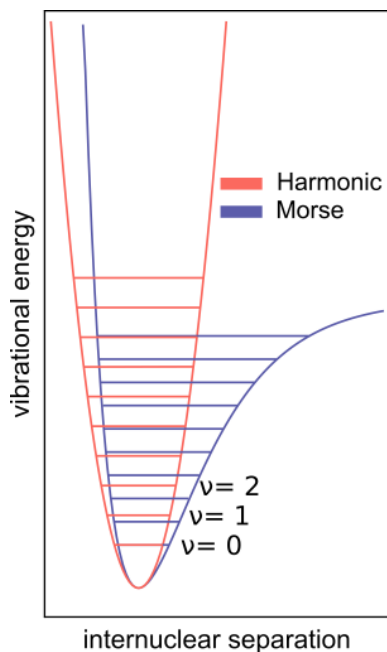


Figure 1.1 ■ Schematic of vibrational energy levels for a harmonic and Morse potential.

Reflection-Absorption Infrared Spectroscopy (RAIRS)

Reflection-absorption infrared spectroscopy (RAIRS) is a surface analytical technique that relies on a photon-in/photon-out approach to probe vibrational modes of adsorbates. Infrared light falls in the frequency range at which excitation of vibrational levels take place (1×10^{14} – $1 \times 10^{13} \text{ s}^{-1}$). A standard RAIRS apparatus operates at very high resolution (typically $\leq 4 \text{ cm}^{-1}$) within a spectral range between 600 – 4000 cm^{-1} . Since many surfaces including single crystals are opaque, a standard transmission experimental set-up is unsuitable, and surface analysis is performed in reflection mode instead. A typical experimental configuration in UHV is shown in Figure 1.2.a. An infrared beam passes

through an IR-transparent window and is focused using a series of mirrors onto the sample. The reflected beam passes through a second window and is collected at the detector. Upon illumination of a sample with IR light, some of the incoming light will be absorbed by the species, reducing the intensity of the reflected light. The detector is usually a mercury cadmium telluride (MCT) photoconductive element. The optical path of the beam on the atmospheric side of the set-up is purged with dry N₂ to remove strong IR absorbents (H₂O and CO₂), whose absorption bands can obscure the signal of the species of interest. Absorption occurs when the electric field of the infrared light resonates with the molecular vibrations, changing the dipole moment of the molecule. Therefore, only vibrations that produce a dipole moment change are infrared active.

The experiment is performed at a grazing incident angle, where the incident beam angle (θ_i) is equal to the reflected beam angle (θ_r) (specular) for a number of reasons. First, sensitivity is an issue since the number of species probed is less than 1×10^{15} molecules per cm². The number of probed species can be optimised by increasing the path length (x) of the incoming and reflected beam, which is proportional to the angle of incidence (θ_i) (Equation 1.7). Besides, at large values of θ_i , the penetration depth decreases d (Figure 1.2.b). This relationship is exploited in various other surface characterisation techniques such as X-ray photoelectron spectroscopy (XPS) to improve surface sensitivity. Secondly, RAIRS requires plane-polarised light, which can be either parallel (p -polarised) or perpendicular to the plane of incidence (s -polarised) (Figure 1.2.b). Upon reflection of s -polarised light, the electric field of the incident beam shifts by nearly 180°. As a result, the incident and reflected beam cancel each other out almost completely, and the resulting electric field at the surface is virtually zero. By contrast, the electric field of p -polarised light lies close to the surface normal. Upon reflection, there is almost no phase shift, and the magnitude of the field at the surface is enhanced. It follows from the relationship between incident angle θ_i and electric field component along the surface normal that this enhancement is optimum at grazing incident angles (Equation 1.8). The fact that the electric field of s -polarised light is virtually zero, with only p -polarised light able to induce vibrational excitation, leads to the so-called *surface selection rule*.⁴ This selection rule states that only vibrational transitions with components of the dynamic dipole moment normal to the surface are infrared active. Also, adsorption of molecules onto a surface causes

valence electrons to screen the molecular dipole by generating an *image dipole moment* (Figure 1.2.b). A molecular dipole moment parallel to the surface is entirely cancelled by the surface image dipole, whereas the surface image dipole reinforces a molecular dipole moment normal to the surface. Thus, only molecules with a component along the surface normal can couple with the electric field of the infrared light. The surface selection rule will be used in the qualitative assessment of molecular adsorption geometry throughout this thesis.

$$d = x \cos \theta_y \quad (1.7)$$

$$I(\theta) \propto \frac{1}{\cos \theta_i} \quad (1.8)$$

Because of the high resolution, a great deal of information can be derived from RAIR spectra. In particular, not only the distinction among various functional groups is possible, but also the type of adsorption site can be readily assigned for simple adsorbates. For example, CO coordination to 3-fold hollow, bridge, or atop sites of Pd(111) give rise to signature peaks at *ca* 1800 cm⁻¹, 1900 cm⁻¹, and 2100 cm⁻¹, respectively. This can be understood in simple terms as the increase of back donation from the metal into the CO π^* orbital and a decrease in bond order. Furthermore, changes due to coverage can also be detected by RAIRS. These changes can manifest as shifting of bands as a result of electronic changes in the sample and intermolecular interactions, or as dramatic changes in the intensity of the absorption bands due to molecular reorientation. Fast acquisition times of modern spectrometers can be exploited to study surface reaction kinetics, where a temperature ramp accompanies the RAIR data acquisition.⁴

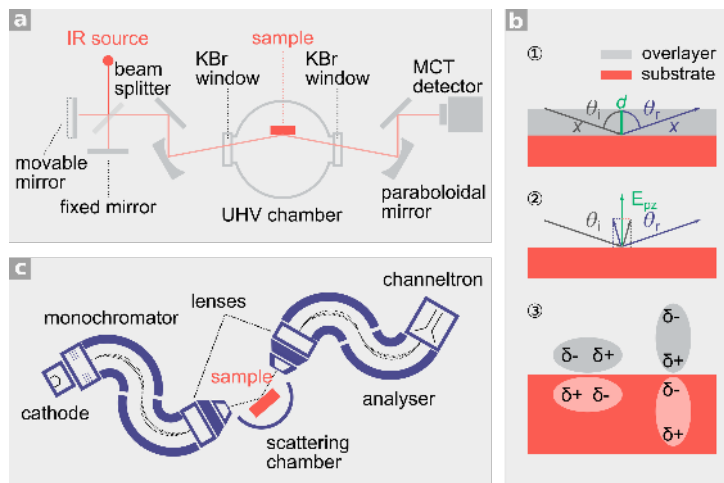


Figure 1.2 ■ Vibrational spectroscopy: RAIRS and HREELS a) Experimental set-up of reflection-absorption infrared spectrometre (RAIRS) b) Grazing incidence set-up. 1) Dependence of probe length on incidence angle. 2) Enhancement of electric field for p -polarised light along the z -direction (E_{pz}). 3) Surface image dipole (pink) for an adsorbate with a dipole parallel and perpendicular to the surface plane. The net effect is a cancellation for the former, and enhancement of the dipole moment for the latter. c) High-resolution electron energy loss spectrometer.

High-Resolution Electron Energy Loss Spectroscopy(HREELS)

Electrons interact strongly with matter, and when scattered from surfaces they can lose energy to the various degrees of freedom of the surface and the adlayer (inelastic process). By comparison to RAIRS, HREELS allows probing vibrational frequencies below 800 cm^{-1} with a sensitivity of 0.01 ML. For this reason, this analytical technique is suitable for the study of metal-molecule bonds and surface phonons, as they fall in the lower frequency range. Unlike RAIRS, the resolution of HREEL spectra is very low (typically around 40 cm^{-1}), and the HREELS technique requires UHV. The *high-resolution* in the acronym is only used to differentiate this technique from other electron spectroscopies used in the study of electronic excitations. In an HREELS experiment, a monochromatized electron beam ($E_0 = 5\text{--}20\text{ eV}$) generated by a LaB_6 filament is directed onto a sample (Figure 1.2.c). The inelastic collision of the incident electron with the surface results in the loss of some of its kinetic energy through the excitation of vibrational modes of energy $h\nu_0$. The scattered beam is then analysed and plotted as a function of kinetic energy loss (E_{kin})

relative to the primary beam (E_0) (Equation 1.9).

$$E_{kin} = E_0 - h\nu_0 \quad (1.9)$$

Three inelastic scattering mechanisms are possible. *Dipole scattering* is a long-range interaction between the electric field associated with a moving electron and the adsorbate or surface phonon. The mechanism is analogous to that described for RAIRS, where the scattered electron emerges at the same angle as the incident beam (specular scattering), and the same surface selection rule applies. The intensity of the peak varies proportionally to E_0 (Equation 1.10), and concentrates around a narrow lobe about the specular direction with a width given by Equation 1.11. In *impact scattering*, the electron's interaction with the scatterer occurs at close range. The electrons are thought of as particles that bounce off the ion cores. Because of momentum exchange, electron scattering is more isotropic and occurs in a wide range of directions ($\theta_i \neq \theta_r$). This mechanism overrides the surface selection rule and allows probing vibrational modes that would otherwise be silent in specular mode. Another short-range impact mechanism is also possible, where the electron is captured by the adsorbate in a negative ion state. This mechanism, known as *resonance scattering*, is highly dependent on E_0 and very short-lived (1×10^{-10} – 1×10^{-15} s). The angular distribution of the scattered electrons through a resonance reflects the symmetry of the negative ion state, that is, whether a σ or π symmetry state is involved.^{3,4}

$$I \propto \sqrt{E_0} \quad (1.10)$$

$$\delta\theta = \frac{\nu h}{2E_0} \quad (1.11)$$

1.3 Temperature Programmed Desorption (TPD)

Temperature programmed desorption (TPD) also referred to as thermal desorption spectroscopy (TDS) is a technique that can provide information about the binding strength of surface-adsorbate and lateral interactions. During a TPD experiment, adsorbates are thermally activated by raising the substrate temperature in a controlled manner. Thermal energy causes the adsorbates to either desorb, undergo an on-surface reaction, or a combination of both scenarios.⁴ A standard experimental set-up involves depositing molecules onto a substrate held at ambient or subambient temperature. A linear temperature ramp is then applied, and the rate of desorption monitored with a quadrupole mass spectrometer (QMS) in direct line of sight of the sample (Figure 1.3.a). The QMS measures the ion current of a selected fragment or series of fragments as a function of time or temperature, which is directly proportional to the number of desorbed species. In flash desorption experiments, the sample is resistively heated by a filament ion beams or lasers to induce rapid desorption rates. In this operation mode, the desorption rate is higher than the pumping speed, producing a sigmoidal shaped spectrum. Most commonly, desorption rates slower than the pumping speed are employed ($\beta = 1\text{--}100\text{ Ks}^{-1}$), which produces peak features in TPD spectra instead. Equation 1.12 illustrates the relationship between initial and final temperature in a linear ramp, where T_f is the final temperature, T_i is the initial temperature, β is the heating rate, and t is the time the temperature ramp takes.

$$T_f = T_i + \beta t \quad (1.12)$$

In the simplest case, the molecules desorb intact from the surface once the thermal energy exceeds the activation energy (desorption-limited desorption). More complex scenarios usually arise where the adsorbates fragment, recombine or rearrange to form new species. The new species can then desorb promptly as soon as they are formed (reaction-limited desorption), or may require further thermal energy (higher temperatures) to overcome the necessary activation energy for desorption. TPD spectra can provide quantitative information of physisorbed and chemisorbed states, coverage, and type of binding

sites. Also, lateral interactions and kinetic order of the desorption process may sometimes be inferred. However, TPD does not provide any information regarding the processes occurring between the adsorption and desorption events. Deviation from ideal cases include site migration of adsorbates during heating, and changes in the pre-exponential factor as a function of coverage. Another limitation of this technique is the destructive nature of data acquisition, which might be impractical if the number of samples available is limited. Depending on the instrument resolution, isobaric molecular fragments can appear indistinguishable. For example, a fragment with a nominal mass-to-charge ratio of $m/z = 28$ amu can equally be assigned to CO, C₂H₄, or N₂.

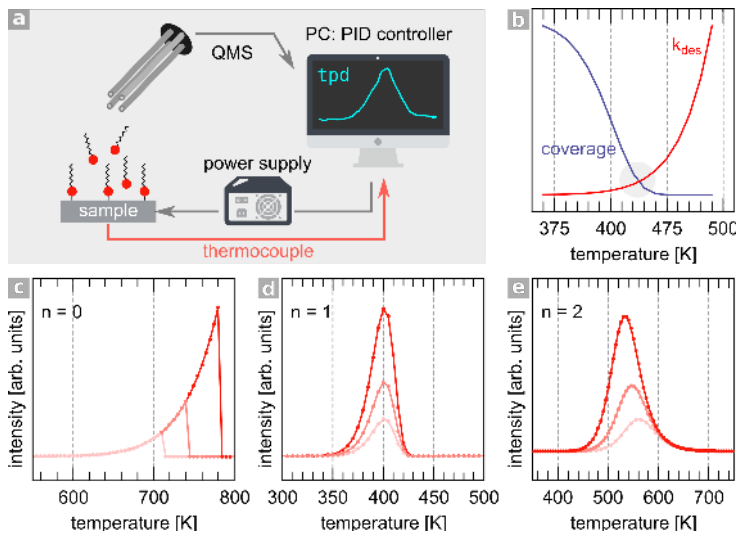


Figure 1.3 ■ Temperature programmed desorption (TPD). **a)** Schematic of a TPD experimental set-up. **b)** TPD peaks are the product of k_{des} and θ terms in Equation 1.17. **c)** Simulated TPD spectra for **c)** zeroth ($z = 1 \times 10^{32} \text{ s}^{-1}$), **d)** first ($z = 1 \times 10^{13} \text{ s}^{-1}$), and **e)** second order ($z = 1 \times 10^{-6} \text{ s}^{-1}$) kinetics at $\beta = 1 \text{ K s}^{-1}$, $E_{des} = 120 \text{ kJ mol}^{-1}$

The desorption rate in TPD can be expressed by Equation 1.13, where θ is the surface coverage, t is time, k_{des} is the desorption rate constant, and n the desorption order.

$$\text{desorption rate} = -\frac{d\theta}{dt} = k_{des}\theta^n \quad (1.13)$$

The desorption rate can be written in term of temperature other than time,

where β represents the heating rate:

$$\frac{d\theta}{dt} = \frac{d\theta}{dT} \frac{dT}{dt} = \frac{d\theta}{dT} \beta \quad (1.14)$$

Replacing and rearranging Equation 1.14 into Equation 1.13 one obtains:

$$desorption\ rate = -\frac{d\theta}{dT} = \frac{k_{des}}{\beta} \theta^n \quad (1.15)$$

The rate constant term k_{des} takes the form of an Arrhenius expression, where z is the pre-exponential factor, E_{des} the activation energy for desorption, R the gas constant, and T the temperature.

$$k_{des} = z \exp\left(\frac{-E_{des}}{RT}\right) \quad (1.16)$$

Inserting the expanded expression of k_{des} into Equation 1.15, one arrives at the Polanyi-Wigner equation:

$$desorption\ rate = -\frac{d\theta}{dT} = \theta^n \frac{z}{\beta} \exp\left(\frac{-E_{des}}{RT}\right) \quad (1.17)$$

The terms in Equation 1.17 indicate that the exponential and the surface coverage factors contribute to the observed the desorption rate. The rate of desorption initially increases exponentially as the temperature is raised. However, the desorption rate does not increase indefinitely, since the surface coverage is limited and becomes depleted as more molecules are thermally desorbed. The peak in the TPD spectra represents the maximum possible desorption rate, after which, the diminishing surface coverage causes the rate to drop. The temperature at which the rate is maximum ($T_{max.}$), and the peak of TPD spectra, is where the first derivative of the function equals zero (Equation 1.18):

$$\frac{E_{des}}{RT_{max.}^2} = n\theta^{n-1} \frac{z}{\beta} \exp\left(\frac{-E_{des}}{RT_{max.}}\right) \quad (1.18)$$

The shape of the peak in TPD spectra depends on the heating rate, the pre-exponential factor, and the kinetic order of the desorption process. Figure 1.3.c-e illustrates the desorption profile for $n = 0, 1$ and 2 while at a fixed E_{des} . For zeroth order kinetics, the desorption rate does not depend on coverage. For example, when the concentration of species is very high as in the case of multilayers, the kinetics are zeroth order. The desorption profile features an exponentially increasing trace which plummets with a common leading edge. $T_{max.}$ shifts up in temperature with increasing coverage. For first-order desorption kinetics, the rate is directly proportional to the coverage. The peaks are asymmetric and $T_{max.}$ remains constant at all coverages for a defined binding site. Second order kinetics feature symmetric peaks around $T_{max.}$, which shift to lower temperatures as the coverage increases. This scenario is often encountered in recombinative desorption, or in systems where repulsive lateral forces are significant. The position of the peak ($T_{max.}$) depends on the activation energy and is highly specific to the adsorbate-substrate bond. The heat of desorption is equal to the heat of adsorption with the proviso that the process is reversible and non-dissociative. As a result, adsorbates occupying binding sites with distinct activation energies will each produce a corresponding peak in the TPD spectra. Strongly-adsorbed molecules will produce a ($T_{max.}$) at high temperatures, whereas the opposite will be true for weakly-bound species (*e.g.*, physisorbed or weakly chemisorbed). The intensity of the peak is proportional to the surface coverage, providing that the activation energy for desorption remain constant for all coverages. In some favourable cases, absolute coverages can be derived if the at least one surface coverage is known. For example, CO adsorption on Rh(111) produces a $(\sqrt{3} \times \sqrt{3}) R30^\circ$ superstructure that can be observed by LEED and represents a coverage of $1/3$ ML. Any other coverage can be derived from TPD spectra by taking the ratio between the reference coverage, and that of the unknown sample.⁵

Some of the investigated cases in this thesis exhibited first-order desorption, that is, $n = 1$. Hence, in these particular cases, Equation 1.18 reduces to:

$$\frac{E_{des}}{RT_{max.}^2} = \frac{z}{\beta} \exp \left(\frac{-E_{des}}{RT_{max.}} \right) \quad (1.19)$$

Rearranging this expression and taking the natural logarithm yields Equa-

tion 1.20:

$$E_{des} = RT_{max.} \left(\ln \left(\frac{zT_{max.}}{\beta} \right) - \ln \left(\frac{E_{des}}{RT_{max.}} \right) \right)$$

$$\text{where } \ln \left(\frac{E_{des}}{RT_{max.}} \right) \equiv 3.46 \quad (1.20)$$

The simplified form of this equation is the Redhead equation, where the second logarithmic term is approximated to a value of 3.46.⁶ The assumptions of this models are that the activation energy and the pre-exponential factor ($z = 1 \times 10^{13} \text{ s}^{-1}$) are coverage independent, and that desorption occurs in a single step. Note that more rigorous TPD analysis tools are available which provide more accurate values of E_{des} .⁷ However, due to the low quality of the data and for comparison purposes, this simplified model was employed in the desorption energies quoted in this work.

1.4 Low Energy Electron Diffraction (LEED)

Low energy electron diffraction is a convenient surface science technique for the characterisation of periodic structures. Information such as unit cell vectors, angles, and commensurability between a substrate and an overlayer can be extracted from LEED patterns. A standard LEED experiment involves directing a collimated beam of electrons onto an earthed conductive sample (Figure 1.4.a). The inelastically scattered beam is filtered off from the elastic beam by a series of grids. The first grid (G1) is earthed to ensure a field-free region; the second and third grids (G2+G3) are held at a negative potential and act as a filter to inelastically scattered electrons. The electron beam is accelerated towards a phosphor screen held at a positive potential (1–7 kV) and focused using a series of condenser optics, which upon electron impact causes the screen to fluoresce. A fourth grid (G4), also earthed, is placed between G3 and the phosphor screen to shield the high positive voltage at which a

phosphor screen is held. Typical energies of the incident beam employed in a LEED experiment lie in the 20–200 eV range. Energy beams of this energy have a De Broglie wavelengths of $\lambda = 0.86\text{--}2.74 \text{ \AA}$ (Equations 1.21-1.23), which is close to interatomic spacing and diffraction occurs. Additionally, the inelastic mean free path (IMFP) of electrons with this kinetic energy is in the order of a few atomic layers, making LEED is a surface-sensitive technique.

De Broglie equation describes the wave properties of particles, where λ = wavelength, h = Planck's constant, p = momentum, m = mass of the particle ($m = m_e$ for electrons), and v = velocity of the particle:

$$\lambda = \frac{h}{p} = \frac{h}{mv} \quad (1.21)$$

The potential energy of the electron ($E_{potential}$) is equal to the acceleration voltage of the beam (V) times the charge of the electron (q), which is transformed into kinetic energy ($E_{kinetic}$). Equating these two expressions one obtains another expression that relates the velocity of the electron (v) to the accelerating voltage of the beam V .

$$\begin{aligned} E_{potential} &= qV \\ E_{kinetic} &= \frac{1}{2}mv^2 \\ E_{potential} &= E_{kinetic} \\ qV &= \frac{1}{2}mv^2 \\ v &= \sqrt{\frac{2qV}{m}} \end{aligned} \quad (1.22)$$

Inserting the expression for v (Equation 1.22) into Equation 1.21, one obtains an expression that relates the acceleration potential of the beam energy (V in eV) to the electron wavelength:

$$\begin{aligned}\lambda &= \frac{h}{m\sqrt{\frac{2qV}{m}}} \\ &= \left(\frac{150.4}{V}\right)^{\frac{1}{2}} (\text{\AA})\end{aligned}\tag{1.23}$$

Scattering of the incident electron wave occurs from highly localised electron density areas in the sample, which interfere constructively and destructively to generate the resulting LEED pattern. 2D scattering manifests as a series of bright spots in a dark background. The pattern and its intensity reflect the orderliness and position of the atoms they have been scattered from in reciprocal space. A diffuse pattern or complete absence of diffraction spots is often indicative of an amorphous surface or superstructure, contamination, or short-range order. Even for a clean surface, some other factors such as surface defects, reconstruction, and relaxation can contribute to the broadening and attenuation of the diffraction pattern. Deviation from the perfect monochromatic collimated beam may arise due to energy and angular spread. As a result, the electron beam is only coherent over a specific range (10–50 nm). Surface atoms that scatter non-coherent electrons cannot form a diffraction pattern. Thus, in practice, a sharp LEED pattern may still be produced by a somewhat disordered structure if some order falls within the coherence length of the beam.

Figure 1.4.b depicts a simplification of the diffraction process for a 1D row of atoms.^{4,5} The difference in the path length between diffracted beams (OB) can be derived from simple geometry arguments. For constructive interference, the difference in path lengths between two diffracted beams OB must satisfy the following:

$$\overline{OB} = n\lambda\tag{1.24}$$

Similarly, \overline{OB} is also related to the modulus of the lattice constant $|a_1|$ and the angle between the incident beam and the diffracted beam θ_{a_1} :

$$\sin\theta_{a_1} = \frac{\overline{OB}}{\overline{OA}}$$

$$\overline{OB} = \overline{OA}\sin\theta_{a_1} = |a_1| \sin\theta_{a_1} \quad (1.25)$$

Substituting Equation 1.24 into Equation 1.25 one obtains Bragg's condition for diffraction, which states that constructive interference occurs when $n =$ integer, with total or partial destructive interference for non-integers values of n :

$$n\lambda = |a_1| \sin\theta_{a_1} \quad (1.26)$$

It follows from this relationship that only periodic structures can produce a diffraction pattern, and the pattern will exhibit the following characteristics:⁸

- The intensity of the pattern is symmetrical about $\theta_{a_1} = 0^\circ$.
- $\sin\theta_{a_1}$ is proportional to $\frac{1}{\sqrt{V}}$.
- $\sin\theta_{a_1}$ is proportional to $|a_1|^{-1}$.

For a constant value of $|a_1|$, the diffracted beam θ_{a_1} is inversely proportional to the beam energy V (Equation 1.23). As a consequence, the diffracted beams will appear closer together for high energy electron beams. The LEED pattern is essentially a scaled representation of the surface structure in reciprocal space and is described as follows. The energy of the incident beam is known and can be expressed as a wave vector:

$$|k_0| = \hbar p \quad (1.27)$$

Rearranging Equation 1.21 and substituting into Equation 1.27:

$$|k_0| = \hbar p = \frac{2\pi}{h} p = \frac{2\pi}{h} \frac{h}{\lambda} = \frac{2\pi}{\lambda} \quad (1.28)$$

Inserting this expression into the Bragg's condition for diffraction (Equation 1.26) and rearranging yields:

$$\Delta k_{a_1\parallel} = |k_0| \sin\theta_{a_1} = n \frac{2\pi}{|a_1|} \quad (1.29)$$

Equation 1.29 is the parallel momentum exchange ($\Delta k_{a_1\parallel}$) between the incident electron beam ($|k_0\rangle$) and the surface, where $\frac{2\pi}{|a|}$ is the reciprocal lattice vector $|a_1^*|$. For an incident electron beam normal to the surface $\Delta k_{\parallel} = 0 \text{ \AA}^{-1}$, therefore for diffraction to arise the electrons must change direction by exchanging parallel momentum with the lattice in quantised units of $\frac{2\pi}{|a_1|}$. A similar expression can be written for the lattice parameter a_2 (Equation 1.30). For constructive interference in 2D and a LEED pattern to emerge, Equation 1.29 and Equation 1.30 must be satisfied simultaneously as expressed by Equation 1.31, where G is the reciprocal lattice vector.

$$\Delta k_{a_2\parallel} = |k_0| \sin\theta_{a_2} = m \frac{2\pi}{|a_2|} \quad (1.30)$$

$$G = |k_{a_1\parallel}| + |k_{a_2\parallel}| = n \frac{2\pi}{|a_1|} + m \frac{2\pi}{|a_2|} \quad (1.31)$$

From this expression, the relationship between the moduli and direction of real and reciprocal space can be readily derived as shown in Equation 1.32, where α is the angle between a_1 and a_1^* , and β the angle between a_2 and a_2^* . Also, the dot product establishes that a_1 and a_2^* are perpendicular to one another, and so are a_2 and a_1^* . An analogous derivation can be achieved for overlayers with real space vectors b_1, b_2 and reciprocal lattice vectors b_1^*, b_2^* . The relationship between real and reciprocal space vectors is illustrated in Figure 1.4.c,d for a $(1\ 1|-1\ 2)$ or $(\sqrt{3} \times \sqrt{3}) R30^\circ$ in Wood's notation.[‡] The number of diffraction spots observed in a LEED pattern for a given energy beam can be worked out by constructing a reciprocal space lattice and counting the number of spots that fall within a circle of radius k_0 (Ewald's circle).

[‡] $\left(\frac{b_1}{a_1} \times \frac{a_2}{b_2} \right) R\theta^\circ$

$$\begin{aligned}
|a_1^*| &= \frac{2\pi}{|a_1| \sin\alpha} \\
|a_2^*| &= \frac{2\pi}{|a_2| \sin\beta} \\
a_1 \cdot a_2^* &= a_2 \cdot a_1^* = 0
\end{aligned} \tag{1.32}$$

Very often one is interested in investigating overlayers formed upon adsorption of molecules onto a clean substrate. If the overlayer exhibits long-range periodic order, a LEED pattern may be detected. Conversion from reciprocal space to real space is achieved by taking the inverse transpose of the reciprocal unit cell matrix (A^*):

$$A^* = \begin{pmatrix} b_1^* \\ b_2^* \end{pmatrix} \times \begin{pmatrix} a_1^* & a_2^* \end{pmatrix} = \begin{pmatrix} b_1^* a_1^* & b_1^* a_2^* \\ b_2^* a_1^* & b_2^* a_2^* \end{pmatrix} \tag{1.33}$$

For example, the unit cell in reciprocal space of the overlayer in Figure 1.4.d can be described in matrix notation as:

$$A^* = \begin{pmatrix} 2/3 & -1/3 \\ 1/3 & 1/3 \end{pmatrix} \tag{1.34}$$

The inverse transpose of the reciprocal space unit cell matrix (A^*) produces the real space unit cell matrix (A):

$$A = \left((A^*)^{-1} \right)^t = \begin{pmatrix} 1 & -1 \\ 1 & 2 \end{pmatrix} \tag{1.35}$$

Qualitative analysis of LEED patterns already yields a great deal of information about the surface and the adsorbate periodicity. However, it reveals no information regarding atomic positions, bond length or angles. Overlayers with the same periodicity and different binding sites will produce exactly the same pattern. However, quantitative measurements of spot intensity as a function

of electron beam generate LEED I-V curves, which aided by iterative fitting of theoretical models, can reveal atomic information. Even though the diffraction process can be described as the two-dimensional elastic scattering of electrons, in reality, some electrons can penetrate a few atomic layers into the bulk, and a z-component contributes to some extent to the total diffraction. Aside from the Braggs condition for constructive interference, multiple scattering and the potential experienced by the electron due to the ion cores (inner potential) also influence the pattern.

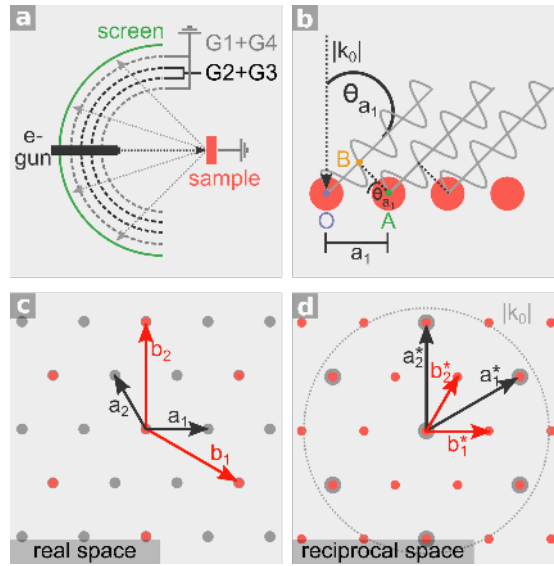


Figure 1.4 ■ Low energy electron diffraction (LEED) **a)** Schematic representation of a LEED apparatus. **b)** Schematic of a 1D row of atoms (red) and diffracted beams (light grey). $|k_0|$: wavevector of the incident beam, θ_{a_1} : angle between the incident beam and the diffracted beam, a : lattice constant; O, A, and B are points. Adapted from reference [5]. **c)** Real-space representation of a hexagonal substrate (grey), and an overlayer (red). The overlayer forms a $(1\ -1\ 1\ 2)$ superstructure (also known as $(\sqrt{3} \times \sqrt{3}) R30^\circ$). a_1 and a_2 are the substrate real space vectors, and b_1 and b_2 are the overlayer real space vectors. **d)** Reciprocal space representation of c), a_1^* and a_2^* are the substrate reciprocal space vectors, b_1^* and b_2^* are the overlayer reciprocal space vectors. The Ewald's circle of radius $r = |k_0|$ is also marked, which encloses the number of diffraction spots observed in a LEED pattern.

1.5 Scanning Tunnelling Microscopy (STM)

Scanning tunnelling microscopy is a powerful surface visualisation tool which has, since its development, played a vital role in the advancement of surface characterisation and nanotechnology.^{9,10} STM permits the visualisation of surfaces in real space and can, in favourable circumstances, achieve atomic resolution. More rigorously, this technique allows the mapping of the local density of states (LDOS). Unlike diffraction techniques, STM does not require the samples under investigation to be periodic. This technique is extremely versatile in that it does not require special experimental set-ups, and can be implemented in vacuum, ambient conditions, and even in the presence of a liquid adlayer at the tip-surface interface. Additionally, data acquisition can be performed *in situ* to study dynamic processes, and simultaneously coupled with other surface analysis tools such as electrochemical cells (EC-STM). The principal disadvantage of STM, however, is that the sample must be conducting, and imposes a practical limit to what materials can be probed. A typical set up involves an atomically sharp metallic tip brought near the surface at a distance of a few angstroms but without electrical contact. For experiments performed in ambient conditions, Pt₈₀Ir₂₀ is the material of choice for tip preparation, whereas electrochemically etched W tips are generally used in UHV environments. A potential difference is applied either to the sample or tip ranging from few mV to V. This causes a shift upwards or downwards of the Fermi level depending on the potential bias. In doing so, a small yet measurable net current flows from the filled states of the tip into the empty states of the sample or *vice versa* (Figure 1.5.a). This current, known as "tunnelling current", provides a means of monitoring changes in tip-sample height. A piezoelectric tube (lead-zirconium-titanate) controls the movement of the tip in the *x*, *y* and *z* directions. During data acquisition, the tip is rastered across the first scan line in the forward and backward directions. Then, the tip steps in the perpendicular direction and the process repeated onto the second, third and successive line scans. Two operation modes are possible: in constant height mode, the tip is held at a fixed position and moved across the surface while monitoring changes in the tunnelling current. This mode is suitable for atomically flat surfaces and allows data acquisition at high scan rates. The disadvantage of constant height mode is the potential damage to the tip by

colliding against protrusions such step edges or islands. For complex samples, the constant current mode is often preferred, where the tunnelling current is maintained constant through a feedback control loop. The piezoelectric tube contracts or retracts along the z -direction (1 \AA mV^{-1}) to maintain the tunnelling current set-point. The measured tunnelling current in constant height mode, or the tip movement in constant current mode, is plotted in a heat map which produces the resulting STM topograph.

Beyond imaging, STM can serve as a tool for the precise manipulation of individual atoms and molecules.¹¹ Another operational mode of this technique is scanning tunnelling spectroscopy (STS), which permits probing the electronic structure of surfaces at specific atomic sites. Furthermore, the second derivative of I-V curves can provide information about adsorbate vibrational modes with ultrasensitivity and high resolution.

The underlying mechanism of STM is based on the quantum tunnelling of electrons. A simplified picture of this phenomenon can be explained using "the particle in a box" model in 1D. In classical mechanics, a particle trapped in a potential well cannot escape unless their total energy is greater than the energy barrier. For electrons in the sample or tip in STM, this energy barrier is equal to the work function of the material (Φ), which is in the order of a few electronvolts (*e.g.*, $\Phi = 5.1 \text{ eV}$ for Au(111)). At 298 K, thermal energy amounts to only *ca* 25 meV, which is insufficient to overcome the work function. However, a non-classical mechanism is possible, where the probability of this event happening is non-zero. The electrons at the Fermi level can tunnel through other than overcoming the potential barrier, as illustrated in Figure 1.5.b. The Schrödinger expression for a one dimensional wave ($\Psi(x)$) can be written as Equation 1.36, where $\hbar = h/2\pi$ with h = Planck's constant, m is the mass of the particle trapped in the potential well ($m = m_e$), $V(x)$ is the potential energy, and E is the sum of kinetic and potential energy.

$$-\frac{\hbar^2}{2m} \frac{d^2\Psi(x)}{dx^2} + V(x)\Psi(x) = E\Psi(x) \quad (1.36)$$

Rearrangement and simplification of Equation 1.36 lead to:

$$-\frac{\hbar^2}{2m} \frac{d^2\Psi(x)}{dx^2} + (V - E)\Psi_x = 0 \quad (1.37)$$

$$\frac{d^2}{dx^2}\Psi(x) + k^2\Psi(x) = 0 \quad (1.38)$$

$$k^2 = \frac{2m(V - E)}{\hbar^2} \quad (1.39)$$

The solutions of the Schrödinger equation for regions A, B, and C shown in Figure 1.5.b are:

$$\Psi_1(x) = Ae^{ikx} + Be^{-ikx} \quad \text{for } x < 0 \quad (1.40)$$

$$\Psi_2(x) = Ce^{kx} + De^{-kx} \quad \text{for } 0 \leq x \leq a \quad (1.41)$$

$$\Psi_3(x) = Ee^{ikx} + Fe^{-ikx} \quad \text{for } x > a \quad (1.42)$$

The wavefunction oscillates in regions A and C, whereas it decays exponentially through the barrier in region B. The tunnelling current (I_t) is proportional to the transmission coefficients of the forward wave in region A and C (Equation 1.43). The tunnelling current depends exponentially on the barrier distance (d) (*i.e.*, the distance between the tip and the surface) and on the difference between the electron energy and the potential barrier ($V - E$) or the work function (Φ). In fact, high resolution is achieved because of the exponential dependence on the tunnelling current. For example, when $\Delta d = 1 \text{ \AA}$ the tunnelling current decreases by one order of magnitude. More rigorous theoretical models of STM such as Tersoff-Hamman can also account for all three dimensions, the density of states of the tip and the sample and their wavefunction overlap.¹²

$$I_t = \frac{|A|^2}{|E|^2} \propto \exp\left(-\frac{2d}{\hbar} \sqrt{2m(V - E)}\right) \quad (1.43)$$

Interpretation of STM data requires some caution. In many cases, the highest LDOS are centred at the atom, and the protrusions can be related to the

atomic position. However, STM images are not a direct topographic image of the surface, but an isosurface of LDOS. Higher conducting domains may be mistakenly attributed to raised features, especially for semiconductors. Besides, regions where the LDOS are low, may strikingly appear as depressions, for example, O/Cu(111).¹³ Besides, selecting a positive or negative bias may reveal additional information by probing empty and filled states, as demonstrated by Stroscio and Feenstra in their study of GaAs.¹⁴ The LDOS of adsorbates do not necessarily correspond to pure HOMOs and LUMOs of the isolated molecules. The interaction between adsorbates and surfaces results in mixing, shifting, and broadening of molecular and surface states. Only under specific conditions, where molecules are electronically decoupled from the substrate, direct visualisation of pure molecular states is possible.¹⁵ Another consideration is that tunnelling may arise from different states other than the HOMO or LUMO, such as those energy levels above and below (*i.e.*, HOMO-1, HOMO-2 and LUMO+1, LUMO+2) may also contribute to the topograph.

The resolution of STM data is affected by several factors such as tip condition, vibration isolation, and the nature of the system under investigation. Thermal drift and piezoelectric creep effects very often arise, which have the effect of distorting the image.¹⁶ When a voltage is applied to expand or contract the piezoelectric element that controls the tip, this will initially do so at a fast rate and will slow down as it approaches the defined scan size. This variation in expansion/contraction rates produces what is known as piezo creep. This effect can occur along the x-direction and is pronounced at the edges of large scan areas, where the forward and backward scans take different times, causing hysteresis. Piezo creep along the z-direction may also occur when the tip runs into a step, as retracting the tip involves a sudden change in the voltage. Cross-coupling of the x and y movements with the z-component may also occur due to non-uniform electric fields.

Thermal drift arises from temperature gradients from different sources in the experimental set-up but can be improved by allowing the system to regain thermal equilibrium. Higher resolution images can also be obtained at cryogenic temperatures; such conditions simultaneously reduce molecular diffusion of adsorbates on the surface and the thermal expansion/contraction of the piezo crystal. Preparation of atomically sharp tips is also required for

high-resolution imaging. Approximately 90–99 % of the total tunnelling current comes from the tip apex. However, variations in the tip geometry can cause two or more apex atoms to take part in tunnelling, giving rise to double-tip image artefacts. Adventitious adsorption of molecules onto the tip can produce noisy images as molecules are dragged across the surface during the scan.

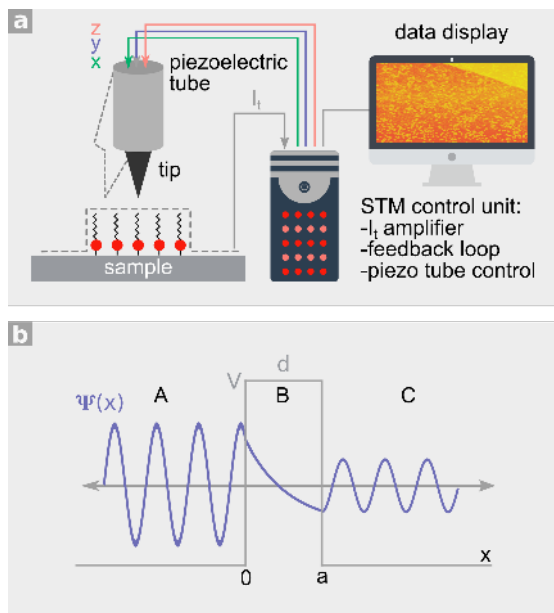


Figure 1.5 ■ Scanning tunnelling microscopy (STM). a) Schematic of a constant current STM experimental set-up. b) One dimensional wavefunction ($\Psi(x)$) bound to a potential well (A), tunnelling through a potential barrier of dimensions V and d (B), and emerging on the other side of the barrier (C).

1.6 General Considerations

Experiments were conducted in three separate stainless steel UHV chambers hosting an Ar ion sputtering gun and annealing facilities for sample cleaning. UHV was attained by a combination of turbomolecular, ion, and entrapment pumps. TPD data were collected in a UHV chamber hosting a LEED-Auger spectrometer (SpectaLEED, Omicron), and a quadrupole mass spectrometer (QMS) in direct line-of-sight with the crystal (SPECTRA, Microvision Plus) ($P_{base} = 3 \times 10^{-10}$ mbar). In all cases the electron impact ionisation energy was

$E_{ion.} = 69.8$ eV. STM measurements were carried out in a second chamber (base pressure $P_{base} = 1 \times 10^{-10}$ mbar) equipped with a scanning tunnelling microscope (VT SPM, Omicron), and a LEED optics (SpectaLEED, Omicron). All the STM images were recorded in constant current mode at room temperature (*ca* 300 K) using an electrochemically etched polycrystalline W tip. The stated voltages correspond to the sample bias. RAIR spectra were acquired at the grazing angle geometry at 300 K in an adjacent chamber to the STM isolated by a gate valve ($P_{base} = 7 \times 10^{-10}$ mbar). A mercury cadmium telluride (MCT) detector was used, which was cooled down over liquid nitrogen. The optical path was purged with N₂ overnight until a reproducible constant background was obtained. The spectra presented is the baseline corrected average over 1000 scans, and is expressed as the change in reflectivity $\Delta R/R_0$. HREEL spectra were acquired in a third chamber ($P_{base} = 3 \times 10^{-11}$ mbar) hosting sample cleaning facilities and an adjacent preparation chamber isolated from the analysis chamber by a gate valve. All HREEL spectra were acquired in specular mode $\theta_{in} = \theta_{out} = 45^\circ$. The spectra were normalised using Equation (1.44), where S' is the normalised signal, S is the unprocessed signal, $S_{min.}$ is the minimum in the unprocessed signal, and $S_{max.}$ is the maximum in the unprocessed signal (elastic peak). FFT filtering was in some cases performed on some spectra and will be indicated in the figure caption. TPD, RAIRS and HREEL spectra have been arbitrarily offset in the ordinate axis to aid visual comparison.

$$S' = \frac{S - S_{min.}}{S_{max.} - S_{min.}} \quad (1.44)$$

All the experiments described in this thesis were performed on (111) truncated single crystal of Pd, Au and Cu. The crystals were cleaned by cycling between Ar ion sputtering ($I_{sample} \geq 10 \mu A$) and annealing. Each cleaning cycle was terminated by an extended annealing cycle of $t = 15$ min to restore a well-ordered surface. In the case of Pd(111), the cleaning routine also involved a third step where the sample was annealed in an oxygen-rich atmosphere (Table 1). This cleaning routine produced LEED patterns with sharp integral order spots and low background intensity, and a featureless HREEL spectra. STM imaging of the surfaces exhibited well-defined monoatomic steps and flat terraces of width $w \geq 200$ nm with little evidence of contamination, which would manifest as bright asperities combined with poor imaging. The sample

temperature was monitored using a type-K thermocouple spot welded to the back of the crystal. Annealing of the sample was achieved by passing a current directly through the crystal, or resistively through a Ta filament or a pyrolytic boron nitride (PBN) plate. Gold deposition was achieved by exposing the crystal to a resistively heated gold wire (99.999 % purity) wound around a W wire ($\varnothing = 0.5$ mm). Image thresholding of STM images was used to derive the coverage and deposition rate. Except for CO and O₂, all the chemicals employed were solid powders. Deposition of the compounds was achieved by resistively heating a borosilicate glass microcapillary containing the chemical wrapped in Ta wire. The sublimed chemical was admitted via a differentially pumped back line isolated from the chamber by a gate valve. In all cases, the doser was outgassed for at least 12 h prior to being admitted into the chamber (Table 2). Dosing temperatures were obtained from mass spectrometry, the fragmentation pattern of the sublimed chemical was monitored until the spectrum was consistent with the structure of the molecule in the gas phase.

Table 1 ■ Crystal cleaning.

Substrate	Ar ion sputtering	Annealing
Pd(111) ^a	1.50 kV	950 K
Au(111)	1.25 kV	775 K
Cu(111)	1.55 kV	800 K

^a $P_{O_2} = 1 \times 10^{-7}$ mbar, $T = 875$ K, $t = 30$ min

Table 2 ■ Chemical doser deposition conditions. *outgas.*: outgassing temperature, *dose.*: dosing temperature.

Compound	T _{outgas.}	T _{dose.}
Melamine, BDH Chemicals, 97.5 %	340 K	365 K
TPA, Sigma-Aldrich, 99 %	330 K	380 K
TBPB, Sigma-Aldrich, 97 %	340 K	435 K
BDBA, Sigma-Aldrich, ≥ 95 %	300 K	453 K
BPBA, Sigma-Aldrich, ≥ 95 %	300 K	443 K
DM NHC	300 K	335 K
DET NHC	300 K	325 K
DISO NHC	300 K	325 K
DBZ NHC	300 K	350 K

Conventions

Whenever the adsorbed molecule formed an ordered structure as visible by STM or LEED, the surface coverage is formally given as the number of adsorbate molecules per unit cell relative to the number of substrate atoms; where 1 ML indicates that there is one molecule per substrate atom (Equation 1.45). In the instances where ordered structures were not resolved, but the molecule underwent reversible desorption (*e.g.*, *DISO NHC*), the surface coverage is given as fractions of a saturated peak in TPD spectra. Whenever neither of these requirements was met, the quantification of dosed material to the surface is given in units of exposure (1 L = 1×10^{-6} Torr s). Note that the quoted exposures are only nominal and do not necessarily reflect the true amount of pure sublimed chemical. Background gases in the manifold line also contribute to the increase in pressure, which varied from one chamber to the next. Unless otherwise stated, dimensions of individual molecular features derived from STM measurements are reported as the mean value measured at full-width half maxima of line profiles and the standard deviation of a sample. Surface directions were derived from LEED patterns and by comparison to the propagation of step edges in STM images, which usually follow the $\langle 1\bar{1}0 \rangle$ direction. The superstructures have been labelled according to the following conventions: 1) \vec{a} is the shortest vector of the superstructure in real space, and vector \vec{b} the longest. 2) The vectors have been selected so that the \vec{b} is the first vector encountered in the anticlockwise direction starting from vector \vec{a} . Adsorbate unit cells are reported relative to primitive unit vectors oriented along the $\langle 1\bar{1}0 \rangle$ surface direction at an angle of 120° from each other.

$$\theta(\text{ML}) = \frac{\text{molecules per unit cell}}{\text{number of substrate atoms per unit cell}} \quad (1.45)$$

Analysis routines

The position of spectral peaks was determined from the zero-crossing of the ordinate in the first derivative of the signal. 1–5 unweighted sliding-average smoothing cycles and interpolation were applied to the raw signal. In the instances where the peaks were too convoluted to be resolved by this method, Gaussian fitting of the signal was employed instead. Desorption activation energies in TPD spectra were derived using a Redhead approximation.⁶ Routine image processing of raw STM data involved global and local plane subtraction, row alignment by median or median of differences, thresholding, skeletonisation, band-stop filter in the Fourier domain, and Gaussian convolution using Gwyddion 2.44¹⁷ and ImageJ 1.50d.¹⁸ Images have not been corrected for drift. Quantitative analysis in real space was carried out by thresholding of a grey scale image or by binary conversion of the topograph using ImageJ.¹⁸ Visual inspection and manual correction of the threshold was sometimes necessary to avoid spurious counting. Unit cell vectors and angles were derived from the fast Fourier transform (FFT) of the topograph. QtiPlot 0.9.9.11,¹⁹ OriginPro 9.1,²⁰ and GNU Octave 4.0.0²¹ were employed for data plotting and analysis. LEED patterns were simulated using LEEDpat 4.2.²² Molecular drawing and representation were done using Blender 2.79,²³ XCrysDen 1.5.60,²⁴ Avogadro 1.1.1,²⁵ and BKChem 0.13.0.²⁶ Inkscape 0.91 was used to group the figures and in the design of diagrams.²⁷

Minimal Spanning Tree (MST) Analysis

One of the analysis tools employed in this project was minimal spanning tree. This tool was first introduced by Dussert *et al.*²⁸ to study order/disorder of lithium thin films. More recently, Ourdjini *et al.*²⁹ implemented MST in the characterisation of porous frameworks synthesised from the self-condensation of BDBA on metal surfaces. In this project, MST analysis has been applied in the characterisation of extended porous 2D structures and is illustrated next with an example of the analysis routine. ImageJ package¹⁸ along with the codes developed by Gilbert Bigras³⁰ were employed, which implement algorithms

developed by Johannes Schindelin and Paul Chew.^{31,32} The analysis consists of the construction of a graph containing a set of points that locate the cells in the porous structure. The image was first processed to delineate the border of the cells. The centre of mass was used to represent the cell nodes position. A tree starts at any random cell and expands by sequential connections of nodes to forms edges. Each edge has been assigned a weight equivalent to the distance between the nodes. An MST is a tree which contains all of the nodes and where the sum of the edges' weight is minimal (Figure 1.6). The construction of more than one MST for a set of points is possible. However, all MST have the same edge weight histogram. The degree of order/disorder is measured by two parameters: the average weight of the edges (m), and the standard deviation (s). These values have been normalised according to Equation 1.46, where m^* is the measured average edge weight, m is the normalised average edge weights, s^* is the measured standard deviation of edge weights, s is the normalised standard deviation of edge weights, N is the total number of cells, S is the area of the convex hull. The derived parameters can then be compared with well characterised distributions such as perfectly ordered and random distributions. For instance, a crystalline hexagonal lattice is characterised by $m = 1.075$ and $s = 0$, and a square lattice by $m = 1.000$ and $s = 0$.

$$\begin{aligned} m &= \frac{m^*(N-1)}{\sqrt{SN}} \\ s &= \frac{s^*(N-1)}{\sqrt{SN}} \end{aligned} \quad (1.46)$$

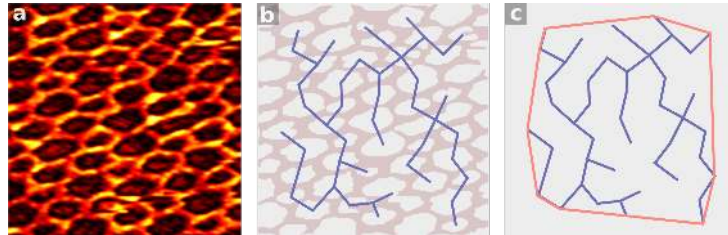


Figure 1.6 ■ Minimum spanning tree analysis (MST) a) Raw image. b) After image processing, the centre of mass of all the cells is determined. These are the nodes of the MST skeleton indicated in blue. c) Skeleton of MST (blue) and convex hull (red).

Moiré Pattern Analysis

In Chapter 1 we discuss the heteroepitaxial growth of gold onto Pd(111) to form AuPd(111) alloys. Gold grows pseudomorphically and STM topographs of the alloy exhibit a Moiré pattern. Moiré fringes arise from the difference in lattice constant and orientation of an overlayer relative to the underlying substrate. This can be thought of as the 2D equivalent of two overlapping sinusoidal functions with almost identical frequency, with the Moiré representing the beating frequency of the resulting wave. In the absence of atomic resolution, the lattice constant of the overlayer can be derived from geometry arguments as described in references [33] and [34]. The hexagonal lattice of Pd(111) can be described as the superposition of three plane waves intersecting one another at 60° as illustrated in Figure 1.7.a. The wave is characterised by a wave vector, where $a_{Pd(111)}$ is the surface lattice constant of Pd(111) Equation (1.49).

$$\bar{k} = \frac{2\pi}{\lambda} \quad (1.47)$$

$$\lambda_{Pd(111)} = \frac{\sqrt{3}}{2} a_{Pd(111)} \quad (1.48)$$

$$\bar{k}_{Pd(111)} = \frac{2}{\sqrt{3}} \frac{2\pi}{a_{Pd(111)}} = \frac{4\pi}{\sqrt{3}} \frac{1}{a_{Pd(111)}} \quad (1.49)$$

The amplitude modulation of the Moiré pattern can be expressed as the difference between the wave vectors of the overlapping lattices as illustrated diagrammatically in Figure 1.7.b in reciprocal space, and expressed by Equation 1.50.

$$\bar{k}_{Moiré} = \bar{k}_{Au\ overlayer} - \bar{k}_{Pd(111)} \quad (1.50)$$

Using the law of cosines on the triangle formed by the wave vectors (Figure 1.7.c), one obtains Equation 1.51, where θ is the angle between the gold overlayer and the Pd(111) substrate.

$$\bar{k}_{Au\ overlay}^2 = \bar{k}_{Pd}^2 + \bar{k}_{Moiré}^2 - 2\bar{k}_{Pd}\bar{k}_{Moiré}\cos(180 - \alpha) \quad (1.51)$$

$$\sin\theta = \frac{\bar{k}_{Moiré}}{\bar{k}_{Au\ overlay}} \sin(180 - \alpha) \quad (1.52)$$

The relationship between α , and the angle between the Moiré pattern and the Pd(111) substrate(γ) is given by:

$$\alpha = \gamma + 120 \quad (1.53)$$

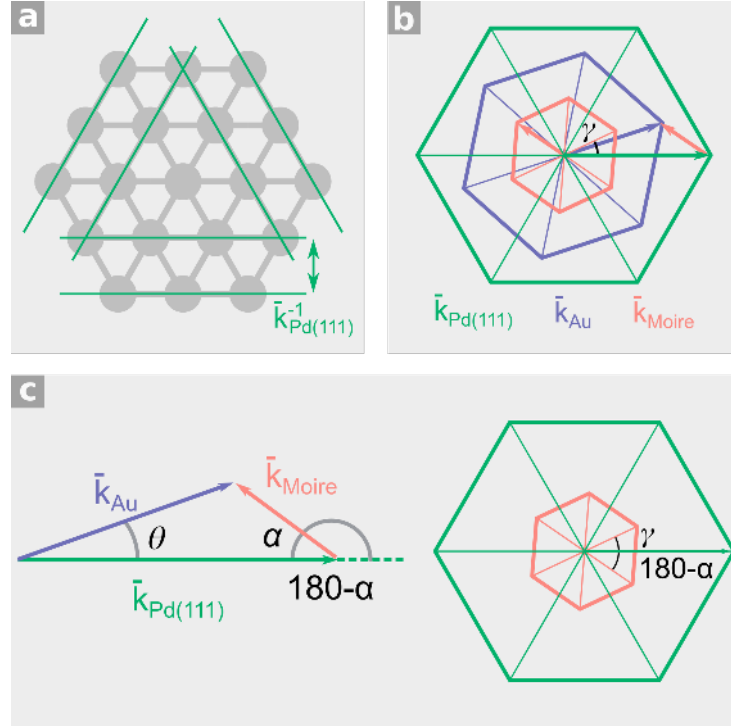


Figure 1.7 ■ Moiré pattern analysis. a) Hexagonal lattice and wavefront indicated by green lines with wave vector $\bar{k}_{Pd(111)}$. b-c) Schematic representation of Equations 1.50-1.53. Adapted from reference [33].

1.7 References

- [1] Y.-W. Chung, *Practical guide to surface science and spectroscopy*, Vol. 1, Academic Press, **2001**.
- [2] G. A. Somorjai, Y. Li, *Introduction to surface chemistry and catalysis*, John Wiley & Sons, **2010**.
- [3] K. K. Kolasinski, K. W. Kolasinski, *Surface science: foundations of catalysis and nanoscience*, John Wiley & Sons, **2012**.
- [4] A. T. Hubbard, *The Handbook of surface imaging and visualization*, CRC press, **1995**.
- [5] G. Attard, C. Barnes, *Oxford Chemistry Primers* **1998**, 59, ALL–ALL.
- [6] P. Redhead, *Vacuum* **1962**, 12, 203–211.
- [7] A. De Jong, J. Niemantsverdriet, *Surf. Sci.* **1990**, 233, 355–365.
- [8] <http://www.chem.qmul.ac.uk/surfaces/scc/>.
- [9] G. Binnig, H. Rohrer, C. Gerber, E. Weibel, *Appl. Phys. Lett.* **1982**, 40, 178–180.
- [10] G. Binnig, H. Rohrer, C. Gerber, E. Weibel, *Phys. Rev. Lett.* **1982**, 49, 57.
- [11] M. F. Crommie, C. P. Lutz, D. M. Eigler *et al.*, *Science* **1993**, 262, 218–220.
- [12] C. J. Chen, *Phys. Rev. Lett.* **1990**, 65, 448.
- [13] F. Wiame, V. Maurice, P. Marcus, *Surf. Sci.* **2007**, 601, 1193–1204.
- [14] R. Feenstra, J. A. Stroscio, J. Tersoff, A. Fein, *Phys. Rev. Lett.* **1987**, 58, 1192.
- [15] C. J. Villagomez, T. Zambelli, S. Gauthier, A. Gourdon, S. Stojkovic, C. Joachim, *Surf. Sci.* **2009**, 603, 1526–1532.
- [16] R. Howland, L. Benatar, P. S. Instruments, *A practical guide to scanning probe microscopy*, Park scientific instruments, **1996**.

- [17] D. Nečas, P. Klapetek, *Open Physics* **2012**, 10, 181–188.
- [18] C. A. Schneider, W. S. Rasband, K. W. Eliceiri, *Nature methods* **2012**, 9, 671–675.
- [19] I. Vasilef, *QtiPlot: data analysis and scientific visualization*, **2011**.
- [20] E. Seifert, *OriginPro 9.1: Scientific Data Analysis and Graphing Software Software Review*, **2014**.
- [21] S. H. John W. Eaton, David Bateman, R. Wehbring, *GNU Octave version 4.0.0 manual: a high-level interactive language for numerical computations*, **2015**, <http://www.gnu.org/software/octave/doc/interpreter>.
- [22] LEEDpat, Version 4.2, utility by K.E. Hermann (FHI) and M.A. Van Hove (HKBU), Berlin/Hong Kong, 2014; see also <http://www.fhi-berlin.mpg.de/KHsoftware/LEEDpat/index.html>.
- [23] B. O. Community, Blender - a 3D modelling and rendering package, Blender Foundation, Blender Institute, Amsterdam.
- [24] A. Kokalj, *Comput. Mater. Sci.* **2003**, 28, 155–168.
- [25] M. D. Hanwell, D. E. Curtis, D. C. Lonie, T. Vandermeersch, E. Zurek, G. R. Hutchison, *J. Cheminform.* **2012**, 4, 17.
- [26] B. Kosata, R. Danne, *Bkchem—a free chemical drawing program*, **2003**.
- [27] Harrington, B. *et al.* (2004–2005). Inkscape. <http://www.inkscape.org/>.
- [28] C. Dussert, G. Rasigni, M. Rasigni, J. Palmari, A. Llebaria, *Phys. Rev. B: Condens. Matter* **1986**, 34, 3528.
- [29] O. Ourdjini, R. Pawlak, M. Abel, S. Clair, L. Chen, N. Bergeon, M. Sassi, V. Oison, J.-M. Debierre, R. Coratger *et al.*, *Phys. Rev. B* **2011**, 84, 125421.
- [30] Gilbert Bigras, Cross Cancer Institute, University of Alberta, Edmonton Canada.
- [31] Johannes Schindelin, Microsoft, Git for Windows.
- [32] L. Paul Chew, Computer Science Department Upson Hall, Cornell University, Ithaca, NY 14853.

- [33] E. K. Vestergaard, PhD thesis, University of Aarhus, **2004**.
- [34] M. E. Blecher, E. A. Lewis, A. Pronschinske, C. J. Murphy, M. F. Mattera, M. L. Liriano, E. C. H. Sykes, *Surf. Sci.* **2016**, *646*, 1–4.

Chapter 2

sCOF Synthesis on a Reactive Metal Surface

2.1 Introduction

Catalysis plays a key role in the manufacture of goods in modern society. A catalytic step is involved at some stage in the production of commodities such as fuels, foodstuff, and plastics; to the maintenance of air quality. By definition, a catalyst is any substance capable of increasing the rate of a chemical reaction by providing an alternative pathway of lower kinetic barriers. A catalyst is often present in small amounts relative to the reactants, and presents certain characteristics. A catalyst is not consumed during reaction, is regenerated after the catalytic cycle, and does not alter the thermodynamics of the reaction. A very important aspect of catalysis research and development is selectivity. In selective catalysis the distribution of products generated by the catalytic cycle is controlled. Enantioselectivity represents a particularly challenging type of selective catalysis. It is a type of chemical transformation whereby one preferred enantiomer, in an enantiomeric pair of a chiral product, is generated in excess (Equation 2.1). Enantiopure chemicals find uses in the fields

of non-linear optics, agriculture, in the aroma and flavour industry, and are particularly important in the pharmaceutical industry. Enantiomeric pairs of chiral drugs possess the same physical properties (density, melting point, solubility, etc.) and are, therefore, indistinguishable. However, each enantiomer in a pair shows a distinctive affinity to *chiral* environments. Drugs are designed to intercept and interact with target receptors constituted by chiral units such as aminoacids, carbohydrates, and lipids; which represent such a chiral environment. Subsequently, the affinity of each enantiomer of a drug for a receptor is distinctive, and ultimately so can their biological effects and metabolism. Ingestion of racemic drugs can result in different scenarios: in the best case, the wrong enantiomer has a low binding affinity to the receptor and exhibits no bioactive effect (*e.g.*, β -blocker (S)-(-)-propranolol is one hundred times more active than its (R)-(+)-enantiomer); or rarely, if binding occurs their pharmacological activity are equivalent (*e.g.*, antidepressant (\pm)-fluoxetine). However, if binding does occur, the effects can be far from beneficial or innocuous and may be catastrophic instead.¹ The Thalidomide tragedy illustrates the case. Popularised in the 1960s, this drug was an over-the-counter antiemetic used to relieve the symptoms in the early stages of pregnancy. The (R)-enantiomer has the effects intended for its use; however, the (S)-enantiomer causes severe congenital defects in the unborn. Unfortunately, in this case, had the drug been provided in its enantiopure form, *in vivo* racemisation occurs, leading to the same catastrophic effects. This case set a precedent for the introduction of rigorous regulations in drug testing and marketing,[‡] and underlines the importance of chirality.

$$ee(\%) = \frac{R - S}{R + S} \times 100 \equiv \frac{[\alpha]_{R \text{ enantiomer}}}{[\alpha]_{\text{mixture}}} \times 100$$

R : molar fraction of R enantiomer
 S : molar fraction of S enantiomer
 $[\alpha]_R$: specific optical rotation of R enantiomer
 $[\alpha]_{\text{mixture}}$: net optical rotation of a mixture

(2.1)

[‡]Directive 65/65/EEC in Europe and Kefauver Harris Amendment in the USA.

Presently, industrial manufacture of chiral compounds still relies heavily on standard chiral resolution of racemic mixtures and, on a smaller scale, on chiral chromatography.² However, this route is intrinsically wasteful, and separation can be non-trivial. For this reason, more efficient approaches such as asymmetric synthesis are preferable. Current catalytic asymmetric synthesis is indeed the domain of enzyme and homogeneous catalysis. In the latter, the active site is tailored by judiciously designed organic ligands around a metal coordination centre. The ligands define the steric bulk and electronic characteristics of the active site, which in turn, control the activity and selectivity. Despite the excellent control over selectivity, homogeneous catalysis suffers from a major disadvantage. The fact that the catalytic reaction takes place in a homogeneous medium makes recovery of the catalyst problematic. In this respect, *heterogeneous* catalysis offers many practical advantages over its homogeneous counterpart. Mainly, it provides more facile and less wasteful isolation of the product and catalyst recovery from the reaction mixture. Incorporating these advantages into selective catalysis would have a significant impact at the industrial level. However, the surface of supported metal catalysts exhibits many active sites with a range of activities. The lack of control over the structure of such sites is often detrimental to selectivity, making heterogeneous catalysis non-selective.

Great efforts have been focused on developing enantioselective heterogeneous catalysts. One of the methods to attain this entails imparting a catalytically active surface with enantiodifferentiating sites via the adsorption of chiral organic modifiers. For example, seminal work by Orito *et al.*³ reported that cinchonidine-modified platinum is effective in the enantioselective hydrogenation of α -ketoesters. Similarly, Izumi⁴ also demonstrated that tartaric acid-modified Raney Nickel is successful at promoting enantiodifferentiation in the hydrogenation of β -ketoesters. Since then, a range of substrates, chiral modifiers, metals, and reactions have been tested.⁵ Significant experimental and theoretical efforts by several research groups attempted to unveil the underlying mechanism responsible for the observed enantioselectivity.^{6,7} Two models were put forward, both having in common that the enantiodifferentiating step is a truly heterogeneous process that takes place at the surface. One of the mechanisms proposed involves a 1-to-1 docking between the chiral modifier and the prochiral substrate mediated by intermolecular interactions.

A second mechanism was suggested where the surface is patterned by an array of modifier molecules, creating chiral interstices that steer the enantiospecific face of the incoming prochiral molecule. The former is the most generally accepted mechanism.^{8,9}

Despite the remarkable enantioselectivity of chiral heterogeneous catalysts, with some exhibiting enantiomeric excesses (*ee* %) above 90 %, ¹⁰ these remain more of a laboratory curiosity and have not made an impact at an industrial scale. This is mainly because of two main problems. Firstly, control over dispersion of the organic modifier is challenging. High modifier coverages can switch off the catalytic activity by blocking the coadsorption of reactant molecules. Additionally, only molecules in the periphery of molecular islands are capable of engaging in the crucial 1-to-1 interaction that eventually leads to enantiodifferentiation. The remaining molecules are just spectators and cannot participate in asymmetric induction. If substrate or solvent molecules have a high affinity for the metal, they may displace and block the adsorption of the chiral modifier, resulting in the loss of enantioselectivity. A second issue is poor chemical and mechanical stability of modifier molecules on the catalyst's surface. Leaching of the modifier into the reaction medium and corrosive etching of the metal result in loss of enantioselectivity. This problem is common to tartaric acid-modified nickel catalysts. Likewise, hydrogenation and loss of the modifier in the course of reaction will have the same undesired effect.⁹

Little attention has been paid to these issues, which preclude the development of scalable enantioselective heterogeneous catalysts. Watson *et al.* ¹¹ stressed the need for robust anchoring methods that prevent leaching and loss of enantioselectivity. The authors employed chiral sulphide ligands to covalently tether pyrrolidine moieties to Pd nanoparticles for the enantioselective hydrogenation of isophorone. The modifier remained intact and anchored to the surface during reaction, producing modest enantiomeric excesses. The requirement of covalent bonding to achieve a robust modified catalyst was therefore apparent. Nonetheless, their approach was still somewhat limited by dispersion of the modifiers. The obtained enantiomeric excesses were dependent on the increasing bulkiness of the alkyl substituents on the sulphide. This behaviour was rationalised as the ability of the modifiers to self-assemble into dense islands, which precludes their dispersion. Moreover, an increase in

enantioselectivity, and drop in activity as a function of modifier concentration, suggested that the surface becomes crowded with modifier molecules which block the access of substrate molecules. Based on the premises outlined by the authors, it is evident that innovative solutions are necessary to address both issues simultaneously.

Nanoscale architectures have emerged in the recent literature as the ultimate means to tailor surface properties.¹² In particular, sCOFs are a type of nanoarchitecture that has developed as single layer equivalents of bulk covalent organic frameworks (COF), an important class of porous materials with applications in gas storage, optoelectronics, and catalysis.^{13–15} Surface-supported synthesis has become the preferred route for low dimensional materials since traditional synthetic approaches often meet with several limitations. For example, as the molecular weight of a material increases, solubility issues arise. Alternative exfoliation methods of bulk crystals are usually limited to initial crystal growth and multilayer formation. Current research of sCOFs has focused mainly on their bottom-up fabrication and fundamental aspects of electron transport for their applications in molecular-based devices.¹⁶ However, despite the success of the more mature field of bulk COFs, much less is known about the prospective applications of sCOFs in catalysis. These single layer frameworks appear as an attractive platform to address the issues outlined above for chirally modified catalysts' surfaces as they offer high thermal stability, functionality, and hosting abilities. On the one hand, covalent bonding guarantees robustness of the framework which can be functionalized to bear chiral centres.^{17–19} On the other hand, structures of tunable size pores can be exploited to host guest molecules, permitting the 1-to-1 interaction necessary for enantiodifferentiation. We aim is to employ on-surface chemistry to fabricate a chiral porous sCOF on a model catalytically active surface. Besides, frameworks containing pores ranging between 1–2 nm in diameter are desirable for hosting of guest molecules (Figure 2.1.a).

In this chapter, we present the investigation of sCOF fabrication on model catalyst surfaces under ultra-high vacuum conditions (UHV). We begin by providing an overview of the current advances in on-surface synthesis, with emphasis on those applied to sCOF fabrication. Then, we introduce the original idea explored by our group of fabricating sCOFs through direct on-surface

reaction of molecular precursors. We provide an account of the challenges encountered that led to its limited success. Next, we illustrate the advantages of using bimetallic alloys as a strategy to dilute surface reactivity and comment on the involvement of ligand and ensemble effects in the surface chemistry. Last, we show a protocol that eventually leads to the fabrication of a porous sCOFs on a AuPd surface with accessible palladium sites.

2.2 Surface Confined Covalent Organic Frameworks (sCOFs)

Molecular self-assembly has been exploited to engineer a myriad of versatile surface nanoarchitectures, many of which are porous.^{20,21} Networks constructed from non-covalent interactions such as hydrogen or halogen bonds ($15\text{--}120\text{ kJ mol}^{-1}$), dipole-dipole ($5\text{--}50\text{ kJ mol}^{-1}$), or van der Waals forces (5 kJ mol^{-1}), have the advantage of exhibiting remarkable long-range crystallinity. This is possible because an error correction mechanism operates, whereby dynamic bond breaking/making produces the most thermodynamically stable structure. A useful feature is that porous networks capable of hosting guest molecules can be tailored by preconfiguring the molecular *tecton*, which allows control over pore size and functionality.²² However, the very same low energy pathway that allows for error correction also represents a disadvantage, since moderate temperatures and solvents are sufficient to disrupt non-covalent interactions. For this reason, thermal, mechanical, and chemical instability is an insurmountable limitation to using non-covalent networks in catalyst modification. Under catalytic reaction conditions, bond breaking, diffusion and desorption of tectons and deterioration of the network is inevitable. Consequently, nanoarchitectures used in catalyst modification must rely on stable bonds capable of withstanding these conditions.

Coordination chemistry is one possibility and lies at the heart of bulk metal organic frameworks (MOFs) and their surface equivalent (SURMOFs), with typical bond energies ranging between $100\text{--}250\text{ kJ mol}^{-1}$.²³ Even stronger yet are covalent bonds ($> 250\text{ kJ mol}^{-1}$), and the library of on-surface reactions that

afford covalent bonding has been expanded in recent years. Many solution-based reactions have their on-surface equivalent, although their mechanism might not necessarily be the same, and many remain elusive. Some of the known on-surface reactions include condensation of boronic acids,²⁴ acyl chlorides,^{25,26} carboxylic acid anhydrides,²⁷ polyester formation,²⁸ and Schiff-base formation,^{22,29} as well as nucleophilic addition to isocyanate,^{30,31} McMurry reaction,³² desulfurisation,³³ Glaser³⁴ and Scholl-type reactions (dehydrogenative coupling),^{35–40} Huisgen dipolar cycloaddition,^{41,42} alkyne cyclotrimerisation,^{43,44} acetyl cyclotrimerisation,⁴⁵ Bergman cyclisation,^{46,47} carbene dimerisation,⁴⁸ decarboxylative coupling,⁴⁹ Sonogashira,^{50–52} Wurtz,⁵³ Fe-catalysed tetracyanobenzene cyclisation,⁵⁴ and Ullmann-type C–C coupling.^{55,56} However, the fabrication of sCOFs is subject to stringent requirements, especially when prepared under UHV conditions. For example, tectons must bear reactive moieties that promote lateral covalent interlinking in two dimensions, preferably with no or easily desorbable byproducts.³⁶ The molecule must be sublimable without undergoing decomposition or side reactions and have a significant sticking coefficient. In the case of bimolecular reactions, stoichiometric amounts of each building block may be required and phase segregation can be limited to phase boundaries.^{28,30} Homomeric polymerisation can circumvent this issue. For our purpose, other considerations are porosity (close-packed structures are unsuitable), and crystallinity of the resulting framework. A narrow size distribution of well-defined pores is desirable, but a mechanism must exist that ensures error correction. Such a mechanism is only possible when the framework can equilibrate with its monomeric building blocks to arrive at their thermodynamic minimum. Dynamic covalent chemistry can achieve this via reversible bond formation and provides a way of combining error correction and robust covalent bonding.⁵⁷ The reversible step is often regulated by the release and reabsorption of a small molecule such as water, which acts as the chemical equilibrium control agent. This is rarely attainable under UHV, and many reactions are kinetically trapped. To this end, the reactions extensively used sCOF synthesis under UHV, which meet some of these requirements, and also in this project are: surface-assisted Ullmann reaction, and (self-) condensation of boronic acids.

Ullmann C–C Coupling

Ullmann coupling is widely used in organic synthetic chemistry for the formation of biphenyls. The reaction mechanism involves oxidative addition of arylhalides to a Cu(I) catalyst via C–X (X = Cl, Br, I) bond scission. Subsequent reductive elimination and coupling with a second activated precursor results in C–C bond formation. Xi and Bent first demonstrated using TPD and HREELS, and Hla and co-workers using STM, that the on-surface analogue also proceeded for iodobenzene to produce biphenyl on Cu(111).^{58–60} Although strictly speaking Ullmann coupling refers to the reaction catalysed by copper, other surfaces such as Ag, Au, and hBN or graphene-decoupled Ni, and different crystallographic orientations have been shown to be active in Ullmann-type coupling.^{61,62} In the seminal work by Grill *et al.*⁵⁵ (2007) the difference in dissociation energy barriers for C–Br and C–I was exploited in the consecutive linking of porphyrins into extended covalent arrays on Au(111).[‡] Since then, this reaction has been extensively used as a major route in the bottom-up synthesis of various low-dimensional nanoarchitectures.^{64–67} The on-surface mechanism is thought to proceed via homolytic C–X cleavage to produce a surface-stabilised radical σ -bonded to an adatom. In a consecutive step, the metal adatom is released, followed by recombination with a second activated precursor to form a C–C σ -bond (Figure 2.1.b).⁶³ The involvement of surface metal atoms in the thermally activated dehalogenation step is generally accepted, activation can also be promoted photochemically or by injecting electrons through an STM tip.^{60,68} Interestingly, Kittlemann and co-workers demonstrated thermally-activated C–C coupling on bulk CaCO₃, which raises the question of whether a different mechanism applies for insulators in the absence of catalytic promotion by a metal.⁶⁹ Extensive STM and spectroscopic evidence exist of a metastable organometallic intermediate (protopolymer state) for Cu and Ag, which has occasionally been reported for Au.^{70–73} The relative stability of the protopolymer state has been explained in terms of relative reaction barriers to transform a protopolymer into a fully covalent state, which is highest for Ag and virtually non-existent for Au, unless kinetically-stabilised.^{63,74–78} A disadvantage of this on-surface reaction is that C–C bond formation is kinetically controlled and irreversible, which prevents error correction of topological

[‡] $\Delta E = E_{\text{C-Br}} - E_{\text{C-I}} = 0.50 \text{ eV}$ in the gas phase. From reference [63].

defects.⁷² Furthermore, halogen atoms are byproducts that bind strongly to metals, which impact on the long-range growth of the framework. sCOFs built using Ullmann coupling exhibit a high density of defects and short-range order.

Condensation Reactions

A well-established type of condensation reaction is Schiff-base formation ($R^1-C=N-R^2$), which has been applied in the synthesis of numerous macrocycles, salen-type ligands, 3D crystalline porous materials, and in the immobilisation of biomolecules onto solid supports.⁷⁹ The reaction is acid-catalysed, and involves nucleophilic addition of an amine to a carbonyl carbon to form a hemiaminal intermediate; followed by dehydration to produce an imine bond. Imine bond formation is thermodynamically-driven by elimination of water. The on-surface equivalent of this reaction has been shown to proceed at the solid-liquid interface as well as under UHV conditions. For the latter, intramolecular proton transfer from adjacent functional groups to the carbonyl performs the equivalent acid-catalysed step required in solution to drive the reaction.^{22,29} The strong imine bond, mild reaction conditions and accessibility of reagents, had made Schiff-base formation an excellent reaction for sCOF synthesis under ambient conditions. More importantly, the dynamic nature of Schiff-bases permits error correction and highly crystalline frameworks, as demonstrated by Liu and co-workers in the condensation reaction between terephthalaldehyde and 1,3,5-tris(4-aminophenyl)benzene on highly-oriented pyrolytic graphite (HOPG). The resulting sCOF possesses domains extending several hundreds of nanometers, with well-defined pores and low density of defects.⁸⁰

Boronic acids also undergo a trimolecular self-condensation reaction to produce a boroxine ring (B_3O_3), and three water molecules per ring as byproducts (Figure 2.1.c). Boronic acids can also react with alcohols and diols to form boronic esters. Pioneering work by Côté *et al.*¹³ (2005) accomplished the synthesis of the first bulk COF with tunable pore sizes using this reaction. Soon after, this reaction was implemented in the synthesis of surface-supported single-layer frameworks.²⁴ The reaction is entropy-driven, and the mechanism initially involves the formation of a dimer held by two O–H...O hydrogen

bonds. Endothermic formation of a first covalent B–O σ -bond releases one water molecule while preserving one hydrogen bond. Successive incorporation of a third molecule produces a second and third new B–O bond, which cyclises into a planar boroxine ring with loss of two more water molecule.⁸¹ Analogous to Schiff-base formation, this reaction can also proceed under reversible conditions, favouring a low density of topological defects in the framework. A thermodynamic regulating agent such as a water-releasing compound mediates the reversible step (*e.g.*, $\text{CuSO}_4 \cdot 5 \text{H}_2\text{O}$ or water itself), and it has been adopted as a routine protocol in high-quality sCOF synthesis.^{82,83} The reaction under ambient conditions is frequently thermally activated on HOPG, whereas Ag produces the most crystalline sCOF of all metals tested so far under UHV.⁸⁴ Polymerisation can be thermally activated, but also induced by an STM tip or by electron beam under UHV.⁸⁵ Even though sCOFs built from boronic acids condensation are thermally robust, a principal disadvantage of this reaction is the poor chemical stability. Boronic acid-based sCOFs degrade easily in ambient conditions, because of boron's tendency to oxidise.

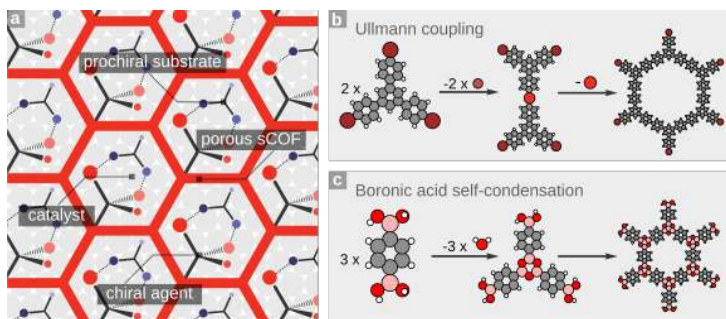


Figure 2.1 ■ Porous chiral sCOFs for enantioselective heterogeneous catalysis. Schematic representation of **a)** Target surface modification of a catalyst employing a porous sCOF bearing chiral centres. Prochiral substrate molecules hosted in the pores interact in a 1-to-1 fashion with chiral agents via intermolecular bonding. Chemical transformation to enantiopure products is subsequently carried out by the exposed surface atoms. **b)** Ullmann reaction of a halogenated precursor. Surface-catalysed C–X scission (X: Br, I, or Cl) results in metal organic bonding for Cu and Ag. In a subsequent step, the metal adatom is released and C–C bond forms with a second and successive activated precursor. Propagation of the reaction produces a covalent framework. **c)** Boronic acid dehydrative self-condensation into a boroxine ring with the release of water as a byproduct. Carbon (grey), Hydrogen (white), Bromine (maroon), Oxygen (red), Boron (pink), Copper (orange).

2.3 Direct Synthesis of sCOFs on Pd(111)

Melamine adsorption on Pd(111): Revisited

The hydrogen accepting/donating capabilities of 1,3,5-triazine-2,4,6-triamine (**melamine**) (Figure 2.2.a) makes this molecule ubiquitous in surface-supported hydrogen-bonded networks.^{86–88} The endocyclic nitrogen atoms of the triazine ring provides three hydrogen bond acceptors, whereas the three exocyclic amino groups act as hydrogen bond donors. This allows melamine to self-assemble into a 2D network either as a single component or in combination with a second synthon. For example, the bicomponent melamine-PTCDI[‡] system is a porous network with host-guest capabilities exploited in surface templating.^{88,89} Previous investigations in our group on the oligomerisation of melamine with electrophiles on Au(111) met with success.^{26,30,90} Hence, the possibility of condensing melamine and terephthalaldehyde (TPA) into a Schiff base-linked sCOF on palladium was speculated (Figure 2.2.b,c).⁹¹ Greenwood and co-workers concluded from their STM and RAIRS investigations that melamine anchors to the surface of Pd(111) through two partially dehydrogenated amino groups, and pairwise arrays of molecules orient almost perpendicularly to the surface plane. A similar adsorption motif has also been proposed for melamine on nickel^{92,93} and copper,^{94–96} which differs from the *flat-lying* orientation of melamine on gold or silver.^{86,89} The adsorption geometry adopted by melamine on palladium impedes lateral interactions of the amino groups with a second reactant and in-plane 2D linking. Greenwood's work outlines the first challenge in the direct synthesis of sCOFs on reactive surfaces. Whereas intermolecular interactions prevail on relatively inert surfaces such as gold permitting diffusion, self-assembly, and the reaction of monomers; on more reactive metals molecule-surface interactions dominate, and can dramatically steer the adsorption geometry and surface chemistry.⁹⁷ Interestingly, Lin and co-workers reported the transformation of *upright* standing melamine on Cu(111) into covalently bound polyguanide via a thermally-activated ring opening reaction (Figure 2.2.d).⁹⁵ Encouraged by their findings, we set out to investigate whether melamine alone could produce a surface polymer via the

[‡]PTCDI: perylene-3,4,9,10-tetracarboxylic di-imide

same mechanism on palladium.

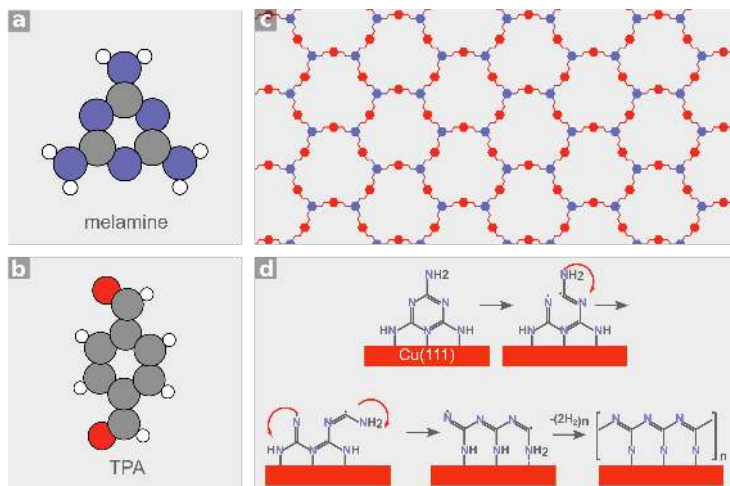


Figure 2.2 ■ Porous sCOFs from Schiff-base formation. Structural model of **a)** 1,3,5-triazine-2,4,6-triamine (melamine) and **b)** Terephthalaldehyde (TPA). **c)** Wireframe representation of target sCOF based on Schiff-base formation between melamine (blue) and TPA (red). **d)** On-surface ring-opening reaction mechanism of melamine to polyguanide on Cu(111) at 575 K as proposed in reference [95].

A melamine-covered palladium surface was prepared by exposing a clean Pd(111) held at 300 K, to melamine in the gas phase ($T_{dose.} = 365$ K). The topography was dominated by elongated bright features 12.4 ± 1.3 Å in length, which did not exhibit long-range order. A line profile across these features revealed two coalesced peaks, indicating that each of them was composed of two smaller units (Figure 2.3.a). These observations conform with the distance between two melamine molecules stacked side by side (13 Å) as measured in high-resolution STM by Greenwood and co-workers.⁹² Heating the sample to 470 K produced the surface shown in Figure 2.3.b. The topography was marked by ragged step edges with the concomitant appearance of globular-shaped features $\varnothing = 5.1 \pm 0.1$ Å in diameter. These were imaged as clusters with no apparent preferred alignment along any surface direction (Figure 2.3.c). Further heating at 580 K removed these species leaving a virtually featureless surface.

The adsorption of melamine on Pd(111) was further characterised by vibrational spectroscopy. HREELS spectra were recorded after deposition of melamine at 300 K followed by systematic annealing of the sample to progressively higher temperatures (Figure 2.3.d). Assignment of the energy losses

is summarised in Table 3, and is based on the calculated normal vibrational modes of a single monodehydrogenated melamine molecule on a Pd(111) surface. The assignment of vibrational modes is in close agreement with that of melamine adsorption on silver nanoparticles reported by Chen *et al.*⁹⁸ and references therein. Geometry optimisation and calculated vibrational spectra were carried out by Peake⁹⁹ in the research group of H. Früchtl.[‡] Gas phase optimisation of a single melamine molecule in the gas phase was performed at the B3LYP/3-31G* level of theory. For the surface and molecule-surface simulations, a 3-layer 4×4 palladium slab was constructed with a vacuum gap of 20 Å. The PBE functional was employed with a plane-wave basis set at an energy cut-off of 400 eV, and a $3 \times 3 \times 1$ k-point sampling. The bottom two layers were kept frozen at the bulk geometry while allowing the uppermost layer to relax during optimisation. The projector augmented wave (PAW) pseudopotential method was employed in the treatment of core electrons. See reference [99] for further details of the calculations.

[‡]Jennifer Peake,^[a] José G. Torres,^[a] and Dr Herbert A. Früchtl.^[a]

[a] EaStCHEM School of Chemistry, University of St Andrews, St Andrews, Fife, United Kingdom.

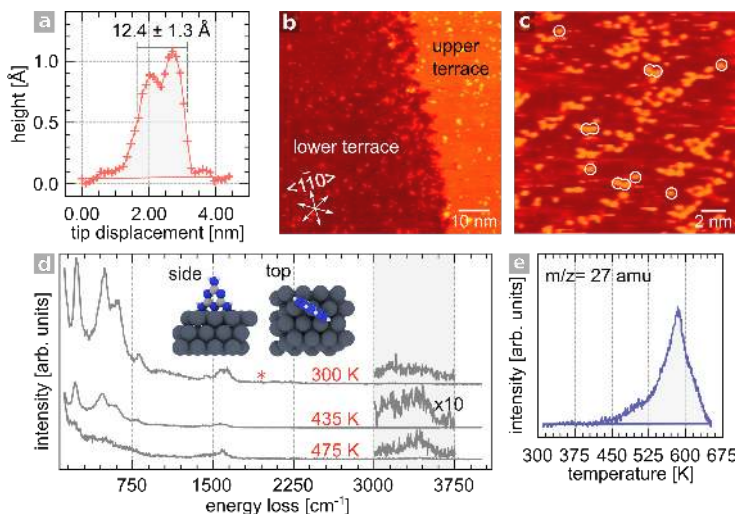


Figure 2.3 ■ Melamine adsorption onto Pd(111). **a)** Line profile across elongated features observed under STM upon deposition of melamine (7 L) on Pd(111) at 300 K. The red curve is a fit of two Gaussian functions. **b)** TPD trace of fragment $m/z = 27$ (HCN^+). Adapted from reference [91] **c)** STM image of adsorbate-induced etching of palladium after annealing at 470 K, $V_t = -1.5$ V, $I_t = 300$ pA **d)** Close-up of preparation in c) with isolated and clusters of globular features highlighted in white, $V_t = -0.9$ V, $I_t = 200$ pA **e)** HREEL spectra of melamine (3×10^3 L) on Pd(111) as a function of annealing temperature. 3000–3750 cm^{-1} region has been expanded in and 435 K spectrum multiplied by 10. The red asterisk marks the position of the energy loss associated with adventitious coadsorbed CO. $E_0 = 4.1$ eV, FWHM = 44.8 cm^{-1} . (inset) side and top view of the DFT-optimised geometry of monodehydrogenated single melamine molecule on Pd(111), $E_{\text{ads}} = -1.81$ eV. Coadsorbed hydrogen atoms are omitted for clarity. Adapted from reference [99].

Table 3 ■ Melamine/Pd(111) HREELS vibrational modes assignment. ν : stretch, β : bending, δ : scissoring, ρ : rocking, ω : wagging, τ : twisting, R: ring vibration, sym.: symmetric, asym.: asymmetric, def.: deformation, breath.: breathing, ip: in plane, op: out of plane.

Energy loss [cm^{-1}]	Assignment
3410	$\nu(\text{NH}_2)_{\text{asym.}}, \nu(\text{NH}_2)_{\text{sym.}}$
3170	$\nu(\text{N}-\text{H})$
1630	$\delta(\text{NH}_2), \nu(\text{C}-\text{NH}_2)$
1575	$\nu(\text{CN}), \beta(\text{NH})_{\text{ip}}$
1435	$\nu(\text{CN}), \delta(\text{NH}_2), \nu(\text{C}-\text{NH}_2), \text{R}_{\text{breath.}}, \beta(\text{NH})_{\text{ip}}$
1005	$\beta(\text{CNC}, \text{NCN})_{\text{ip}}, \rho(\text{NH}_2), \text{R}_{\text{breath.}}$
810	$\text{R}_{\text{op def.}}$
730	$\beta(\text{NH})_{\text{op}}$
605	$\beta(\text{CNC}, \text{NCN})_{\text{ip}}$
555	$\beta(\text{CNC}, \text{NCN})_{\text{ip}}, \tau(\text{NH}_2)$
485	$\beta(\text{C}-\text{NH})_{\text{ip}}$
325	$\beta(\text{C}-\text{NH}_2)_{\text{ip}}$
230	$\nu(\text{Pd}-\text{N})$

The weak losses at 3410 and 3170 cm^{-1} in the 300 K spectrum correspond to $\nu(\text{NH}_2)$ and $\nu(\text{NH})$ respectively; and those in the 1630–1435 cm^{-1} range are characteristic of $\beta(\text{NH}_2)$ and $\nu(\text{C}=\text{N})$ modes, consistent with the structure of melamine. The surface selection rule for the specular scattering regime dictates that only those dipoles with a component parallel to the surface normal are active, and is the case for the losses noted above. Therefore, from the relative orientation of these dipoles relative to the surface normal, it is deduced that the adsorption motif of melamine is close to perpendicular to the surface plane. However, the energy loss at 810 cm^{-1} assigned to the triazine ring out-of-plane deformation is also active, which would be silent for a perfectly perpendicular geometry. The simultaneous observation of the latter along with the $\nu(\text{C}=\text{N})$ and $\beta(\text{NH}_2)$ modes suggests altogether a somewhat tilted orientation of the molecular plane of melamine. This result is in agreement with the partially dehydrogenated melamine adsorption model on Pd(111) put forward by Greenwood *et al.*⁹² in their experimental and theoretical work. In their model, pairwise melamine molecules tilt away from the surface normal and towards each other as a result of H-bonding between NH_2 groups. Annealing the sample up to 435 K resulted in an overall attenuation of the spectral features intensity, and a redshift of $\Delta\nu \simeq 20 \text{ cm}^{-1}$. Further heating at 475 K dramatically transformed the spectrum. The intense energy losses below 1000 cm^{-1} vanished. The disappearance of signature peaks such as the ring out-of-plane deformation and bending modes of NH_2 and CNC undoubtedly indicates the loss of the triazine ring structure and further dehydrogenation of the amino groups. The spectrum at this temperature is remarkably similar to that of HCN chemisorption on Pd(111) and s-triazine decomposition to HCN.^{100,101} Hence, the remaining surface species are ascribed to HCN, a known thermal degradation product of solid melamine.¹⁰² The remaining energy losses are assigned to $\nu(\text{HC}=\text{N})$ at 1575 cm^{-1} , and $\nu(\text{H}-\text{CN})$ at 3320 cm^{-1} . This interpretation is wholly consistent with the detection of fragment $m/z = 27$ (HCN) by Greenwood⁹¹ in TPD experiments (Figure 2.3.e), further supporting the presence of these species.

Overall, the combined STM and HREELS data suggest that melamine does not undergo a ring-opening polymerisation reaction on Pd(111). STM images of the annealed sample were distinctively different from those obtained by Lin *et al.*⁹⁵ on Cu(111). The integrity of the melamine molecule is already

lost at 475 K as evident from HREELS at this temperature. The ragged step edges are a clear indication of adsorbate-induced etching caused by HCN, a thermal degradation product of melamine. These were imaged as aggregates of globular units that showed no evidence of covalent bonding. We speculate that self-assembly of melamine is required in order for ring-opening polymerisation to proceed. Notably, melamine assembles in rows along the $\langle 11\bar{2} \rangle$ direction on Cu(111) prior to the formation of polyguanide. In turn, this may be related to the 7.27 % difference in lattice constant between Cu(111) and Pd(111). Melamine has been shown to self-assemble on Ni(111),⁹³ whose lattice constant differs by only 2.35 % from that of Cu(111), which might be a more suitable substrate for observing ring-opening polymerisation.

TPA adsorption on Pd(111): Revisited

Greenwood envisaged TPA as a potential electrophile for the synthesis of a Schiff-base sCOF (Figure 2.2.b). In this pursuit, understanding the surface chemistry of TPA on reactive surfaces is fundamental before evaluating the more complex polymerisation with melamine. Based on the structures resolved under STM and RAIR spectra, Greenwood proposed that TPA undergoes an on-surface Tishchenko self-condensation reaction on Pd(111) to produce polyterephthalate.⁹¹ We further investigated the surface chemistry of TPA using TPD and complementary STM imaging.

The surface chemistry of aldehydes on platinum group metals (PGM)[‡] is primarily directed by the hapticity the carbonyl group (Figure 2.4.a). In the monohapto configuration $\eta^1(\text{O})$ oxygen binds to the surface via electron donation from its lone pair of electrons, while the carbon tilts away from the surface without any significant interaction. This type of bonding is purely electrostatic. On the one hand, the interactions between the lone pair of electrons on oxygen and the localised *d*-electrons of the metal give rise to Pauli repulsive forces. On the other hand, *s*-electrons are less localised and more mobile than *d*-electrons, and can screen the lone pair of electrons to minimise the repulsion. As a result, a partial positive charge is created in the *s*-band

[‡]Also nickel is included in this discussion.

which electrostatically stabilises the oxygen atom (dative bonding).¹⁰³ In the dihapto configuration $\eta^2(\text{C}, \text{O})$ both carbon and oxygen interact with the surface. This interaction can be understood in terms of the Dewar-Chat-Duncanson model, whereby molecular frontier orbitals overlap with metal d -states. Electron density is donated from the carbonyl's bonding π -orbital into the metal, and simultaneously back-donated from the metal d -bands into the carbonyl's antibonding π^* orbital. Therefore, bonding to the surface is strengthened, while the $\text{C}=\text{O}$ bond order is reduced.^{104–111} This bonding model is analogous to that of metal complexes containing $\eta^2(\text{C}, \text{O})$ aldehydes ligands.^{112–114} These two adsorption modes are not restricted to aldehydes alone, and are also known for dimethylsulfoxide, acetonitrile, and ketones,^{115–117} and play a crucial role in selective hydrogenation.^{118–121} The dihapto configuration is thermodynamically favoured over the monohapto, and is the precursor to aldehyde decomposition via decarbonylation. The monohapto configuration plays a pivotal role in the polymerisation of small aldehydes on PGM surfaces at subambient temperatures. The initiation step in the polymerisation of aldehydes involves $\eta^1(\text{C})$ acyl species generated en route to decarbonylation, where the oxygen atom points away from the surface. In this adsorption motif, acyl species interact with $\eta^1(\text{C}, \text{O})$ aldehydes, leading to initiation and propagation of the polymerisation reaction. This mechanism has been proposed on the basis of spectroscopic data that revealed the coexistence of $\eta^1(\text{O})$ formaldehyde, paraformaldehyde, and CO at the polymerisation stage.¹⁰⁹ The involvement of acyl species as initiators has also been derived indirectly from experiments on Ag surfaces. C–H scission and acyl formation does not proceed on the clean unmodified silver surface. Neither does polymerisation or decomposition take place, but reversible desorption instead. However, oxygen-modified Ag activates C–H scission, and formaldehyde and acetaldehyde polymerise, which supports the role of acyl species in the mechanism.^{122–124} The requirement of $\eta^1(\text{O})$ aldehydes finds support in the oxidation of alcohols on PGM, which proceeds via a $\eta^2(\text{C}, \text{O})$ aldehyde intermediate, and an identical decarbonylation pathway. However, polymerisation starting from the $\eta^2(\text{C}, \text{O})$ aldehyde intermediate has never been observed, which validates the proposal that only $\eta^1(\text{O})$ aldehydes are precursors to polymerisation.^{125–127} Electronegative surface modifiers such as oxygen are known to stabilise the monohapto configuration by suppressing back donation from the metal, which becomes more electron accepting. Decarbonylation is suppressed and polymerisation may proceed favourably on

certain PGM and oxides surfaces.^{107,110,124,126,128–131}

A Pd(111) crystal held at 300 K was exposed to TPA ($T_{dose} = 380$ K, Figure S2.1) and inspected under LEED. For all the exposures employed, no extra diffraction spots were present aside from a hexagonal $p(1 \times 1)$ pattern due to the substrate. This observation signifies that long-range periodic superstructures do not form under these experimental conditions. The surface topography, as examined by STM, was characterised by nanometer-sized structures in the shape of strings, loops, and branches identical to those reported by Greenwood⁹¹ (Figure 2.4.b). In agreement with LEED, these species lacked long-range order. A high density of these species was imaged at the upper and lower terrace side of step edges, likely due to the lower coordination and higher chemisorption energy of these sites.^{132–134} We found that sequential scanning over the same area at low scanning speeds (220 nm s^{-1}) caused these features to aggregate along the perpendicular scanning direction. The aggregates could be reversibly redispersed at higher scanning speeds (1000 nm s^{-1}) as illustrated in Figure 2.4.c. Annealing to 335 K removed most of these features. Although at first glance these features resemble polymers, the observed mechanical tip-induced manipulation demonstrates that these species are undoubtedly not covalently bonded.

TPD data of TPA adsorbed onto Pd(111) revealed fragment $m/z = 28$ amu desorbing in two overlapping first order peaks at $T_{max1} = 368$ K and $T_{max2} = 426$ K (Figure 2.4.d and Figure S2.1). Using a crude Redhead analysis with an assumed pre-exponential factor $z = 1 \times 10^{13} \text{ s}^{-1}$, we derived activation energies entirely consistent with desorption-limited evolution of CO from bridge ($E_{bridge} = 99.4 \text{ kJ mol}^{-1}$) and fcc hollow sites ($E_{hollow} = 116 \text{ kJ mol}^{-1}$).¹³⁵ The onset of desorption is 300 K, implying that TPA undergoes dissociative adsorption at this temperature. Admittedly, some adventitious background CO may contribute to the signal, particularly to T_{max2} , which becomes indistinguishable in the absence of isotopic labels. Nevertheless, the observed desorption from hollow and bridge sites is symptomatic of high CO coverage ($\theta \geq 0.50 \text{ ML}$),¹³⁶ strongly suggesting that CO is generated from decarbonylation of TPA. This proposal is in agreement with the well-established decomposition mechanism of oxygenates.¹³⁰ TPD spectra were also collected for wider temperature ranges, however, no additional peaks appeared that could indicate reaction-limited

desorption of CO from polyterephthalate decomposition (inset in Figure 2.4.d). Analogously, fragment $m/z = 30$ was also detected in two overlapping peaks centred at $T_{max1} = 370$ K and $T_{max2} = 455$ K Figure 2.4.e, assigned to the parent ion of $\eta^2(\text{C}, \text{O})$ -formaldehyde ($\text{H}_2\text{CO}^{\bullet+}$). The desorption of formaldehyde is reaction-limited and likely arises from at least two distinct adsorption sites (inset in Figure 2.4.e). The possibility of this fragment belonging to the isobaric molecular ion of ethane ($\text{C}_2\text{H}_6^{\bullet+}$) from the hydrogenation of the phenyl moiety was discounted. Stacchiola *et al.*¹³⁷ reported only marginal yields of ethane formation from ethylene adsorption on a hydrogen-saturated Pd(111). This reaction pathway is mostly relevant to more open crystal surfaces such a Pd(110).¹³⁸

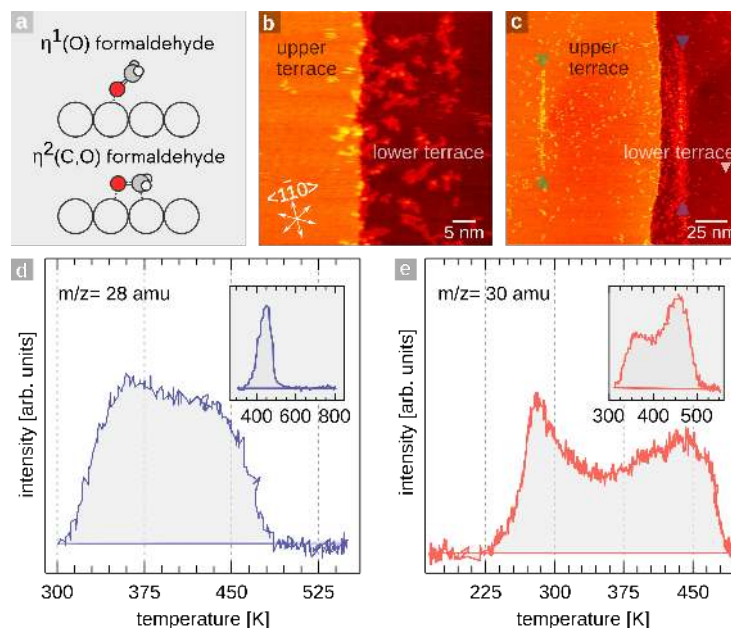


Figure 2.4 ■ TPA adsorption onto Pd(111). **a)** Schematic representation of monohapto $\eta^1(\text{O})$ and dihapto $\eta^2(\text{C}, \text{O})$ formaldehyde. The monohapto configuration is key in the polymerisation of small aldehydes, whereas the strongly bound dihapto is the precursor state to decarbonylation. **b)** STM image of TPA deposited onto Pd(111) at 300 K **c)** Aggregation was firstly induced on the lower terrace (blue), then the tip was moved onto the upper terrace (green) and the process repeated, followed by simultaneous imaging of both terraces. TPD traces of **d)** CO ($m/z = 28$ amu) upon adsorption of TPA at 300 K, $\beta = 1.0 \text{ K s}^{-1}$ (inset) extended temperature range did not reveal further CO desorption, $\beta = 7.7 \text{ K s}^{-1}$; and **e)** H_2CO ($m/z = 30$ amu), 19 L, $\beta = 0.6 \text{ K s}^{-1}$ (inset) H_2CO desorption after TPA was deposited at 300 K, 8 L, $\beta = 1.0 \text{ K s}^{-1}$.

The fact that the desorption profiles of formaldehyde and CO are coincident implies that they arise from a common precursor. This conforms with the existence of surface-bound acyl species generated via C–H scission, a well-

known intermediate in aldehydes decarbonylation. Stabilisation of $\eta^2(\text{C}, \text{O})$ aldehydes at high temperatures depends partly on the nature of the substituent group, and on the presence of carbon species which inhibit the dehydrogenation route to CO.^{109,127,139,140} Similar to CO desorption, the early onset further supports dissociative adsorption of TPA. In order to verify this proposal, TPA was deposited on a substrate held at 165 K and the thermal desorption trace of $m/z = 30$ monitored (2.4.d). A new peak was detected at $T_{max3} = 280$ K which is a signature of $\eta^1(\text{O})$ formaldehyde desorption.¹⁰⁹ This confirms that TPA decomposition readily occurs at subambient temperatures. By comparison, decarbonylation starts as early as 200 K for the closely related system benzaldehyde/Pd(111).¹⁴¹

Surprisingly, negligible hydrogen yields ($m/z = 2$ amu) were detected (Figure S2.1), considering the dehydrogenating character and high solubility of hydrogen in palladium. However, this behaviour was also seen for benzaldehyde/Pd(111) by Pang *et al.*,¹⁴¹ and was explained as the result of recombinative desorption of benzene precursors with surface hydrogen. The authors validated the mechanism by isotopic labelling experiments, whereby up to six deuteria were shown to incorporate into the benzene ring. The authors also concluded from the isotope labelling experiment that, the ring moiety adopts a parallel adsorption geometry relative to the surface plane. By contrast to Pang *et al.* results, benzene desorption was not detected in our experiments, hinting that this fragment remains adsorbed on the surface. Formyl species must instead recombine with surface hydrogen to produce formaldehyde.

In RAIR spectra reported by Greenwood,⁹¹ weak absorptions at 1724 cm^{-1} and 1653 cm^{-1} were assigned to $\nu(\text{C}=\text{O})$ of free and surface-bound ester carbonyl; and a 1255 cm^{-1} peak to $\nu(\text{C}-\text{O})$ of ester linkages. In light of our STM and TPD results, the spectra were reinterpreted as follows. The absorption at 1724 cm^{-1} was reassigned to an aldehydic $\nu(\text{C}=\text{O})$ mode due to $\eta^1(\text{C})-\text{HCO}$.^{142,143} Bridging and chelating $\eta^2(\text{C}, \text{O})-\text{H}_2\text{CO}$ give rise to $\nu(\text{C}=\text{O})$ modes at 1305 cm^{-1} and 1255 cm^{-1} , respectively. Similarly, the $\rho(\text{CH}_2)$ mode of $\eta^2(\text{C}, \text{O})-\text{H}_2\text{CO}$ also occurs at 1250 cm^{-1} .^{144,145} In either case, the reassignment of the absorption band at 1255 cm^{-1} to $\eta^2(\text{C}, \text{O})-\text{H}_2\text{CO}$ is justified. Last, the absorption at 1653 cm^{-1} was assigned to the carbonyl stretch $\nu(\text{CO})$ of carbon monoxide. The significant red shift compared to expected values of 2100 cm^{-1} ,

1900 cm⁻¹, or 1800 cm⁻¹, has been explained by Williams and Medlin¹²⁷ and Pang *et al.*¹⁴¹ as the result of electron donation by the benzene moiety, and change in the work function of Pd(111).

From the combined STM and TPD data, and by extrapolating the vast literature of oxygenates on PGM surfaces, we conclude that dissociative adsorption of TPA on Pd(111) readily occurs below room temperature. Subject to refinement, Figure 2.5 illustrates a plausible reaction mechanism of TPA under the investigated conditions. We postulate that decarbonylation of TPA proceeds via scission of the aldehydic C–H to produce $\eta^1(\text{C})$ –acyl. This step likely proceeds below 165 K since intact molecular desorption of TPA ($m/z = 134$ amu) was not detected. Further C–C cleavage produces $\eta^1(\text{C})$ –formyl precursors that lead to the competitive formation of formaldehyde and carbon monoxide. Isotopic labelling experiments of acetaldehyde and propanal on Pd(111) have established that C–H bond scission is the rate-limiting step to carbon monoxide. We found no topographic evidence that could denote the presence of covalently bound oligomers, and neither could we detect high molecular mass fragments by multiplexing between 2–150 amu during TPD experiments. Thereby, the species imaged under STM must correspond to decomposition fragments bonded by non-covalent forces. To our knowledge, on-surface formation of polyesters from aldehydes has not been documented in the literature. Only for few cases involving small aldehydes such as formaldehyde or acetaldehyde, polymerisation to paraformaldehyde and paraldehyde/polyacetaldehyde proceeds on PGM surfaces, respectively. These are only stable at temperatures ≤ 250 K and decompose back to their monomeric form. Adsorption of aldehydes with larger substituents occurs exclusively in the dihapto configuration which, as described above, does not lead to polymerisation. Hence, the proposal of an on-surface Tishchenko reaction of TPA on Pd(111) is refuted.

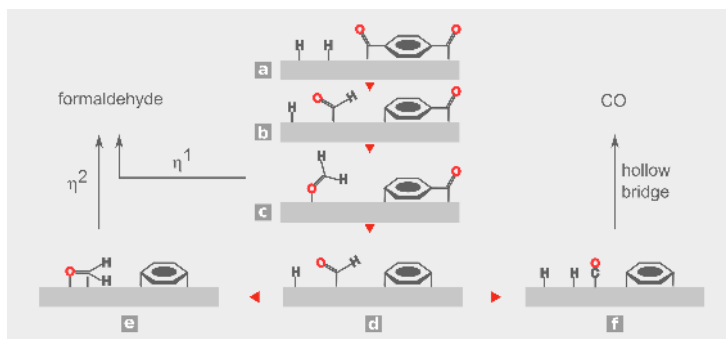


Figure 2.5 ■ Surface reaction of TPA on Pd(111). **a)** Adsorption at 165 K may readily result in C–H scission and generation of acyl species. **b)** C–C cleavage results in decarbonylation and surface formyl species. **c)** formyl recombines with surface hydrogen to produce monohapto formaldehyde, whose desorption gives rise to the peak at $T_{max3} = 280$ K **d)** In a possibly second decarbonylation step, formyl species can either **e)** desorb as dihapto formaldehyde by scavenging surface hydrogen, giving rise to two peaks at $T_{max1} = 370$ K and $T_{max2} = 455$ K in TPD spectra, or **e)** dehydrogenate to produce CO as manifested in two peaks at $T_{max1} = 368$ K and $T_{max2} = 426$ K in TPD spectra.

2.4 sCOF Synthesis on AuPd(111) Thin-film Alloys

AuPd(111) Thin-film Alloys

The results obtained from the adsorption of melamine and TPA on Pd(111) demonstrate that the reactive nature of palladium precludes depositing and reaction of monomers in a controlled manner. On reactive surfaces, molecular precursors must overcome high diffusion energy barriers in order to assemble, and thermally-activated decomposition can overwhelm the formation of well-defined surface architectures.^{62,146} As stated before, the first major challenge in sCOF synthesis on catalyst surfaces is the integration of two concepts: controlled surface modification and preservation of surface reactivity. To this end, alloying is extensively used as a means of controlling the chemical properties of heterogeneous metal catalysts and provides an alternative substrate for on-surface synthesis.

By definition, a metallic system of two or more components constitutes an alloy, irrespective of the precise manner of mixing.¹⁴⁷ The resulting mixed metallic system often exhibits markedly different physical and chemical prop-

erties from the parent metals. For instance, catalytic activity and/or selectivity can be promoted by the synergetic addition of a second component to a single metal catalyst, often outperforming the catalytic properties of the individual constituents. The experimentally observed alloying effect is frequently rationalised in terms of structural and electronic modifications referred to as ensemble and ligand effects, respectively. The ensemble effect is associated with the spatial organisation of atoms; mainly, it denotes special atomic arrangements that prove optimal for a certain chemical transformation (activity) which is often in competition with other parallel reactions (selectivity). This notion was first introduced by Ballandin and Kobozev¹⁴⁷ who envisaged the requirement of specific ensembles of atoms for molecules of distinct sizes and binding characteristics. For example, if two hypothetical competing reactions are catalysed by two distinct active sites of different sizes (*e.g.*, hexamers vs dimers), dilution of the catalytically active metal by a second inert metal will deplete the number of active ensembles. As a result, the activity at the larger ensemble will rapidly decrease in favour of the smaller ensemble, and the reaction that takes place at the latter will be kinetically enhanced. Furthermore, electronic effects such as charge transfer between the components in an alloy and orbital rehybridisation, also affect the immediate chemical environment (ligand) of active sites. Consequently, the binding motif and strength of adsorbates are altered on alloy surfaces, which impacts on the kinetics of the catalytic cycle.^{148,149}

The *d*-band model, first introduced by Hammer and Nørskov¹⁵⁰ and recently expanded by Bhattacharjee *et al.*¹⁵¹, has been successfully applied to rationalise trends in atomic and molecular¹⁰³ chemisorption on the basis of electronic effects (Figure 2.6.a). This model assumes that adsorption energies can be decomposed into two terms (Equation 2.2). Firstly, the E_{sp-hyb} term describes the coupling of the adsorbate's energy levels with the surface *s,p*-band, which gives rise to a broadening and downshifting of the adsorbate state. This interaction is attractive and its magnitude virtually the same to all transition metals, because of their broad and half-filled *s,p*-bands. Secondly, the E_{d-hyb} term embodies the contribution from the coupling between the adsorbate-induced bonding state formed after coupling with the metal's *s,p*-band, and the *d*-bands. Hybridisation of these states results in the downshift of the bonding level and the generation of an antibonding level above the

metal d -band. Unlike ΔE_{sp-hyb} , the ΔE_{d-hyb} energy term is distinctive for each transition metal and predominant in the overall chemisorption energy (ΔE). The magnitude of this term depends on the occupancy of the metal's d -states (f_d) which contributes to the filling of the antibonding level, as well as on the repulsive orthogonalisation energy between d -states and the adsorbate's molecular orbitals.¹⁴⁸ The latter is proportional to the coupling matrix element (V_{ad}), and high values can shift the position of the antibonding level above the Fermi level. Equation 2.3 illustrates the relationship between the parameters describing the metal and adsorbate (f_a, ϵ_a). The first term is the attractive hybridisation energy for partially filled anti-bonding states, whereas the second term represents the repulsive orthogonalisation energy between the adsorbate and the metal d -states. A major parameter that provides a practical descriptor of the link between electronic effects and adsorption energies is the position of the d -band centre (ϵ_d) relative to the Fermi level.¹⁴⁹ Changes in the d -band profile are self-compensated by the system by shifting the d -states up or down in order to maintain the same number of d -electrons. An upwards shift of the d -centre is interpreted as an enhancement of the binding and activity of the metal, whereas the opposite is true for a downshift. Any modification to the substrate such as strain, charge transfer, or a change in coordination number as in the case of open surfaces, has a direct impact on the positioning of the d -band centre. To this end, the growth of a foreign metal overlayer onto a host metal to produce thin-film alloys is an effective method to controllably induce shifting and tuning surface reactivity (Figure 2.6.b). Admittedly, changes in the alloy composition will affect both the distribution of atomic ensembles and the electronic structure of active sites. However, the extent to which ensemble and ligand effects dominate is highly specific to the system dealt with.

$$\Delta E = \Delta E_{sp-hyb} + \Delta E_{d-hyb} \quad (2.2)$$

$$\Delta E_{d-hyb} = -C(f_a, f_d) \frac{V_{ad}^2}{|\epsilon_a - \epsilon_d|} + \alpha V_{ad}^2 \quad (2.3)$$

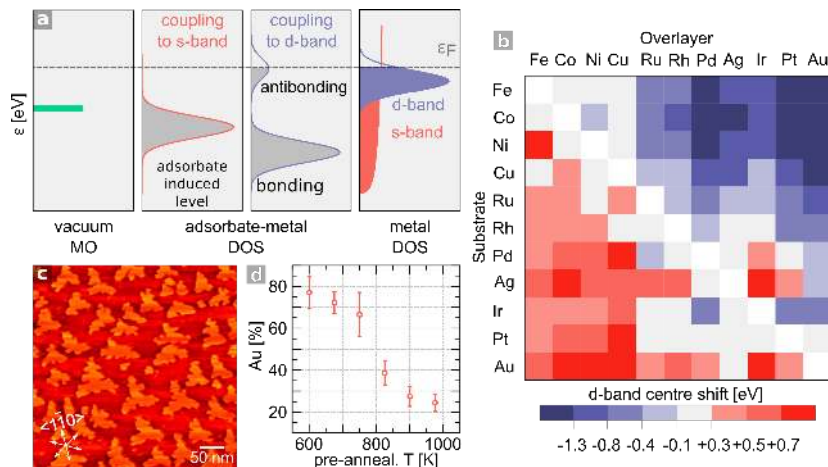


Figure 2.6 ■ Surface alloys and ligand effects. **a)** Schematic of d -band model developed by Hammer and Nørskov¹⁵⁰ to explain distinct reactivities of transition metals. First, discrete molecular orbitals couple to the metal s,p -band to form a broad resonance level. This interaction is assumed to be independent of the metal (ΔE_{sp-hyb}). Hybridisation of the adsorbate-induced bonding level with the d -band results in further splitting into bonding and antibonding levels. The filling of the antibonding depends on the nature of the metal (number of d -electrons), giving rise to distinct contributions to the ΔE_{d-hyb} energy term, and consequently to the adsorption energy (ΔE). Dash line represents the position of the metal's Fermi level (ϵ_F). **b)** Shifting of d -band centre arising from the growth of a foreign metal overlayer on a host transition metal. Note that the systems shown do not necessarily represent stable alloys and intermixing effects are not taken into account. Adapted from references [148,149]. **c)** STM topograph of dendritic growth of gold ($\theta = 0.4$ ML) on Pd(111), $V_t = 0.1$ V, $I_t = 900$ pA. **d)** Gold concentration of topmost layer as function of pre-annealing temperature in a 4 ML-thick gold film on Pd(111) as probed by medium-energy ion scattering spectroscopy (MEISS). Significant palladium enrichment of topmost layer starts at temperatures ≥ 600 K. Adapted from reference [152].

Our objective was to find a platform that offered a compromise between surface reactivity and monomer mobility that would favour on-surface polymerisation and sCOF growth. Our attention was drawn to alloys of palladium with gold, an inert metal. AuPd bimetallic alloys are exploited as highly selective heterogeneous catalysts for many reactions, including the industrially important production of vinyl acetate monomer (VAM),¹⁵³ low temperature CO oxidation,¹⁵⁴ hydrodesulfurisation,¹⁵⁵ H_2O_2 synthesis¹⁵⁶ and acetylene trimerisation.¹⁵⁷

A conventional approach in modelling alloys in UHV, also used in this project, consists of physical vapour deposition of one metal onto a bulk crystal of a second metal. The AuPd(111) thin-film alloy system is an example of such an approach, whereby gold grows pseudomorphically on Pd(111) for coverages of up to 1 ML, and then relaxes to its natural lattice spacing in a layer-by-layer (Frank van der Merwe) growth mode (Figure 2.6.c).¹⁵⁸ A particularly attractive

feature of this system is that a solid solution forms across the entire composition range and virtually all Au:Pd ratios are accessible by simply varying the pre-annealing temperature. Intermixing of the constituents is insignificant at 300 K; however, it becomes more pronounced at temperatures ≥ 600 K as gold diffuses into the bulk and the surface becomes palladium-enriched.^{135,159–162} Owens *et al.*¹⁶³ employed medium-energy ion scattering spectroscopy (MEISS) in the characterisation of the layers composition and the variation of gold content for the first layer is reproduced in Figure 2.6.d. Monte Carlo studies by Boscoboinik *et al.*¹⁶⁴ suggested that the repulsion between gold atoms in the alloy leads to a larger proportion of isolated palladium atoms compared to the expected for a truly random distribution. Liu and Nørskov¹⁶⁵ decoupled ligand and ensemble effects in AuPd alloys using DFT methods and concluded that for the latter, a linear correlation can be drawn between adsorption energy and the ratio of the alloy constituents. Furthermore, the contribution of ensemble effects to the total adsorption energy dominates over ligand effects for simple adsorbates such as CO, N, and O. Strong evidence in favour of a predominant ensemble effect has also been evoked to explain the observed selectivity in diverse reactions.^{155,159,166,167} For example, AuPd alloys are highly selective catalysts for small-scale production of H₂O₂ from H₂ and O₂. Pd monomers are required to activate H₂ dissociation, yet these ensembles cannot dissociate O₂. Thereby, decomposition of H₂O₂ to H₂O, its most thermodynamically stable product, is inhibited.¹⁶⁸ Essentially, the catalytically active Pd is diluted in a matrix of gold atoms, the least active component. As the Au:Pd ratio increases, contiguous palladium ensembles decrease in size, and eventually converted into palladium singletons isolated by gold.

Charge transfer from palladium to gold is expected since the latter is the more electronegative element. However, although gold donates 5*d*-electrons to palladium, this charge transfer is compensated by gold gaining *s,p*-type electrons from palladium.¹⁶⁹ Ruban *et al.*¹⁴⁸ showed that a gold monolayer deposited on Pd(111) results in minor shifting of the *d*-band centre, which translates into weak ligand effects (Figure 2.6.b). Contrasting with the notion of a predominant ensemble effect in AuPd alloys, Lee *et al.*¹⁷⁰ showed that only 10 % surface concentration of gold switches off CO adsorption on palladium threefold hollow sites. This low concentration is insufficient to completely dilute palladium to monomers, and an interpretation based on ligand effects

was therefore favoured instead. Similarly, a theoretical study by Zhang *et al.*¹⁷¹ on CO oxidation concluded that gold concentrations of at least 50 %, contribute to the observed rate enhancement. This was rationalised in terms of a lower adsorption energy barriers for O and CO. Their interpretation also pointed towards electronic effect rather than active ensembles. Despite the lack of a general consensus on an all-encompassing mechanism that can explain the observed activity and selectivity for all reactions, it is generally agreed that AuPd alloys offer improved catalytic performance over pure Pd or Au.

In the next sections, we employed AuPd(111) thin-film alloys as a platform for examining the surface chemistry of sCOF precursors. Although a detailed composition analysis and characterisation at each stage was not possible in this project, this system is fairly well documented, and we made use of relevant literature to draw conclusions from our observations on the functionalized AuPd(111) thin-film alloys.

Melamine adsorption on AuPd(111)

The morphology of metal vapour deposited gold films on a clean Pd(111) sample and the effect of temperature were examined under STM. At submonolayer coverages, nucleation of gold starts at step edges as well as on terraces in the form of dendritic islands with a triangular envelope, which reflects the three-fold symmetry of the underlying Pd(111) substrate (Figure 2.6.c). The growth of the next layer, prior to completion of a full monolayer, was observed for the second and consecutive layers, which eventually developed into the appearance of gold clusters at higher coverages ($\theta \sim 4$ ML). LEED data only revealed a $p(1 \times 1)$, in agreement with previous reports.¹⁵⁸ Thermal treatment of the deposited films at 715–800 K facilitates gold diffusion, and resulted in the smoothing of the island step-edges and merging into larger islands. Further heating at $T \geq 865$ K removes any evidence of isolated gold islands; the surface appeared homogeneous, seemingly featureless, and with flat terraces (Figure S2.2). This is due to further intermixing and gold diffusion into the bulk. These observations are wholly consistent with the detailed study by Owens¹⁵² on the morphology and composition of AuPd(111) thin-films.

In order to examine the behaviour of melamine on palladium-rich AuPd islands, 0.6 ML of gold was deposited onto Pd(111) and the surface annealed to 730 K. The prepared surface was then exposed to melamine (25 L) at 300 K. Imaging of the prepared surface at 300 K did not render images of sufficient resolution. Therefore, the sample was heated to 730 K to induce ordering and desorption of any possible multilayer. A high density of clusters composed of globular features \varnothing 0.5–1 nm in diameter populated the prepared islands, as well as the exposed Pd(111) surface (Figure 2.7.a,b). These features are assigned to the decomposition products of melamine, analogous to those observed on pure Pd(111). No evidence was found of *flat-lying* melamine molecules, which were expected to manifest as triangular features assembled into hexagons.^{86,172} Neither was any evidence found of features that could hint melamine polymerisation to polyguanide, which rules out a ring-opening reaction on the alloy surface. The fact that these globular features were also imaged on the islands and persisted up to 770 K, suggests that these species must necessarily arise from melamine in a chemisorbed state, since physisorbed melamine desorbs intact at this temperature from Au(111) (Figure S2.2).¹⁷³ This observation strongly suggests the presence of palladium atoms in the islands, which are best described as AuPd islands. This is expected from the pre-annealing treatment purposely conducted to induce palladium-enrichment. Additionally, bare areas within the island likely reflect gold-like sites that became exposed following the desorption of physisorbed melamine. The STM data suggest that melamine and its decomposition products bind to the created palladium sites within the AuPd islands. These results do not conform with the intended diluting effect by gold on the binding strength. In other words, melamine acts as a titrant by chemisorbing to palladium-like sites, whereas it only physisorbs to gold-like sites.

Adsorption of melamine on Au(111) and AuPd(111) alloy surfaces was further characterised using HREELS (Figure 2.7.c). Spectra were recorded in specular mode after exposing the prepared Au(111) or AuPd(111) alloy surface to melamine at 300 K. Gold evaporation was carried out in a similar manner as described for STM imaging experiments. The prepared AuPd(111) surface was titrated with CO before melamine deposition. Complete passivation of the Pd(111) substrate by gold ($\theta \sim 1.0$ ML) was evident from absent CO vibrations (Figure S2.2). Assignment of the energy losses of melamine on Au(111) sum-

marised in Table 4, is based on the calculated normal vibrational modes of a single melamine molecule adsorbed onto a modelled gold slab. A negligible effect of the $(22 \times \sqrt{3})$ reconstruction of Au(111) was assumed. Optimisation and calculated vibrational spectra were carried out by Peake⁹⁹ using the same theoretical methods described for melamine adsorption onto Pd(111) (*vide supra*).

Before proceeding to examine the adsorption of melamine onto AuPd(111) alloys, the adsorption of melamine on Au(111) is discussed for comparison (spectrum 1 in Figure 2.7.c). HREEL spectra exhibited clear differences from that of melamine adsorption onto Pd(111) (Figure 2.3.d). Signature losses at 3485 cm^{-1} , 1580 cm^{-1} , and 1005 cm^{-1} assigned to NH_2 stretching, scissoring and rocking modes respectively, were low in intensity or completely absent. Similarly, losses associated with CNC and NCN bending modes in the $375\text{--}700\text{ cm}^{-1}$ range were markedly weak. The dipole moments of these vibrational modes lie along the molecular plane; therefore, the weak intensity is accounted for as a result of melamine aligning parallel to the surface plane. The triazine ring out-of-plane deformation at 805 cm^{-1} , and wagging modes of the NH_2 group at 225 cm^{-1} , whose dipole moments lie normal to the molecular plane, were dominant spectral features. This also supports this interpretation. Loss of spectral features was observed after heating the sample to 350 K, consistent with desorption of physisorbed melamine (Figure S2.2). DFT simulations carried out by Peake⁹⁹ found that a *flat-lying* geometry is optimal for melamine binding onto Au(111) at a binding energy of $E_{ads} = -1.15\text{ eV}$ (Figure 2.7.d). The combined HREELS and DFT results consistently agree with earlier experimental and theoretical investigations of this system.^{86,174}

Turning now to the adsorption of melamine on AuPd(111), the relative intensities of the energy losses highlighted in spectrum 2 (Figure 2.7.c) exhibited some similarities to that on pure gold. Passivation of Pd(111) by gold causes melamine to adopt a geometry similar to that of melamine adsorption on Au(111). Notably, the vibrational modes located below 700 cm^{-1} are even further attenuated or entirely absent, as in the case of the 560 cm^{-1} and 610 cm^{-1} modes. Accounting for the attenuation of these modes is not straightforward, but may result from variations in the assembly of melamine on an inhomogeneous and defective gold layer. Nevertheless, the main features of the spectrum

are still consistent with a predominantly *flat-lying* adsorption geometry on the gold-rich AuPd(111) alloy.

Annealing the prepared AuPd(111) surface to 745 K, and redeposition of melamine produced HREEL spectrum 3 in Figure 2.7.c. Unlike on the gold-rich AuPd(111) alloy, the signature modes of NH₂ vibrations of melamine were substantially enhanced on this surface and the triazine ring out-of-plane deformation mode noticeably attenuated. The pre-annealing treatment of the sample at 745 K was expected to promote substantial intermixing and changes in the alloy composition (See Figure 2.6.d). The transformation of the spectra was interpreted as the reorientation of melamine on this alloy surface. We deduced that the presence of palladium sites causes melamine to bind with its molecular plane tilted closer to the surface normal. Certainly, the spectrum does not mimic exactly that of melamine on Pd(111). Energy losses at 600 cm⁻¹, 490 cm⁻¹ and 405 cm⁻¹ in the fingerprint region are highly convoluted in the signal for the alloy, whereas these are well-defined strong losses on Pd(111). Melamine bound to coexisting mixed gold and palladium sites may account for the complex spectral features in this region, but a comprehensive interpretation is challenging.

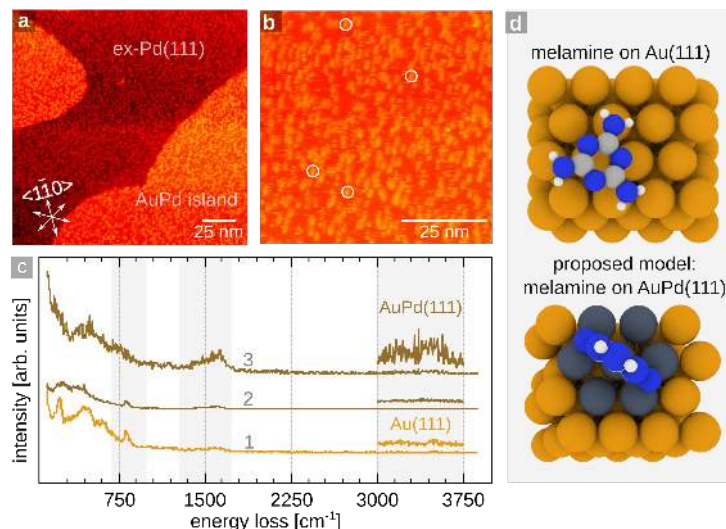


Figure 2.7 ■ Melamine on Au(111) AuPd(111). **a)** Large-scale STM image of melamine deposited onto AuPd(111). Labelled in the image are the exposed underlying Pd(111) substrate (ex-Pd(111)), and formed AuPd(111) island. **b)** Expanded region of a AuPd(111) island with features assigned to decomposition products of melamine. **c)** HREEL spectra of melamine adsorbed onto 1) Au(111), 2) gold-rich AuPd(111) prepared by depositing gold onto Pd(111) held at 300 K, and 3) AuPd(111) after annealing to 745 K to induce Pd-enrichment of the surface. Highlighted grey areas indicate the region of signature energy losses associated with NH_2 stretching ($3000\text{--}3750\text{ cm}^{-1}$), NH_2 bending ($1350\text{--}1650\text{ cm}^{-1}$) and triazine ring out-of-plane deformation modes (805 cm^{-1}). $E_0 = 4.1\text{ eV}$, $\text{FWHM} = 44.8\text{ cm}^{-1}$. **d)** DFT-optimised geometry of melamine on Au(111) (top). A flat-lying adsorption is favoured, $E_{\text{ads}} = -1.15\text{ eV}$. Adapted from reference [99]. Proposed model of melamine binding to palladium-rich AuPd(111) alloys whereby melamine is presumed to bind Pd ensembles in an upright geometry (bottom).

Table 4 ■ Melamine/Au(111) HREELS vibrational modes assignment. ν : stretch, β : bending, δ : scissoring, ρ : rocking, ω : wagging, τ : twisting, R: ring vibration, sym.: symmetric, asym.: asymmetric, def.: deformation, breath.: breathing, ip: in plane, op: out of plane.

Energy loss [cm^{-1}]	Assignment
3485	$\nu(\text{NH}_2)_{\text{sym.}}$
1580	$\delta(\text{NH}_2)$, $\nu(\text{C}-\text{NH}_2)$, $\nu(\text{CN})$
1440	$\nu(\text{CN})$, $\delta(\text{NH}_2)$, $\nu(\text{C}-\text{NH}_2)$, $\text{R}_{\text{breath.}}$
805	$\text{R}_{\text{op def.}}$
610	$\text{R}_{\text{breath.}}$
560	$\beta(\text{CNC}, \text{NCN})_{\text{ip}}$, $\tau(\text{NH}_2)$
470	} $\beta(\text{C}-\text{NH}_2)_{\text{ip}}$, $\tau(\text{NH}_2)$
435	
225	
	$\omega(\text{NH}_2)$

From the data collected on this system, it was deduced that ensemble effects direct the adsorption of melamine on this alloy. It is postulated that melamine

adopts an *upright* chemisorbed geometry on palladium sites, and an otherwise *flat-lying* physisorbed state on gold sites (Figure 2.7.d). An electronic effect whereby the reactivity of the entire palladium surface is modulated by the presence of gold atoms does not seem to be relevant for this system; instead, a local surface chemistry dominated by palladium sites, which retain their activity, seems a more satisfactory explanation for the experimental results. A similar conclusion was reached by Wang *et al.*⁹⁶ in their combined STM/DFT study of melamine adsorption on CuAu(111) alloys. Their findings demonstrated that melamine co-exists in two *flat-lying* physisorbed phases on gold-like sites, and an *upright* chemisorbed state on Cu-like sites.

In conclusion, this alloying approach proved unsuccessful for our purpose since only on the gold-rich alloy surface does melamine adopt the *flat-lying* geometry necessary for 2D polymerisation. However, for this composition, catalytic activity is completely lost. A second important consideration is the reactivity of melamine. Despite the widespread use of melamine in hydrogen-bonded networks, producing a fully covalent 2D framework is very likely to be unsuccessful. Although some experimental evidence favours a predominant aromatic structure of melamine in the solid state,^{175,176} resonance structures of melamine are possible.^{94,177} This resonance effect is reflected in the C–NH₂ bond length (1.347 Å), which is significantly shorter than an ordinary primary amine (≈ 1.5 Å), but very close to the C=N bond length in the aromatic triazine ring (1.348 Å). Consequently, a sp^2 rather than sp^3 character is a more adequate description of the hybridisation of the amino nitrogen atoms in melamine (Figure S2.3).^{178–182} As a result, melamine is less basic than ordinary primary amines, with the endocyclic nitrogens being, in fact, the most basic.^{183,184} The amino groups behave more as amidines than amines, and their successive activation towards nucleophilic attack is difficult even under harsh conditions in solution chemistry.¹⁸⁵ In addition, substitution at the third amino group does not lead to an on-surface reaction with electrophiles.^{26,30,90} For this reason, we conclude that melamine is not a suitable building block for sCOF synthesis.

sCOF Synthesis from Halogenated precursors on AuPd(111)

In the previous sections, key challenges were identified associated with both the alloy activity and the reactivity of the molecules used as monomers in 2D polymerisation. In an attempt to meet our target surface modification, we turn our attention to an alternative surface reaction and alloying protocol. With the purpose of alleviating the number of parameters associated with bicomponent sCOF synthesis (*e.g.*, sequential deposition of monomers, flux, substrate temperature, sticking probability of the second monomer in the presence of another monomer, phase segregation, etc), efforts were instead focused on identifying a surface reaction that allowed efficient sCOF fabrication. Hence, the initial pursuit of imine-based sCOF synthesis was abandoned in favour of Ullmann reaction. As discussed in the introduction, Ullmann coupling belongs to a class of reactions that produces C–C bonds via homolytic cleavage of halogenated precursors on a variety of metal surfaces, including Au(111). In this section, we employed 1,3,5-Tris(4-bromophenyl)benzene (**TBPB**) (Figure 2.8.a) for the fabrication of a high-quality porous sCOF on a reactive surface.

Blunt *et al.*⁶⁶ studied the adsorption of TBPB on Au(111) under UHV condition, and reported the formation of a close-packed monolayer at room temperature. The interaction responsible for the self-assembly of TBPB is halogen bonding between neighbouring TBPB molecules. An attractive electrostatic force exists between the electropositive σ -hole and the electronegative belt of neighbouring Br atoms, as well as between the electronegative belt around Br atoms and hydrogen atoms.^{186–191} More importantly, the authors realised that activation of TBPB onto a substrate held at 410 K facilitated monomer diffusion, resulting in a porous sCOF that extended over the entire surface. Gutzler *et al.*⁶¹ provided experimental evidence of the catalytic role of the substrate in this reaction step. The reaction proceeded favourably on metallic surfaces, but no evidence of C–C coupling was found on the inert HOPG surface. Thermal treatment simply results in reversible desorption of the TBPB monolayer.

We reproduced the deposition on TBPB on Au(111) under similar conditions described by Blunt *et al.*, and the sample was examined under STM. Figure 2.8.b,c illustrates the halogen-bonded array formed after exposing a clean Au(111) held at 300 K to TBPB in the gas phase ($T_{dose.} = 435$ K, 310 L). The

self-assembled monolayer is described by the unit cell vectors $\bar{a} = 1.62 \text{ nm}$, $\bar{b} = 2.41 \text{ nm}$, with an included angle of $\angle(\bar{a}, \bar{b}) = 61.5^\circ$, and contains two TBPB molecules per unit cell ($\theta = 0.043 \text{ ML}$ with respect an unreconstructed Au(111) layer). The periodic structure conforms with the observations by Blunt *et al.*⁶⁶ in UHV and with *phase 1*, as referred to in the work by Russell *et al.*¹⁹² from solution deposition of TBPB on Au(111). Heating the as-prepared sample to 475 K induces homolytic cleavage of the C–Br bonds and generates the activated precursor[†] which undergoes C–C coupling with adjacent molecules (Figure 2.8.d). This preparation produces a close-packed arrangement of kinetically trapped dimers, which inhibits the formation of an open framework. Instead, depositing TBPB onto Au(111) held at 475 K facilitates the sequential addition of monomer, and the fabrication of an extended porous sCOF (Figure 2.8.e). The pivotal role of precursor surface mobility to create high-quality sCOFs has been addressed in detailed experimental and theoretical work by Bieri *et al.*¹⁴⁶ The idealised sCOF is composed of hexagonal pores with a wall-to-wall length of $l = 2.1 \text{ nm}$ (Figure 2.8.f). However, since this reaction is kinetically controlled, and no self-correcting mechanism exists that can revert C–C bond formation, a defective sCOF results which contains *i*-gonal pores (*i*: penta-, hexa-, hepta-).⁷²

A control experiment was carried out whereby TBPB was directly deposited onto Pd(111) held at 300 K. Unlike adsorption on Au(111), a halogen-bonded self-assembled layer did not form. Instead, dissociative adsorption of TBPB via debromination readily occurred at this temperature. The Y-shaped features highlighted in Figure 2.9.a are assigned to the activated precursor, whereas the accompanying circular features are assigned to Br adatoms generated from C–Br cleavage. Interestingly, the measured interatomic spacing between Br atoms ($5.6 \pm 0.7 \text{ \AA}$) is closer to a (2×2) -Br than to a $(\sqrt{3} \times \sqrt{30})R30^\circ$ -Br structure, with the latter being the expected for halogen adsorption on 3-fold sites of Pd(111).^{193,194} Dehalogenation of TBPB at 300 K on Pd(111) is not unexpected given the high catalytic activity of this metal. Microscopic kinetic studies of the on-surface Ullmann reaction on Pd-decorated Au(111) by Adisoejoso *et al.*¹⁹⁵ have shown an enhanced catalytic effect with respect to clean Au(111). Furthermore, a two-step mechanism was proposed where C–C coupling is the rate-limiting step, with an activation energy of $E_a = 0.41 \pm 0.03 \text{ eV}$.

[†]Through this section, the term "activated precursor" will be used to refer to a fully or partially debrominated TBPB molecule.

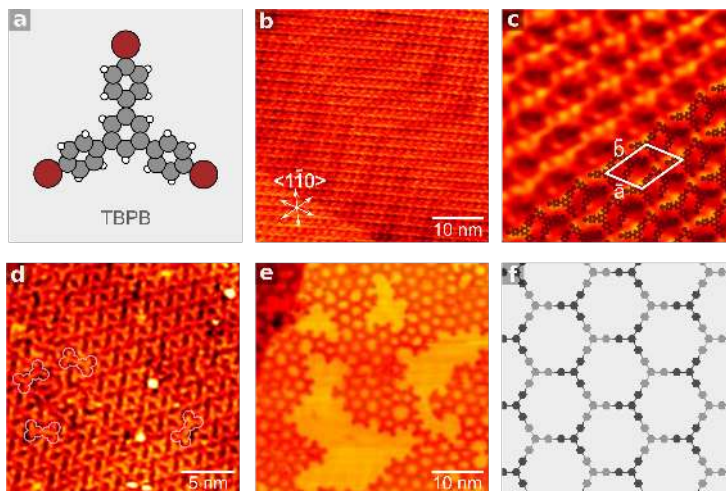


Figure 2.8 ■ TBPB adsorption onto Au(111). **a)** Structural model of 1,3,5-Tris(4-bromophenyl)benzene (TBPB). **b)** STM image of TBPB monolayer on Au(111) formed at 300 K. **c)** Structure of halogen-bonded monolayer of TBPB ($\theta = 0.043$ ML) with unit cell overlaid on STM image. Image size 37.5×37.5 nm². FFT filtering was applied on the image. **d)** STM image of prepared monolayer followed heating at 475 K, $t = 10$ min. Highlighted in white circles are adjacent TBPB molecules that underwent dehalogenation and C–C coupling. **e)** TBPB deposited onto Au(111) substrate held at 475 K. All images were acquired at $V_t = -0.6$ V, $I_t = 300$ pA. **f)** Idealised honeycomb porous sCOF.

Annealing to (or deposition TBPB at) 475 K induced extensive decomposition of the monomer, with no evidence of self-assembly or formation of covalent structures. Similarly, Morchutt *et al.*⁶² deposited TBPB on Ni(111) with comparable results and were only able to observe polymerisation after electronic decoupling of the surface by a graphene layer. This behaviour strongly supports the argument that diffusion energy barriers for the activated precursor must be significant on palladium, and cannot be overcome by heating without decomposition becoming a competing side reaction. These results further discouraged a direct synthesis of sCOFs on palladium.

Next, we hypothesised that deposition of TBPB on a gold-rich AuPd(111) thin-film alloy should emulate the surface chemistry observed on Au(111), and that a porous sCOF would form. Since the framework exhibits remarkable thermal stability on the gold surface (Figure 2.11), we conjectured that palladium enrichment of the topmost layer could be promoted by thermal annealing in a successive step while preserving the integrity of the sCOF (Figure 2.9.b,c). The morphology of metal-on-metal epitaxy is greatly affected by the conditions employed, including flux, deposition temperature, and annealing

treatment. Such conditions impact directly on the interplay between kinetics and thermodynamics of growth.^{196,197} For instance, Ruff *et al.*¹⁹⁸ and Gleich *et al.*¹⁹⁹ exploited the temperature dependence of gold epitaxy on Pd(111) to create dendritic islands with a high density of Au step sites for CO adsorption at subambient temperatures. As discussed in the previous section, we found that heteroepitaxial growth of gold onto Pd(111) at 300 K results in Stranski-Krastanov growth of 3D gold islands at high coverages (Figure 2.9.d). Pre-annealing at temperatures above 800 K produces surfaces with a flat topography, however, extensive intermixing and palladium enrichment already occurs at this temperature.^{161,199} With the aim of producing a gold-rich surface with a smooth morphology suitable for sCOF fabrication and their characterisation under STM, we devised a deposition procedure that involved gold evaporation with the substrate held at 330 K, followed by annealing for 30 min at 575 K. The rationale behind this preparation protocol resides in the desorption of adventitious background gases, and most importantly, enhanced diffusion of gold atoms upon impingement onto the Pd(111) substrate. This protocol was expected to favour the formation of uniform flat layers. Note that the thermal treatment temperature at 574 K does not compromise the alloy composition, and the surface remains gold-rich throughout the preparation. Pronounced changes in alloy composition are expected to appear at temperatures above 600 K (Figure 2.6.d).^{135,159,161}

Deposition of 4 monolayers equivalent (MLE) of gold under the described preparation resulted in the surface shown in Figure 2.9.e. A long-range hexagonal Moiré pattern was observed, with a mean modulation maxima repeat at a period of $\bar{a}_{\text{Moiré}} = 79.59 \pm 1.55 \text{ \AA}$, and a corrugation of approximately 20 pm at $V_t = -0.6 \text{ V}$, $I_t = 300 \text{ pA}$. The pattern was not entirely ordered; some regions presented slightly longer periodicities and distorted away from a perfect hexagonal lattice. This may arise from inhomogeneity in the growth of underlying layers.⁹⁶ Moiré and dislocations patterns arise often in heteroepitaxially grown metal thin films.²⁰⁰ Propagation beyond the first layer is not uncommon, Blecher *et al.*²⁰¹ showed the Moiré pattern generated from Pd films grown on Au(111) and Cu(111) presented no changes in the pattern in the course of deposition 1 to 4 ML, and even after 10 ML in some cases.²⁰² In this case, the Moiré pattern arises as a consequence of the 4.9 % lattice mismatch between the (111) plane of Au (2.88 Å) and Pd (2.75 Å). Owens¹⁵² also described a

hexagonal Moiré pattern of periodicity ~ 80 Å after depositing 1–2 ML of gold on Pd(111) at 300 K, and proposed two explanations: the overlayer is either a compressed Au layer sitting on Pd(111); or a mixed AuPd surface alloy. Similarly to the work by Blecher *et al.*²⁰¹ and Vestergaard²⁰³, the periodicity of the Moiré pattern ($\bar{a}_{\text{Moiré}}$) was modelled as the resulting envelope beating of two overlapping waves of different wavelength (Figure 2.9.f). The Moiré pattern is represented as the difference in wavevectors of two overlaying lattices: the underlying substrate ($\bar{k}_{\text{Pd}(111)}$), and overlayer ($\bar{k}_{\text{Au overlayer}}$) (Equation 2.4). See *Methods* chapter for detailed description of the derivation. From the measured Moiré periodicity and angles, a value of $\bar{a}_{\text{Au overlayer}} = 2.85$ Å was derived, which represent a 1.04 % contraction of the lattice spacing with respect to the natural 2.88 Å in Au(111). This value reflects the pseudomorphic growth of gold for the first layer.¹⁵⁸

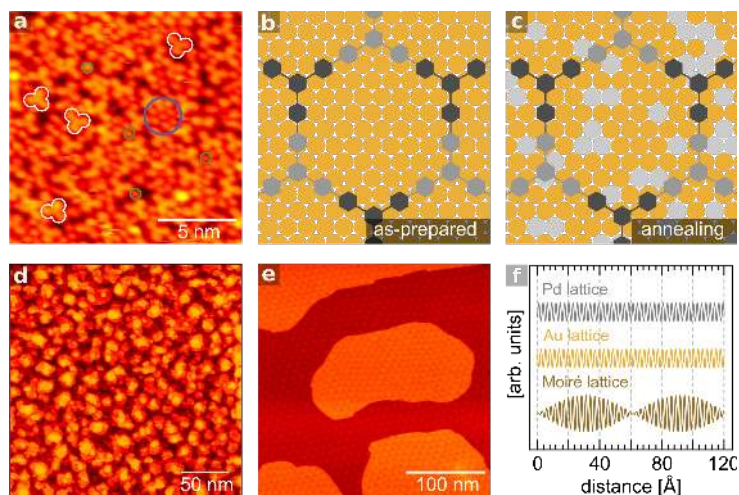


Figure 2.9 ■ TBPB adsorption onto Pd(111) and preparation of sCOF/AuPd(111). **a)** STM image of TBPB monolayer on Pd(111). Highlighted in the image are features assigned to the activated precursor (white), individual split-off Br atoms (green), and hexagonal array of Br atoms (blue). **b)** Schematic of hypothesized fabrication of sCOF on a gold-rich AuPd(111) from TBPB under same deposition conditions as on Au(111). **c)** Annealing the preformed sCOF above 600 K would induce intermixing and palladium enrichment of topmost layer. **d)** STM image of 3D islands formed upon cumulative deposition of *ca* 4 MLE of gold on Pd(111) at 300 K, *rate* = 0.04 MLmin⁻¹. **e)** STM image of AuPd(111) alloy prepared under the conditions detailed above. **f)** Unidimensional model of Moiré pattern formation by superposition of two waves with wavelengths proportional to $\bar{a}_{\text{Pd}(111)}$ and $\bar{a}_{\text{Au}(111)}$. A wavepacket is produced whose envelope has a modulation maxima repeat at a period of 60.9 Å. This periodicity is markedly smaller than that observed experimentally (79.59 ± 1.55 Å), which hints compression of the Au overlayer. Images a) and d) were acquired at $V_t = -0.6$ V, $I_t = 300$ pA; image d) was acquired at $V_t = -0.6$ V, $I_t = 200$ pA.

$$\bar{k}_{\text{Moiré}} = \bar{k}_{\text{Au overlayer}} - \bar{k}_{\text{Pd(111)}} \quad (2.4)$$

Deposition of TBPB on the AuPd(111) alloy surface held at 475 K resulted in a defective, aperiodic, porous framework which extended over the entire surface (Figure 2.10.a). The apparent length of the segments making up the pore walls of the framework ($l = 13.5 \pm 0.8 \text{ \AA}$) is in good agreement with two C–C coupled monomers as measured from the centroid of the middle phenyl ring.⁶⁶ No evidence was found of metal adatoms incorporation within the network; such a bonding motif would manifest as protrusions at the molecule-adatom-molecule junction, and produce longer bond lengths.⁶¹ Hence, the framework formed on the AuPd(111) surface is undoubtedly fully covalent, and the possibility of metal organic bonding is discounted. The sCOF is comprised of 45 % hexagonal ($A_{\square} = 3.0 \pm 0.4 \text{ nm}^2$) and 40 % pentagonal pores ($A_{\square} = 2.0 \pm 0.5 \text{ nm}^2$), whereas the remaining accounts for heptagonal (12 %), or rarely square pores. Only closed and well-defined pores were taken into account in the pore distribution from a $40 \times 40 \text{ nm}^2$ STM image ($n = 78$ pores). 50 % of the pores were hexagonal, in agreement with the reported by Blunt *et al.*⁶⁶. A minimal spanning tree analysis (MST)^{84,204} of the framework yield-ed a mean edge value $m_{\text{AuPd}} = 0.78$ and a standard deviation of $s_{\text{AuPd}} = 0.22$, which is close to the values $m_{\text{Au}} = 0.74$ and $s_{\text{Au}} = 0.21$ derived for the sCOF fabricated on Au(111). These values deviate significantly from the expected for a perfectly crystalline hexagonal lattice ($m_{\square} = 1.075$, $s_{\square} = 0$), and quantitatively illustrate the degree of disorder in the structure expected for the kinetically driven reaction (Figure S2.6). Overall, this is strong evidence of the surface chemistry on the gold-rich AuPd(111) being similar to that on Au(111).

Along with the sCOF, islands of periodically arranged, close-packed protrusions were resolved on top of a Moiré background (Figure 2.10.d). We assigned these features to Br adatoms, the byproduct of the on-surface reaction.^{205–207} The apparent Br–Br distance was $6.8 \pm 0.1 \text{ \AA}$, and the superstructure is rotated by approximately 20° from the Moiré pattern direction (Figure 2.10.e). These dimensions are consistent with a commensurate $(\sqrt{7} \times \sqrt{7})R19.1^\circ$ -Br superstructure, previously reported for halogen adsorption such as Br/Au(111),^{208–210} Br/Ag(111),²¹¹ and I/Pt(111).^{212,213} The periodicity of the Moiré pattern was the same as that observed for the as-prepared surface alloy, and does not arise

from the Br overlayer, for which a shorter periodicity of 13 \AA would be expected.²⁰⁹ Close examination of the framework also revealed that most of the pores hosted adsorbed species (Figure 2.10.f). Although monomers and dimers became trapped in closed and open pores, these were resolved as Y-shaped features. Instead, we believe that Br adatoms populate the pores in the framework. Assuming the same packing as in the $(\sqrt{7} \times \sqrt{7})R19.1^\circ\text{-Br}$ superstructure, a hexagonal pore is sufficiently large to host at least four Br adatoms. Some pores remained populated even after annealing to 675 K, at which temperature Br desorbs completely from Au(111).^{214–217} However, Br binds more strongly to Pd (3.21 eV) than it does to Au (2.37 eV),²¹⁸ and require higher temperatures to desorb. This would be the case if the top layer became palladium-enriched following the described preparation.^{219–221}

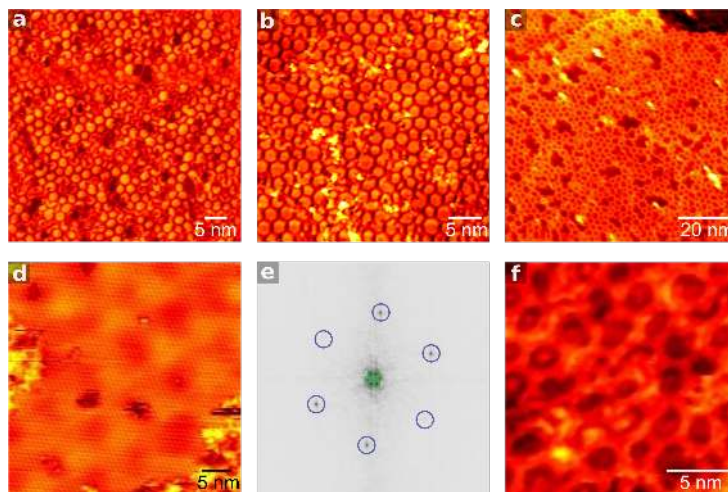


Figure 2.10 ■ sCOF on AuPd(111) alloys and coadsorbed Br. STM image of sCOF prepared by sublimation of TBPB onto a gold-rich AuPd(111) alloy held at 475 K, and heated for $t = 10$ min at **a)** 575 K, $V_t = 0.6$ V, $I_t = 300$ pA **b)** 675 K, $V_t = -0.6$ V, $I_t = 100$ pA and **c)** 785 K, $V_t = 0.6$ V, $I_t = 100$ pA. **d)** Coexisting Br island on AuPd(111). **e)** FFT of image d); inner green circles highlight spots associated with the substrate Moiré pattern, outer blue circles highlight spots correspond to the $(\sqrt{7} \times \sqrt{7})R19.1^\circ\text{-Br}$ superstructure. **f)** STM image of pores populated by Br adatoms. Images d) and f) were acquired at $V_t = -0.6$ V, $I_t = 200$ pA.

The thermal stability of the sCOF was assessed by heating the surface at successively higher temperatures for $t = 10$ min, and imaging under STM at 300 K. The sCOF retained its porosity and remained stable to decomposition up to at least 785 K (Figure 2.10.b,c). Degradation of the porous framework, and appearance of features likely associated with carbonaceous species, occurred

after heating at 885 K. By comparison, Gutzler *et al.*⁶¹ reported extensive decomposition and loss of porosity of this sCOF prepared on Cu(111) at 675 K. The stability also differed greatly from that on Au(111), for which the sCOF remained stable at much higher temperatures (Figure 2.11.b). The decomposition of the sCOF on the alloy is likely to be a consequence of two processes: firstly, annealing induces gold diffusion into the bulk, with the concomitant emergence of active ensembles of palladium atoms. Secondly, the rate of dehydrogenative decomposition to surface carbon increases at higher temperatures.¹⁵⁹

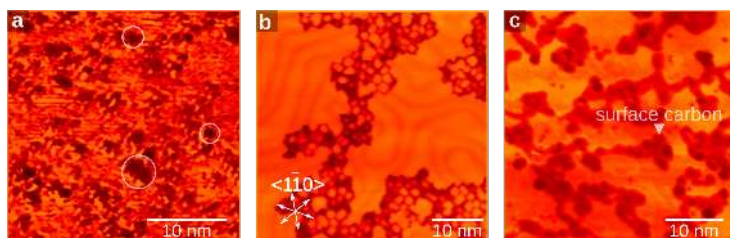


Figure 2.11 ■ **TBPB and sCOF decomposition.** **a)** Deposition of TBPB onto Pd(111) held at 475 K. No evidence of nanostructure formation was found. Clusters several nanometers long attributed to decomposition highlighted in white. **b)** sCOF/Au(111) after heating at 975 K. **c)** sCOF/AuPd(111) after heating at 885 K. Images a) and c) were acquired at $V_t = -0.6$ V, $I_t = 300$ pA; image b) was acquired at $V_t = -1.0$ V, $I_t = 100$ pA.

CO Titration of sCOF/AuPd(111)

The preparation protocol described above proved successful for sCOF synthesis on the gold-rich alloy and exhibited modest thermal stability. The temperature range within which the sCOF is stable is sufficient to induce moderate palladium enrichment in clean AuPd(111) (Figure 2.6.d). In order to assess if intermixing could also be induced in the sCOF/AuPd(111) system, palladium sites were probed by CO titration. The high affinity of CO for palladium makes it a very suitable titrant, to not only identify palladium enrichment, but also the type of site (3-fold, bridge, or atop). The sCOF/AuPd(111) was annealed to various temperatures and exposed to CO ($\simeq 600$ L, $P_{\text{CO}} = 1 \times 10^{-6}$ mbar) at 300 K. The chamber was then allowed to reach UHV, and the sample examined under RAIRS.

Figure 2.12.a shows the RAIR spectra of CO dosed on sCOF/AuPd(111) after the sample was annealed to 675 K and 775 K. Negligible CO uptake was

detected for the 675 K sample, likely due to either a low amount of palladium and/or to Br blocking adsorption sites. After annealing to 775 K two peaks at 1905 cm^{-1} and 2021 cm^{-1} emerged, accompanied by two weaker absorptions at 2063 cm^{-1} and 2140 cm^{-1} . Accordingly, the 1905 cm^{-1} absorption is assigned to a $\nu(\text{CO})$ on Pd bridge sites, whereas the absorption at 2021 cm^{-1} with the shoulder at 2063 cm^{-1} is assigned to $\nu(\text{CO})$ on Pd atop sites.^{135,136,160,166,199,222–225} Gao *et al.*²²⁴ also reported a shoulder for this band which the authors attributed to CO-induced segregation of Pd atop sites. This absorption is at a lower wavenumber compared to the literature value of 2090 cm^{-1} on the clean alloy. This redshift likely arises as a consequence of back donation into the $2\pi^*$ orbital of CO by the aromatic rings in the sCOF through the surface.²²⁶ A featureless spectrum below 1900 cm^{-1} suggests the absence of 3-fold hollow sites. The estimated alloy composition of a clean surface annealed at 775 K is $\text{Au}_{40}\text{Pd}_{60}$, for which only Pd atop sites should be available on the surface.¹³⁵ The fact that we also observe CO on bridge sites with an intensity comparable to that of CO on atop sites, suggests palladium-enrichment of the surface with respect to the clean AuPd(111) system.^{135,163} However, it is noteworthy that the Pd concentration is likely to be underestimated because of adsorbates such as the sCOF, residual Br adatoms, and CO can promote further surface segregation of Pd atoms.^{163,225,227,228} In the words of Haire *et al.*²²⁹, *the surface composition will self-adjust, so enrichment in the element whose interaction with the adsorbate is the strongest is thermodynamically favoured.* Nevertheless, the clean AuPd(111) system should provide a reliable lower-limit of the surface palladium concentration relevant to the discussion of our results.

Interestingly, a weak feature emerged at 2140 cm^{-1} which is too blueshifted to be assigned to CO on pure Pd sites, but resembles more closely palladium-modified Au atop sites.¹³⁵ CO is not stable on Au at ambient temperatures, and complete desorption is expected at approximately 255 K.^{135,161,224} A tentative explanation for this feature is the entrapment of CO underneath the sCOF. Atoms^{230,231} and small molecules such as H_2O ,²³² NO_2 ,²³³ O_2 ,²³⁴ or CO^{235,236} have been shown to intercalate at the graphene/metal interface both in the mbar and UHV regimes.^{237–239} Defects, domain boundaries, edges, and wrinkles in graphene facilitate the diffusion and intercalation processes; the confinement of molecules takes place as a result of both geometrical and electronic effects.^{231,240} For instance, Mu *et al.*²³⁷ showed that CO remained trapped at

the graphene/Pt(111) interface under UHV up to $\simeq 500$ K, when exposing the sample to $P_{\text{CO}} = 1 \times 10^{-6}$ mbar. Independently, Yao *et al.*²³⁹ observed experimentally and using density functional theory, that the confinement effect of the graphene layer produces a redshift in the Pt atop-bound CO stretching frequency and a sharp desorption peak in TPD spectra. Such an intercalation phenomenon has been reported for porous networks as well. Emmez *et al.*²⁴¹ reported CO and D₂ permeation through a porous SiO₂ film (silicatene) grown on Ru(0001). A complex CO uptake kinetic profile was derived that involved an activated gas transport step through the nanometre-sized pores and diffusion across the surface. In graphene, hexagonal boron nitride layers,^{242–244} and the silicatene system, decoupling of the substrate and the network as a consequence of CO intercalation has been demonstrated. Accordingly, we conjecture that the pores and defects in our network could provide the diffusion channels necessary for CO permeation and intercalation at the sCOF/AuPd(111) interface. We postulate that the peak at 2140 cm^{-1} in our data could belong to CO confined underneath the sCOF and adsorbed on gold-like atop sites. However, this notion was not investigated further.

The sCOF/AuPd(111) was also interrogated using TPD. For comparative purposes, we first describe the behaviour of CO desorption on the clean AuPd(111) alloy (Figure S2.4). A single peak at $T_{\text{max}1} \simeq 345$ K is observed for the 625 K-alloy, which was assigned to CO desorption from atop palladium sites. For pre-annealing temperatures between 670–810 K, the desorption trace broadens with a $T_{\text{max}2} = 385$ K assigned to CO desorption from bridge palladium sites. For the samples preannealed at 810 K and above, the desorption traces extended to higher temperatures. A third peak also emerged, which was assigned to CO desorption from 3-fold hollow palladium sites. Correspondingly, CO desorbed from clean Pd(111) in a broad trace that convoluted all three peaks. The development of all three types of adsorption sites with increasing pre-annealing temperature is in good agreement with the work by Li *et al.*¹³⁵.

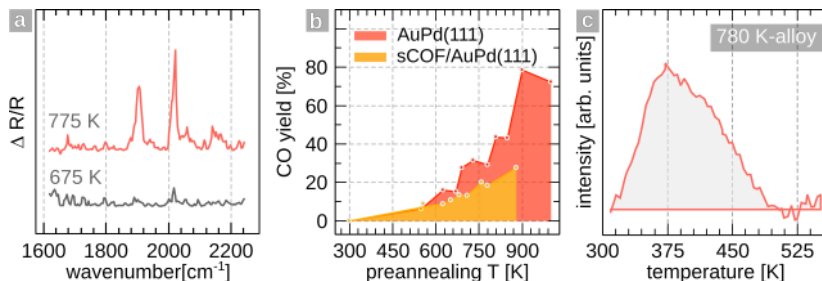


Figure 2.12 ■ Titration of palladium sites in sCOF/AuPd(111). a) RAIR spectra of sCOF/AuPd(111) titrated after heating at 675 K and 775 K. Spectra are the average of 1000 scans at a resolution of 8 cm^{-1} . b) CO yield from AuPd(111) and sCOF/AuPd(111) derived from TPD spectra. c) TPD trace of $m/z = 28$ amu (CO) after heating the sCOF/AuPd(111) to 780 K.

Titration of the sCOF/AuPd(111) revealed marginal yields of CO desorption for the 600–700 K-alloys, which amounted to $\sim 10\%$.[‡] Upon annealing to 760–780 K the CO yield increases to approximately 20 %, which represents only half of that obtained for the clean system (Figure 2.12.b). We speculate that the lower CO yield is due to the blocking of Pd sites by Br, analogous to the weak adsorption detected in RAIRS experiments. This is particularly important because of the high binding energy of Br to palladium as discussed before. However, it was not possible to determine from TPD alone whether the observed increase in the CO yield is a consequence of further Pd-enrichment, Br desorption, or a combination of both factors. CO desorption occurred in a broad trace peaking at $T_{max.} \simeq 380\text{ K}$, which correlates well with bridge palladium sites detected at 1905 cm^{-1} in RAIR spectra (Figure 2.12.c). However, CO desorption from atop palladium sites could not be resolved by contrast to the band detected at 2021 cm^{-1} in RAIRS. A plausible explanation for this discrepancy is site migration of CO from atop to bridge sites prior to desorption in the TPD experiments.¹³⁶

In summary, RAIRS and TPD data provided some evidence of CO adsorption after annealing of the preformed sCOF on the gold-rich AuPd(111) alloy. CO adsorption is presumed to be the result of a change in the composition of the topmost layer, and emergence of palladium sites as first hypothesized for this preparation protocol. Bridge and atop sites were identified, and palladium enrichment of the surface relative to the clean AuPd(111) system was surmised. Admittedly, we cannot conclusively ascertain if CO adsorption occurred in the

[‡]The yield is expressed relative to the integrated signal of a CO-saturated Pd(111) crystal.

pores, or at the exposed areas uncovered by the sCOF. A marked difference in the surface chemistry of TBPB on the alloy compared to the parent metals was evident. This protocol is expected to be transferable to sCOF built from other molecular precursors, providing that they exhibit sufficient thermal stability to withstand the intermixing step. Some examples in the literature have reported thermally robust frameworks constructed from on-surface reactions other than Ullmann coupling.^{28,245} In the next section we examine this possibility.

2.5 sCOF Synthesis from Boronic Acid Precursors on AuPd(111)

Earlier in this chapter, the condensation of boronic acids was introduced as another important reaction used in sCOF synthesis. By comparison to Ullmann coupling, boronic acid condensation only produces water as a byproduct, and the surface remains free of contaminants. Moreover, under thermodynamic equilibrium conditions, highly crystalline frameworks form. Using the alloy preparation described in the previous section, the fabrication of a sCOF from the self-condensation of benzene-1,4-diboronic acid (**BDBA**) on AuPd(111) was investigated (Figure 2.13.a). The gold-rich AuPd(111) was exposed to BDBA ($T_{dose.} = 453\text{--}463\text{ K}$, 1600 L), and the sample examined under STM at 300 K. Under these preparation conditions, the resulting sample was characterised by extensive etching and reshaping of step edges. The etching was found to correlate linearly with the number scans, and the rate accelerated by the scanning bias. At scanning conditions $V_t = -0.4\text{ V}$, $I_t = 300\text{ pA}$, an average etching rate of $r_{-0.4\text{ V}} = 167.4 \pm 13.3\text{ nm}^2\text{scan}^{-1}$ was derived. Decreasing the bias to -0.6 V , while maintaining the tunnelling current at 300 pA, resulted in an almost nine-fold increase of the rate at $r_{-0.6\text{ V}} = 1458.2 \pm 65.0\text{ nm}^2\text{scan}^{-1}$. Notably, the etching rate slowed down markedly as the islands became smaller in size (Figure S2.5). This decline in rate is likely associated with a higher surface free energy of the smaller islands and higher activation energy for atom extraction. The same etching phenomenon also occurred upon deposition of BDBA onto Au(111) (Figure 2.14.b). One unanticipated finding was the formation of nanometer-sized strips at the surface step edges. These strips were exactly one atomic layer in height but lengthened upon cumulative scanning of the same area. Deliberate formation of similar structures, often termed *magic gold fingers*, is well-documented for other types of molecules such as amino acids,^{246,247} thiols,^{248–250} or by electric field-induced tip manipulation.^{251–253} To our knowledge, this effect has not been previously described for boronic acids on either AuPd(111) or Au(111) surfaces. The growth of *gold fingers* on AuPd(111) did not follow the STM fast scan direction, which is parallel to the frame for all images recorded; instead gold fingers grew exclusively along the $\langle 1\bar{1}0 \rangle$ surface direction or its symmetry equivalent. Detachment and isolation of gold

fingers from step edges was possible by continuous tip rastering, and complete erosion of the parent island (Figure 2.13.c, inset). Their length extended over several hundreds of nanometers and seemed to be limited only by the size of the terrace they occupied. However, the minimum width of a stable finger was limited to 3.66 ± 0.24 nm, and repeatedly scanning over the gold fingers promoted their segmentation rather than further narrowing. This minimum stability width value is in excellent agreement with the studies by Yin *et al.*²⁵³ Furthermore, similar to our observations, tip-induced growth of gold fingers on Au(111) has been reported to take place preferentially along the $\langle 1\bar{1}0 \rangle$ surface direction.^{250,251,254} The mechanism involves a combination of atom extraction from the step edge connecting two neighbouring fingers and atom attachment of the fingertips.^{251,255,256} We postulate that the same mechanism is also relevant to the formation of gold fingers on AuPd(111). Although this system shares many similarities with the tip-induced mechanism described by Guo and Yin,^{251,252} it must be noted that first, moderate tunnelling conditions were employed herein. Secondly, this phenomenon was not observed on the clean AuPd(111); and last, nanofingers would still form after annealing at 660 K, compared to the 400 K stability limit in the work by Guo *et al.* Collectively, the experimental evidence strongly supports an active involvement of BDBA in the mass transport of gold atoms and nanofinger formation on AuPd(111). The nature of the species mediating gold transport is unknown. Although BDBA coordination to Au atoms is suspected, arylboronato metal complexes have been rarely reported.^{257–259} However, the possibility of generating geminally diaurated arenes from arylboronic acids has been reported, and it is perhaps a relevant intermediate in the etching phenomenon.^{260,261}

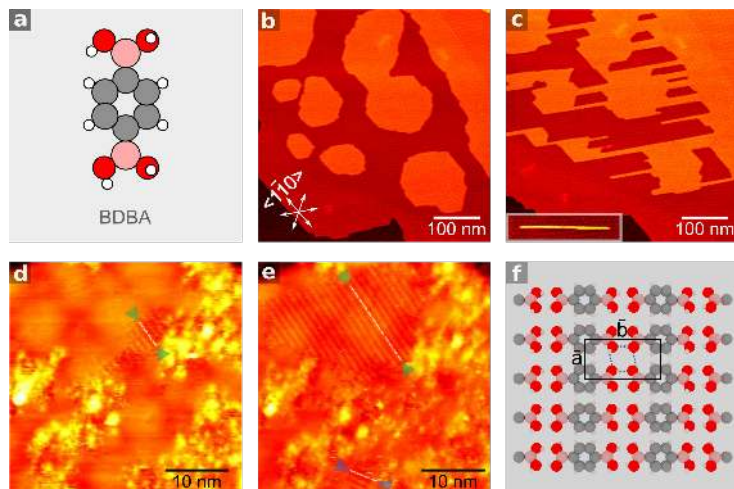


Figure 2.13 ■ BDBA adsorption onto AuPd(111). **a)** Structural model of Benzene-1,4-diboronic acid (BDBA). Boron (pink), Carbon (grey), Hydrogen (white), and Oxygen (red). Sequential STM images of **b)** AuPd(111) exposed to BDBA (1600 L), and **c)** same area after 9 scans (52 min); (inset) isolated gold finger, image size $45.90 \times 21.91 \text{ nm}^2$. Sequential STM image of **d)** as-prepared sample heated at 660 K, and **e)** same area after 6 scans (29 min). Formation of BDBA SAM ($\theta = 0.13 \text{ ML}$) is highlighted in white. Images **b)** and **c)** were acquired at $V_t = -0.4 \text{ V}$, $I_t = 300 \text{ pA}$; images **d)** and **e)** at $V_t = -0.6 \text{ V}$, $I_t = 300 \text{ pA}$. **f)** Model of BDBA SAM on AuPd(111) with unit cell $\vec{a} = 0.52 \text{ nm}$, $\vec{b} = 1.04 \text{ nm}$ and intramolecular H-bonding. Colour coding of atoms as before.

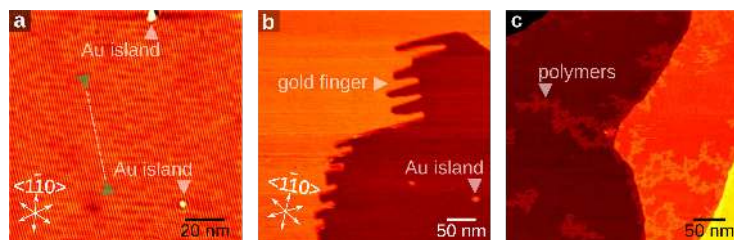


Figure 2.14 ■ BDBA adsorption onto Au(111) **a)** BDBA self-assembled layer on Au(111), 415 L. Direction of BDBA row propagation (green) aligns $16.0 \pm 1.0^\circ$ off the $\langle 1\bar{1}0 \rangle$ surface direction. Etched gold islands are also visible (white). **b)** Gold nanofinger on Au(111) in the presence of BDBA. **c)** Heating the BDBA monolayer to 445 K results mostly in desorption and polymerisation localised at step edges. All images were acquired at $V_t = -0.6 \text{ V}$, $I_t = 300 \text{ pA}$.

Due to the constant surface etching, molecular resolution was not achieved under these experimental conditions. However, heating the sample to 660 K produced marked changes in the topography. Firstly, a periodic row superstructure was visible, whose formation could be monitored *in situ*. Unlike on Au(111), the rows propagated both along the $\langle 1\bar{1}0 \rangle$ (green) and $\langle 11\bar{2} \rangle$ (blue) surface directions (Figure 2.13.d,e). The structure can be described by

the unit cell vectors $\bar{a} = 0.52 \text{ nm}$ and $\bar{b} = 1.04 \text{ nm}$, with an included angle of $\angle(\bar{a}, \bar{b}) = 86.2^\circ$. The structure contains one feature per unit cell ($\theta = 0.13 \text{ ML}$ with respect to gold sites in an unreconstructed Au(111) layer). These dimensions are identical to the unit cell of hydrogen-bonded BDBA on Au(111),⁸⁴ on KCl(001),²⁶² and similar to the lamellar crystal structure adopted by bulk BDBA (Figure 2.14.a).²⁶³ Hence, the superstructure is unambiguously assigned to self-assembled BDBA molecules on the AuPd(111) surface (Figure 2.13.f). The propagation directions of BDBA rows on AuPd(111) differed from those on Au(111), which is probably related to the lattice difference of these substrates. Despite this subtle difference, BDBA-substrate interactions must be insignificant, since it does not prevent nor perturb the formation of the well-known hydrogen-bonded superstructure. This is certainly true for BDBA adsorption on Ag(111). Migration energy barriers have been predicted to be lower than 0.1 eV, resulting in a non-preferential adsorption of BDBA on this surface.

Branched features extending several tens of nanometers were simultaneously imaged along with the hydrogen-bonded superstructure (Figure 2.15.a). Features with dimensions entirely consistent with boroxine entities were resolved within the branched construction. Therefore, the nature of these species is unequivocally assigned to polymers produced from the cyclo-condensation of BDBA (Figure 2.15.b). Despite using deposition conditions which should afford saturation coverage, the polymer covered less than 20 % of the total surface area. This was also the case on Au(111), where heating a BDBA monolayer resulted mostly in monomer desorption, with limited polymerisation localised mainly at step edges (Figure 2.14.c). Evidence of partially condensed monomers and unreacted molecules was also found (Figure 2.15.b). Notably, the etching phenomenon described before would still take place, although it subsided considerably. The drop in etching rate is probably a consequence of the decrease in BDBA coverage after heating. The quality of the sCOF was very poor, and exhibited a predominantly branched morphology. Only rarely were well-defined, closed, hexagonal pores imaged ($\varnothing = 1.5 \text{ nm}$), to such an extent that a quantitative description of the sCOF by a pore distribution and MST analysis with a suitable sample size was impractical. Post-annealing of the preformed polymers did not aid self-healing of the defective network. Taking into consideration the similar surface chemistry of BDBA on Au(111), the limited degree of polymerisation, and low crystallinity of the sCOF on

the gold-rich AuPd(111), was somewhat expected. Ourdjini *et al.*⁸⁴ carried out detailed quantitative MST analysis of sCOF formation on Cu, Ag, and Au substrates. Their results conclusively established that the reaction on Au(111) produced very defective sCOFs. By contrast, silver offers the best compromise between adsorption and surface mobility and produces higher quality sCOFs.²⁴ Furthermore, Sassi *et al.*⁸¹ modelled BDBA and showed that, formation of the boroxine ring is an activated process involving several transition states with energy barriers of about 1 eV.[‡] Self-assembly of BDBA into the hydrogen-bonded superstructure is a non-activated exothermic process favoured over polymerisation. Although polymerisation can be promoted thermally, BDBA desorption becomes also a competing side process. Overall, these factors account for the low polymerisation yields obtained on the weakly interacting Au(111) surface, and would similarly explain the low yields obtained on the gold-rich AuPd(111). Furthermore, the etching phenomenon, which persists even at high temperatures on the AuPd(111) alloy, may well become a competing process that factors in the reduced crystallinity and limited polymerisation.

In this respect, the gold-rich AuPd(111) offered no significant improvement over using clean Pd(111) or a palladium enriched AuPd(111) alloy as evident from control experiments on these surfaces. A high density of molecular features was visible after dosing BDBA (1600 L) onto Pd(111) held at 300 K. Y-shaped features consistent with cyclo-condensation of BDBA to boroxine entities were identified by STM, as well as unreacted BDBA monomers. Branched, covalently linked oligomers resulting from further condensation, and short-range porous nanostructures were occasionally imaged. (Figure 2.15.c). It must be stressed that it is unclear whether these species formed spontaneously upon adsorption onto the Pd(111) substrate, or were preformed *en route* to adsorption. In-crucible self-condensation of boronic acids is favoured over sublimation,²⁶⁴ to such an extent that we noticed a dramatic decrease in flux after 2–3 depositions. Reloading of the doser with fresh BDBA powder was necessary in order to sustain high fluxes.

A similar scenario was found for BDBA deposited onto a palladium rich AuPd(111) alloy surface. The AuPd(111) was prepared as described before, followed by annealing at 775 K for $t = 10$ min to induce palladium enrichment

[‡]Energy barriers calculated for the reaction in vacuum.

of the topmost surface layer. Sublimation of BDBA (3500 L) onto the palladium-enriched AuPd(111) alloy held at 300 K resulted in the same etching behaviour described for Au(111) and gold-rich AuPd(111). This phenomenon was absent for Pd(111), which hints at a specific affinity of BDBA for gold (Figure S2.7). Molecular features related to cyclo-condensation of BDBA appeared after heating the sample at 485 K (Figure 2.15.d). The higher density of molecular species on Pd(111) and palladium-rich AuPd(111) alloy reflects the higher binding of BDBA and the oligomers to these surfaces. No significant changes in the molecular arrangement were detected following thermal treatment on either Pd(111) or AuPd(111). The surfaces remained covered by a highly dense layer of trimers, short oligomers, and unreacted monomers, but extended domains of porous sCOF were absent. More dramatic changes in the topography occurred after heating the samples at 590 K. At this temperature individual molecular features were no longer discernible, likely due to dehydrogenative decomposition of the organic layer.

CO titration of the samples was carried out to establish whether palladium enrichment took place following thermal treatment of the samples. RAIR spectra of the sCOF/AuPd(111) were collected under UHV, after exposing the sample to 990 L of CO at 300 K (Figure 2.15.e). Under these conditions, a weak absorption emerged at 2068 cm^{-1} that resembled CO adsorption on atop palladium sites (Figure 2.15.e, pink curve). In order to verify whether this absorption was in fact due to CO adsorption, and not just a spurious feature from background subtraction, the experiment was repeated. This time, a background CO pressure of $P_{\text{CO}} = 9.7 \times 10^{-7}$ mbar was maintained during the acquisition of RAIR spectra. A very strong absorption was visible at 2084 cm^{-1} , along with weaker ones located at 2022 and 1909 cm^{-1} (Figure 2.15.e, orange curve). The peaks at 2084 and 2022 cm^{-1} are both assigned to CO adsorption on atop palladium sites, whereas the peak at 1909 cm^{-1} suggests the presence of bridge palladium sites in much lower concentration relative to atop sites.^{135,136,160,166,199,222–225} Overall, the RAIR data confirmed the presence of palladium sites at the sCOF/AuPd(111) interface. This finding is postulated to arise from the thermal treatment following the described preparation protocol.

Titration of the palladium-rich AuPd(111) alloy exposed to BDBA is also presented for comparison (Figure 2.15.e, blue curve). A strong peak at 2079

cm^{-1} accompanied by a weaker absorption at 1900 cm^{-1} were detected, and are assigned to CO adsorption on atop and bridge palladium sites, respectively. The presence of palladium sites is also in agreement with the high density of molecular species imaged under STM on this surface.

The thermal stability of the sCOF on the AuPd(111) alloy surface was examined in a similar manner described for the sCOF synthesised from Ullmann coupling. The sample was heated to progressively higher temperatures, and the sample examined under STM at 300 K. The polymers remained largely unchanged up to 705 K, at which temperature its morphology exhibited noticeable changes attributed to polymer degradation (Figure 2.15.f). Ourdjini *et al.*⁸⁴ reported similar decomposition temperatures for the sCOF on Au(111). Notably, the AuPd(111) substrate also exhibited clear signs of modification. First, the Moiré maxima showed an almost two-fold increase in the periodicity ($16.30 \pm 1.77\text{ nm}$), and the hexagonal pattern was noticeably distorted. This is a clear indication of intermixing and the emergence of active palladium ensembles, likely a contributing factor in polymer degradation. Moreover, depression features approximately $\varnothing = 0.72\text{ nm}$ in diameter surrounded by a brighter ring dominated the surface topography, and remained visible above 800 K. Features of similar characteristics have been reported for oxygen adsorption on nickel, copper, and silver surfaces.^{265–268} Oxygen atoms often appear as minima because charge transfer effects deplete the local density of states at the adsorption site.²⁶⁹ The brighter ring around the depressions has been associated with Friedel’s oscillations caused by electronic screening of adsorbed foreign atoms.^{268,270} We suspect that the depression features observed on the AuPd(111) alloy correspond to O/Pd(111) or palladium oxide, with B_3O_3 as the source of oxygen from polymer decomposition.

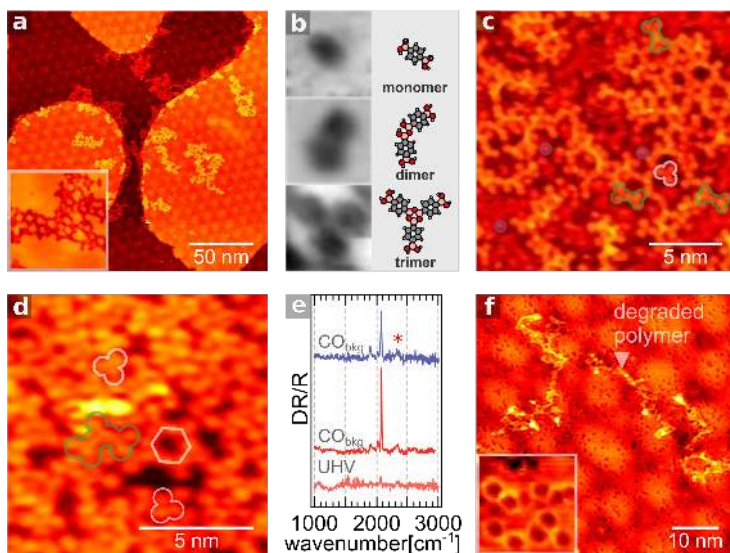


Figure 2.15 ■ BDBA self-condensation on Pd(111) and AuPd(111) alloys. **a)** STM image of polymers formed from BDBA self-condensation on AuPd(111) after heating the sample at 660 K; (inset) close-up highlights pores in the polymer, image size $16.08 \times 16.08 \text{ nm}^2$. **b)** Features imaged under STM assigned to the BDBA monomer, condensed dimer, and trimer. Colour coding of atoms in accompanying models as before. All the images in the panel are $1.78 \times 1.78 \text{ nm}^2$ in size, $V_t = -0.4 \text{ V}$, $I_t = 400 \text{ pA}$. **c)** BDBA deposited onto Pd(111) at 300 K, (1600 L). BDBA monomers (blue) and trimerised BDBA molecules are highlighted (white), as well as further two condensed trimers (green) within an oligomer (green), $V_t = -0.3 \text{ V}$, $I_t = 300 \text{ pA}$. **d)** BDBA adsorption on palladium-rich AuPd(111) alloy, 3500 L at 300 K. Trimerised BDBA molecules are highlighted (white), as well as oligomers produced from further condensation of trimers (green). Well-defined pores (white dashed line) were occasionally identified, $V_t = -0.3 \text{ V}$, $I_t = 100 \text{ pA}$. **e)** CO titration of palladium sites at sCOF/AuPd(111) examined under RAIRS at constant background CO pressure (CO_{bkg}) of $P_{\text{CO}} = 9.7 \times 10^{-7} \text{ mbar}$ (orange), and under UHV (pink). Also shown is the titration of BDBA deposited onto the palladium-rich AuPd(111) alloy (blue) at a constant background CO pressure of $P_{\text{CO}} = 7.0 \times 10^{-7} \text{ mbar}$. The asterisk marks absorption peak due to background CO_2 in the optical path. Spectra are the average of 1000 scans at a resolution of 8 cm^{-1} . **f)** Degradation of polymers followed heating to 705 K, (inset) close-up of depression features and surrounding bright ring, image size $5.1 \times 5.1 \text{ nm}$, $V_t = -0.3 \text{ V}$, $I_t = 300 \text{ pA}$.

Schlögl *et al.*²⁶⁴ developed a sequential condensation-coupling polymerisation strategy that permitted sCOF synthesis using a single molecular precursor. Soon after, Faury *et al.*²⁷¹ showed using 4-bromophenylboronic acid precursors (BPBA), that such a protocol improves considerably the crystallinity and yield of the resulting sCOF compared to boronic acid self-condensation alone. The reaction is thermally activated, and the proposed mechanism appears to involve two stages (Figure 2.16.a). First, three monomers, each bearing one boronic acid moiety, condense to form the boroxine ring unit. Then, the preformed boroxine trimer, which also bears at least one C–Br functionality at each apex of the trimer, undergoes homolytic cleavage to produce a surface-stabilised

radical. The activated precursors combine in the normal C–C coupling fashion of Ullmann coupling to generate a sCOF. With the intention of improving the quality of the boroxine-based sCOF on the AuPd(111) surface, the combined condensation/coupling strategy was also investigated.

Firstly, deposition of BPBA (290 L, $T_{dose} = 445$ K) onto a Au(111) substrate held at 525 K was performed as a control experiment. Under these experimental conditions, a porous sCOF formed, which extended over the entire surface (Figure 2.16.b). The sCOF was comprised mostly of 55 % pentagonal ($A_{\square} = 1.76 \pm 0.28 \text{ nm}^2$) and 36 % hexagonal ($A_{\square} = 2.82 \pm 0.38 \text{ nm}^2$) pores. Square (7 %), heptagonal or bigger pores (2 %) accounted for the remainder. MST analysis of the framework yielded a mean spanning length of $m_{Au} = 0.88$ with a standard deviation of $s_{Au} = 0.11$, in excellent agreement with the study by Faury *et al.*²⁷¹ Due to the large number of pentagonal pores, m and s deviate from the predicted line for a hexagonal tiling and lie in the vicinity of the square tiling instead (Figure S2.6). Nonetheless, these values point to a degree of order approaching that of boronic acid self-condensation on silver surfaces, the best substrate known for high-quality sCOF synthesis based on this reaction.

Next, BPBA deposition (260 L) was carried out on the gold-rich AuPd(111) alloy held at 485 K. Polymeric structures were resolved following this preparation. However, in a similar manner observed for the related BDBA molecule on AuPd(111), the gold islands underwent restructuring on consecutive scans (Figure S2.7). Acquisition of high-resolution images of the polymer was possible after heating the sample to 660 K, at which temperature the etching process was significantly reduced. The sCOF covered approximately 70 % of the surface, and exhibited some well-defined pores (Figure 2.16.c). Nonetheless, a branched morphology was still predominant. As stated previously, we suspect that the etching phenomenon is associated with the poor quality of the produced sCOF, which seems to be more pronounced on the AuPd(111) compared to pure Au(111). The sCOF remained thermally stable up to 705 K, with signs of degradation appearing upon heating at 785 K. Characterisation of the sCOF/AuPd(111) by CO titration experiments revealed weak absorptions at 1897 cm^{-1} and 2021 cm^{-1} in RAIR spectra due to bridge and atop palladium sites, respectively (Figure 2.16.d). The weak intensity of these peaks indicates limited CO adsorption, likely due to a blocking effect by residual Br atoms

generated during polymerisation. This is similar to the case reported for the sCOF synthesised from TBPB precursors in an earlier section.

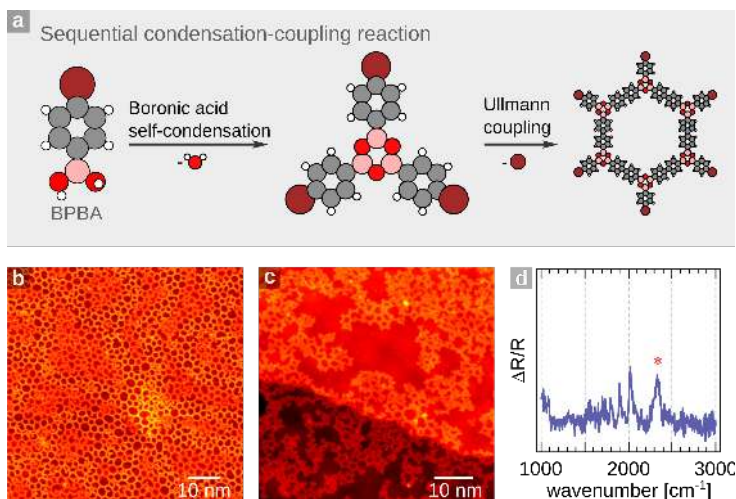


Figure 2.16 ■ sCOF synthesis from sequential condensation-coupling reaction of BPBA. **a)** Reaction scheme leading to polymerisation of BPBA. The first step involves the condensation of the boronic acid termini on BPBA into the boroxine ring unit. In a second step, the preformed trimer undergoes Ullmann C–C coupling with a second and subsequent activated precursors to form polymers. The ideal framework is comprised of hexagonal pores with a wall-to-wall length of $l = 2.3$ nm. STM images of sCOF fabricated using the condensation-coupling reaction of BPBA on **b)** Au(111) and **c)** AuPd(111). Image **b)** was acquired at $V_t = -0.6$ V, $I_t = 300$ pA and **c)** at $V_t = -0.6$ V, $I_t = 200$ pA. **d)** RAIR spectra of sCOF/AuPd(111) acquired after heating the sample to 785 K and exposed to 2400 L of CO. Spectrum is an average of 1000 scans at a resolution of 4 cm^{-1} . Asterisk marks absorption peak due to background CO_2 in the optical path.

In summary, the protocol devised in the previous section was implemented for the self-condensation reaction of BDBA, and for the sequential condensation-coupling reaction of BPBA. Unexpectedly, etching of the AuPd(111) surface was a recurrent phenomenon observed at 300 K, which persisted even after heating at 660 K. The etching process led to the formation of nanostructures similar in appearance to *magic gold fingers* documented in the literature. The STM data provided definite evidence of an active involvement of the boronic acid moiety in the etching phenomenon for both molecules. Self-assembly of BDBA into its well-known hydrogen-bonded structure was also recognised on the AuPd(111) surface. Despite propagating along a different surface direction on the alloy from that seen on Au(111), the molecular packing of BDBA was not affected. The self-condensation of BDBA generated a poor quality sCOF and in low yield, which was anticipated from previous reports addressing

the on-surface reaction on Au(111). However, the combined STM and CO titration experiments conclusively proved that palladium enrichment of the sCOF-coated alloy surface took place. With the purpose of improving the quality of the boroxine-based sCOF, the sequential condensation-coupling reaction of BPBA was briefly explored. Both crystallinity and yield improved massively when the synthesis was carried out on Au(111). On the other hand, the crystallinity was still compromised on the alloy surface. Besides, the residual Br atoms generated during polymerisation significantly limited CO adsorption on the palladium-rich alloy. Therefore, the sequential reaction strategy did not provide a tangible improvement over using Ullmann coupling alone on the AuPd(111) system.

2.6 Summary and Outlook

In this chapter, the topic of enantioselective catalysis and its pivotal role in many areas including drug synthesis was introduced. The current understanding of enantiodifferentiation at the interface of heterogeneous catalysts was briefly reviewed. More importantly, critical challenges preventing the use of supported chiral catalysts technology at an industrial level were identified. In particular, the poor stability and problematic dispersion of chiral agents deposited as single molecules motivated the work presented in this chapter. With the ultimate goal of functionalising catalytic surfaces at the nanoscale, we envisaged sCOFs as potential templating scaffolds to robustly tether chiral modifiers, while simultaneously alleviating the dispersion issue. The principal target of this project was laid out: to create a robust porous architecture over a catalytically active surface under UHV conditions. The pores must bear a chiral centre, or permit postmodification to introduce chirality so that the surface is imparted with enantioselectivity. Overall, the pores in the framework should be regarded as chiral nanoreactors. A list of recently developed on-surface reactions that afford covalent bonding was reviewed, with particular emphasis on the two most popular reactions in sCOF synthesis: on-surface Ullmann coupling and boronic acid condensation. Initial investigations on the adsorption of melamine and TPA as monomers for an imine-based sCOF on palladium

exemplified the first challenges of a direct on-surface synthesis on reactive surfaces. Decomposition, unsuitable binding geometry, and high diffusion barriers preclude the use of such surfaces for high-quality sCOF synthesis. A protocol based on thin-film AuPd alloys was devised that allowed sufficient surface mobility for activated TBPB monomers to polymerise on a gold-rich AuPd(111) alloy. Titration experiments demonstrated the emergence of palladium sites after thermal treatment of the preformed sCOF on the gold-rich AuPd(111) surface. This protocol was transferable to the self-condensation of BDBA which, unlike Ullmann coupling, does not pollute the surface with byproducts. However, the crystallinity and yield of the boroxine-based sCOF was seriously compromised. The unexpected etching of the AuPd(111) surface was observed for BDBA and the related molecule BPBA, presumably due to the boronic acid functionality forming a transient complex with extracted gold atoms. Interestingly, the very same etching phenomenon produced *magic gold fingers* under mild tunnelling conditions. Whenever possible, pore distribution and MST analysis were employed in the characterisation of sCOF morphology. The effect of a sequential condensation-coupling strategy on the crystallinity and yield of the sCOF was briefly investigated.

Overall, a proof of concept for the fabrication of sCOFs on catalytically relevant alloy surfaces was presented. We anticipate that this fabrication protocol could be transferable to other on-surface reactions. The findings presented in this chapter should make a significant contribution to the current knowledge of on-surface synthesis, with some implications for the advancement of rational design of enantioselective heterogeneous catalysis. Future investigation could involve elemental characterisation of the sCOF/AuPd(111) alloy, which was not covered in this work. Mainly, the project would have benefited from a composition characterisation of the sCOF-covered alloy at each preparation stage. Furthermore, though achieving a highly crystalline sCOF was not the principal priority in this project; we acknowledge that this aspect will be crucial to creating well-defined chiral active sites, and will require further development. Unfortunately, synthesis under UHV meets with many inherent constraints and practical limitations. Improved methods relying on dynamic covalent chemistry and error-correction in ambient chemistry should be adopted, as already demonstrated by others.^{22,82,83} We are confident that the work under UHV conditions presented herein will motivate further work involving surface

modification of more realistic catalytic systems. Mainly, core-shell Pd@Au nanoparticles modified by chiral sCOFs in ambient conditions seems the next natural step to expand this investigation. The possibility of introducing chiral centres into the pores of the sCOF remained unanswered in this project. However, we foresee that this challenge will be overcome using chiral monomers in sCOF synthesis, or more likely, via the post-functionalisation of preformed achiral sCOFs bearing suitable reactive groups.²⁷² Notably, successful examples of bulk chiral COF have recently been reported.^{17,19,273–276} Maturing of the field of 2D synthesis will eventually lead to the realisation of such a vision. All in all, we trust that future work will move towards sCOF synthesis over supported nanoparticles under ambient conditions.

2.7 References

- [1] L. A. Nguyen, H. He, C. Pham-Huy, *Int. J. Biomed. Sci* **2006**, 2, 85–100.
- [2] H. Blaser, F. Spindler, M. Studer, *Appl. Catal. A* **2001**, 221, 119–143.
- [3] Y. Orito, N. Shuichi *et al.*, *J. Synth. Org. Chem Jpn.* **1979**, 37, 173–174.
- [4] Y. Izumi, *Adv. Catal.* **1983**, 32, 215–271.
- [5] T. Mallat, E. Orglmeister, A. Baiker, *Chem. Rev.* **2007**, 107, 4863–4890.
- [6] T. Jones, C. J. Baddeley, *Surf. Sci.* **2002**, 519, 237–249.
- [7] M. O. Lorenzo, C. J. Baddeley, C. Muryn, R. Raval, *Nature* **2000**, 404, 376–379.
- [8] C. J. Baddeley, *Top. Catal.* **2003**, 25, 17–28.
- [9] G. Kyriakou, S. K. Beaumont, R. M. Lambert, *Langmuir* **2011**, 27, 9687–9695.
- [10] H.-U. Blaser, *Tetrahedron: Asymmetry* **1991**, 2, 843–866.
- [11] D. J. Watson, R. B. R. John Jesudason, S. K. Beaumont, G. Kyriakou, J. W. Burton, R. M. Lambert, *J. Am. Chem. Soc.* **2009**, 131, 14584–14589.
- [12] D. Bonifazi, S. Mohnani, A. Llanes-Pallas, *Chem.–Eur. J.* **2009**, 15, 7004–7025.
- [13] A. P. Côté, A. I. Benin, N. W. Ockwig, M. O’Keeffe, A. J. Matzger, O. M. Yaghi, *Science* **2005**, 310, 1166–1170.
- [14] X. Feng, X. Ding, D. Jiang, *Chem. Soc. Rev.* **2012**, 41, 6010–6022.
- [15] S.-Y. Ding, W. Wang, *Chem. Soc. Rev.* **2013**, 42, 548–568.
- [16] D. F. Perepichka, F. Rosei, *Science* **2009**, 323, 216–217.
- [17] H. Xu, J. Gao, D. Jiang, *Nat. Chem.* **2015**, 7, 905–912.
- [18] H.-L. Qian, C.-X. Yang, X.-P. Yan, *Nat. Commun.* **2016**, 7, 12104.

- [19] X. Wang, X. Han, J. Zhang, X. Wu, Y. Liu, Y. Cui, *J. Am. Chem. Soc.* **2016**, *138*, 12332–12335.
- [20] T. Kudernac, S. Lei, J. A. Elemans, S. De Feyter, *Chem. Soc. Rev.* **2009**, *38*, 402–421.
- [21] A. G. Slater, L. M. Perdigao, P. H. Beton, N. R. Champness, *Acc. Chem. Res.* **2014**, *47*, 3417–3427.
- [22] L. Xu, X. Zhou, Y. Yu, W. Q. Tian, J. Ma, S. Lei, *ACS Nano* **2013**, *7*, 8066–8073.
- [23] J. V. Barth, *Surf. Sci.* **2009**, *603*, 1533–1541.
- [24] N. A. Zwaneveld, R. Pawlak, M. Abel, D. Catalin, D. Gigmes, D. Bertin, L. Porte, *J. Am. Chem. Soc.* **2008**, *130*, 6678–6679.
- [25] C. H. Schmitz, J. Ikononov, M. Sokolowski, *J. Phys. Chem. C* **2009**, *113*, 11984–11987.
- [26] S. Jensen, J. Greenwood, H. Früchtl, C. J. Baddeley, *J. Phys. Chem. C* **2011**, *115*, 8630–8636.
- [27] M. Treier, R. Fasel, N. R. Champness, S. Argent, N. V. Richardson, *Phys. Chem. Chem. Phys.* **2009**, *11*, 1209–1214.
- [28] A. C. Marele, R. Mas-Balleste, L. Terracciano, J. Rodríguez-Fernández, I. Berlanga, S. S. Alexandre, R. Otero, J. M. Gallego, F. Zamora, J. M. Gómez-Rodríguez, *Chem. Commun.* **2012**, *48*, 6779–6781.
- [29] S. Weigelt, C. Busse, C. Bombis, M. M. Knudsen, K. V. Gothelf, T. Strunskus, C. Wöll, M. Dahlbom, B. Hammer, E. Lægsgaard *et al.*, *Angew. Chem.* **2007**, *119*, 9387–9390.
- [30] S. Jensen, H. Früchtl, C. J. Baddeley, *J. Am. Chem. Soc.* **2009**, *131*, 16706–16713.
- [31] J. Greenwood, H. A. Früchtl, C. J. Baddeley, *J. Phys. Chem. C* **2013**, *117*, 4515–4520.
- [32] O. D. Arado, H. Mönig, J.-H. Franke, A. Timmer, P. A. Held, A. Studer, H. Fuchs, *Chem. Commun.* **2015**, *51*, 4887–4890.

- [33] L. E. Dinca, C. Fu, J. M. MacLeod, J. Lipton-Duffin, J. L. Brusso, C. E. Szakacs, D. Ma, D. F. Perepichka, F. Rosei, *ACS Nano* **2013**, *7*, 1652–1657.
- [34] Y.-Q. Zhang, N. Kepčija, M. Kleinschrodt, K. Diller, S. Fischer, A. C. Papa-georgiou, F. Allegretti, J. Björk, S. Klyatskaya, F. Klappenberger *et al.*, *Nat. Commun.* **2012**, *3*, 1286.
- [35] S. Weigelt, J. Schnadt, A. K. Tuxen, F. Masini, C. Bombis, C. Busse, C. Isvoranu, E. Ataman, E. Lægsgaard, F. Besenbacher *et al.*, *J. Am. Chem. Soc.* **2008**, *130*, 5388–5389.
- [36] S. Haq, F. Hanke, M. S. Dyer, M. Persson, P. Iavicoli, D. B. Amabilino, R. Raval, *J. Am. Chem. Soc.* **2011**, *133*, 12031–12039.
- [37] D. Zhong, J.-H. Franke, S. K. Podiyanachari, T. Blömker, H. Zhang, G. Kehr, G. Erker, H. Fuchs, L. Chi, *Science* **2011**, *334*, 213–216.
- [38] S. Haq, F. Hanke, J. Sharp, M. Persson, D. B. Amabilino, R. Raval, *ACS Nano* **2014**, *8*, 8856–8870.
- [39] Q. Sun, C. Zhang, H. Kong, Q. Tan, W. Xu, *Chem. Commun.* **2014**, *50*, 11825–11828.
- [40] Q. Sun, C. Zhang, L. Cai, L. Xie, Q. Tan, W. Xu, *Chem. Commun.* **2015**, *51*, 2836–2839.
- [41] F. Bebensee, C. Bombis, S.-R. Vadapoo, J. R. Cramer, F. Besenbacher, K. V. Gothelf, T. R. Linderoth, *J. Am. Chem. Soc.* **2013**, *135*, 2136–2139.
- [42] O. Díaz Arado, H. Mönig, H. Wagner, J.-H. Franke, G. Langewisch, P. A. Held, A. Studer, H. Fuchs, *ACS Nano* **2013**, *7*, 8509–8515.
- [43] H. Zhou, J. Liu, S. Du, L. Zhang, G. Li, Y. Zhang, B. Z. Tang, H.-J. Gao, *J. Am. Chem. Soc.* **2014**, *136*, 5567–5570.
- [44] J. Liu, P. Ruffieux, X. Feng, K. Müllen, R. Fasel, *Chem. Commun.* **2014**, *50*, 11200–11203.
- [45] B. Yang, J. Björk, H. Lin, X. Zhang, H. Zhang, Y. Li, J. Fan, Q. Li, L. Chi, *J. Am. Chem. Soc.* **2015**, *137*, 4904–4907.
- [46] Q. Sun, C. Zhang, Z. Li, H. Kong, Q. Tan, A. Hu, W. Xu, *J. Am. Chem. Soc.* **2013**, *135*, 8448–8451.

- [47] B. Schuler, S. Fatayer, F. Mohn, N. Moll, N. Pavliček, G. Meyer, D. Peña, L. Gross, *Nat. Chem.* **2016**, *8*, 220–224.
- [48] M. Matena, T. Riehm, M. Stöhr, T. A. Jung, L. H. Gade, *Angew. Chem.* **2008**, *120*, 2448–2451.
- [49] H.-Y. Gao, P. A. Held, M. Knor, C. Mück-Lichtenfeld, J. Neugebauer, A. Studer, H. Fuchs, *J. Am. Chem. Soc.* **2014**, *136*, 9658–9663.
- [50] V. K. Kanuru, G. Kyriakou, S. K. Beaumont, A. C. Papageorgiou, D. J. Watson, R. M. Lambert, *J. Am. Chem. Soc.* **2010**, *132*, 8081–8086.
- [51] C. Sánchez-Sánchez, F. Yubero, A. R. González-Elipé, L. Feria, J. F. Sanz, R. M. Lambert, *J. Phys. Chem. C* **2014**, *118*, 11677–11684.
- [52] C. Sánchez-Sánchez, N. Orozco, J. P. Holgado, S. K. Beaumont, G. Kyriakou, D. J. Watson, A. R. González-Elipé, L. Feria, J. Fernández Sanz, R. M. Lambert, *J. Am. Chem. Soc.* **2015**, *137*, 940–947.
- [53] Q. Sun, L. Cai, Y. Ding, H. Ma, C. Yuan, W. Xu, *Phys. Chem. Chem. Phys.* **2016**, *18*, 2730–2735.
- [54] M. Abel, S. Clair, O. Ourdjini, M. Mossoyan, L. Porte, *J. Am. Chem. Soc.* **2010**, *133*, 1203–1205.
- [55] L. Grill, M. Dyer, L. Lafferentz, M. Persson, M. V. Peters, S. Hecht, *Nat. Nanotechnol.* **2007**, *2*, 687–691.
- [56] Q. Sun, L. Cai, H. Ma, C. Yuan, W. Xu, *Chem. Commun.* **2016**, *52*, 6009–6012.
- [57] Y. Jin, C. Yu, R. J. Denman, W. Zhang, *Chem. Soc. Rev.* **2013**, *42*, 6634–6654.
- [58] M. Xi, B. E. Bent, *Surf. Sci.* **1992**, *278*, 19–32.
- [59] M. Xi, B. E. Bent, *J. Am. Chem. Soc.* **1993**, *115*, 7426–7433.
- [60] S.-W. Hla, L. Bartels, G. Meyer, K.-H. Rieder, *Phys. Rev. Lett.* **2000**, *85*, 2777.
- [61] R. Gutzler, H. Walch, G. Eder, S. Klotz, W. M. Heckl, M. Lackinger, *Chem. Commun.* **2009**, 4456–4458.
- [62] C. Morchutt, J. Björk, S. Krotzky, R. Gutzler, K. Kern, *Chem. Commun.* **2015**, *51*, 2440–2443.

- [63] J. Bjork, F. Hanke, S. Stafstrom, *J. Am. Chem. Soc.* **2013**, *135*, 5768–5775.
- [64] M. Bieri, M. Treier, J. Cai, K. Aït-Mansour, P. Ruffieux, O. Gröning, P. Gröning, M. Kastler, R. Rieger, X. Feng *et al.*, *Chem. Commun.* **2009**, 6919–6921.
- [65] J. Cai, P. Ruffieux, R. Jaafar, M. Bieri, T. Braun, S. Blankenburg, M. Muoth, A. P. Seitsonen, M. Saleh, X. Feng *et al.*, *Nature* **2010**, *466*, 470–473.
- [66] M. O. Blunt, J. C. Russell, N. R. Champness, P. H. Beton, *Chem. Commun.* **2010**, *46*, 7157–7159.
- [67] Q. Fan, C. Wang, Y. Han, J. Zhu, W. Hieringer, J. Kuttner, G. Hilt, J. M. Gottfried, *Angew. Chem. Int. Ed.* **2013**, *52*, 4668–4672.
- [68] D. Sloan, Y.-M. Sun, H. Ihm, J. White, *J. Phys. Chem. B* **1998**, *102*, 6825–6830.
- [69] M. Kittelmann, P. Rahe, M. Nimmrich, C. M. Hauke, A. Gourdon, A. Kuhnle, *ACS Nano* **2011**, *5*, 8420–8425.
- [70] M. Bieri, S. Blankenburg, M. Kivala, C. A. Pignedoli, P. Ruffieux, K. Müllen, R. Fasel, *Chem. Commun.* **2011**, *47*, 10239–10241.
- [71] M. Di Giovannantonio, M. El Garah, J. Lipton-Duffin, V. Meunier, L. Cardenas, Y. Fagot Revurat, A. Cossaro, A. Verdini, D. F. Perepichka, F. Rosei *et al.*, *ACS Nano* **2013**, *7*, 8190–8198.
- [72] J. Eichhorn, T. Strunskus, A. Rastgoo-Lahrood, D. Samanta, M. Schmittel, M. Lackinger, *Chem. Commun.* **2014**, *50*, 7680–7682.
- [73] Q. Fan, T. Wang, L. Liu, J. Zhao, J. Zhu, J. M. Gottfried, *J. Chem. Phys.* **2015**, *142*, 101906.
- [74] A. Saywell, W. Gren, G. Franc, A. Gourdon, X. Bouju, L. Grill, *J. Phys. Chem. C* **2013**, *118*, 1719–1728.
- [75] H. Zhang, H. Lin, K. Sun, L. Chen, Y. Zaganyarski, N. Aghdassi, S. Duhm, Q. Li, D. Zhong, Y. Li *et al.*, *J. Am. Chem. Soc.* **2015**, *137*, 4022–4025.
- [76] H. Zhang, J.-H. Franke, D. Zhong, Y. Li, A. Timmer, O. D. Arado, H. Mönig, H. Wang, L. Chi, Z. Wang *et al.*, *Small* **2014**, *10*, 1361–1368.
- [77] Q. Sun, L. Cai, H. Ma, C. Yuan, W. Xu, *ACS Nano* **2016**, *10*, 7023–7030.

- [78] T. A. Pham, F. Song, M.-T. Nguyen, Z. Li, F. Studener, M. Stöhr, *Chem.–Eur. J.* **2016**, *22*, 5937–5944.
- [79] J. L. Segura, M. J. Mancheño, F. Zamora, *Chem. Soc. Rev.* **2016**, *45*, 5635–5671.
- [80] X.-H. Liu, C.-Z. Guan, S.-Y. Ding, W. Wang, H.-J. Yan, D. Wang, L.-J. Wan, *J. Am. Chem. Soc.* **2013**, *135*, 10470–10474.
- [81] M. Sassi, V. Oison, J.-M. Debierre, S. Humbel, *ChemPhysChem* **2009**, *10*, 2480–2485.
- [82] C.-Z. Guan, D. Wang, L.-J. Wan, *Chem. Commun.* **2012**, *48*, 2943–2945.
- [83] J. F. Dienstmaier, D. D. Medina, M. Dogru, P. Knochel, T. Bein, W. M. Heckl, M. Lackinger, *ACS Nano* **2012**, *6*, 7234–7242.
- [84] O. Ourdjini, R. Pawlak, M. Abel, S. Clair, L. Chen, N. Bergeon, M. Sassi, V. Oison, J.-M. Debierre, R. Coratger *et al.*, *Phys. Rev. B* **2011**, *84*, 125421.
- [85] S. Clair, O. Ourdjini, M. Abel, L. Porte, *Chem. Commun.* **2011**, *47*, 8028–8030.
- [86] F. Silly, A. Q. Shaw, M. R. Castell, G. Briggs, M. Mura, N. Martsinovich, L. Kantorovich, *J. Phys. Chem. C* **2008**, *112*, 11476–11480.
- [87] W. Xu, M. Dong, H. Gersen, E. Rauls, S. Vázquez-Campos, M. Crego-Calama, D. N. Reinhoudt, I. Stensgaard, E. Laegsgaard, T. R. Linderorth *et al.*, *Small* **2007**, *3*, 854–858.
- [88] R. Madueno, M. T. Räisänen, C. Silien, M. Buck, *Nature* **2008**, *454*, 618–621.
- [89] J. A. Theobald, N. S. Oxtoby, M. A. Phillips, N. R. Champness, P. H. Beton, *Nature* **2003**, *424*, 1029–1031.
- [90] J. Greenwood, C. J. Baddeley, *Langmuir* **2013**, *29*, 653–657.
- [91] J. Greenwood, PhD thesis, University of St Andrews, **2013**.
- [92] J. Greenwood, H. A. Früchtel, C. J. Baddeley, *J. Phys. Chem. C* **2013**, *117*, 22874–22879.
- [93] J. Greenwood, H. A. Früchtel, C. J. Baddeley, *J. Phys. Chem. C* **2012**, *116*, 6685–6690.

- [94] S. Pan, Q. Fu, T. Huang, A. Zhao, B. Wang, Y. Luo, J. Yang, J. Hou, *Proc. Natl. Acad. Sci.* **2009**, *106*, 15259–15263.
- [95] Y.-P. Lin, O. Ourdjini, L. Giovanelli, S. Clair, T. Faury, Y. Ksari, J.-M. Themlin, L. Porte, M. Abel, *J. Phys. Chem. C* **2013**, *117*, 9895–9902.
- [96] L. Wang, P. Li, H. Shi, Z. Li, K. Wu, X. Shao, *J. Phys. Chem. C* **2017**, *121*, 7977–7984.
- [97] J. Lipton-Duffin, J. Miwa, M. Kondratenko, F. Cicoira, B. Sumpter, V. Meunier, D. Perepichka, F. Rosei, *Proc. Natl. Acad. Sci.* **2010**, *107*, 11200–11204.
- [98] X. Chen, Y. Hu, J. Gao, Y. Zhang, S. Li, *Appl. Spectrosc.* **2013**, *67*, 491–497.
- [99] J. Peake, MSc thesis, University of St Andrews, **2014**.
- [100] M. Kordesch, W. Stenzel, H. Conrad, *Surf. Sci.* **1987**, *186*, 601–623.
- [101] M. Kordesch, W. Stenzel, H. Conrad, *Surf. Sci.* **1988**, *205*, 100–116.
- [102] L. Costa, G. Camino, *J. Therm. Anal.* **1988**, *34*, 423–429.
- [103] L. G. M. Pettersson, A. Nilsson, *Top. Catal.* **2014**, *57*, 2–13.
- [104] B. Sexton, A. Hughes, N. Avery, *Appl. Surf. Sci.* **1985**, *22*, 404–414.
- [105] B. Sexton, A. Hughes, N. Avery, *Surf. Sci.* **1985**, *155*, 366–386.
- [106] L. J. Richter, W. Ho, *J. Chem. Phys.* **1985**, *83*, 2165–2169.
- [107] A. Anton, J. Parmeter, W. Weinberg, *J. Am. Chem. Soc.* **1986**, *108*, 1823–1833.
- [108] M. Henderson, G. Mitchell, J. White, *Surf. Sci.* **1987**, *188*, 206–218.
- [109] J. Davis, M. Barteau, *J. Am. Chem. Soc.* **1989**, *111*, 1782–1792.
- [110] C. Houtman, M. A. Barteau, *Surf. Sci.* **1991**, *248*, 57–76.
- [111] T. R. Bryden, S. J. Garrett, *J. Phys. Chem. B* **1999**, *103*, 10481–10488.
- [112] R. A. Head, *J. Chem. Soc. Dalton Trans.* **1982**, 1637–1639.
- [113] W. E. Buhro, S. Georgiou, J. M. Fernandez, A. T. Patton, C. E. Strouse, J. Gladysz, *Organometallics* **1986**, *5*, 956–965.

- [114] W. Schröder, K. R. Pörschke, Y.-H. Tsay, C. Krüger, *Angew. Chem. Int. Ed. Engl.* **1987**, *26*, 919–921.
- [115] C. Houtman, M. A. Barteau, *J. Phys. Chem.* **1991**, *95*, 3755–3764.
- [116] A. Vargas, S. Reimann, S. Diezi, T. Mallat, A. Baiker, *J. Mol. Catal. A: Chem.* **2008**, *282*, 1–8.
- [117] J. Davis, M. Barteau, *Surf. Sci.* **1989**, *208*, 383–403.
- [118] F. Delbecq, P. Sautet, *J. Catal.* **2002**, *211*, 398–406.
- [119] J. R. McManus, M. Saliccioli, W. Yu, D. G. Vlachos, J. G. Chen, J. M. Vohs, *J. Phys. Chem. C* **2012**, *116*, 18891–18898.
- [120] D. I. Jerdev, A. Olivas, B. E. Koel, *J. Catal.* **2002**, *205*, 278–288.
- [121] S. H. Pang, J. W. Medlin, *ACS Catal.* **2011**, *1*, 1272–1283.
- [122] E. Stuve, R. Madix, B. Sexton, *Surf. Sci.* **1982**, *119*, 279–290.
- [123] A. Capote, R. Madix, *J. Am. Chem. Soc.* **1989**, *111*, 3570–3577.
- [124] M. J. Webb, S. M. Driver, D. A. King, *J. Phys. Chem. B* **2004**, *108*, 1955–1961.
- [125] J. Davis, M. Barteau, *Surf. Sci.* **1988**, *197*, 123–152.
- [126] J. Davis, M. Barteau, *Surf. Sci.* **1990**, *235*, 235–248.
- [127] R. M. Williams, J. W. Medlin, *Surf. Sci.* **2014**, *619*, 30–38.
- [128] R. Madix, T. Yamada, S. Johnson, *Appl. Surf. Sci.* **1984**, *19*, 43–58.
- [129] A. Anton, J. Parmeter, W. Weinberg, *J. Am. Chem. Soc.* **1985**, *107*, 5558–5560.
- [130] M. Mavrikakis, M. A. Barteau, *J. Mol. Catal. A: Chem.* **1998**, *131*, 135–147.
- [131] R. M. Williams, J. W. Medlin, *Langmuir* **2014**, *30*, 4642–4653.
- [132] J. T. Yates Jr, *J. Vac. Sci. Technol. A* **1995**, *13*, 1359–1367.
- [133] C. E. Tripa, T. S. Zubkov, J. T. Yates Jr, M. Mavrikakis, J. K. Nørskov, *J. Chem. Phys.* **1999**, *111*, 8651–8658.

- [134] L. Zhang, Z. Cheng, Q. Huan, X. He, X. Lin, L. Gao, Z. Deng, N. Jiang, Q. Liu, S. Du *et al.*, *J. Phys. Chem. C* **2011**, *115*, 10791–10796.
- [135] Z. Li, F. Gao, Y. Wang, F. Calaza, L. Burkholder, W. T. Tysoe, *Surf. Sci.* **2007**, *601*, 1898–1908.
- [136] W. K. Kuhn, J. Szanyi, D. W. Goodman, *Surf. Sci.* **1992**, *274*, L611–L618.
- [137] D. Stacchiola, S. Azad, L. Burkholder, W. Tysoe, *J. Phys. Chem. B* **2001**, *105*, 11233–11239.
- [138] T. Sekitani, T. Takaoka, M. Fujisawa, M. Nishijima, *J. Phys. Chem.* **1992**, *96*, 8462–8468.
- [139] R. B. Barros, A. R. Garcia, L. M. Ilharco, *J. Phys. Chem. B* **2001**, *105*, 11186–11193.
- [140] M. B. Griffin, E. L. Jorgensen, J. W. Medlin, *Surf. Sci.* **2010**, *604*, 1558–1564.
- [141] S. H. Pang, A. M. Román, J. W. Medlin, *J. Phys. Chem. C* **2012**, *116*, 13654–13660.
- [142] M. Borasio, O. Rodríguez de la Fuente, G. Rupprechter, H.-J. Freund, *J. Phys. Chem. B* **2005**, *109*, 17791–17794.
- [143] W. J. Mitchell, J. Xie, T. A. Jachimowski, W. H. Weinberg *et al.*, *J. Am. Chem. Soc.* **1995**, *117*, 2606–2617.
- [144] C. M. Truong, M.-C. Wu, D. W. Goodman, *J. Am. Chem. Soc.* **1993**, *115*, 3647–3647.
- [145] Z. Li, Z. Zhang, B. D. Kay, Z. Dohnalek, *J. Phys. Chem. C* **2011**, *115*, 9692–9700.
- [146] M. Bieri, M.-T. Nguyen, O. Gröning, J. Cai, M. Treier, K. Aït-Mansour, P. Ruffieux, C. A. Pignedoli, D. Passerone, M. Kastler *et al.*, *J. Am. Chem. Soc.* **2010**, *132*, 16669–16676.
- [147] V. Ponec, *Appl. Catal. A* **2001**, *222*, 31–45.
- [148] A. Ruban, B. Hammer, P. Stoltze, H. L. Skriver, J. K. Nørskov, *J. Mol. Catal. A: Chem.* **1997**, *115*, 421–429.

- [149] T. Bligaard, J. K. Nørskov, *Electrochim. Acta* **2007**, 52, 5512–5516.
- [150] B. Hammer, J. Nørskov, *Nature* **1995**, 376, 238.
- [151] S. Bhattacharjee, U. V. Waghmare, S.-C. Lee, *Sci. Rep.* **2016**, 6, 35916.
- [152] T. G. Owens, PhD thesis, University of St Andrews, **2007**.
- [153] Y.-F. Han, J.-H. Wang, D. Kumar, Z. Yan, D. Goodman, *J. Catal.* **2005**, 232, 467–475.
- [154] J. Xu, T. White, P. Li, C. He, J. Yu, W. Yuan, Y.-F. Han, *J. Am. Chem. Soc.* **2010**, 132, 10398–10406.
- [155] A. Venezia, V. La Parola, G. Deganello, B. Pawelec, J. Fierro, *J. Catal.* **2003**, 215, 317–325.
- [156] B. E. Solsona, J. K. Edwards, P. Landon, A. F. Carley, A. Herzing, C. J. Kiely, G. J. Hutchings, *Chem. Mater.* **2006**, 18, 2689–2695.
- [157] A. F. Lee, C. J. Baddeley, C. Hardacre, R. M. Ormerod, R. M. Lambert, G. Schmid, H. West, *J. Phys. Chem.* **1995**, 99, 6096–6102.
- [158] Y. Kuk, L. Feldman, P. Silverman, *Phys. Rev. Lett.* **1983**, 50, 511.
- [159] C. J. Baddeley, M. Tikhov, C. Hardacre, J. R. Lomas, R. M. Lambert, *J. Phys. Chem.* **1996**, 100, 2189–2194.
- [160] C.-W. Yi, K. Luo, T. Wei, D. Goodman, *J. Phys. Chem. B* **2005**, 109, 18535–18540.
- [161] T. Wei, J. Wang, D. W. Goodman, *J. Phys. Chem. C* **2007**, 111, 8781–8788.
- [162] Z. Li, O. Furlong, F. Calaza, L. Burkholder, H. C. Poon, D. Saldin, W. T. Tysoe, *Surf. Sci.* **2008**, 602, 1084–1091.
- [163] T. Owens, T. Jones, T. Noakes, P. Bailey, C. J. Baddeley, *J. Phys. Chem. B* **2006**, 110, 21152–21160.
- [164] J. A. Boscoboinik, C. Plaisance, M. Neurock, W. T. Tysoe, *Phys. Rev. B* **2008**, 77, 045422.
- [165] P. Liu, J. K. Nørskov, *Phys. Chem. Chem. Phys.* **2001**, 3, 3814–3818.

- [166] M. Chen, D. Kumar, C.-W. Yi, D. W. Goodman, *Science* **2005**, 310, 291–293.
- [167] H. C. Ham, J. A. Stephens, G. S. Hwang, J. Han, S. W. Nam, T. H. Lim, *Catal. Today* **2011**, 165, 138–144.
- [168] F. Gao, D. W. Goodman, *Chem. Soc. Rev.* **2012**, 41, 8009–8020.
- [169] P. Nascente, S. De Castro, R. Landers, G. Kleiman, *Phys. Rev. B: Condens. Matter* **1991**, 43, 4659.
- [170] A. F. Lee, S. F. Hackett, G. J. Hutchings, S. Lizzit, J. Naughton, K. Wilson, *Catal. Today* **2009**, 145, 251–257.
- [171] J. Zhang, H. Jin, M. B. Sullivan, F. C. H. Lim, P. Wu, *Phys. Chem. Chem. Phys.* **2009**, 11, 1441–1446.
- [172] C. H. Schmitz, J. Ikononov, M. Sokolowski, *Surf. Sci.* **2011**, 605, 1–6.
- [173] S. Jensen, PhD thesis, University of St Andrews, **2010**.
- [174] M. Mura, F. Silly, V. Burlakov, M. R. Castell, G. A. D. Briggs, L. N. Kantorovich, *Phys. Rev. Lett.* **2012**, 108, 176103.
- [175] A. C. Larson, D. T. Cromer, *J. Chem. Phys.* **1974**, 60, 185–192.
- [176] B. Jürgens, E. Irran, J. Senker, P. Kroll, H. Müller, W. Schnick, *J. Am. Chem. Soc.* **2003**, 125, 10288–10300.
- [177] S.-S. Ju, C.-C. Han, C.-J. Wu, A. M. Mebel, Y.-T. Chen, *J. Phys. Chem. B* **1999**, 103, 582–596.
- [178] E. Hughes, *J. Am. Chem. Soc.* **1941**, 63, 1737–1752.
- [179] J. Varghese, A. O’Connell, E. Maslen, *Acta Crystallogr. Sect. C: Cryst. Struct. Commun.* **1977**, 33, 2102–2108.
- [180] F. H. Allen, O. Kennard, D. G. Watson, L. Brammer, A. G. Orpen, R. Taylor, *J. Chem. Soc. Perkin Trans. 2* **1987**, S1–S19.
- [181] R. J. Meier, B. Coussens, *J. Mol. Struct. (Theochem.)* **1990**, 209, 303–312.
- [182] Y. Wang, C. Pittman Jr, S. Saebo, *J. Org. Chem.* **1993**, 58, 3085–3090.
- [183] S. Mukherjee, J. Ren, *J. Am. Soc. Mass Spectrom.* **2010**, 21, 1720–1729.

- [184] N. E. Mircescu, M. Oltean, V. Chiş, N. Leopold, *Vib. Spectrosc.* **2012**, 62, 165–171.
- [185] A. Ruiz-Carretero, J. R. Ramírez, A. Sánchez-Migallón, A. de la Hoz, *Tetrahedron* **2014**, 70, 1733–1739.
- [186] T. Clark, M. Hennemann, J. S. Murray, P. Politzer, *J. Mol. Model.* **2007**, 13, 291–296.
- [187] P. Politzer, P. Lane, M. C. Concha, Y. Ma, J. S. Murray, *J. Mol. Model.* **2007**, 13, 305–311.
- [188] P. Metrangolo, F. Meyer, T. Pilati, G. Resnati, G. Terraneo, *Angew. Chem. Int. Ed.* **2008**, 47, 6114–6127.
- [189] R. Gatti, J. M. MacLeod, J. A. Lipton-Duffin, A. G. Moiseev, D. F. Perepichka, F. Rosei, *J. Phys. Chem. C* **2014**, 118, 25505–25516.
- [190] S. Yasuda, A. Furuya, K. Murakoshi, *RSC Adv.* **2014**, 4, 58567–58572.
- [191] R. Gutzler, O. Ivasenko, C. Fu, J. L. Brusso, F. Rosei, D. F. Perepichka, *Chem. Commun.* **2011**, 47, 9453–9455.
- [192] J. C. Russell, M. O. Blunt, J. M. Garfitt, D. J. Scurr, M. Alexander, N. R. Champness, P. H. Beton, *J. Am. Chem. Soc.* **2011**, 133, 4220–4223.
- [193] D. Lloyd, F. Netzer, *Surf. Sci.* **1983**, 131, 139–147.
- [194] F. Netzer, M. El Gomati, *Surf. Sci.* **1983**, 124, 26–38.
- [195] J. Adisojoso, T. Lin, X. S. Shang, K. J. Shi, A. Gupta, P. N. Liu, N. Lin, *Chem.–Eur. J.* **2014**, 20, 4111–4116.
- [196] H. Roder, E. Hahn, H. Brune, J.-P. Bucher, K. Kern, *Nature* **1993**, 366, 141–143.
- [197] R. Q. Hwang, M. C. Bartelt, *Chem. Rev.* **1997**, 97, 1063–1082.
- [198] M. Ruff, S. Frey, B. Gleich, R. Behm, *Appl. Phys. A: Mater. Sci. Process.* **1998**, 66, S513–S517.
- [199] B. Gleich, M. Ruff, R. Behm, *Surf. Sci.* **1997**, 386, 48–55.

- [200] A. Trant, T. Jones, J. Gustafson, T. Noakes, P. Bailey, C. J. Baddeley, *Surf. Sci.* **2009**, *603*, 571–579.
- [201] M. E. Blecher, E. A. Lewis, A. Pronschinske, C. J. Murphy, M. F. Mattera, M. L. Liriano, E. C. H. Sykes, *Surf. Sci.* **2016**, *646*, 1–4.
- [202] M. Wasniowska, N. Janke-Gilman, W. Wulfhekel, M. Przybylski, J. Kirschner, *Surf. Sci.* **2007**, *601*, 3073–3081.
- [203] E. K. Vestergaard, PhD thesis, University of Aarhus, **2004**.
- [204] C. Dussert, G. Rasigni, M. Rasigni, J. Palmari, A. Llebaria, *Phys. Rev. B: Condens. Matter* **1986**, *34*, 3528.
- [205] J. Beggan, N. Boyle, M. Pryce, A. Cafolla, *Nanotechnology* **2015**, *26*, 365602.
- [206] H. Walch, R. Gutzler, T. Sirtl, G. Eder, M. Lackinger, *J. Phys. Chem. C* **2010**, *114*, 12604–12609.
- [207] M. M. Blake, S. U. Nanayakkara, S. A. Claridge, L. C. Fernández-Torres, E. C. H. Sykes, P. S. Weiss, *J. Phys. Chem. A* **2009**, *113*, 13167–13172.
- [208] N. Tao, S. Lindsay, *J. Phys. Chem.* **1992**, *96*, 5213–5217.
- [209] O. Magnussen, B. Ocko, J. Wang, R. Adzic, *J. Phys. Chem.* **1996**, *100*, 5500–5508.
- [210] B. Ocko, O. Magnussen, J. Wang, R. Adić, T. Wandlowski, *Physica B* **1996**, *221*, 238–244.
- [211] M. L. Foresti, G. Aloisi, M. Innocenti, H. Kobayashi, R. Guidelli, *Surf. Sci.* **1995**, *335*, 241–251.
- [212] J. L. Stickney, S. D. Rosasco, G. N. Salaita, A. T. Hubbard, *Langmuir* **1985**, *1*, 66–71.
- [213] M. Labayen, S. A. Furman, D. A. Harrington, *Surf. Sci.* **2003**, *525*, 149–158.
- [214] C. Bronner, J. Björk, P. Tegeder, *J. Phys. Chem. C* **2014**, *119*, 486–493.
- [215] A. Batra, D. Cvetko, G. Kladnik, O. Adak, C. Cardoso, A. Ferretti, D. Prezzi, E. Molinari, A. Morgante, L. Venkataraman, *Chem. Sci.* **2014**, *5*, 4419–4423.

- [216] K. A. Simonov, N. A. Vinogradov, A. S. Vinogradov, A. V. Generalov, E. M. Zagrebina, N. Mårtensson, A. A. Cafolla, T. Carpy, J. P. Cunniffe, A. B. Preobrajenski, *J. Phys. Chem. C* **2014**, *118*, 12532–12540.
- [217] L. Smykalla, P. Shukrynau, M. Korb, H. Lang, M. Hietschold, *Nanoscale* **2015**, *7*, 4234–4241.
- [218] I. A. Pašti, S. V. Mentus, *Electrochim. Acta* **2010**, *55*, 1995–2003.
- [219] A. F. Lee, P. J. Ellis, I. J. Fairlamb, K. Wilson, *Dalton Trans.* **2010**, *39*, 10473–10482.
- [220] W. Tysoe, R. Lambert, *Surf. Sci.* **1982**, *115*, 37–47.
- [221] W. Tysoe, N. Spencer, R. Lambert, *Surf. Sci.* **1982**, *120*, 413–426.
- [222] A. Bradshaw, F. Hoffmann, *Surf. Sci.* **1978**, *72*, 513–535.
- [223] F. Maroun, F. Ozanam, O. Magnussen, R. Behm, *Science* **2001**, *293*, 1811–1814.
- [224] F. Gao, Y. Wang, D. W. Goodman, *J. Phys. Chem. C* **2009**, *113*, 14993–15000.
- [225] H. Y. Kim, G. Henkelman, *ACS Catal.* **2013**, *3*, 2541–2546.
- [226] J. Bertolini, G. Dalmai-Imelik, J. Rousseau, *Surf. Sci.* **1977**, *68*, 539–546.
- [227] C. J. Baddeley, L. H. Bloxham, S. C. Laroze, R. Raval, T. C. Noakes, P. Bailey, *J. Phys. Chem. B* **2001**, *105*, 2766–2772.
- [228] I.-H. Svenum, J. A. Herron, M. Mavrikakis, H. Venvik, *Catal. Today* **2012**, *193*, 111–119.
- [229] A. R. Haire, J. Gustafson, A. G. Trant, T. E. Jones, T. C. Noakes, P. Bailey, C. J. Baddeley, *Surf. Sci.* **2011**, *605*, 214–219.
- [230] M. Iannuzzi, *J. Phys. Chem. C* **2015**, *119*, 22198–22207.
- [231] L. Jin, Q. Fu, Y. Yang, X. Bao, *Surf. Sci.* **2013**, *617*, 81–86.
- [232] M. Temmen, O. Ochedowski, M. Schleberger, M. Reichling, T. Bollmann, *New J. Phys.* **2014**, *16*, 053039.
- [233] P. Sutter, J. T. Sadowski, E. A. Sutter, *J. Am. Chem. Soc.* **2010**, *132*, 8175–8179.

- [234] A. Dong, Q. Fu, M. Wei, Y. Liu, Y. Ning, F. Yang, H. Bluhm, X. Bao, *Surf. Sci.* **2015**, 634, 37–43.
- [235] L. Jin, Q. Fu, A. Dong, Y. Ning, Z. Wang, H. Bluhm, X. Bao, *J. Phys. Chem. C* **2014**, 118, 12391–12398.
- [236] M. Wei, Q. Fu, Y. Yang, W. Wei, E. Crumlin, H. Bluhm, X. Bao, *J. Phys. Chem. C* **2015**, 119, 13590–13597.
- [237] R. Mu, Q. Fu, L. Jin, L. Yu, G. Fang, D. Tan, X. Bao, *Angew. Chem. Int. Ed.* **2012**, 51, 4856–4859.
- [238] Q. Fu, X. Bao, *Chin. J. Catal.* **2015**, 36, 517–519.
- [239] Y. Yao, Q. Fu, Y. Zhang, X. Weng, H. Li, M. Chen, L. Jin, A. Dong, R. Mu, P. Jiang, *Proc. Natl. Acad. Sci.* **2014**, 111, 17023–17028.
- [240] Y. Zhang, Q. Fu, Y. Cui, R. Mu, L. Jin, X. Bao, *Phys. Chem. Chem. Phys.* **2013**, 15, 19042–19048.
- [241] E. Emmez, B. Yang, S. Shaikhutdinov, H.-J. Freund, *J. Phys. Chem. C* **2014**, 118, 29034–29042.
- [242] H. Cun, M. Iannuzzi, A. Hemmi, S. Roth, J. Osterwalder, T. Greber, *Nano Lett.* **2013**, 13, 2098–2103.
- [243] H. Cun, M. Iannuzzi, A. Hemmi, J. Osterwalder, T. Greber, *ACS Nano* **2014**, 8, 7423–7431.
- [244] T. Brugger, H. Ma, M. Iannuzzi, S. Berner, A. Winkler, J. Hutter, J. Osterwalder, T. Greber, *Angew. Chem. Int. Ed.* **2010**, 49, 6120–6124.
- [245] S. A. Krasnikov, C. M. Doyle, N. N. Sergeeva, A. B. Preobrajenski, N. A. Vinogradov, Y. N. Sergeeva, A. A. Zakharov, M. O. Senge, A. A. Cafolla, *Nano Res.* **2011**, 4, 376–384.
- [246] K. Wilson, H. Früchtel, F. Grillo, C. J. Baddeley, *Chem. Commun.* **2011**, 47, 10365–10367.
- [247] V. Humblot, A. Vallee, A. Naitabdi, F. Tielens, C.-M. Pradier, *J. Am. Chem. Soc.* **2012**, 134, 6579–6583.

- [248] V. Arima, R. I. Blyth, F. Matino, L. Chiodo, F. D. Sala, J. Thompson, T. Regier, R. Del Sole, G. Mele, G. Vasapollo *et al.*, *Small* **2008**, *4*, 497–506.
- [249] F. Chen, A. Zhou, H. Yang, *Appl. Surf. Sci.* **2009**, *255*, 6832–6839.
- [250] J. A. Boscoboinik, R. R. Kohlmeier, J. Chen, W. T. Tysoe, *Langmuir* **2011**, *27*, 9337–9344.
- [251] Q. Guo, F. Yin, R. E. Palmer, *Small* **2005**, *1*, 76–79.
- [252] F. Yin, R. Palmer, Q. Guo, *Surf. Sci.* **2006**, *600*, 1504–1509.
- [253] F. Yin, R. Palmer, Q. Guo, *J. Phys.: Condens. Matter* **2009**, *21*, 445001.
- [254] S. Phark, Z. G. Khim, S. Yoon, *Curr. Appl. Phys.* **2008**, *8*, 822–827.
- [255] Z. Wang, M. Moskovits, *J. Appl. Phys.* **1992**, *71*, 5401–5409.
- [256] N. Totó, R. Ferrando, Q. Guo, R. L. Johnston, *Phys. Rev. B: Condens. Matter* **2007**, *75*, 195434.
- [257] H. Chen, P. P. Power, S. C. Shoner, *Inorg. Chem.* **1991**, *30*, 2884–2888.
- [258] T. Miyamoto, H. Ichida, *Chem. Lett.* **1991**, *20*, 435–436.
- [259] D. Vidovic, J. A. Moore, J. N. Jones, A. H. Cowley, *J. Am. Chem. Soc.* **2005**, *127*, 4566–4567.
- [260] D. V. Partyka, M. Zeller, A. D. Hunter, T. G. Gray, *Angew. Chem. Int. Ed.* **2006**, *118*, 8368–8371.
- [261] J. E. Heckler, M. Zeller, A. D. Hunter, T. G. Gray, *Angew. Chem. Int. Ed.* **2012**, *124*, 6026–6030.
- [262] R. Pawlak, L. Nony, F. Bocquet, V. Oison, M. Sassi, J.-M. Debierre, C. Lop-pacher, L. Porte, *J. Phys. Chem. C* **2010**, *114*, 9290–9295.
- [263] P. Rodriguez-Cuamatzi, G. Vargas-Díaz, T. Maris, J. D. Wuest, H. Hoepfl, *Acta Crystallogr. Sect. E: Struct. Rep. Online* **2004**, *60*, o1316–o1318.
- [264] S. Schlögl, T. Sirtl, J. Eichhorn, W. M. Heckl, M. Lackinger, *Chem. Commun.* **2011**, *47*, 12355–12357.
- [265] F. Besenbacher, J. K. Nørskov, *Prog. Surf. Sci.* **1993**, *44*, 5–66.

- [266] E. Kopatzki, R. Behm, *Surf. Sci.* **1991**, 245, 255–262.
- [267] F. Yang, Y. Choi, P. Liu, J. Hrbek, J. A. Rodriguez, *J. Phys. Chem. C* **2010**, 114, 17042–17050.
- [268] F. Wiame, V. Maurice, P. Marcus, *Surf. Sci.* **2007**, 601, 1193–1204.
- [269] N. Lang, *Phys. Rev. Lett.* **1986**, 56, 1164.
- [270] L. Petersen, P. Laitenberger, E. Lægsgaard, F. Besenbacher, *Phys. Rev. B: Condens. Matter* **1998**, 58, 7361.
- [271] T. Faury, S. Clair, M. Abel, F. Dumur, D. Gigmes, L. Porte, *J. Phys. Chem. C* **2012**, 116, 4819–4823.
- [272] C. Steiner, J. Gebhardt, M. Ammon, Z. Yang, A. Heidenreich, N. Hammer, A. Görling, M. Kivala, S. Maier, *Nat. Commun.* **2017**, 8, 14765.
- [273] H. Xu, X. Chen, J. Gao, J. Lin, M. Addicoat, S. Irle, D. Jiang, *Chem. Commun.* **2014**, 50, 1292–1294.
- [274] H.-S. Xu, S.-Y. Ding, W.-K. An, H. Wu, W. Wang, *J. Am. Chem. Soc* **2016**, 138, 11489–11492.
- [275] X. Han, Q. Xia, J. Huang, Y. Liu, C. Tan, Y. Cui, *J. Am. Chem. Soc.* **2017**, –.
- [276] C.-A. Wang, Y.-W. Li, Y. Han, J. Zhang, R.-T. Wu, G.-F. He, *Polym. Chem.* **2017**, –.

2.8 Appendix A

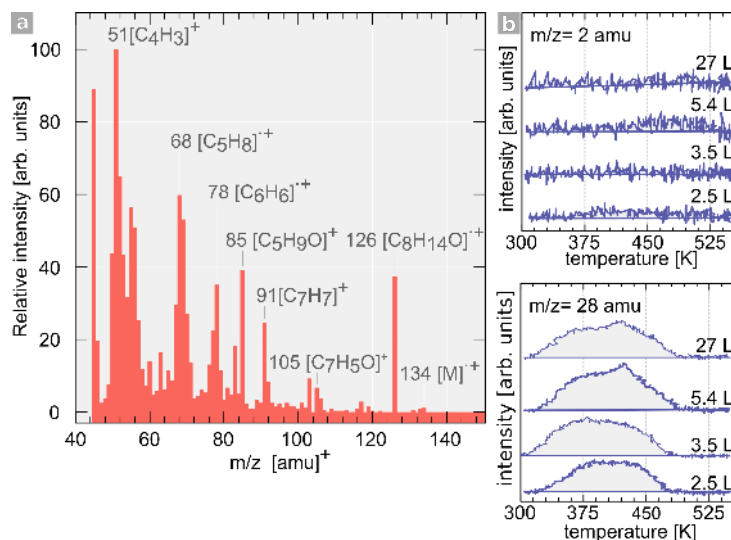


Figure S2.1 ■ TPA adsorption onto Pd(111): revisited. a) Gas phase mass spectra of TPA ($T_{\text{dose}} = 353\text{--}428\text{ K}$). [M] indicates parent ion of TPA. $m/z = 105$ amu is a signature of benzoyl compounds, whereas $m/z = 51$, 78 and 91 amu are characteristic fragmentation ions of benzene. Fragments $m/z = 126$, 85 and 68 amu likely arise from rearrangement and hydrogen transfer, as manifested by the subsequent loss of [C₃H₇]⁺ ($m/z = 43$ amu) in $126 \rightarrow 85$ amu, and [OH]⁺ ($m/z = 17$ amu) in $85 \rightarrow 68$ amu. $E_{\text{ion}} = 69.8\text{ eV}$ b) H₂ and CO traces from TPA decomposition, $\beta = 1.0\text{ K s}^{-1}$.

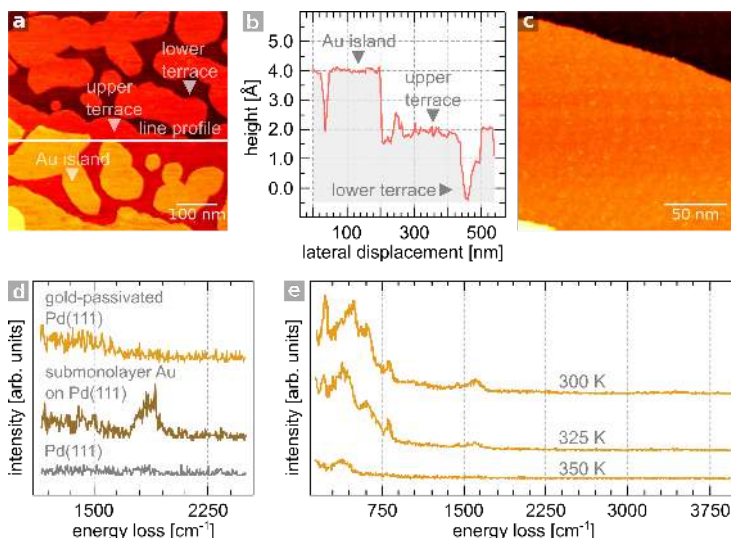


Figure S2.2 ■ Melamine adsorption onto AuPd(111) alloys **a)** STM image shows smoothing of gold islands ($\theta = 0.4$ ML) deposited onto Pd(111) at 300 K and subsequent annealing to 715 K. Terrace termination and gold islands are highlighted. **b)** corresponding line profile of **a)** indicates that the deposited islands are approximately 2 Å in height, consistent with the growth of an atomic-thick overlayer. **c)** STM image of same sample as in **a)** after further annealing to 865 K. Extensive intermixing and gold diffusion occurs at this temperature, with no longer evidence of individual islands. $V_t = -0.1$ V, $I_t = 900$ pA **d)** HREEL spectra of clean Pd(111) surface, submonolayer, and ~ 1 ML coverage of gold onto Pd(111) exposed to CO, 65 L. Passivation of Pd(111) by gold is evident from the titration experiment, as the $\nu(\text{CO})$ mode at 1860 cm^{-1} is lost. **e)** HREEL spectra of melamine adsorbed onto Au(111) as a function of temperature. Spectral features are lost upon heating to 350 K due to desorption of physisorbed melamine. $E_0 = 4.1$ eV, FWHM = 64.4 cm^{-1}

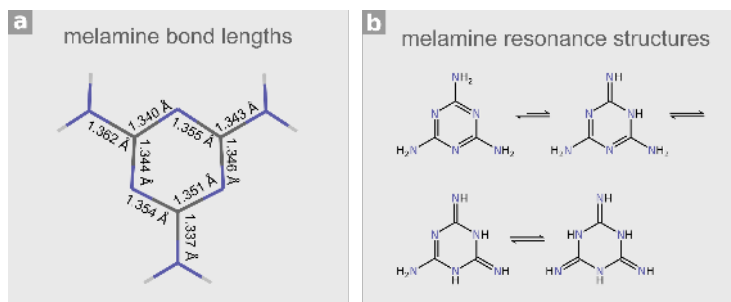


Figure S2.3 ■ Resonance effect in melamine. **a)** C–N bond lengths in melamine. Carbon (grey), Hydrogen (white), Nitrogen (blue). Adapted from reference [179]. **b)** Possible resonance structures of melamine.

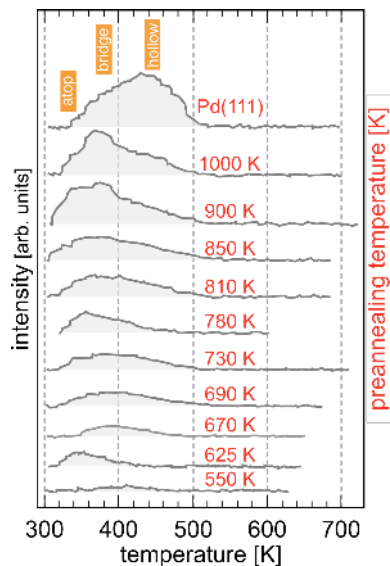


Figure S2.4 ■ Titration of AuPd(111) alloy. TPD traces of fragment $m/z = 28$ amu (CO) at increasing pre-annealing temperature. $P_{\text{CO}} = 1 \times 10^{-6}$ mbar, $\beta = 5.3 \text{ Ks}^{-1}$. T_{max} for desorption of atop, bridge, and hollow sites is marked.

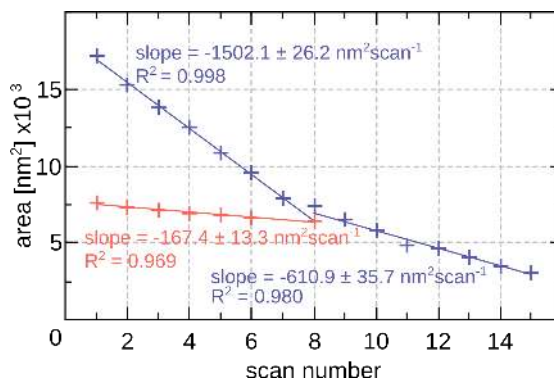


Figure S2.5 ■ Tip-induced etching of AuPd(111) alloy in the presence of BDBA. Area of island versus scan number acquired at biases: -0.6 V (blue) and at -0.4 V (red).

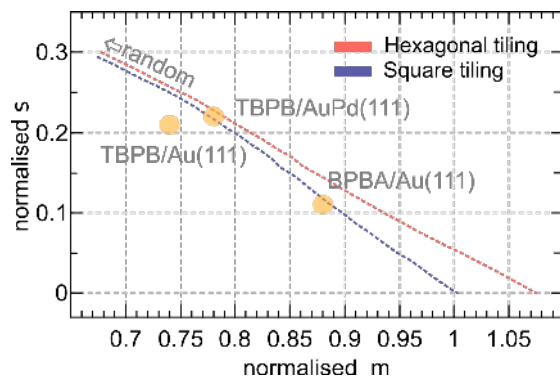


Figure S2.6 ■ Minimal spanning tree (MST). Normalised m and s values for sCOFs synthesised from different molecular precursors. Trend lines for ideal hexagonal (red) and square (blue) tiling are also shown. Adapted from reference [84].

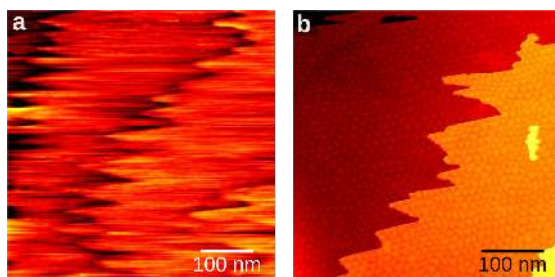


Figure S2.7 ■ Surface etching of AuPd(111) in the presence of boronic acid-bearing molecules. STM image of **a)** BDBA on palladium-enriched AuPd(111) and **b)** BPBA on AuPd(111). Images were acquired at $V_t = -0.6$ V, $I_t = 300$ pA.

Chapter 3

N-Heterocyclic Carbenes: A New Class of Surface Ligand

3.1 Introduction

The ability to rationally design an interface at the molecular level is a crucial aspect of nanotechnology. In this respect, the spontaneous formation of molecular assemblies is a valuable tool to tailor interfacial physicochemical properties of solid surfaces. Self-assembled monolayers (SAMs) generated by the adsorption of molecular units, both from solution or the gas phase, often form crystalline structures on the surfaces of metals, semiconductors, or oxide substrates. The molecular unit comprising a SAM is very often dissected into three structural components (Figure 3.1.a). 1) A functional group with a high affinity for a given substrate termed *ligand* or *headgroup*, anchors the molecule to the substrate via a chemical bond. If the affinity is high enough, the headgroup can displace other adsorbed molecules of lower affinity. 2) A functional group at the interface between the SAM and the medium it is exposed to, referred

to as the *terminal functional group*, determines the surface properties (e.g., hydrophobicity/hydrophilicity, sensing capabilities, or affinity for biomolecules). 3) a variable length backbone, the *linker*, connects the headgroup with the terminal functional group. Predefining the molecular units through synthetic modification of any of these three structural components allows the fabrication of SAMs with highly predictable stability, thickness, crystallinity and functional characteristics. Moreover, post-modification of the terminal functional group, using conventional solution chemistry and electrochemical reactions, adds extra flexibility to the tailoring of these systems.^{1–3} Among the many molecular self-assembly systems known, organosulphur compounds constitute by far the most extensively studied class. Disulphides ($R_1-S-S-R_2$), thiols ($R-S-H$), and thioethers (R_1-S-R_2) are extensively used in SAM fabrication on gold substrates, which exploit the aurophilicity of the S-headgroup atoms. The bonding mechanism involves homolysis of the sulfhydryl terminus ($R-SH$) to generate a thiyl radical ($R-SH^\bullet$), and subsequent covalent binding to a gold atom ($R-S-Au$) (Figure 3.1.b).⁴ The released H^\bullet atom is believed to reductively desorb as molecular hydrogen (H_2) in vacuum and to oxidatively convert to water in the presence of O_2 in solution.⁵ Notably, a long-standing debate about the exact adsorption site and bonding motif of thiols on gold at the atomic scale has been recently settled in light of new microscopic data. It has been conclusively demonstrated that $RS-Au-SR$ complexes form, with the gold adatom bridging across two substrate gold atoms, and S atoms occupying atop sites (Figure 3.1.c).^{6–9} Besides the advantageous flexibility in the functionalization of these compounds, gold as a substrate also offers many advantages. For example, gold requires fairly simple cleaning procedures, is chemically stable towards oxidation, and biocompatible. Additionally, gold possesses convenient physical characteristics for the spectroscopic characterisation of adsorbed films by SPR, RAIRS, and SERS techniques.

Since the first reports on the self-assembly of organic layers on solid surfaces,^{10–12} the structure-function relation governing these systems, and their potential applications has spurred interest in a diverse range of fields including catalysis,¹³ (bio)sensing,^{14–16} and corrosion inhibition.^{17,18} Well-defined binding geometries of the molecular unit is critical for the formation of densely packed and uniform SAMs for most applications. In solution, alkanethiols generally achieve an *upright* binding mode via a two-step process. At low

coverage, a phase of *flat-lying* species, commonly referred to as the *striped phase*, dominates. At higher concentrations and over extended periods of time, the *striped phase* transforms into a densely packed SAM, with a realignment of the principal molecular axis at a small angle from the surface normal (Figure 3.1.d).¹⁹ Conversely, the formation of well-ordered thiolate SAMs onto gold via vapour deposition under UHV conditions is less straightforward, as substantial kinetic barriers exist for the transition from *flat-lying* to the thermodynamically-favoured *upright* geometry.²⁰

Among other considerations, stability is a necessary requirement for the widespread commercial use of any functional device.²¹ In this regard, the limitation of current thiol-based SAM technology has been acknowledged.²² These films are inherently prone to oxidative degradation to sulfonates,^{23–27} are UV and thermally unstable above 375 K,^{28–31} are destroyed by some solvents,³² and decompose to sulphides on moderately reactive surfaces.^{33,34} Strategies have been proposed to overcome some of these limitations, mainly via the use of multidentate ligands and interchain crosslinking.³² However, the origin of these limitations lie ultimately in the nature of the ligand-surface interaction that anchors the molecule to the substrate; that is, it is intrinsic to the S–Au bond strength. Novel approaches have been explored that rely on the exploitation of other headgroup-substrate interactions such as phosphines and alkylamines adsorption onto gold, irreversible covalent bonding of silanes to silicon oxide substrates,^{31,35,36} and carbon bonding to metallic and non-metallic substrates.[§] The latter has spurred great interest not only because of the stronger C–Au ($388.84 \text{ kJmol}^{-1}$) compared to traditional S–Au bonds (337.7 kJmol^{-1}),³⁷ but also because of its high conductivity, a valuable feature for molecular junction applications.³⁸ Some approaches to generate C–M σ -bonds between modifiers and a substrate include aryl radicals formation from diazonium salts^{39,40} 1,2-hydride shift of terminal alkynes,^{41,42} and desilylation chemistry⁴³ (Figure 3.1.e). Another chemical species that can create a C–M σ -bond are carbenes. These species have revolutionised many fields including organocatalysis, metallorganic catalysis, metallopharmaceuticals, organometallic materials; and have opened new avenues for surface functionalization.

[§]Strictly speaking, this type of films are not a SAM, as these are often irreversible processes. However, the definition of SAM has been expanded in this discussion to include covalently bonded monolayers on solid surfaces.

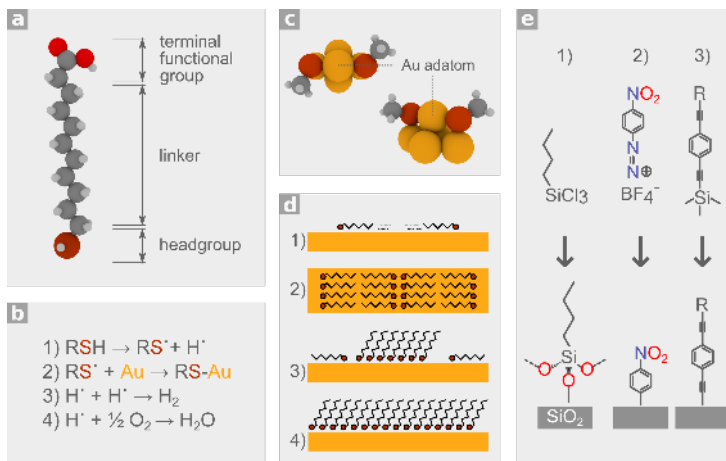


Figure 3.1 ■ Self-assembled monolayers (SAMs). **a)** Structural components of the molecular unit 10-carboxy-1-decanethiol. **b)** Surface reaction mechanism of thiol adsorption on gold. **c)** Current atomic model of thiol adsorption on Au(111) invokes the formation of a $R_1S-Au-SR_2$ complex with a gold adatom. The Au adatom sits on a bridge site, and S-atoms on atop gold sites. Carbon (grey), gold (yellow), hydrogen (white), sulphur (orange). **d)** 1) at low coverage, alkane thiols exist as a highly mobile 2D gas. 2) at a critical coverage, alkanethiols assemble in a *flat-lying* motif referred to as the *striped phase* 3) lateral pressure induces the conformational transition from *flat-lying* to an *upright* mode at the domain boundaries of the *striped phase* 4) high-density islands of *upright* alkanethiols grow at the expense of the *striped phase* until full saturation is reached. Adapted from reference [19]. **e)** Strategies for SAM fabrication from covalent bonding other than $S-Au$. 1) Silane to siloxane on SiO_2 , 2) aryl radical from dediazotisation of diazonium salts on various supports, 3) desilylation reaction.

N-Heterocyclic Carbenes (NHCs)

In this chapter, we refer to *carbenes*, *free carbenes* or *persistent carbenes* as a class of molecules that possesses a divalent neutral carbon atom and a lone pair of electrons. Note that these are entirely different chemical species from the organometallic compounds with a generic formula $L_n \rightarrow M=CR_1R_2$ also termed carbenes, where L_n : coordinative ligands, and CR_1R_2 : divalent carbon ligand. Mainly, the latter refers to Schröck and Fischer carbenes, which are stable complexes that do not exhibit the reactivity of free carbenes.

Heterocyclic carbenes are a specific type of persistent carbenes that exists within a ring structure and contains at least one heteroatom. The type of the heteroatom in the ring can be S, O, P, Si, or B. Compounds with nitrogen as the heteroatom are termed *N-heterocyclic carbenes (NHCs)*, and are by far the most stable and studied type of heterocyclic carbene. These species have traditionally been recognised as transient reactive intermediates in some reactions.

For example, Breslow⁴⁴ (1958) speculated that a zwitterionic or carbenic form of thiamine, was the active form of this organocatalyst in furoin synthesis from furfural. Wanzlick and Öfele were pioneers of the field and reported for the first time on the reactivity and stability of NHCs generated *in situ*, and their complexation to a metal center.^{45–47} Because of their intrinsic high instability and reactivity, unambiguous identification and isolation of free carbenes remained elusive for a long time. It was not until 1988 when Bertrand *et al.*⁴⁸ reported the first ever isolable phosphinocarbene. Independently Arduengo *et al.*⁴⁹ isolated the first crystalline, imidazolylidene-based *N*-heterocyclic carbene (Figure 3.2.a), and demonstrated the use of NHCs as ligands in metal coordination complexes.⁵⁰

Following Arduengo's report, the major carbenic form of these species versus an ylidic form ($\text{N}=\text{C}^-\text{N}^+$) was proposed based on different characterisation methods.^{51–53} However, a significant degree of $p_\pi - p_\pi$ delocalisation was theoretically predicted later on for these species, which turned out to be a crucial factor in their stabilisation.^{54,55} In this respect, two main mechanisms contribute to the stabilisation of these, otherwise, unstable and short-lived species. On the one hand, the carbenic carbon (C2) can be kinetically stabilised by the substituents at the heteroatom positions. The steric hindrance of adjacent substituents stabilise the free carbene by posing a high kinetic barrier to dimerisation to the enetetramine form. Arduengo's carbene (**IAd**) relies on this type of stabilisation by bearing two sterically demanding adamantyl groups at the *N*, *N* position (Figure 3.2.a). A second mechanism also operates, whereby the carbenic carbon (C2) is electronically stabilised by the adjacent heteroatoms. Most often, stable NHCs exist in the ground state as singlet carbenes, where the lone pair occupies an sp^2 -hybrid orbital, while a p -orbital remains vacant. In triplet state NHCs, sp^2 - and p -orbitals are singly occupied by each electron of the lone pair (Figure 3.2.b). The stabilisation of singlet carbenes by the synergetic effect of heteroatoms is two-fold and schematically illustrated in Figure 3.2.c for an NHC and other heteroatomic carbenes. On the one hand, the adjacent nitrogen atoms in NHCs inductively withdraw electron density away from the carbenic carbon via the σ -bond, which lowers the energy of the occupied sp^2 -orbital. In doing so, the energy gap for the singlet to triplet state transition required for NHC dimerisation increases. On the other hand, the nitrogen lone pair donates electron density mesomerically into the empty p -orbital on the carbenic carbon.

This contribution to the stabilisation is usually represented as a curved line between the N–C–N when drawing their chemical structure.⁵⁶

Other structural factors also provide additional stabilisation. For example, although 5-membered rings constitute the vast majority of NHCs, extra steric and electronic stabilisation can be gained from smaller or larger ring structures. Variations in the N–C2–N angle, imposed by the ring size, alters the extent of orbital overlap between the carbenic carbon and the adjacent nitrogens, and can enhance steric hindrance at the C2 position. Similarly, the cyclic nature of the ring forces the C2 carbon into an almost sp^2 arrangement, favouring a singlet state.⁵⁷ The degree of saturation of the ring backbone also plays an important role. Imidazolylidines NHCs with an unsaturated ring backbone have a larger singlet to triplet transition energy gap; hence they remain as free carbenes and are stable towards dimerisation. The opposite is true for imidazolidin-2-ylidenes with a saturated backbone, which tend to dimerise. Poater *et al.*⁵⁸ derived an empirical expression that relates steric and electronic parameters with the thermodynamics of NHC dimerisation ($E_{dimer.}$), which was shown to correlate linearly with dimerisation energy values predicted by DFT (Equation 3.1). The steric factor is described by their percentage of buried volume ($\%V_{buried}$),⁵⁹ and the electronic factor by the singlet to triplet transition energy gap ($E_{singlet \rightarrow triplet}$). For $E_{dimer.} \geq 0 \text{ kJmol}^{-1}$ the free NHC is stable as a monomer, whereas for $E_{dimer.} \leq -83.68 \text{ kJmol}^{-1}$, the dimer is favoured. For certain cases, equilibration between monomeric and dimeric forms is possible, such as benzimidazolium NHC derivatives.

$$E_{dimer.} = A \cdot \%V_{buried} + B \cdot E_{singlet \rightarrow triplet} + C$$

$A, B, C = \text{empirically fitted parameters}$

(3.1)

Since the seminal work by Bertrand and Arduengo, the field of NHCs has expanded very rapidly. The strong σ -donating character and weak π -accepting ability of NHCs soon found use as exceptional ancillary ligands to transition metal complexes.⁶⁰ The field of homogeneous catalysis was revolutionised, as NHCs outperformed traditional phosphine ligands in metathesis,⁶¹ cross-coupling,⁶² and asymmetric hydrogenation reactions.⁶³ For example, the second generation of Grubb's catalysts for olefin metathesis replaces a phosphine

ligand with an NHC, increasing in this way the catalyst affinity for olefins by several orders of magnitude.⁶⁴ The strong binding of NHCs makes these compounds very versatile ligands which form complexes with almost every element in the periodic table, and in different oxidation states. In particular, ligated NHCs are significantly more kinetically stable than classical phosphine ligands, hence more resistant to thermal and oxidative degradation. NHC binding to metal centres is primarily via the strongly donating σ -bond of the lone electron pair, into the σ -accepting d_z^2 metal orbital. However, some contribution to the overall binding from π -backdonation of the metal d_{xz}/d_{yz} orbitals into the C–N antibonding π^* orbital is also possible, as well as π -donation from the NHC π -system into d_{xz}/d_{yz} orbitals on the metal (Figure 3.2.d).^{65–67} Nevertheless, the NHC–metal interaction is often represented as a σ -bond, so as to accommodate the empirical fact that the ligand is able to rotate around the bond. It is worth noting that, although the vast majority of reports of NHCs bound to metal centres involve coordination via the C2 position, bonding via the C4 or C5 is also possible. This special case constitutes a class of NHCs termed mesoionic or abnormal carbenes (**aNHCs**), and are stabilised by only one nitrogen atom. Hence, the stabilisation gained inductively and mesomerically from the adjacent nitrogen is exceedingly reduced. As a result, the reactivity of aNHCs are markedly different as they tend to be even more electron-donating and more π -accepting.

Another feature that makes NHCs very attractive is their highly flexible synthesis. Most commonly, free NHCs are prepared from deprotonation of azolium salts, thereby, derivatisation and modular synthesis of NHCs rely on well-established heterocyclic chemistry. Other synthetic routes also exist and are summarised in Figure 3.3. The electron-donating/electron-accepting substituents, both at the *N*, *N*-positions and at the ring backbone, provide a means of independently tuning the electronic and steric properties, and reactivity of NHCs. Quantification of the electronic characteristic of NHCs is done in a similar way to phosphines using the Tolman electronic parameter (TEP).⁶⁹ These synthetic routes are suitable for the multigram preparation of NHCs. However inert atmospheres are necessary to exclude air and moisture during the handling of free carbenes. A way to circumvent dealing directly with such reactive species is by using easily handled masked NHCs precursors (Figure 3.3). Thermolysis of NHC adducts is a very convenient way to generate

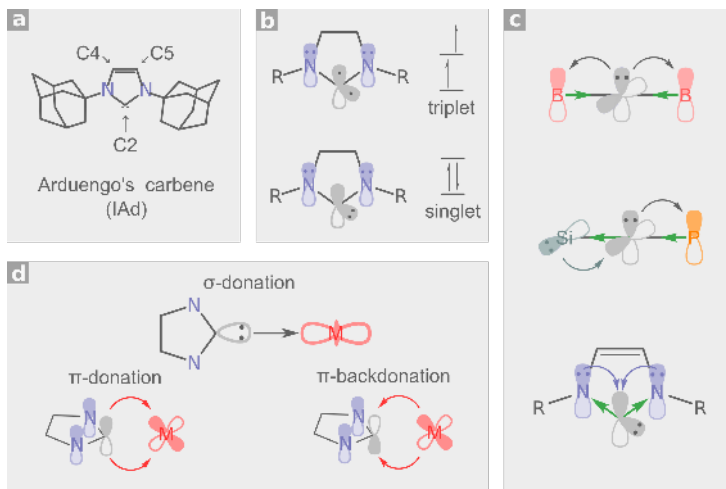


Figure 3.2 ■ Stabilisation and bonding of *N*-Heterocyclic carbenes. **a)** Structural model of first isolable *N*-heterocyclic carbene 1,3-bis(1-adamantyl)imidazol-2-ylidene (**1Ad**) known as Arduengo's carbene.⁴⁹ **b)** Singlet and triplet state NHC. **c)** Inductive and mesomeric stabilisation in linear and bent persistent carbenes. **d)** Binding of NHC to a metal centre (M). Adapted from reference [68].

the free NHC *in situ*, with the release of a small molecule as a by-product.

NHCs have been used extensively as stabilising agents for metal nanoparticles, nanocrystals, allotropes, and many complexes with transition metals are known. However, only very recently have the first reports appeared on the modification of planar surfaces by these species.⁷³ The group of Siemeling reported for the first time on the adsorption of the enetetramine form of an NHC onto Au/Si(111).⁷⁴ Later, the groups of Johnson,⁷⁵ and Crudden⁷⁶ independently explored the surface chemistry, stability and applications of these films on Au(111). Remarkably, NHC films withstand harsh thermal treatments and electrochemical cycling, as well as a battery of chemical tests, including pH extremes, boiling organic solvents, displacement by thiols, and even oxidising conditions (H₂O₂, 1 % v/v).⁷⁶ Their exceptional robustness supersedes traditional thiolate-based SAMs, which is associated with a stronger Au–C bond. In the following sections, STM, TPD, and HREELS techniques were employed to investigate the assembly, chemisorption, and binding geometry of these interesting species to planar gold and copper surfaces under UHV conditions.

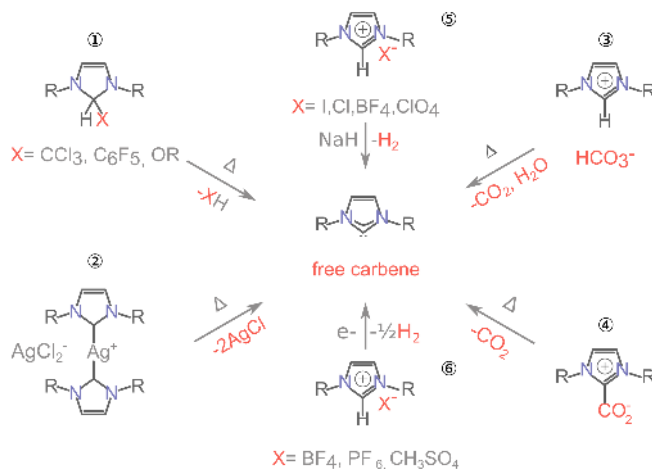


Figure 3.3 ■ Common routes to free *N*-heterocyclic carbenes (NHCs) from their precursors. **1–4**) thermolysis of masked NHCs liberates the free carbene along with a small molecule as a by-product. **3**) the counterion also serves as a base to deprotonate the imidazolium ion. **5**) generation of free carbene via deprotonation of an imidazolium salt with a strong base (usually NaH), **6**) and electrochemically with the release of H₂.^{68,70–72}

3.2 NHC Monolayers on Au(111)

NHC adducts were employed throughout the experiments described in this and the next chapter. These allow handling and mounting of the chemical doser onto the UHV system without special considerations. Bench-stable NHC bicarbonate salts were synthesised, characterised, and supplied by our collaborators in the Crudden research group.[‡] The carbonate counterion simultaneously serves as a mask, so that the compounds are stable in ambient conditions, and as a base to deprotonate the imidazolium ion. The free carbene is liberated on demand by heating, producing CO₂ and H₂O as by-products (reaction scheme 3 in Figure 3.3).⁷⁶ The molecular model of the free NHCs employed in this investigation are shown in Figure 3.4. The molecular body is a benzimidazol-2-ylidene, with methyl, ethyl, and isopropyl wingtip groups at the *N*, *N* positions.

Firstly, the sublimation conditions for the sublimation and liberation of the

[‡]Prof. Cathleen M. Crudden,^[a,b] Mina R. Narouz,^[a] and Christene A. Smith.^[a]

[a] Queen's University, Department of Chemistry, Chernoff Hall, Kingston, Ontario, Canada.

[b] Institute of Transformative Bio-Molecules (WPI-ITbM), Nagoya University, Chikusa, Nagoya, Japan.

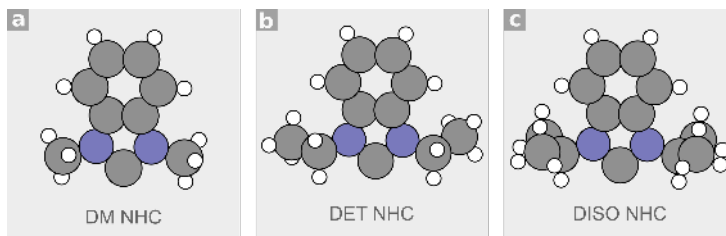


Figure 3.4 ■ Structural model of free NHCs generated from bicarbonate NHC salts. **a)** Free 1,3-Dimethyl-benzimidazol-2-ylidene (**DM NHC**) derived from the thermolysis of 1,3-Dimethyl-1H-benzo[d]imidazol-3-ium hydrogen carbonate salt precursor **b)** Free 1,3-Diethyl-benzimidazol-2-ylidene (**DET NHC**) derived from the thermolysis of 1,3-Diethyl-1H-benzo[d]imidazol-3-ium hydrogen carbonate salt precursor and **c)** Free 1,3-Diisopropyl-benzimidazol-2-ylidene (**DISO NHC**) derived from the thermolysis of 1,3-Diisopropyl-1H-benzo[d]imidazol-3-ium hydrogen carbonate precursor. Carbon (grey), Hydrogen (white), and Nitrogen (blue).

free NHCs had to be determined in order to reproducibly dose the molecules. For all instances, the temperature of the doser containing the chemical was gradually increased while monitoring the fragmentation pattern by gas phase mass spectrometry (Figure S3.1). The chemical doser was inspected visually after the adsorption experiments; the powder acquired a yellow tinge which is known for the dimeric form of benzimidazole-2-ylidene.⁷⁴ Fèvre *et al.* performed extensive thermogravimetric, ^1H , and ^{13}C NMR characterisation of NHC bicarbonate salts and found that heating the compound under high vacuum produces a mixture of free and dimeric enetetramine NHC species.^{70,71} A similar equilibrium between dimeric and free NHC is also known in solution.⁷⁷ Hence, it is reasonable to expect that a mixture of free NHC and its dimeric enetetramine form on sublimation. Nevertheless, the equilibrium between the dimeric and monomeric form is known to shift toward the latter upon adsorption on a metal surface.^{74,78–81}

Once the sublimation conditions were determined, thermal desorption experiments of NHC films were performed. A clean Au(111) crystal held at 300 K was exposed to DISO NHC ($T_{\text{dose}} = 325$ K). Multiplexing between 1–150 amu while ramping the temperature revealed the desorption of fragments $m/z = 2$, 27, 39 and 41 amu from the surface. Assignment of the fragments is as follows: $\text{H}_2^+\bullet$ ($m/z = 2$ amu), HCN^+ ($m/z = 27$ amu), and C_3H_3^+ ($m/z = 39$ amu) from the benzene moiety, and C_3H_5^+ ($m/z = 41$ amu) from the isopropyl groups. The detection of these fragments is consistent with the structure of adsorbed DISO NHC onto the Au(111) surface. No other signals were detected that could

indicate coadsorption of the carbonate counterion, mainly, we did not observe desorption of fragments $m/z = 60, 44$ or 28 amu. Figure 3.5.a displays the TPD spectra recorded as a function of coverage. Surface coverage was controlled by adjusting the exposure time of the Au(111) substrate to the sublimed NHC. All traces displayed a desorption peak centered at $T_{max1} = 605$ K, which saturated above *ca* 20 L. A full monolayer was, therefore, defined as the integrated area of the saturated peak T_{max1} in the TPD spectra, and submonolayers as fractions thereof. The position of T_{max1} did not shift substantially with increasing coverage, which is symptomatic of relatively weak lateral molecular interactions. The desorption profile of T_{max1} is typical of first-order desorption kinetics, which accommodates a mechanism involving intact desorption of DISO NHC from Au(111), and subsequent fragmentation at the mass spectrometer. Under these assumptions, a crude Redhead analysis⁸² with a pre-exponential factor of $z = 1 \times 10^{13} \text{ s}^{-1}$ yields a desorption energy of $E_{des.} = 158 \pm 10 \text{ kJmol}^{-1}$,[‡] in good agreement with the calculated adsorption energy of $E_{calc.} = 149 \text{ kJmol}^{-1}$ for this molecule and similar to its derivatives.^{76,83} By comparison, Bernasek and colleagues used a similar method and derived the chain length-independent chemisorption energy of alkanethiols on Au(111) to be $E_{des.} = 126 \text{ kJmol}^{-1}$.⁸⁴ A shoulder would occasionally develop at $T_{max2} = 510$ K, which unlike T_{max1} , did not correlate with exposure. Therefore, T_{max2} does not correspond to the formation of multilayers but is instead tentatively assigned to DISO NHC film desorption from defect sites.

DISO NHC films were further examined by HREEL spectroscopy acquired in the specular geometry in which the dipole scattering mechanism is in operation. Hence, the surface selection rule provides direct experimental evidence of the relative geometry of adsorption. Figure 3.5.b shows the sample after saturation exposure at 300 K, as well as after heating to the indicated temperature. Table 5 summarises the assignment of the energy losses. The assignment is based on the simulated normal vibrational modes of a modelled DISO NHC – Au – Cl complex in the gas phase, at the M06/SDD level of theory (Gaussian 09).⁸⁵

The energy losses observed at 2960 cm^{-1} and 3070 cm^{-1} are assigned to $\nu(\text{C-H})$ of the isopropyl and aromatic ring, respectively. The $500\text{--}1000 \text{ cm}^{-1}$

[‡]The error in the derived chemisorption energy is due to the uncertainty in the pre-exponential factor $z = 1 \times 10^{11}\text{--}1 \times 10^{13} \text{ s}^{-1}$

range corresponds to the coalescence of at least three peaks located at 750 cm^{-1} , 870 cm^{-1} , and 930 cm^{-1} . The losses at 870 cm^{-1} and 930 cm^{-1} are assigned to C–H bending modes of the isopropyl groups, whereas the peak at 750 cm^{-1} is characteristic of a benzene ring C–H out-of-plane bending. The noticeable inhomogeneous broadening, and the variations in the intensity of this region as a function of temperature, are possibly due to changes in the molecular packing in the film and rotation of the isopropyl groups. This broadening was completely absent for other sets of HREELS data, which implies a dependency on sample preparation (Figure S3.2). The $1240\text{--}1600\text{ cm}^{-1}$ region contains bands related to C–N and C=C stretches, whose dipole moments lie along the main molecular axis. The fact that these modes are active and relatively intense with respect to the 750 cm^{-1} mode, suggests that the molecular plane of DISO NHC must be aligned perpendicular to the plane of the Au(111) surface. This *upright* binding mode is in agreement with that predicted by theoretical calculations, and also the case for deposition from solution on the same substrate.^{76,86} The detection of these signature vibrational modes strongly supports the intact adsorption of DISO NHC on the Au(111) surface. These bands persisted after heating the sample up to 605 K , at which temperature, all signature molecular vibration were lost to produce a spectrum of a clean surface. This behaviour conforms with the reversible desorption mechanism proposed based on the TPD spectra. It is noteworthy that no vibrational bands were detected that could indicate coadsorption of the carbonate counterion, confirming the liberation of the free carbene via the mechanism described in reference [70], and the clean formation of a DISO NHC layer on Au(111).

Interestingly, a weak yet persistent energy loss was apparent at 420 cm^{-1} . Laurentius *et al.* reported the same energy loss for covalently bound nitrobenzene films on Au(111) and gold nanoparticles derived from the corresponding diazonium salt. Independently, Guo *et al.*⁸⁷ reported a band at 415 cm^{-1} for films generated by electro-reduction of aryldiazonium salts on roughened gold electrodes; and Ahmad *et al.*⁸⁸ observed a band at 413 cm^{-1} for films created on gold nanorods. In each case, the authors concluded from their combined experimental and DFT results that this vibrational mode corresponds to a $\nu(\text{C–Au})$. Similarly, gas phase photoelectron spectroscopy of $\text{Au}(\text{CH}_2)_2^-$ and $\text{Au}(\text{CN})_2^-$ complexes exhibit a $\nu(\text{C–Au})$ vibration band at 480 cm^{-1} and at 400 cm^{-1} , respectively.^{89,90} Earlier studies on CN^- adsorption on gold also report peaks

appearing in the 250–400 cm^{-1} region due to stretching and bending modes of C–Au bonds. Therefore, the peak at 420 cm^{-1} in the HREEL spectra is unambiguously assigned to a $\nu(\text{C–Au})$ from covalently bound DISO NHC via the carbenic carbon (C2).^{91,92}

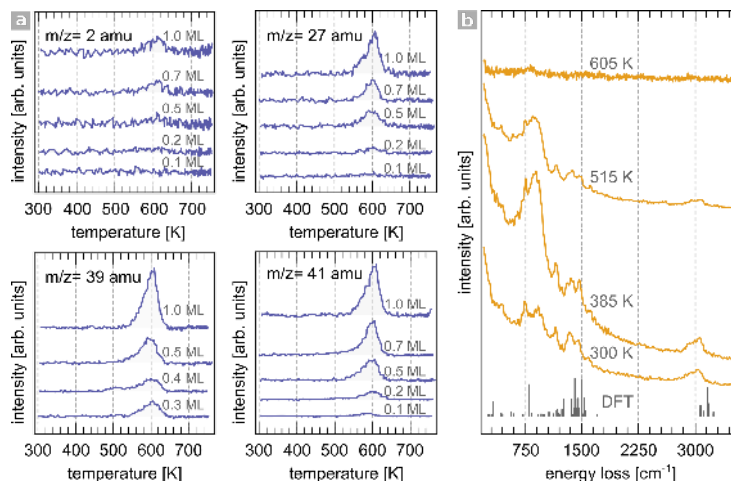


Figure 3.5 ■ Adsorption of DISO NHC on Au(111). **a)** TPD spectra of fragments $m/z = 2$ amu (H_2^{+}), 27 amu (HCN^+), 39 amu (C_3H_3^+), and 41 amu (C_3H_5^+) collected following exposure of DISO NHC to Au(111) held at 300 K, $\beta = 3.5 \text{ Ks}^{-1}$. **b)** HREEL spectra as a function of temperature. Signals have been smoothed by FFT filtering. The spectrum of the film heated to 605 K has been multiplied by 100. The simulated normal vibrational modes of a model DISO NHC–Au–Cl complex used in the energy loss assignment is also displayed (DFT). $E_0 = 5.0 \text{ eV}$, FWHM = 47.3 cm^{-1} .

Table 5 ■ DISO NHC/Au(111) HREELS vibrational modes assignment. ν : stretch, β : bending, δ : scissoring, ρ : rocking, ω : wagging, τ : twisting, R: ring vibration, sym.: symmetric, asym.: asymmetric, def.: deformation, breath.: breathing, ip: in plane, op: out of plane.

Energy loss [cm^{-1}]	Assignment
3070	$\nu(\text{C–H})_{\text{R}}$
2960	$\nu(\text{C–H})_{\text{alkyl}}$
1615	$\text{R}_{\text{def.}}$
1465	$\nu(\text{C=C})$, $\nu(\text{C–N})$, $\delta(\text{CH}_2)$, $\beta(\text{C–H})$, $\beta(\text{CH}_3)_{\text{asym.}}$
1360	$\nu(\text{C=C})$, $\nu(\text{C–N})$, $\tau(\text{CH}_2)$, $\omega(\text{CH}_2)$, $\beta(\text{CH}_3)_{\text{sym.}}$
1240	$\nu(\text{C–N})$
1155	$\text{R } \beta(\text{C–H})_{\text{i.p}}$
1015	$\text{R}_{\text{breath.}}$
930	$\beta(\text{C–(CH}_3)_2)$
870	$\beta(\text{C–(CH}_3)_2)$
750	$\text{R } \beta(\text{C–H})_{\text{o.p}}$
650	$\text{R}_{\text{stretch}}$
420	$\nu(\text{C–Au})$

The morphology of DISO NHC monolayers was investigated using LEED and STM. LEED experiments conducted at 300 K only revealed a $p(1 \times 1)$ diffraction pattern due to Au(111) across a range of exposures and annealing temperatures. This indicates the absence of long-range ordered superstructures under the examined experimental conditions. STM imaging was performed on samples prepared in a similar manner as described for TPD and HREELS experiments. Molecular resolution of the as-prepared sample was not attained under any tunnelling condition. Streakiness was recurrent throughout the imaging, which is often indicative of highly mobile adsorbates. Notably, the herringbone reconstruction remained visible upon saturation exposure to DISO NHC. Heating the sample to 375 K produced vacancies 2.4 Å deep, which equates to one atomic step (Figure 3.6.a,b). Heating to 500 K promoted further vacancy formation, along with the appearance of raised areas about 2.4 Å in height, consistent with gold adatom islands (Figure 3.6.c,d). Both vacancies and adatoms features were highly mobile within the timescale of the imaging. The origin of these features cannot be attributed to adventitious adsorption of residual background gases, as this has never been reported for Au(111).⁹³ The etch-pitting is attributed to the adsorption of DISO NHC, which extracts atoms from the first surface layer. This phenomenon is analogous to that often encountered in thiol adsorption on gold. However, the vacancy density and gold islands accounted for less than 1 % of the surface area, by contrast to the 4.4 % required to lift the herringbone reconstruction ($22 \times \sqrt{3}$) completely.⁹³ Interestingly, the density of etch pits for films prepared under UHV was significantly lower than that reported for films deposited from solution.⁷⁶ The fact that the herringbone reconstruction remained visible, even after saturation exposure, was quite unexpected. We anticipated that the adsorption of DISO NHC would lift the reconstruction, as this has traditionally been provided as proof of strong molecule-adsorbate interactions.⁹⁴ Heating above 600 K restored a clean surface.

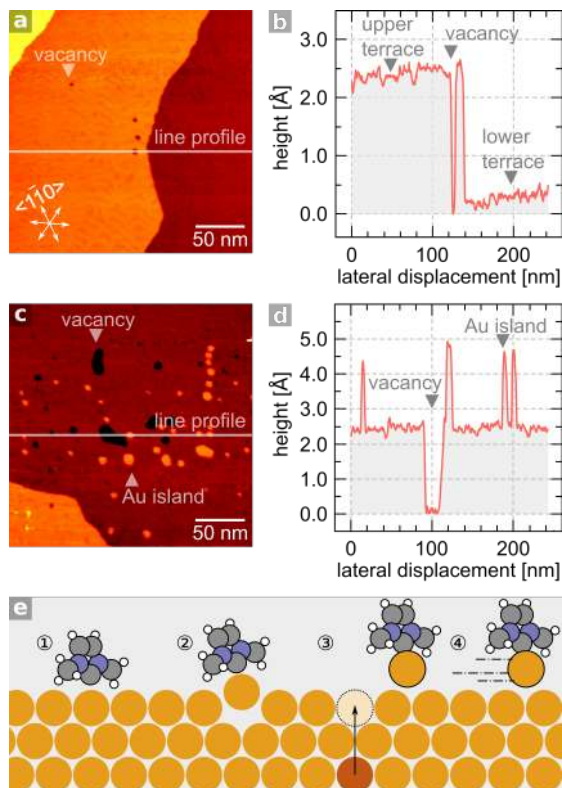


Figure 3.6 ■ DISO NHC induces vacancies and gold adatom islands on Au(111). **a)** STM image of DISO NHC deposited onto Au(111) (1200 L) and heated to 375 K **b)** corresponding line profile of image **a)** **c)** STM image of the sample heated to 500 K. **d)** corresponding line profile of image **c)**. Images were acquired at $V_t = -0.4$ V, $I_t = 600$ pA. **e)** Current model for NHC binding to Au(111) proposed by Wang *et al.*⁹⁵. 1) adsorption of free NHC onto Au(111). 2) NHC attaches to an atop gold atom and pulls it out of the surface plane. 3) a NHC–Au adatom complex forms along with a vacancy, which is replenished by gold atoms from the bulk. 4) the NHC “rides” on top of the gold adatom and diffuses over the surface.

Moreover, a robust C–Au and high thermal stability of DISO NHC may seem at first glance dissonant with highly diffusive species. However, soon after the course of this investigation, Wang *et al.*⁹⁵ published a detailed study on the adsorption of a series of imidazol-2-ylidenes on Au(111) generated from CO₂ adducts. Similarly to us, the authors reported that the herringbone reconstruction remains intact upon adsorption of NHCs. The authors provided compelling molecular dynamic simulations describing a mechanism whereby the extracted gold adatoms are simultaneously replenished by atoms from the bulk (Figure 3.6.e). The authors also noted that the formed NHC–Au

complexes are highly mobile even at 77 K due to a *ballbot-type* motion. In this binding model, the NHC "rides" upon a gold adatom and diffuses rapidly over the surface, while the robustness of the C–Au bond remains unaffected. The energy barrier for gold adatom extraction decreases by one order of magnitude in the presence of NHCs (12 kJmol⁻¹) with respect to the same process in their absence (125 kJmol⁻¹). Once the NHC–Au complex forms, the diffusion energy barrier is only 10 kJmol⁻¹.⁹⁵ Their proposed dynamic binding mechanism would certainly explain the lack of molecular resolution in our STM images collected at 300 K, and challenges the presumed static binding model. Critically, the strong binding of DISO NHC to Au(111) and high diffusivity are not mutually exclusive properties. It is worth noting that an alternative non-covalent bonding has also been proposed by Kim *et al.*⁸⁶ for NHCs bearing bulky substituents. Based on DFT modelling, the authors concluded that some NHCs bind to the surface of Au(111) through a molecular dipole, which results in a sizeable reduction of the work function of Au(111).

Next, the effects of the wingtip groups at the *N, N*-position on the adsorption of NHCs was investigated. DM NHC and DET NHC films were prepared in a similar manner as described for DISO NHC and characterised by thermal desorption. Unlike DISO NHC, the TPD spectra for DM NHC revealed marginal yields for fragments $m/z = 15$ amu (CH_3^+) and $m/z = 39$ amu (C_3H_3^+) even after prolonged exposures (Figure 3.7.a). For instance, the maximum desorption yield of C_3H_3^+ was only 16.1 % relative to 1.0 ML of DISO NHC for the same fragment. Moreover, the integrated area of the peak did not correlate with exposure time. A similar behaviour was found for films generated from DET NHC, where the desorption traces of fragments $m/z = 27$ amu (HCN^+) and $m/z = 39$ amu (C_3H_3^+ , yield = 28.4 %) was very low (Figure 3.7.b). In both cases, DM NHC and DET NHC traces peaked at $T_{\text{max.}} = 568$ K. Two main pieces of information were derived from TPD data. Firstly, DM and DET NHCs do not form multilayers, as confirmed by the absence of low-temperature desorption peaks. Secondly, it appears that DM and DET monolayers do not undergo reversible thermal desorption, but remain attached to the gold surface. The distinctive behaviour of DM and DET NHC compared to DISO NHC suggests that these molecules might adsorb in a different geometry from that of DISO NHC. Hence, further characterisation of these films was performed by HREEL spectroscopy.

The HREEL spectra of DM and DET NHC monolayers were virtually the same (Figure 3.7.c,d). The assignment is summarised in Table 6 and was done by comparison to modelled NHC–Au–Cl complexes of DM and DET NHC in the gas phase. In both cases, a peak at *ca* 760 cm⁻¹ assigned to a C–H out-of-plane bending mode dominated the spectra. C–N, C=C, and C–H stretches appeared very weak or entirely absent. Strong energy losses below 300 cm⁻¹ were detected, whose assignment remains at this stage elusive. These bands could be either due to internal torsional and ring bending modes or possibly due to molecule-surface stretching and bending modes. The spectra remained mostly unchanged after heating the monolayer at 530 K, at which temperature the peaks were less defined. The spectra of these films differ drastically from that of DISO NHC. Mainly, strong energy losses for DM and DET NHCs appeared weak for DISO NHC, and *vice versa*. This suggests that DM and DET NHCs adopt a binding geometry with its molecular axis oriented largely along the surface plane. That is, in contrast to DISO NHC, DM and DET NHC adopt a *flat-lying* geometry. It is worth mentioning that our findings do not support the results reported by Weidner *et al.*⁷⁴. The authors found that monolayers of single DET NHC orient at an angle of 30° relative the surface normal. A possible source for this disagreement could be the method employed in the film preparation. Unlike our films, the authors deposited the enetetramine form of DET NHC onto a Au/Si(111) surface from a THF solution. They also noted the presence of oxygen contamination and in the form of C=O bonds, which is typical of carbene decomposition to urea products.⁴⁵ Thus, the film reported by Weidner *et al.*⁷⁴ might, in fact, be a mixture of species.

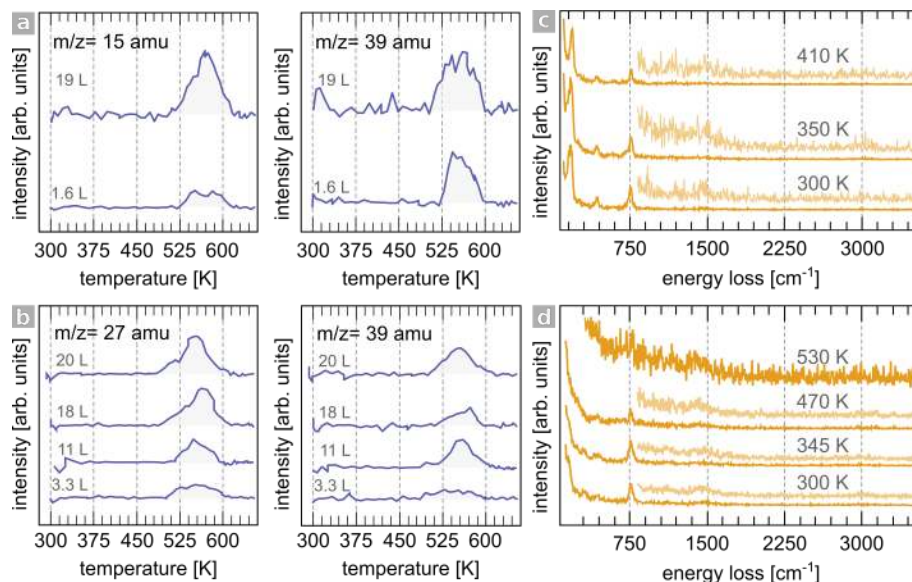


Figure 3.7 ■ Adsorption of DM NHC and DET NHC on Au(111). **a)** TPD spectra of fragments $m/z = 15$ amu (CH_3^+) and 39 amu (C_3H_3^+) collected following exposure of DM NHC to Au(111) crystal held at 300 K, $\beta = 3.5 \text{ Ks}^{-1}$. **b)** TPD spectra of fragments $m/z = 27$ amu (HCN^+) and 39 amu (C_3H_3^+) collected following exposure of DET NHC to Au(111) crystal held at 300 K, $\beta = 3.5 \text{ Ks}^{-1}$. **c)** HREEL spectra of DM NHC film (600 L) on Au(111) at 300 K, and heated to the indicated temperature. Intensity of the 825–3550 cm^{-1} region has been multiplied by 10. **d)** HREEL spectra of DET NHC film (500 L) on Au(111) at 300 K and heated to the indicated temperature. $E_0 = 5.0 \text{ eV}$, $\text{FWHM} = 47.3 \text{ cm}^{-1}$.

Table 6 ■ DM NHC and DET NHC adsorption on Au(111) HREELS vibrational modes assignment. ν : stretch, β : bending, δ : scissoring, ρ : rocking, ω : wagging, τ : twisting, γ : torsion, R: ring vibration, sym.: symmetric, asym.: asymmetric, def.: deformation, breath.: breathing, ip: in plane, op: out of plane.

Energy loss [cm^{-1}]		Assignment
DM NHC	DET NHC	
3000	3000	$\nu(\text{C}-\text{H})_{\text{alkyl}}$
1445	1445	$\nu(\text{C}=\text{C})$, $\nu(\text{C}-\text{N})$, $\delta(\text{CH}_2)$, $\beta(\text{CH}_3)_{\text{asym.}}$
755	760	R $\beta(\text{C}-\text{H})_{\text{o,p}}$
585		R _{stretch}
430	430	R _{o,p}
	300	R _{o,p} or molecule-surface vibration?
245	230	$\gamma(-\text{CH}_3)$ or molecule-surface vibration?
170		molecule-surface vibration?
155		molecule-surface vibration?

Low-energy electron diffraction data of DM and DET NHC monolayers only revealed a $p(1 \times 1)$ pattern due to the substrate across a range of exposures and annealing temperatures. Similarly to DISO NHC, STM images of DM NHC were predominantly characterised by streakiness, with the herringbone

reconstruction still present. Notably, islands of nanometer-sized features were briefly resolved, which exhibited some apparent local order (Figure 3.8.a). However, high-resolution imaging proved extremely difficult, as these features rapidly disappeared from one scan to the next. The features are suspected to be $(\text{NHC})_2\text{Au}$ complexes, which have been theoretically predicted to be the most stable form of DM NHC binding to Au(111) (Figure 3.8.b). The binding of $(\text{DM NHC})_2\text{Au}$ is stabilised by van der Waals forces between the aromatic ring and the surface and agostic interactions between the hydrogens on the CH_3 groups and the surface.⁹⁶ Additionally, similar species generated from imidazolium-2-ylidene adsorption onto Au(111) were resolved under STM at 77 K by Wang *et al.*⁹⁵. Conclusive evidence also exists of such complexes forming at the interface of gold nanoparticles. Combined experimental and DFT simulations carried out by Rodríguez-Castillo *et al.*⁹⁷ suggested that the bonding of DM NHC to gold nanoparticles involves the stretching of surface atoms, which is an intermediate step in the formation of $(\text{NHC})_2\text{Au}^{\text{I}}$ complexes detected spectroscopically.^{98,99} This form of bonding resembles the recent model of thiols bonding to gold surfaces, as discussed in the introduction. Tang and Jiang⁹⁶ showed that complexation with extracted adatoms was also energetically favourable for other ligands such as alkenyls. Hence, this binding motif might be a more general scenario than first anticipated. The notion of NHC complexes forming from extracted adatoms is further explored in the next section.

The surface morphology remained unchanged until the sample was heated to 435 K, at which temperature the surface topography was dominated by a high density of oligomeric features (Figure 3.8.c). These features are assigned to the decomposition products of the DM NHC monolayer. [2+2] cycloaddition and electrocyclic rearrangements are possible reaction pathways to polymers on Au(111) at elevated temperatures.¹⁰⁰ The low desorption yield obtained in TPD experiments and the imaging of these species after heating conform with the formation of non-desorbing polymeric residues. This behaviour contrasts drastically with the STM images of DISO NHC, where a clean surface was restored following heating above 600 K. This difference must necessarily arise because of the smaller methyl functionality at the *N*, *N*-position.

In conclusion, the possibility of generating NHC monolayers on a Au(111)

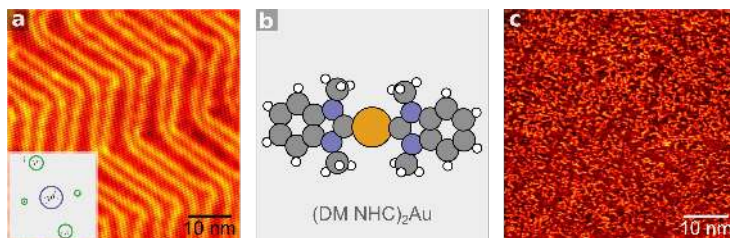


Figure 3.8 ■ STM topography of DM NHC films. **a)** STM image of Au(111) after deposition of DM NHC. Some indication of local ordering was observed as indicated by the FFT of the image in the inset. Highlighted are the spots corresponding to the herringbone pattern (blue) and the nanometer-sized features (green). **b)** Structural model of proposed (DM NHC)₂Au complex giving rise to the features in image a). **c)** Decomposition products of DM NHC monolayer after heating to 435 K.

surface from NHC bicarbonate salt precursors was demonstrated. The chemisorption energy of DISO NHC was derived from thermal desorption experiments, which is significantly higher than traditional alkanethiol monolayers. The origin of this higher stability is attributed to the robust C–Au bond as shown by other authors. The crucial role of functional groups at the *N*, *N*-position in the adsorption geometry was evident. HREEL spectroscopy provided evidence of bulky isopropyl groups favouring an *upright* binding, whereas a *flat-lying* adsorption is preferred for the smaller methyl and ethyl groups. Such a dramatic effect of wingtips can be explained by comparing the sterics of NHCs to their closely related phosphine ligands. The spatial arrangement of traditional *sp*³-hybridised phosphine ligands resembles a cone-shaped envelope, and the cone angle is used as a measure of their steric bulk. By contrast, the spatial arrangement of substituents at the *N*, *N*-position in NHCs are best described as a fan- or umbrella-shaped, with the substituents oriented more closely towards the metal centre they bind to. As a result, variations in substituents at *N*, *N*-position have a large impact on the steric environment around the metal centre.⁶⁸ Furthermore, the distinct binding geometry dictates the fate of the monolayer. Monolayers of *upright* DISO NHC desorb cleanly, whereas those with *flat-lying* DM and DET NHCs decompose leaving residues on the surface. Although molecular resolution was not attained under STM due to the high mobility of these species, their adsorption was deduced indirectly from their effect on the substrate. A low-density of etch-pits and gold islands were observed for DISO NHC, and residual decomposition products of the DM NHC monolayer. We speculate that DM and DET NHCs form complexes with gold adatoms of the type (NHC)₂Au, whereas DISO NHC forms an NHC–Au

ballbot type complex with a gold adatom.

3.3 NHC Monolayers on Cu(111)

Copper and its alloys are extensively used as construction material, and because of its high conductivity, this material is of considerable importance in the semiconductor industry. Copper corrosion is an important issue, and its passivation has been the subject of many investigations.^{101,102} A successful strategy to achieve copper passivation is the adsorption of a protective organic film. Several classes of molecules such as carboxylic acids, amines, thiols, and azoles have been used as passivators.¹⁰³ In particular, organic modifiers containing heteroatoms exhibit enhanced passivating action against copper corrosion, such as benzotriazole.¹⁰⁴

Although synthetic routes to copper complexes with NHC ligands are well-known,^{105–107} their interaction with solid copper surfaces represents a gap in the literature, let alone their uses as corrosion inhibitors. To our knowledge, the study by Choi *et al.*¹⁰⁸ is the only example of NHC ligands used in the stabilisation of CuSe nanodisks, where an NHC–Cu bond was presumed. In this section, we attempt to answer some fundamental questions concerning NHC adsorption on a model Cu(111) surface. First, whether NHCs would form stable monolayers on copper; secondly, whether the structure of the NHC would affect the bonding orientation of the ligand on the surface; and thirdly, whether this would vary with ligand density.

Generation of free DM, DET and DISO NHCs was carried out from bicarbonate salts precursors as described before (Figure 3.3). Figure 3.9.a shows the TPD spectra of fragments $m/z = 2, 27, 39$ and 41 amu detected after deposition of DISO NHC on a Cu(111) crystal held at 300 K. Similarly to the deposition on Au(111), the coverage was controlled by the exposure time of Cu(111) to the sublimed DISO NHC. The assignment of the fragments is as before: $H_2^{+\bullet}$ ($m/z = 2$ amu), HCN^+ ($m/z = 27$ amu), and $C_3H_3^+$ ($m/z = 39$ amu) from the benzene moiety, and $C_3H_5^+$ ($m/z = 41$ amu) from the isopropyl groups. The detection of these fragments is consistent with the desorption of DISO NHC

from the Cu(111) surface. All traces displayed a single peak with a maximum desorption temperature at $T_{max} = 570$ K, which saturated at exposures ≥ 49 L. Multilayers did not form, as evident from the absence of lower temperature desorption peaks. A full monolayer was therefore defined as the integrated area of the saturated peak T_{max1} in the TPD spectra, and submonolayers as fractions thereof. Increasing coverage did not affect the position of T_{max1} , which suggests weak repulsive lateral interactions among DISO NHC molecules. The desorption profiles of DISO NHC from Cu(111) bear many similarities with desorption from Au(111). Hence, the same mechanism involving intact monolayer desorption, with subsequent fragmentation at the mass spectrometer, is proposed for the DISO NHC/Cu(111) system.

A crude Redhead analysis⁸² with a pre-exponential factor of $z = 1 \times 10^{13} \text{ s}^{-1}$ yields a desorption energy of $E_{des.} = 158 \pm 10 \text{ kJmol}^{-1}$, which is similar to the chemisorption energy derived for Au(111) within error.[†] By comparison, the experimentally derived value is significantly higher than the chemisorption energy of heptanethiol adsorbed onto Cu(110) ($E_{des.} = 117 \text{ kJmol}^{-1}$) derived using a similar approach.¹⁰⁹ DFT calculations carried out at the Mosey research group,[‡] in a similar fashion described for DISO NHC adsorption on Au(111), predict a chemisorption energy of $E_{calc.} = 182.6 \text{ kJmol}^{-1}$. The PBEsol exchange-correlation functional was employed with a $3 \times 3 \times 1$ k-point sampling, and a kinetic energy cut-off of 544.23 eV. See reference [76] for further details of the calculations. The discrepancy between the experimental and theoretical chemisorption energies could be due to either an overestimation by the functional, which can be up to 20 kJmol^{-1} , or because of the model itself; as the involvement of adatoms to form a *ballbot*-type complex was not considered. Nonetheless, these results confirm that DISO NHC forms highly stable monolayers on copper.

[†]The error in the derived chemisorption energy is due to the uncertainty in the pre-exponential factor $z = 1 \times 10^{11} - 1 \times 10^{13} \text{ s}^{-1}$

[‡]Dr. Nicholas J. Mosey^[a]

[a] Queen's University, Department of Chemistry, Chernoff Hall, Kingston, Ontario, Canada.

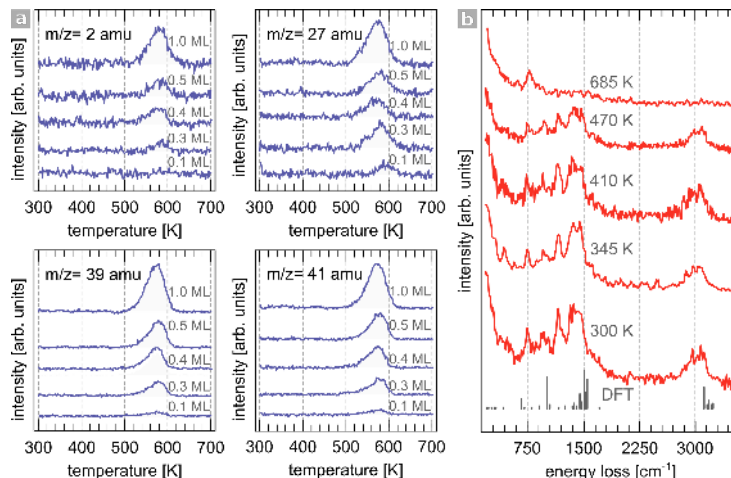


Figure 3.9 ■ Adsorption of DISO NHC on Cu(111). **a)** TPD spectra of fragments $m/z = 2$ amu (H_2^{+}), 27 amu (HCN^+), 39 amu (C_3H_3^+), and 41 amu (C_3H_5^+) collected following exposure of DISO NHC to Cu(111) held at 300 K, $\beta = 2.1 \text{ K s}^{-1}$. **b)** HREEL spectra as a function of temperature. Signals have been smoothed by FFT filtering, or by unweighted sliding-averaging. The spectrum of the film heated to 685 K has been multiplied by 10. The simulated normal vibrational modes of a model DISO NHC–Cu–Cl complex used in the assignment are also displayed (DFT). $E_0 = 5.0 \text{ eV}$, FWHM = 33.5 cm^{-1} .

Table 7 ■ DISO NHC/Cu(111) HREELS vibrational modes assignment. ν : stretch, β : bending, δ : scissoring, ρ : rocking, ω : wagging, τ : twisting, R: ring vibration, sym.: symmetric, asym.: asymmetric, def.: deformation, breath.: breathing, ip: in plane, op: out of plane.

Energy loss [cm^{-1}]	Assignment
3095	$\nu(\text{C-H})_{\text{R}}$
2980	$\nu(\text{C-H})_{\text{alkyl}}$
1620	$\text{R}_{\text{def.}}$
1480	$\nu(\text{C}=\text{C})$, $\nu(\text{C}-\text{N})$, $\delta(\text{CH}_2)$, $\beta(\text{C}-\text{H})$, $\beta(\text{CH}_3)_{\text{asym.}}$
1365	$\nu(\text{C}=\text{C})$, $\nu(\text{C}-\text{N})$, $\tau(\text{CH}_2)$, $\omega(\text{CH}_2)$, $\beta(\text{CH}_3)_{\text{sym.}}$
1165	$\text{R } \beta(\text{C}-\text{H})_{\text{i.p}}$
960	$\beta(\text{C}-(\text{CH}_3)_2)$
755	$\text{R } \beta(\text{C}-\text{H})_{\text{o.p}}$
580	$\text{R}_{\text{stretch}}$
430	$\nu(\text{C}-\text{Cu})$

The DISO NHC monolayer was further probed by HREEL spectroscopy in the specular geometry (Figure 3.9.b). In this regime, only vibrational modes whose dynamic dipole moments have a component along the surface normal are detected. Table 7 summarises the assignment of the energy losses by comparison to normal modes of a model DISO NHC–Cu–Cl complex in the gas phase. Geometry optimisation and simulated IR spectra were carried

out at the M06/SDD level of theory using Gaussian09.⁸⁵ The HREEL spectra displayed characteristic energy losses due to alkyl and aryl C–H stretches, as well as modes in the 1240–1600 cm⁻¹ region due to $\nu(\text{C–N})$ and $\nu(\text{C=C})$ stretching, and C–H bending modes. An energy loss at 430 cm⁻¹ was detected that was assigned to a $\nu(\text{C–Cu})$. In short, these vibrational modes are consistent with the structure of adsorbed DISO NHC. The relative intensity of these modes is essentially the same as observed for the adsorption of DISO NHC on Au(111). Thus, it was deduced that the molecular plane of DISO NHC lies predominantly perpendicular to the surface plane of Cu(111), in agreement with the predicted geometry by DFT simulations (Figure 3.10). The spectra of the sample heated to higher temperatures were largely unaltered up to 565 K, which signifies that the monolayer and integrity of DISO NHC remained intact. Above this temperature, all spectral features were lost to yield a virtually featureless spectrum. The thermal behaviour of the monolayer is remarkably similar to that on Au(111), hence a clean reversible desorption of the DISO NHC monolayer from Cu(111) is also proposed.



Figure 3.10 ■ DFT optimised geometry of DISO NHC adsorption on Cu(111). DISO NHC adsorbs on Cu atop sites with its molecular plane oriented perpendicularly relative to the (111) plane. Calculations were carried out by the Mosey Group.

The morphology of the DISO NHC monolayer was analysed by LEED, which only produced a $p(1 \times 1)$ hexagonal pattern due to the underlying substrate at saturation and submonolayer coverage, and across a range of temperatures. STM topographs of the Cu(111) surface saturated with DISO NHC were characterised by the presence of vacancies approximately 2.1 Å deep, which corresponds to one atomic step. This implies that DISO NHC can extract Cu adatoms from Cu(111) surface. Some indication of step edges decorated

by adsorbates was visible (inset, Figure 3.11.a) High molecular resolution was challenging under the examined experimental conditions, possibly because of highly diffusive species analogous to those formed on Au(111). Temperature did not have any tangible effect on the surface morphology; neither did it promote self-assembly. Heating the sample at 625 K yielded images of a mostly clean surface, that is, no evidence of decomposed fragments was found. However, etch-pits located mostly at the step edges remained (Figure 3.11.c).

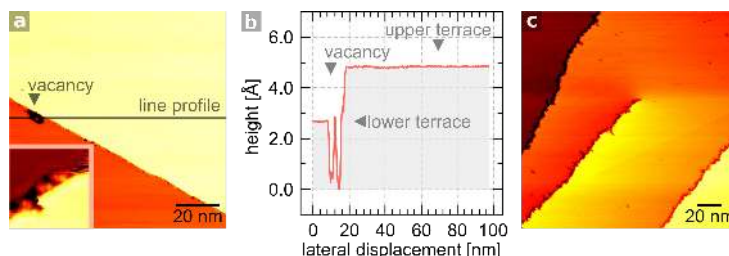


Figure 3.11 ■ DISO NHC induces vacancies on Cu(111). **a)** STM image of DISO NHC deposited onto Cu(111) (2400 L), (inset) close up of step decorated by adsorbates. Image size $7.1 \times 7.1 \text{ nm}^2$ **b)** corresponding line profile of image **a)** **c)** STM image of the sample heated to 625 K. Image **a)** was acquired at $V_t = -0.6 \text{ V}$, $I_t = 300 \text{ pA}$, and **c)** at $V_t = -0.3 \text{ V}$, $I_t = 300 \text{ pA}$.

The effect of functional groups at the *N*, *N*-positions of NHCs on the binding and adsorption onto copper was investigated next. TPD spectra of DM NHC for fragments $m/z = 2 \text{ amu}$ ($\text{H}_2^{\bullet+}$) and 27 amu (HCN^+) are displayed in Figure 3.12.a. HCN desorption peaked at $T_{\text{max}} = 570 \text{ K}$ concurrently with hydrogen evolution, which signifies that these two desorption events are related. Unlike TPD spectra for DISO NHC desorption from Cu(111), the intensity of the peaks did not correlate with exposure, hinting at a more complex mechanism than simply reversible desorption. Hydrogen evolution ($m/z = 2$) occurred in two overlapping peaks located at $T_{\text{max}1} = 532 \text{ K}$ and $T_{\text{max}2} = 590 \text{ K}$, and are assigned to sequential thermally activated dehydrogenation steps.¹¹⁰ A marginal yield of 5.3% was detected for fragment $m/z = 39 \text{ amu}$ (C_3H_3^+) relative to 1.0 ML of DISO NHC, which implies that the ring moiety remains adsorbed on the surface. All in all, it can be concluded from the TPD data that DM NHC adsorption is not reversible and is stable on the Cu(111) surface up to *ca* 475 K, the onset temperature for the first dehydrogenation step. TPD spectra of DET NHC followed very closely that of DM NHC, with desorption traces peaking at $T_{\text{max}} = 570 \text{ K}$. Thus, a similar interpretation is proposed (Figure 3.12.b).

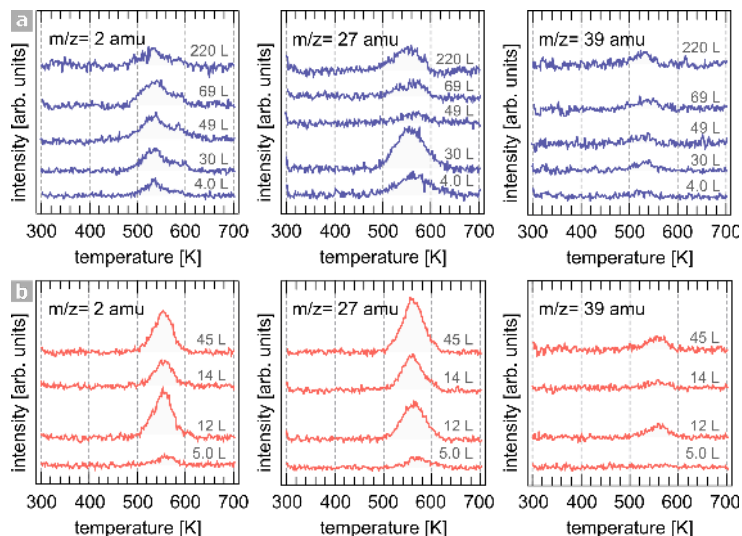


Figure 3.12 ■ TPD spectra of DM and DET NHC monolayers on Cu(111). Desorption of fragments $m/z = 2, 27$ and 39 amu for **a)** DM NHC and **b)** DET NHC deposited on Cu(111), $\beta = 2.1 \text{ K s}^{-1}$

Qualitatively identical HREEL spectra were obtained following adsorption of DM NHC and DET NHC on Cu(111) (Figure 3.13.a,b). In every case, the spectrum was dominated by a very strong energy loss at *ca* 730 cm^{-1} for DM and DET NHC, assigned to the out-of-plane bending mode of aromatic C–H bonds. A medium intensity energy loss due to a ring out-of-plane deformation was also detected at 410 cm^{-1} for DM NHC, and at 395 cm^{-1} for DET NHC. The dipole moments of these two active vibrational modes are normal to the molecular plane. Weak energy losses at 2940 cm^{-1} and 3075 cm^{-1} are assigned to the alkyl and aromatic ring C–H stretches, respectively. Similarly, the $1250\text{--}1600 \text{ cm}^{-1}$ region associated with the convolution of C–N and C=C stretches, and C–H bending modes appeared very weak. Collectively, the relative intensities of the energy losses are a strong indication that the molecular planes of DM and DET NHCs align approximately parallel to the surface plane. Astoundingly, this is exactly the same scenario observed for the adsorption of these NHCs on Au(111), which confirms that the functional groups play a pivotal role in orchestrating the adsorption geometry. It must be noted that, in all cases, HREEL spectra of DM, DET, and DISO NHC monolayers were devoid of any peaks associated with bicarbonate or any form of its derivatives.¹¹¹ Thus, the prepared NHC layers are free from any adventitious coadsorption of the

counterion. This is consistent with the mechanism described in reference [70], whereby a free NHC is generated cleanly, with only water and CO₂ produced as by-products.

The thermal stability of the film was also assessed by HREELS. The spectra of samples heated at progressively higher temperature were collected at 300 K. The intense aromatic $\beta(\text{C}-\text{H})_{\text{o.p}}$ mode remained visible up to 560 K for both DM and DET NHC, and diminished in intensity at higher temperatures. This observation is in agreement with the film retaining its integrity up to this temperature and conforms with the conclusion derived from TPD spectra. Interestingly, two new energy losses at 290 cm⁻¹ and 165 cm⁻¹ were detected for the DM NHC film after heating to 407 K. These new vibrational modes lie in a spectral region often associated with adsorbate–metal vibrations and are perhaps an indication of new species. The evolution of the HREEL spectra as a function of coverage was also examined. The spectra of DET NHC showed increasingly more defined peaks at 395 cm⁻¹ and 735 cm⁻¹ which saturated for exposures ≥ 130 L, as expected for a gradual increase in surface coverage (Figure 3.13.c). Interestingly, upon prolonged exposures of DM NHC to Cu(111), significant enhancement of the weaker energy losses was observed, which implied an increasing amount of *upright* species at higher surface coverage (Figure 3.13.d). However, the energy loss at 730 cm⁻¹ was not suppressed; therefore, it is inferred that the spectrum does not represent a change in the orientation as a function of coverage but, must instead reflect the coexistence of *upright* and *flat-lying* species. The coexistence of two different adsorption geometries is not uncommon, and a very similar interpretation has been proposed for the coverage dependence of benzoic acid on Cu(110).¹¹²

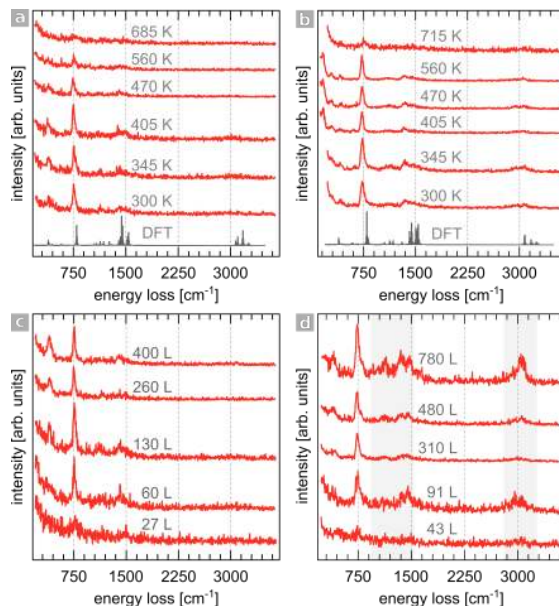


Figure 3.13 ■ HREEL spectra of DM and DET NHC films on Cu(111). **a)** DET NHC film (130 L) deposited at 300 K and heated to indicated temperature. **b)** DM NHC film (120 L) deposited at 300 K and heated to indicated temperature. In each case, the simulated normal vibrational modes of a model NHC–Cu–Cl (NHC: DM or DET) complex at the M06/SDD level of theory are also displayed (DFT). HREELS as a function of increasing exposure of **c)** DET NHC and **d)** DM NHC. Highlighted in grey are the enhancement of modes. $E_0 = 5.0$ eV, FWHM = 28.6 cm^{-1} .

Table 8 ■ DM NHC and DET NHC adsorption on Cu(111) HREELS vibrational modes assignment. ν : stretch, β : bending, δ : scissoring, ρ : rocking, ω : wagging, τ : twisting, γ : torsion, R: ring vibration, sym.: symmetric, asym.: asymmetric, def.: deformation, breath.: breathing, ip: in plane, op: out of plane.

Energy loss [cm^{-1}]		Assignment
DM NHC	DET NHC	
3075		$\nu(\text{C}-\text{H})_{\text{ring}}$
2940	3000	$\nu(\text{C}-\text{H})_{\text{alkyl}}$
1460	1500	$\nu(\text{C}=\text{C})$, $\nu(\text{C}-\text{N})$, $\delta(\text{CH}_2)$, $\beta(\text{CH}_3)_{\text{asym.}}$
1350	1410	$\nu(\text{C}=\text{C})$, $\nu(\text{C}-\text{N})$, $\tau(\text{CH}_2)$, $\omega(\text{CH}_2)$, $\beta(\text{CH}_3)_{\text{sym.}}$
1130	1160	R $\beta(\text{C}-\text{H}_{\text{i.p.}})$
1030		R _{breath.}
730	735	R $\beta(\text{C}-\text{H})_{\text{o.p.}}$
610		R _{stretch}
410	395	R _{def.}
290		molecule–surface vibration?
165		molecule–surface vibration?

Similarly to the case of DISO NHC, molecular resolution was not attained

during STM imaging under the reported experimental conditions. However, the presence of adsorbates was inferred indirectly from the effect their adsorption had on the substrate. Upon sublimation of DET NHC on the substrate, the copper surface topography displayed etch-pits one atomic step deep, which further supports the lifting of Cu adatom from the (111) plane (Figure 3.14.a,b). Heating had no appreciable effect for most samples up to 580 K. At this temperature, oligomeric features formed, which covered approximately 10 % of the surface area (Figure 3.14.c). These species are attributed to the dehydrogenative decomposition products of DET NHC, consistent with the TPD and HREEL findings. By comparison, this observation is opposite to the case of DISO NHC monolayers, which did not leave residues on the surface after heating to high temperatures. This difference emphasises how distinct binding geometries impact on the decomposition mechanism of NHC monolayers.

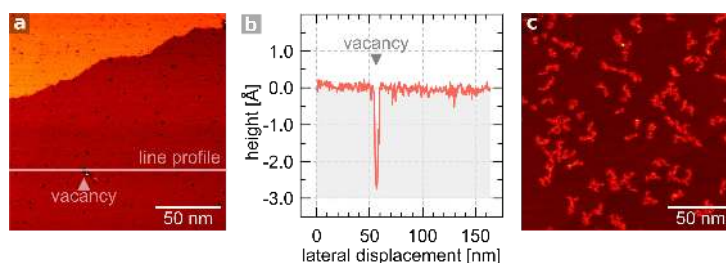


Figure 3.14 ■ DET NHC induces vacancies on Cu(111). a) STM image of DET NHC deposited onto Cu(111) (540 L). b) corresponding line profile of image a) c) STM image of the sample heated to 580 K. Image a) was acquired at $V_t = -0.6$ V, $I_t = 300$ pA, and c) at $V_t = -0.5$ V, $I_t = 200$ pA.

Monolayers prepared from DM NHC analysed by STM revealed extensive etch-pitting. The surface topography was characterised by trenches of a depth equivalent to a single Cu atom (2.13 ± 0.22 Å) (Figure 3.15.a). These trenches emanated from nodal points such as surface steps, screw dislocations, etch pits and other trenches. Half of the sampled trenches were 12.89 nm or shorter in length (Figure 3.15.b). The average width of the trenches was 2.08 ± 0.66 nm, however, at nodal points such as pits, the width can reach several nanometers. The etching appeared to propagate mostly, but not limited to, along the $\langle 11\bar{2} \rangle$ and $\langle 1\bar{1}0 \rangle$ surface directions and rotations thereof. Evidence of a very dynamic monolayer was gathered from the consecutive scanning of the same area. Self-healing of the vacancies over the timescale of the imaging (in the order of 14 min per frame) was captured (Figures 3.15.c,d). On closer inspection, elliptical features hosted in the trenches were resolved (Figure

3.15.e). The main molecular axis length was $3.4 \pm 0.7 \text{ \AA}$, and the intermolecular stacking distance $3.8 \pm 0.6 \text{ \AA}$. These distances are consistent with individual DM NHC molecules oriented perpendicular to the surface (*upright* species) stacked via intermolecular $\pi - \pi$ interactions.¹¹³ The trenches density, and therefore the coverage of *upright* species, could be increased by extending the exposure, which correlates with the behaviour observed in HREEL spectra.

Coexisting islands of ordered arrays were assigned to a SAM of *flat-lying* molecules, which constitutes the predominant phase seen in HREELS at lower exposures (Figure 3.15.f). The unit cell dimensions of the SAM can be described by the vectors $\vec{a} = 0.85 \text{ nm}$ and $\vec{b} = 1.89 \text{ nm}$, with an included angle of $\angle(\vec{a}, \vec{b}) = 66.8^\circ$. The closest fit of the measured dimensions to a commensurate cell is a (1 -3|9 4) superstructure occupying 31 copper atoms ($\vec{a}_{comm.} = 0.919 \text{ nm}$, $\vec{b}_{comm.} = 1.991 \text{ nm}$, $\angle(\vec{a}, \vec{b})_{comm.} = 72.43^\circ$).[‡] Each unit cell contains a molecular feature $0.91 \pm 0.09 \text{ nm}$ in length with two distinct lobes. Due to their high diffusivity, the island shape fluctuated in shape within the imaging timescale at 300 K. These species are tentatively ascribed to the enetetramine form of DM NHC adsorbed on the Cu(111) surface resulting from the Wanzlick equilibration between free DM NHC and its dimer.¹¹⁴ Enetetramines were previously postulated by Weidner *et al.*⁷⁴ as potential precursors to NHC-functionalised surfaces, but have never previously been imaged on a surface.

[‡]comm.: commensurate

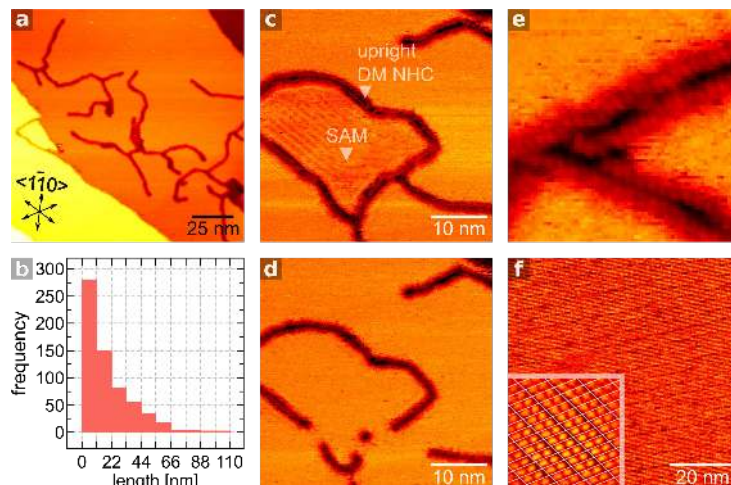


Figure 3.15 ■ DM NHC induces monoatomic deep trenches on Cu(111). **a)** Trenches on the Cu(111) following exposure to DM NHC (280 L) at 300 K, $V_t = -0.6$ V, $I_t = 300$ pA **b)** Length histogram of trenches. $n_{\text{trenches}} = 627$, $\bar{x} = 18.6$ nm, $s = 17.5$ nm, $Md = 12.89$ nm, $min. = 0.17$ nm, $max. = 106.4$ nm, $n_{\text{junctions}} = 592$. **c)** STM image of SAM enclosed within trenches and *upright* species decorating the edges, $V_t = -0.3$ V, $I_t = 600$ pA. **d)** Same area as in image c) showing self-healing of vacancies and disappearance of SAM, $V_t = -0.3$ V, $I_t = 600$ pA **e)** Close up of *upright* DM NHC adsorbed at the edges of trenches, $V_t = -0.2$ V, $I_t = 400$ pA. Image size 7.6×7.6 nm². **f)** SAM of *flat-lying* species assigned to enetetramine form of DM NHC, $V_t = -0.4$ V, $I_t = 300$ pA (inset) FFT filtered STM image of enetetramine SAM (0.065 ML) after exposure of DM NHC (2300 L) onto Cu(111) with $(1 \ -3|9 \ 4)$ unit cell marked by overlaid grid, $V_t = -0.6$ V, $I_t = 300$ pA. Image size 9.9×9.9 nm².

Heating the sample to 365 K resulted in the formation of a new ordered molecular arrangement and disappearance of *upright* species. Reflectional and rotational domains were identified, and Moiré fringes were observed with a period of $\bar{a}_{\text{Moiré}} = 13.0$ Å, and a corrugation of approximately 25 pm at $V_t = -0.6$ V, $I_t = 300$ pA (Figure 3.16.a). Additionally, *in situ* defect correction and growth of a predominant domain were visible, likely directed by the crystallographic direction of steps at which the SAM nucleates. The unit cell vectors of the newly formed SAM are $\bar{a} = 1.55$ nm and $\bar{b} = 2.43$ nm, and the angle between the vectors is $\angle(\bar{a}, \bar{b}) = 77.6^\circ$. These dimensions conform with a commensurate $(7 \ 4|1 \ 10)$ superstructure ($\bar{a}_{\text{comm.}} = 1.555$ nm, $\bar{b}_{\text{comm.}} = 2.438$ nm, $\angle(\bar{a}, \bar{b}) = 80.08^\circ$) which occupies an area of 66 Cu atoms (Figure 3.16.b). The dimensions of the main feature comprising the unit cell ($l = 1.68 \pm 0.05$ nm, $w = 1.11 \pm 0.05$ nm) are too large to be attributed to a single DM NHC molecule, or to its enetetramine dimer as in the case of the $(1 \ -3|9 \ 4)$ structure generated at 300 K. Defects in the SAM indicated that these features were further composed of two distinct subunits, which we postulate correspond to pairs of $(\text{NHC})_2\text{Cu}$ complexes

(Figure 3.16.c). The assignment is justified on the bases that the incorporation of copper atoms to form the $\text{Cu}(\text{NHC})_2$ complexes produces physically larger molecular entities, and a lower local DM NHC coverage (0.061 ML) than in the case for the enetetramines (0.065 ML). Furthermore, the appearance of this new structure coincides with the emergence of two new peaks in the HREEL spectra at 290 cm^{-1} and 165 cm^{-1} at this temperature, and may related to the formation of these new species. Although characterisation of the oxidation state of these species was not covered in this study, a vast number of mono-NHC and cationic bis-NHC complexes have been isolated and characterised with Cu in the +1 oxidation state, and in one instance with Cu in the zerovalent state.^{107,115} These species were also detected by mass spectrometry for NHC-treated Cu foils.¹¹⁶ Additionally, soon after the publication of these results, Jiang *et al.*¹¹⁷ independently reached the same conclusion from their combined XPS, STM and DFT studies on 1,3-dimethyl-1H-imidazol-3-ium-2-ide adsorption onto Au(111), Ag(111), and Cu(111) surfaces. The second type of feature resolved in the unit cell were two smaller protrusions intercalated between the main one, which were assigned to copper adatoms. Extraction of copper atoms from step edges is a thermally activated process, and their incorporation into molecular assemblies is ubiquitous in the literature.^{112,118,119} Unlike the SAM obtained at 300 K, this molecular array could be easily imaged over extended periods of time and tunnelling conditions. Remarkably, their appearance was greatly affected by the tunnelling bias as illustrated in Figure 3.16.d-f, which is often symptomatic of probing molecular orbitals of different occupancy and energy level (*e.g.*, HOMO, HOMO^{-1} , LUMO, and LUMO^{+1}). The images acquired at positive sample biases will resemble unoccupied molecular states (*i.e.*, electron tunnelling from filled tip states into LUMO^{+n}), whereas the opposite will be true for images acquired at negative biases (*i.e.*, electron tunnelling from HOMO^{-n} into unoccupied tip states).¹²⁰ Theoretical simulations of these $(\text{NHC})_2\text{Cu}$ complexes adsorption on Cu(111), and assignment of the probed states is ongoing work. Further heating of the monolayer to 575 K resulted in the appearance of irregular features which covered approximately 20 % of the surface area (Figure S3.3). These were assigned to decomposition products, similar to those obtained for DET NHC monolayers. Figure 3.17 illustrates the postulated surface reaction undergone by DM NHC based on the combined experimental evidence.

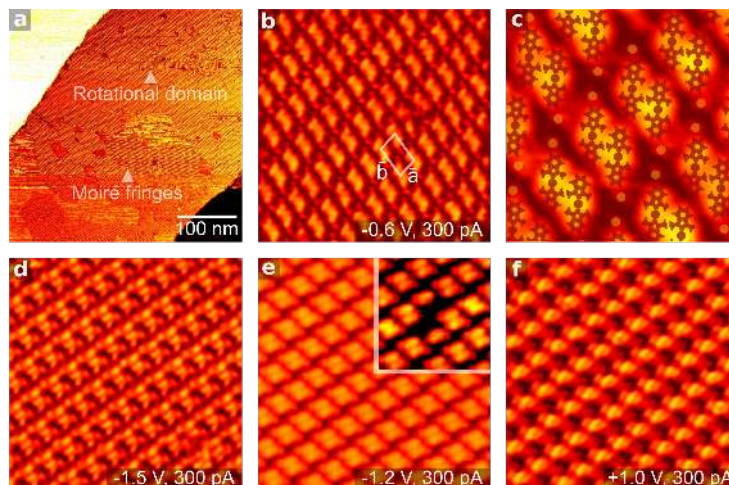


Figure 3.16 ■ SAM of $(\text{NHC})_2\text{Cu}$ on Cu(111) formed after annealing to 365 K. **a)** Large-scale STM image of SAM of $(\text{NHC})_2\text{Cu}$ complexes. Rotational and reflectional domains were imaged as well as Moiré fringes. **b)** High-resolution image of features comprising the SAM with $(7\ 4|1\ 10)$ unit cell marked in white. Image size $18.22 \times 18.22\ \text{nm}^2$. **c)** Proposed model of SAM in **b)** with $(\text{NHC})_2\text{Cu}$ complexes overlaid, and intercalated by Cu adatoms (orange dots). **d-f)** $(7\ 3|-1\ 9)$ reflectional domain of **b)** imaged at different biases and constant current (inset) defects in the $(\text{DMNHC})_2\text{Cu}$ SAM revealed the existence of two dimers per feature. Inset size $8.11 \times 8.11\ \text{nm}^2$.

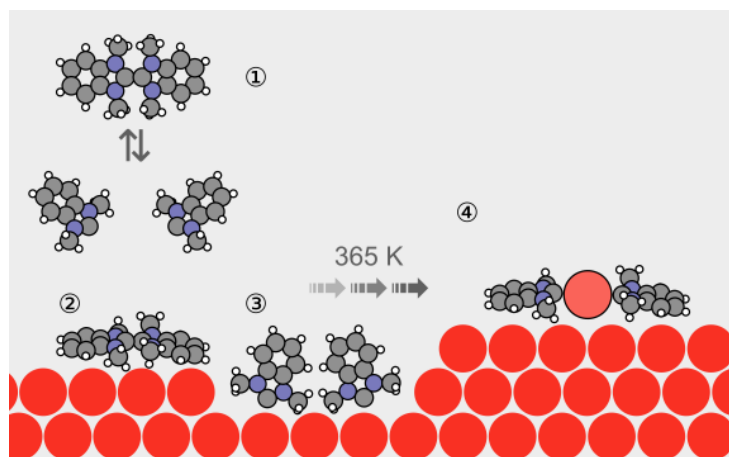


Figure 3.17 ■ Surface chemistry of DM NHC on Cu(111). 1) Wanzlick equilibrium between free DM NHC and its enetetramine form. 2) SAM of *flat-lying* enetetramine $(1\ -3|9\ 4)$ coexists with 3) *upright* DM NHC hosted in trenches. 4) Heating to 365 K generates a new SAM of $(\text{DMNHC})_2\text{Cu}$ complexes $(7\ 4|1\ 10)$.

In conclusion, the formation of NHC monolayers on Cu(111) was demonstrated. In all cases, the films were generated cleanly from bicarbonate NHC precursors without contamination of the surface from the counterion. The drastic effect of functional groups at the *N, N*-position on the binding geometry was also demonstrated. Mainly, sterically demanding isopropyl groups forces the carbene to adopt an *upright* geometry, whereas less bulky methyl and ethyl groups favour a mainly *flat-lying* adsorption. However, the coexistence of an *upright* phase was also detected for DM NHC in STM and confirmed spectroscopically by HREELS. The binding geometry of these NHCs, in turn, dictates the thermal stability of the film. *Flat-lying* DM and DET NHC undergo dehydrogenative decomposition at temperatures above 475 K, leaving organic residues on the surface. By contrast, DISO NHC undergoes a clean reversible first-order kinetics desorption. Interestingly, the NHC films on Cu(111) mimicked very closely that of the NHC films on Au(111), and an almost identical value for the chemisorption energy for DISO NHC was derived. STM imaging of the copper surface topography, following adsorption of NHCs, showed extensive etch pitting in every case. Although some evidence was gathered of step edge decoration for DISO and DET NHC, only did DM NHC yielded molecularly resolved images. A very dynamic and complex monolayer was obtained, with evidence of coexisting single and dimeric DM NHC species, which on heating incorporates copper adatoms and transform into a SAM of (NHC)₂Cu complexes. Although the formation of complexes of the form (DET NHC)₂Cu is presumed given the extensive evidence of copper vacancies formed and the identical spectroscopic footprint, it is intriguing why these species could not be imaged as in the case of DM NHC. A plausible explanation is that a very subtle balance exists between intermolecular interactions and surface diffusion of the adsorbed complex, and the latter is favoured for (DET)₂Cu. The fact that appropriately designed NHCs bind to copper with high bond energies has important practical implications for functional surfaces.

3.4 Summary and Outlook

In this chapter, we initiated a discussion about the main challenges of current SAM technology, which has traditionally relied on the affinity of organo-sulphur compounds to gold substrates. The “*anatomy*” of molecular units that confers modified surfaces their overall physicochemical properties was described. The origin of SAM stability was recognised to be intrinsically linked to the nature of the *ligand*, in other words, the type of bonding that anchors the molecular unit to the surface is a crucial contributor to durable films. A synopsis was provided of emerging approaches that exploit alternative anchorage for the fabrication of robust monolayers, with emphasis on NHCs as extraordinary ligands. The foremost goal of the study presented in this chapter was to determine whether NHC films could be generated *in vacuo* on gold and copper surfaces and to assess the effect of substituents at the *N*, *N*-position in the binding, orientation, and assembly of the layer. This study has shown that thermolysis of bicarbonate precursors is an efficient method to cleanly generate NHC films on Au(111) and Cu(111). One of the most significant findings to emerge from this study is the critical effect of substituents on the monolayer irrespective of the chosen surface. These results have far-reaching implications in the rational design of planar interfaces for specific applications, where robustness and the relative orientation of the molecular unit are important considerations. To that end, the application of NHC-based monolayers on gold surfaces in biosensing devices has been reported, and their superior performance benchmarked against current technology demonstrated.^{121,122} Films generated from NHC precursors offer several advantages over other types of covalently bonded monolayers. For example, silane chemistry suffers from self-polymerisation issues,¹²³ and diazonium salt-derived films are prone to uncontrollable polymerisation that lead to multilayer formation.⁴⁰ Besides, because of the flexibility of NHC synthesis, it is easy to envisage future research on interfaces bearing chiral NHCs, abnormal NHCs, and novel NHC-based metal organic and covalent frameworks.^{124,125}

The results obtained on Cu(111) deserve special mention, as this is the first study reporting on solid copper surfaces modified by NHCs. A complex and dynamic layer was obtained upon adsorption of NHCs on Cu(111), in

particular for the DM NHC, where the coexistence of different species was evident. Films of NHC ligands may serve as a protective layer for copper-based devices, such as those employed in circuitry. Moreover, the etching properties of metallic copper by NHCs may be utilised in patterning processes and in ultra-cleaning of semiconductors in electronic devices.^{126,127} We trust these findings will encourage further research into NHC films on planar copper substrates and nanoparticles.

Finally, some important limitations of this study need to be considered, which would constitute a case for future work on these systems. Firstly, although the formation of an NHC monolayer on Cu(111) was apparent, the assignment of the adsorbed species detected remains tentative. Note that the interpretation was carried out based on apparent dimensions measured by STM, and by extrapolation of well-established NHC chemistry. This study would benefit from a thorough theoretical input to support the proposed models. Secondly, the oxidation state of copper adatoms in the proposed (NHC)₂Cu complex remains elusive. Further characterisation using X-ray photoelectron spectroscopy (XPS) can provide insight into this question. Thirdly, it must be noted that, in all cases, the orientations of NHCs were deduced from the relative intensity of signature vibrational modes in HREEL spectra, and indirectly from the thermal desorption behaviour of the monolayers. Based on this, the orientation with respect to the surface plane has been discussed in terms of *up-right* or *flat-lying* adsorption throughout the text. Obviously, this classification is very imprecise and ambiguous, as it can allude to any range of angles. More adequate techniques are necessary to obtain this information experimentally, such as angle-resolved near-edge X-ray absorption spectroscopy (NEXAFS). This technique can reveal the precise orientation of molecules adsorbed on surfaces with high accuracy.¹²⁸

In summary, NHCs are very interesting species whose applications have transcended pure organometallic chemistry. Despite ample evidence of their role in the stabilisation of nanoparticles, their interaction with planar solid surface has just only started to emerge. This study will serve as a base for future investigation of other NHC SAMs, and their applications.

3.5 References

- [1] L. Yan, C. Marzolin, A. Terfort, G. M. Whitesides, *Langmuir* **1997**, *13*, 6704–6712.
- [2] C. D. Hodneland, M. Mrksich, *Langmuir* **1997**, *13*, 6001–6003.
- [3] J. P. Collman, N. K. Devaraj, C. E. Chidsey, *Langmuir* **2004**, *20*, 1051–1053.
- [4] H. Häkkinen, *Nat. Chem.* **2012**, *4*, 443–455.
- [5] J. C. Love, L. A. Estroff, J. K. Kriebel, R. G. Nuzzo, G. M. Whitesides, *Chem. Rev.* **2005**, *105*, 1103–1170.
- [6] P. Maksymovych, D. C. Sorescu, J. T. Yates Jr, *Phys. Rev. Lett.* **2006**, *97*, 146103.
- [7] P. Maksymovych, J. T. Yates Jr, *J. Am. Chem. Soc.* **2008**, *130*, 7518–7519.
- [8] O. Voznyy, J. J. Dubowski, J. T. Yates Jr, P. Maksymovych, *J. Am. Chem. Soc.* **2009**, *131*, 12989–12993.
- [9] O. Voznyy, J. J. Dubowski, *Langmuir* **2009**, *25*, 7353–7358.
- [10] I. Langmuir, *Trans. Faraday Soc.* **1920**, *15*, 62–74.
- [11] L. Blackman, M. Dewar, H. Hampson, *J. Chem. Technol. Biotechnol.* **1957**, *7*, 160–171.
- [12] R. G. Nuzzo, D. L. Allara, *J. Am. Chem. Soc.* **1983**, *105*, 4481–4483.
- [13] S. T. Marshall, M. O'brien, B. Oetter, A. Corpuz, R. M. Richards, D. K. Schwartz, J. W. Medlin, *Nat. Mater.* **2010**, *9*, 853.
- [14] D. Mandler, I. Turyan, *Electroanalysis* **1996**, *8*, 207–213.
- [15] M. Mrksich, G. M. Whitesides, *Annu. Rev. Biophys. Biomol. Struct.* **1996**, *25*, 55–78.
- [16] T. Wink, S. Van Zuilen, A. Bult, W. Van Bennekom, *Analyst* **1997**, *122*, 43R–50R.

- [17] J. Scherer, M. Vogt, O. Magnussen, R. Behm, *Langmuir* **1997**, *13*, 7045–7051.
- [18] G. K. Jennings, J. C. Munro, T.-H. Yong, P. E. Laibinis, *Langmuir* **1998**, *14*, 6130–6139.
- [19] G. E. Poirier, E. D. Pylant, *Science* **1996**, *272*, 1145–1148.
- [20] F. Schreiber, *Prog. Surf. Sci.* **2000**, *65*, 151–257.
- [21] Z. Liu, A. A. Yasseri, J. S. Lindsey, D. F. Bocian, *Science* **2003**, *302*, 1543–1545.
- [22] C. Vericat, M. Vela, G. Benitez, P. Carro, R. Salvarezza, *Chem. Soc. Rev.* **2010**, *39*, 1805–1834.
- [23] Y. Li, J. Huang, R. T. McIver Jr, J. C. Hemminger, *J. Am. Chem. Soc.* **1992**, *114*, 2428–2432.
- [24] M. J. Tarlov, J. G. Newman, *Langmuir* **1992**, *8*, 1398–1405.
- [25] M. H. Schoenfish, J. E. Pemberton, *J. Am. Chem. Soc.* **1998**, *120*, 4502–4513.
- [26] G. Yang, N. A. Amro, Z. B. Starkewolfe, G.-y. Liu, *Langmuir* **2004**, *20*, 3995–4003.
- [27] M. Cerruti, S. Fissolo, C. Carraro, C. Ricciardi, A. Majumdar, R. Maboudian, *Langmuir* **2008**, *24*, 10646–10653.
- [28] E. a. a. Delamarche, B. Michel, H. Kang, C. Gerber, *Langmuir* **1994**, *10*, 4103–4108.
- [29] N. Prathima, M. Harini, N. Rai, R. Chandrashekara, K. Ayappa, S. Sampath, S. Biswas, *Langmuir* **2005**, *21*, 2364–2374.
- [30] G. Mani, D. M. Johnson, D. Marton, V. L. Dougherty, M. D. Feldman, D. Patel, A. A. Ayon, C. M. Agrawal, *Langmuir* **2008**, *24*, 6774–6784.
- [31] A. Chandekar, S. K. Sengupta, J. E. Whitten, *Appl. Surf. Sci.* **2010**, *256*, 2742–2749.
- [32] L. Srisombat, A. C. Jamison, T. R. Lee, *Colloids Surf. A* **2011**, *390*, 1–19.
- [33] J. C. Love, D. B. Wolfe, R. Haasch, M. L. Chabinyc, K. E. Paul, G. M. Whitesides, R. G. Nuzzo, *J. Am. Chem. Soc.* **2003**, *125*, 2597–2609.

- [34] A. Kudelski, *J. Raman Spectrosc.* **2003**, *34*, 853–862.
- [35] S. R. Cohen, R. Naaman, J. Sagiv, *J. Phys. Chem.* **1986**, *90*, 3054–3056.
- [36] C. Haensch, S. Hoepfner, U. S. Schubert, *Chem. Soc. Rev.* **2010**, *39*, 2323–2334.
- [37] Y. Santiago-Rodriguez, J. A. Herron, M. C. Curet-Arana, M. Mavrikakis, *Surf. Sci.* **2014**, *627*, 57–69.
- [38] Z.-L. Cheng, R. Skouta, H. Vazquez, J. Widawsky, S. Schneebeli, W. Chen, M. Hybertsen, R. Breslow, L. Venkataraman, *Nat. Nanotechnol.* **2011**, *6*, 353–357.
- [39] S. Mahouche-Chergui, S. Gam-Derouich, C. Mangeney, M. M. Chehimi, *Chem. Soc. Rev.* **2011**, *40*, 4143–4166.
- [40] M. M. Chehimi, *Aryl diazonium salts: new coupling agents and surface science*, John Wiley & Sons, **2012**.
- [41] S. Zhang, K. L. Chandra, C. B. Gorman, *J. Am. Chem. Soc.* **2007**, *129*, 4876–4877.
- [42] M. Ford, R. Hoft, A. McDonagh, *J. Phys. Chem B* **2005**, *109*, 20387–20392.
- [43] Y. Fu, S. Chen, A. Kuzume, A. Rudnev, C. Huang, V. Kaliginedi, M. Baghernejad, W. Hong, T. Wandlowski, S. Decurtins *et al.*, *Nat. Commun.* **2015**, *6*, 6403.
- [44] R. Breslow, *J. Am. Chem. Soc.* **1958**, *80*, 3719–3726.
- [45] H. Wanzlick, *Angew. Chem. Int. Ed.* **1962**, *1*, 75–80.
- [46] H.-W. Wanzlick, H.-J. Schönherr, *Angew. Chem. Int. Ed.* **1968**, *7*, 141–142.
- [47] K. Öfele, *J. Organomet. Chem.* **1968**, *12*, P42–P43.
- [48] A. Igau, H. Grutzmacher, A. Baceiredo, G. Bertrand, *J. Am. Chem. Soc.* **1988**, *110*, 6463–6466.
- [49] A. J. Arduengo, R. L. Harlow, M. Kline, *J. Am. Chem. Soc.* **1991**, *113*, 361–363.

- [50] A. J. Arduengo III, S. F. Gamper, J. C. Calabrese, F. Davidson, *J. Am. Chem. Soc.* **1994**, *116*, 4391–4394.
- [51] D. A. Dixon, A. J. Arduengo III, *J. Phys. Chem.* **1991**, *95*, 4180–4182.
- [52] A. J. Arduengo III, H. Bock, H. Chen, M. Denk, D. A. Dixon, J. C. Green, W. A. Herrmann, N. L. Jones, M. Wagner, R. West, *J. Am. Chem. Soc.* **1994**, *116*, 6641–6649.
- [53] A. J. Arduengo III, D. A. Dixon, K. K. Kumashiro, C. Lee, W. P. Power, K. W. Zilm, *J. Am. Chem. Soc.* **1994**, *116*, 6361–6367.
- [54] C. Boehme, G. Frenking, *J. Am. Chem. Soc.* **1996**, *118*, 2039–2046.
- [55] C. Heinemann, T. Müller, Y. Apeloig, H. Schwarz, *J. Am. Chem. Soc.* **1996**, *118*, 2023–2038.
- [56] D. Bourissou, O. Guerret, F. P. Gabbai, G. Bertrand, *Chem. Rev.* **2000**, *100*, 39–92.
- [57] M.-D. Su, S.-Y. Chu, *Chem. Phys. Lett.* **1999**, *308*, 283–288.
- [58] A. Poater, F. Ragone, S. Giudice, C. Costabile, R. Dorta, S. P. Nolan, L. Cavallo, *Organometallics* **2008**, *27*, 2679–2681.
- [59] H. Clavier, S. P. Nolan, *Chem. Commun.* **2010**, *46*, 841–861.
- [60] W. A. Herrmann, M. Elison, J. Fischer, C. Köcher, G. R. Artus, *Angew. Chem. Int. Ed.* **1995**, *34*, 2371–2374.
- [61] G. C. Vougioukalakis, R. H. Grubbs, *Chem. Rev.* **2009**, *110*, 1746–1787.
- [62] G. C. Fortman, S. P. Nolan, *Chem. Soc. Rev.* **2011**, *40*, 5151–5169.
- [63] F. Wang, L.-j. Liu, W. Wang, S. Li, M. Shi, *Coord. Chem. Rev.* **2012**, *256*, 804–853.
- [64] M. S. Sanford, J. A. Love, R. H. Grubbs, *J. Am. Chem. Soc.* **2001**, *123*, 6543–6554.
- [65] H. Jacobsen, A. Correa, A. Poater, C. Costabile, L. Cavallo, *Coord. Chem. Rev.* **2009**, *253*, 687–703.
- [66] S. Díez-González, S. P. Nolan, *Coord. Chem. Rev.* **2007**, *251*, 874–883.

- [67] D. Nemcsok, K. Wichmann, G. Frenking, *Organometallics* **2004**, 23, 3640–3646.
- [68] M. Albrecht, *Angew. Chem. Int. Ed.* **2015**, 54, 5822–5822.
- [69] R. Dorta, E. D. Stevens, N. M. Scott, C. Costabile, L. Cavallo, C. D. Hoff, S. P. Nolan, *J. Am. Chem. Soc.* **2005**, 127, 2485–2495.
- [70] M. Fèvre, J. Pinaud, A. Leteneur, Y. Gnanou, J. Vignolle, D. Taton, K. Miqueu, J.-M. Sotiropoulos, *J. Am. Chem. Soc.* **2012**, 134, 6776–6784.
- [71] M. Fèvre, P. Coupillaud, K. Miqueu, J.-M. Sotiropoulos, J. Vignolle, D. Taton, *J. Org. Chem.* **2012**, 77, 10135–10144.
- [72] B. Liu, Y. Zhang, D. Xu, W. Chen, *Chem. Commun.* **2011**, 47, 2883–2885.
- [73] A. V. Zhukhovitskiy, M. J. MacLeod, J. A. Johnson, *Chem. Rev.* **2015**, 115, 11503–11532.
- [74] T. Weidner, J. E. Baio, A. Mundstock, C. Große, S. Karthäuser, C. Bruhn, U. Siemeling, *Aust. J. Chem.* **2011**, 64, 1177–1179.
- [75] A. V. Zhukhovitskiy, M. G. Mavros, T. Van Voorhis, J. A. Johnson, *J. Am. Chem. Soc.* **2013**, 135, 7418–7421.
- [76] C. M. Crudden, J. H. Horton, I. I. Ebralidze, O. V. Zenkina, A. B. McLean, B. Drevniok, Z. She, H.-B. Kraatz, N. J. Mosey, T. Seki *et al.*, *Nat. Chem.* **2014**, 6, 409.
- [77] F. E. Hahn, L. Wittenbecher, D. Le Van, R. Fröhlich, *Angew. Chem. Int. Ed.* **2000**, 39, 541–544.
- [78] F. E. Hahn, T. v. Fehren, L. Wittenbecher, R. Fröhlich, *Z. Naturforsch. B Chem. Sci.* **2004**, 59, 544–546.
- [79] M. F. Lappert, *J. Organomet. Chem.* **2005**, 690, 5467–5473.
- [80] M. F. Lappert, *J. Organomet. Chem.* **1988**, 358, 185–213.
- [81] D. Cardin, B. Cetinkaya, M. Lappert, *Chem. Rev.* **1972**, 72, 545–574.
- [82] P. Redhead, *Vacuum* **1962**, 12, 203–211.
- [83] B. Adhikari, S. Meng, M. Fyta, *Nanoscale* **2016**, 8, 8966–8975.

- [84] D. J. Lavrich, S. M. Wetterer, S. L. Bernasek, G. Scoles, *J. Phys. Chem. B* **1998**, *102*, 3456–3465.
- [85] M. Frisch, G. Trucks, H. B. Schlegel, G. Scuseria, M. Robb, J. Cheeseman, G. Scalmani, V. Barone, B. Mennucci, G. Petersson *et al.*, *Inc. Wallingford CT* **2009**, *200*, .
- [86] H. K. Kim, A. S. Hyla, P. Winget, H. Li, C. M. Wyss, A. J. Jordan, F. A. Larrain, J. P. Sadighi, C. Fuentes-Hernandez, B. Kippelen *et al.*, *Chem. Mater* **2017**, *29*, 3403–3411.
- [87] L. Guo, L. Ma, Y. Zhang, X. Cheng, Y. Xu, J. Wang, E. Wang, Z. Peng, *Langmuir* **2016**, *32*, 11514–11519.
- [88] R. Ahmad, L. Boubekeur-Lecaque, M. Nguyen, S. Lau-Truong, A. Lamouri, P. Decorse, A. Galtayries, J. Pinson, N. Felidj, C. Mangeney, *J. Phys. Chem. C* **2014**, *118*, 19098–19105.
- [89] H.-T. Liu, X.-G. Xiong, P. D. Dau, Y.-L. Wang, D.-L. Huang, J. Li, L.-S. Wang, *Nat. Commun.* **2013**, *4*, 2201.
- [90] X.-B. Wang, Y.-L. Wang, J. Yang, X.-P. Xing, J. Li, L.-S. Wang, *J. Am. Chem. Soc.* **2009**, *131*, 16368–16370.
- [91] C. A. Murray, S. Bodoff, *J. Chem. Phys* **1986**, *85*, 573–584.
- [92] G. Beltramo, T. Shubina, S. Mitchell, M. Koper, *J. Electroanal. Chem.* **2004**, *563*, 111–120.
- [93] G. Poirier, *Langmuir* **1997**, *13*, 2019–2026.
- [94] H. Zhang, J.-H. Franke, D. Zhong, Y. Li, A. Timmer, O. D. Arado, H. Mönig, H. Wang, L. Chi, Z. Wang *et al.*, *Small* **2014**, *10*, 1361–1368.
- [95] G. Wang, A. Rühling, S. Amirjalayer, M. Knor, J. B. Ernst, C. Richter, H.-J. Gao, A. Timmer, H.-Y. Gao, N. L. Doltsinis *et al.*, *Nat. Chem.* **2017**, *9*, 152–156.
- [96] Q. Tang, D.-e. Jiang, *Chem. Mater.* **2017**, *29*, 6908–6915.
- [97] M. Rodríguez-Castillo, G. Lugo-Preciado, D. Laurencin, F. Tielens, A. Van Der Lee, S. Clément, Y. Guari, J. M. López-de Luzuriaga, M. Monge, F. Remacle *et al.*, *Chem. Eur. J.* **2016**, *22*, 10446–10458.

- [98] J. Crespo, Y. Guari, A. Ibarra, J. Larionova, T. Lasanta, D. Laurencin, J. M. López-de Luzuriaga, M. Monge, M. E. Olmos, S. Richeter, *Dalton Trans.* **2014**, 43, 15713–15718.
- [99] J. Vignolle, T. D. Tilley, *Chem. Commun.* **2009**, 7230–7232.
- [100] B. Cirera, N. Giménez-Agulló, J. Björk, F. Martínez-Peña, A. Martín-Jimenez, J. Rodríguez-Fernandez, A. M. Pizarro, R. Otero, J. M. Gallego, P. Ballester *et al.*, *Nat. Comm.* **2016**, 7, 11002.
- [101] M. Antonijevic, M. Petrovic, *Int. J. Electrochem. Sci* **2008**, 3, 1–28.
- [102] M. B. P. Mihajlović, M. M. Antonijević, *Int. J. Electrochem. Sci* **2015**, 10, 1027–1053.
- [103] P. E. Laibinis, G. M. Whitesides, D. L. Allara, Y. T. Tao, A. N. Parikh, R. G. Nuzzo, *J. Am. Chem. Soc.* **1991**, 113, 7152–7167.
- [104] M. Finšgar, I. Milošev, *Corros. Sci.* **2010**, 52, 2737–2749.
- [105] A. J. Arduengo III, H. R. Dias, J. C. Calabrese, F. Davidson, *Organometallics* **1993**, 12, 3405–3409.
- [106] S. Diez-Gonzalez, S. P. Nolan, *Synlett* **2007**, 2007, 2158–2167.
- [107] J. D. Egbert, C. S. Cazin, S. P. Nolan, *Catal. Sci. Technol.* **2013**, 3, 912–926.
- [108] J. Choi, N. Kang, H. Y. Yang, H. J. Kim, S. U. Son, *Chem. Mater.* **2010**, 22, 3586–3588.
- [109] G. Loepp, S. Vollmer, G. Witte, C. Wöll, *Langmuir* **1999**, 15, 3767–3772.
- [110] M. Röckert, M. Franke, Q. Tariq, D. Lungerich, N. Jux, M. Stark, A. Kaftan, S. Ditze, H. Marbach, M. Laurin *et al.*, *J. Phys. Chem. C* **2014**, 118, 26729–26736.
- [111] Y. Kim, T. S. B. Trung, S. Yang, S. Kim, H. Lee, *ACS Catal.* **2016**, 6, 1037–1044.
- [112] Q. Chen, C. Perry, B. Frederick, P. Murray, S. Haq, N. Richardson, *Surf. Sci.* **2000**, 446, 63–75.
- [113] C. Janiak, *Dalton Trans.* **2000**, 3885–3896.

- [114] V. P. Böhm, W. A. Herrmann, *Angew. Chem. Int. Ed.* **2000**, 39, 4036–4038.
- [115] D. S. Weinberger, N. Amin SK, K. C. Mondal, M. Melaimi, G. Bertrand, A. C. Stuckl, H. W. Roesky, B. Dittrich, S. Demeshko, B. Schwederski *et al.*, *J. Am. Chem. Soc.* **2014**, 136, 6235–6238.
- [116] C. M. Crudden, J. H. a. Horton, s.
- [117] L. Jiang, B. Zhang, G. Médard, A. P. Seitsonen, F. Haag, F. Allegretti, J. Reichert, B. Kuster, J. V. Barth, A. C. Papageorgiou, *Chem. Sci.* **2017**, s.
- [118] C. Perry, S. Haq, B. Frederick, N. Richardson, *Surf. Sci.* **1998**, 409, 512–520.
- [119] L. Dong, Q. Sun, C. Zhang, Z. Li, K. Sheng, H. Kong, Q. Tan, Y. Pan, A. Hu, W. Xu, *Chem. Commun.* **2013**, 49, 1735–1737.
- [120] J. Repp, G. Meyer, S. M. Stojković, A. Gourdon, C. Joachim, *Phys. Rev. Lett.* **2005**, 94, 026803.
- [121] C. M. Crudden, J. H. Horton, M. R. Narouz, Z. Li, C. A. Smith, K. Munro, C. J. Baddeley, C. R. Larrea, B. Drevniok, B. Thanabalasingam *et al.*, *Nat. Commun.* **2016**, 7, 12654.
- [122] Z. Li, K. A. Munro, M. Narouz, B. Hao, C. M. Crudden, J. H. Horton, H. Hao, *ACS Appl. Mater. Interfaces* **2017**, s.
- [123] M. Wang, K. M. Liechti, Q. Wang, J. White, *Langmuir* **2005**, 21, 1848–1857.
- [124] A. J. Boydston, K. A. Williams, C. W. Bielawski, *J. Am. Chem. Soc.* **2005**, 127, 12496–12497.
- [125] M. Matena, T. Riehm, M. Stöhr, T. A. Jung, L. H. Gade, *Angew. Chem.* **2008**, 120, 2448–2451.
- [126] B. Vermeire, L. Lee, H. G. Parks, *IEEE Trans. Semicond. Manuf.* **1998**, 11, 232–238.
- [127] Y. Lin, Y. Chen, K. Chan, F. Pan, I. Hsieh, A. Chin, *J. Electrochem. Soc.* **2001**, 148, F73–F76.
- [128] G. Hähner, *Chem. Soc. Rev.* **2006**, 35, 1244–1255.

3.6 Appendix B

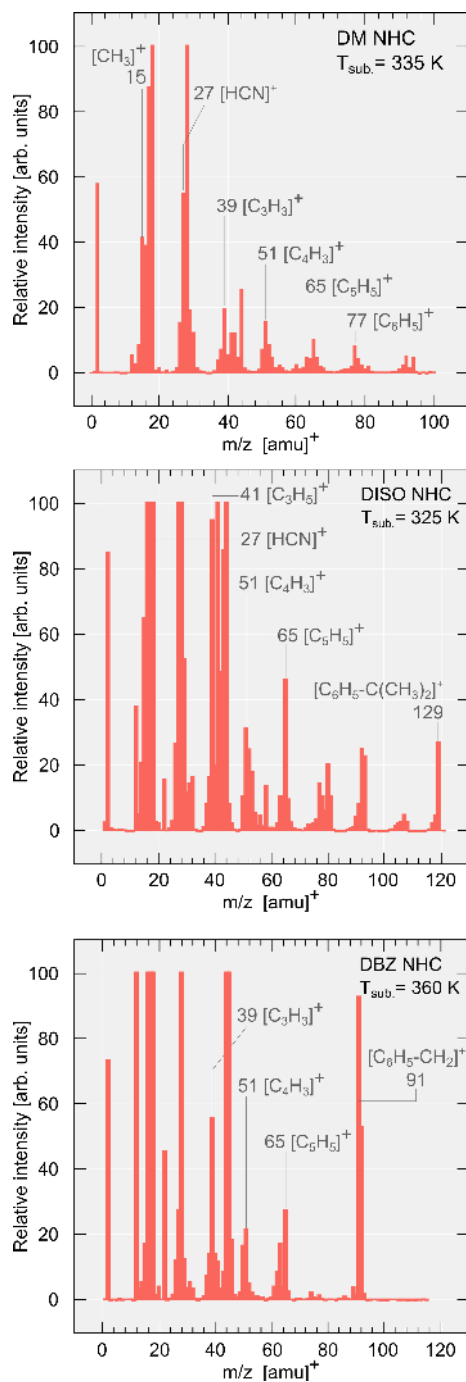


Figure S 3.1 ■ Gas phase mass spectra of DM NHC, DISO NHC, and DBZ NHC. Characteristic fragments of benzene ring and side groups are assigned. $E_{\text{ion.}} = 69.8$ eV.

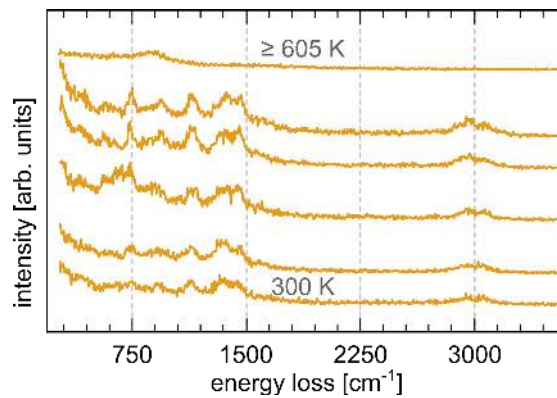


Figure S3.2 ■ HREELS of DISO NHC adsorption onto Au(111)
 Temperature increases from bottom to top. $E_0 = 5.0$ eV, FWHM = 47.3 cm^{-1} .

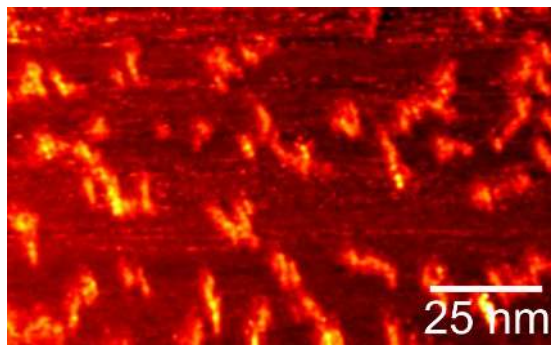


Figure S 3.3 ■ STM image DM NHC monolayer on Cu(111) heated to 575 K. Features are attributed to a degraded monolayer. Image was acquired at $V_t = -0.6$ V, $I_t = 300$ pA.

Chapter 4

NHC interaction with $\text{Cu}_x\text{O}/\text{Cu}(111)$

4.1 Introduction

Having established that NHC monolayers can be easily generated from their bicarbonate adducts under UHV, in this chapter we explore whether these monolayers can serve as a protective coating for copper surfaces. Surface passivation is a common strategy in the prevention of properties of a material being lost due to chemical reactions with the environment it is exposed to. In particular, copper is susceptible to corrosive deterioration in oxidising atmospheres. Corrosion inhibition is a far-reaching field, with implications for infrastructure, cultural heritage preservation, biomedical implants, and electronics. A critical aspect of corrosion inhibition is the design of a physical barrier at the metal surface that inhibits chemical reactions with the environment. In this respect, several studies have sought to understand the mechanism that leads to passivation, and many others have examined candidate molecules for corrosion inhibition.¹⁻⁴ Laibinis and Whitesides⁵ first showed that SAMs of alkanethiols can significantly reduce the rate of copper oxidation and that the extent of inhi-

bition was correlated with the increasing length of the alkane chain linker. The authors hypothesised that a sufficiently dense SAM acts as a low permeability physical barrier that deters O₂ diffusion through the film, preventing reaction with the metal. Notably, the authors also found that alkanethiols are capable of reducing Cu^{II} to Cu⁰; with similar conclusions reached by other researchers in the field.^{6–9} Factors found to influence the degree of corrosion inhibition were explored in later studies, including pretreatment of the copper surface,¹⁰ electrolytes,¹⁰ solvent,¹¹ temperature,¹² and substituents.¹³ Postmodification of the preformed alkanethiol SAM with silanes have also shown to enhance inhibition efficiency.^{14–16} In some cases, the inhibition efficiency of alkanethiols was demonstrated to surpass that of benzotriazole, a widely used corrosion inhibitor.¹⁰ Nevertheless, the protection provided by alkanethiols is in all cases only temporary. The monolayer ultimately undergoes chemical degradation to sulfonates and sulphides, and loses its corrosion inhibiting ability.

As mentioned in the previous chapter, there have been no reports on the uses of NHC films as passivating agents against corrosion of copper. The use of strong ligand-substrate bonds has been acknowledged as a determining factor for long-term corrosion inhibition of metal substrates.¹⁷ To this end, the exceptional stability of NHC films could offer an improved solution to overcome the known disadvantages of alkanethiols-passivated copper substrates. Recent investigations of NHC monolayers on planar gold surfaces and gold nanocrystals have yielded very encouraging results regarding stability against oxidative degradation.^{18,19} However, unlike gold, copper is easily oxidised under ambient conditions at room temperature. Hence, we proceeded to perform exploratory investigations of the interaction of NHC-protected copper surfaces with oxygen in a controlled atmosphere, as well as their interaction with a model copper oxide.

4.2 Cu_xO/Cu(111): A Model Copper Oxide

In this section, a succinct review of oxygen adsorption on Cu(111) and formation of a model copper oxide is presented. The preparation conditions leading to the growth of a thin oxide layer are detailed, and the different oxide

phases identified and characterised by LEED and STM. The overall oxygen surface coverage is also estimated. Last, we postulate a mechanism to explain the coexistence of the different oxide phases detected.

Oxygen dissociatively chemisorbs on Cu(111) at 300 K and above ($E_{chem.} = 460 \text{ kJmol}^{-1}$) with a low activation barrier ($E_a = 8.4\text{--}17 \text{ kJ mol}^{-1}$), and a sticking probability of $ca\ S \simeq 1 \times 10^{-3}$.²⁰ Under low oxygen exposure, single O atoms preferentially occupy fcc sites.²¹ Oxide formation takes place at high oxygen exposure, with the resulting oxide structure being highly dependent on the preparation conditions. Ordered and disordered phases have long been known, with newly found ones reported recently.^{22,23} For instance, exposure of Cu(111) to high oxygen doses at 300 K results in the formation of a disordered surface oxide. Matsumoto *et al.*²⁴ and Wiame *et al.*²¹ showed that the surface oxide extends preferentially along the high symmetry $\langle 1\bar{1}0 \rangle$ direction of Cu(111) and equivalent thereof. The oxide develops by ejection of copper atoms from step edges (step oxide), from the terrace plane (terrace oxide), or by recombination of the extracted copper atoms with diffusing oxygen atoms on the terraces (added oxide).^{24,25} On the other hand, heating at temperatures above 400 K under large oxygen exposure can generate ordered oxide films.²⁴ In order to produce a high coverage, topographically flat, thin oxide layer suitable to study the adsorption of NHCs by STM, we opted for a high-temperature preparation. The preparation conditions employed were adapted from the work by Yang *et al.*, and involved exposing a clean Cu(111) held at 675 K to O_2 ($P_{O_2} \simeq 1.0 \times 10^{-6}$ mbar) for $t = 20$ min, followed by post-annealing at 800 K for $t = 10$ min.²⁶ This preparation led to the formation of a surface oxide which exhibited two distinctive structures as observed by STM. These two structures are shown in Figure 4.1.a, and referred to as *phase I* and *phase II*. HREEL spectroscopy confirmed that only a thin layer was produced following this preparation, as opposed to a bulk oxide (*vide infra*).

Phase I

Jensen *et al.*²⁷ and Matsumoto *et al.*²⁴ independently reported that, under similar experimental conditions used in our preparation, two ordered oxides structures can grow epitaxially on Cu(111), with unit cells: $(4\ 3| -3\ 5)^{\dagger}$ and $(9\ 1|1$

[†] $\bar{a} = 0.9216 \text{ nm}$, $\bar{b} = 1.789 \text{ nm}$, $\angle(\bar{a}, \bar{b}) = 95.68^\circ$, $A = 1.641 \text{ nm}^2$.

5)[‡]. These structures are respectively 29 and 44 times larger than the $p(1 \times 1)$ unit cell of Cu(111); hence commonly referred to as the "29" and "44" reconstructions.²⁷ The atomic structure of these reconstructions resembles closely a truncated (111) surface of bulk Cu₂O, with the undercoordinated copper atoms removed (Figure 4.1.b). The ideal Cu₂O(111) layer is a buckled honeycomb lattice made up of O–Cu–O linear bonds, with a lattice periodicity of $\bar{a} = \bar{b} = 0.60$ nm.²⁸ However, the ordered oxide layer grown on Cu(111) distorts from this ideal structure into the "29" and "44" reconstructions to remain commensurate with the underlying $p(1 \times 1)$ of Cu(111).^{24,27,29,30} These structures can be regarded as single-layer precursors to the formation of bulk cuprous oxide.^{31,32} The substructure of the "44" reconstruction contains 8 distorted hexagons per unit cell, whereas the "29" reconstruction contains only 6 (Figure 4.1.c). The reconstructions exhibit two types of oxygen species: lattice oxygen, which makes up the hexagonal Cu₂O(111)-like structure, and chemisorbed oxygen embedded in the distorted hexagonal cells in the substructure.

Inspection of *phase I* in the STM image revealed that the unit cell of the superstructure can be described by the vectors $\bar{a} = 1.17$ nm and $\bar{b} = 1.77$ nm, at an angle of $\angle(\bar{a}, \bar{b}) = 93.7^\circ$ with respect to each other (Figure 4.1.d,e). These dimensions are in good agreement with a commensurate $(4\ 3|-3\ 5)$; that is, *phase I* corresponds to a "29" reconstruction. Figure 4.1.f shows an overlaid model of the "29" reconstruction onto the STM image. The influence of electronic effect in the contrast mechanism of STM imaging requires special consideration when imaging oxide surfaces. Since oxygen atoms have a low density of states at the Fermi level available for tunnelling, these often appear as depression features. Hence, images of the copper oxide layer are likely dominated by metal states, and the apparent height of the tip does not reflect a direct topographic map of the oxide surface.²⁴ LEED data also supported the formation of this structure, where rotational and reflectional domains were identified (Figure 4.2). The unit cell vectors derived from LEED experiments were $\bar{a} = 0.88$ nm, $\bar{b} = 1.70$ nm, with an included angle of $\angle(\bar{a}, \bar{b}) = 97.3^\circ$. Surprisingly, Yang *et al.* reported that this preparation produces a "44" reconstruction, which remained unaltered after the post-annealing step at 800 K.²⁶ Instead, the obtained "29" structure seems more consistent with the findings by Matsumoto *et al.*, who produced the "29" reconstruction by heating a Cu(111) in oxygen ($P_{O_2} = 5.0 \times 10^{-7}$ mbar)

[‡] $\bar{a} = 1.171$ nm, $\bar{b} = 2.184$ nm, $\angle(\bar{a}, \bar{b}) = 103.3^\circ$, $A = 2.489$ nm².

at 673 K, followed by post-annealing at 723 K; and by heating a preformed "44" structure at 675 K.²⁴ Recently, Therrien *et al.*³³ performed a comprehensive computational and experimental study which revealed the atomically precise structure of this reconstruction (Figure 4.1.c). The authors determined that, besides the lattice oxygen, the structure contains a total of five chemisorbed oxygen atoms embedded in five of the total six distorted hexagonal cells in the substructure. The overall oxygen coverage amounts to 0.586 ML, in fair agreement with the experimental value of 0.52 ± 0.03 ML determined by Jensen *et al.*^{27,34}

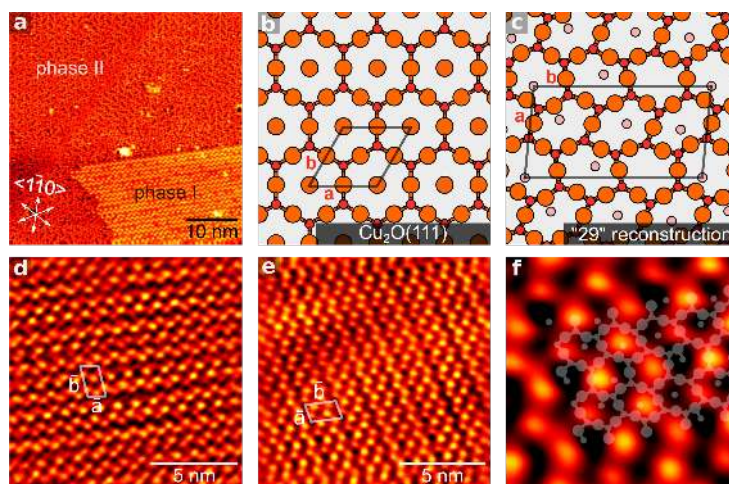


Figure 4.1 ■ Formation of a model copper oxide thin layer. **a)** STM image of a thin oxide layer prepared by exposing a clean Cu(111) held at 675 K to 1300 L of O₂, followed by annealing to 800 K for $t = 10$ min. Two structures were resolved referred to as *phase I* and *phase II* as indicated in the image. **b)** Truncated (111) plane of bulk Cu₂O. Unit cell is marked ($a = b = 0.60$ nm, $\angle(a, b) = 60^\circ$) **c)** Atomic structure of "29" reconstruction with unit cell highlighted. Copper (orange), lattice Oxygen (red), chemisorbed Oxygen (pink). Adapted from reference [33]. STM image of **d)** *phase I* with "29" reconstruction unit cell highlighted (4 3|-3 5), and **e)** (1 -3|-8 -5) reflectional domain. **f)** Overlaid structural model of "29" reconstruction on STM image. Image size 3.50×3.50 nm² Images a) and d) were acquired at $V_t = -1.0$ V, $I_t = 600$ pA, images d) and f) were acquired at $V_t = -1.0$ V, $I_t = 700$ pA.

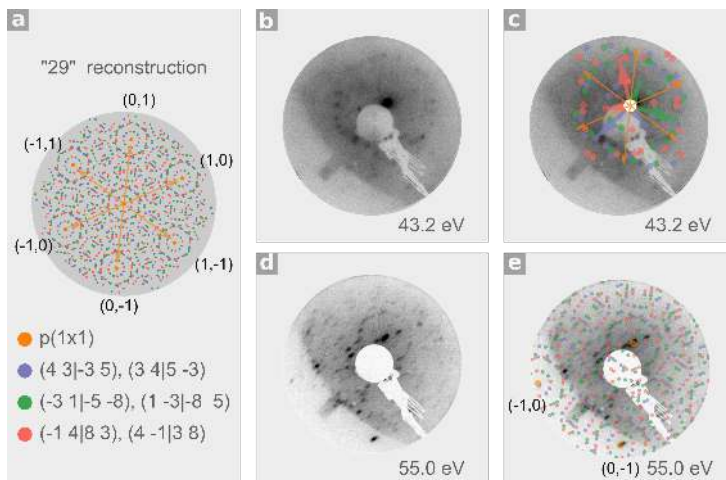


Figure 4.2 ■ LEED of oxidised Cu(111). **a)** Simulated LEED pattern of "29" reconstruction. Rotational and reflectional domains are colour coded. **b)** LEED pattern of copper oxide collected at 43.2 eV **c)** with overlaid simulated LEED pattern. Unit cell vectors for all three rotational domains are shown; orange arrows indicate direction of $p(1 \times 1)$ substrate unit cell vectors. **d)** LEED pattern collected at 55.0 eV with **e)** overlaid simulated pattern.

Phase II

Phase II constitutes the predominant phase observed for the prepared surface oxide. This phase corresponds to the "disordered oxide" as referred to in previous reports in the literature for the initial stages of copper oxidation and in the degradation of the "29" and "44" structures (Figure 4.3.a).^{21,24,27,35} The structure features a hexagonal lattice with a high density of irregular pentagonal and heptagonal topological defects. This is evident from the parameters derived from an MST analysis on the framework, where the values of $m_{5-7} = 0.86$ and $s_{5-7} = 0.11$ hint at the presence of an underlying hexagonal tiling (See Appendix A). The pentagonal and heptagonal defects are found close to one another, often forming "5-7-7-5" units (Figure 4.3.b). Yang *et al.*²² showed that this structure, which they refer to as the "5-7" Cu_2O oxide structure is, in fact, the oxygen-deficient precursor phase of a hexagonal $\text{Cu}_2\text{O}(111)$ -like structure. In turn, the hexagonal $\text{Cu}_2\text{O}(111)$ -like structure precedes the formation of the "44" structure at saturation oxygen coverage.²⁶ The authors also demonstrated that the "5-7-7-5" units originate from the same Stone-Wales mechanism known for the hexagonal lattices of sp^2 -hybridised materials.³⁶⁻³⁸ The conversion mechanism from the hexagonal $\text{Cu}_2\text{O}(111)$ -like into the 5-7 Cu_2O oxide structure, takes

place via an in-plane 90° rotation of a $-\text{O}-\text{Cu}-\text{O}-$ bond, as schematically illustrated in Figure 4.3.c.

The coexistence of the oxygen-rich *phase I* ($\theta_{\text{O}} = 0.586 \text{ ML}$) and oxygen deficient *phase II* ($\theta_{\text{O}} = 0.375 \text{ ML}$), is proposed to arise from the 5–7 Cu_2O structure (*phase I*) emerging at the expense of the "29" reconstruction (*phase II*) removal. This scenario would be possible under oxygen depletion conditions. For example, by oxygen dissolution into the bulk during the post-annealing at 800 K, or due to low oxygen partial pressure during the preparation. We speculate that this occurs in a similar fashion as the reduction of the "44" reconstruction proposed by Yang *et al.* as illustrated in Figure 4.3.d.²⁶ It must be also noted that a third phase was also detected in small domains (inset, Figure 4.3.a). This phase (*phase III*) was observed to develop at the domain boundaries of *phase II*, and its structure consists of hexagons approximately 1.5 nm apart. This phase was identified as the "open honeycomb" structure composed of Cu_3O units described by Matencio *et al.*, and represents an even more oxygen-deficient copper oxide phase ($\theta_{\text{O}} = 0.074 \text{ ML}$).²³ Similarly to our results, Matencio *et al.* showed that this phase is always found to coexist with denser phases, such as the 5–7 Cu_2O oxide structure, and the "44" reconstruction.²³

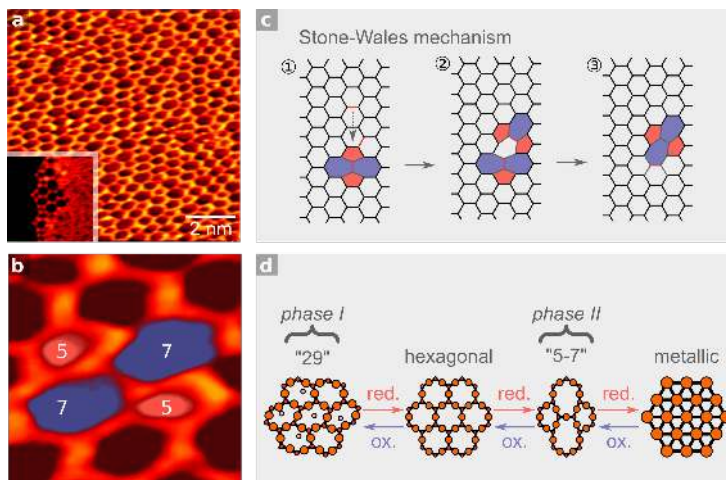


Figure 4.3 ■ Phase II: a defective hexagonal structure. STM image of **a)** *phase II* known as the 5–7" Cu_2O oxide structure, which features a defective hexagonal lattice. MST analysis output: $n = 580$ cells, *normalised* $m = 0.86$, *normalised* $ss = 0.11$, *normalised* $\min. = 0.331$, *normalised* $\max. = 1.24$ (inset) *phase III* growing at the domain boundary of *phase II*. Image size $12.1 \times 12.1 \text{ nm}^2$. **b)** STM close-up of defects highlighting the "5-7-7-5" unit. Image size $1.59 \times 1.59 \text{ nm}^2$ **c)** Schematic representation of the Stone-Wales mechanism. 1) Each segment in the lattice represents a $-\text{O}-\text{Cu}-\text{O}-$ chain. A chain undergoing a 90° rotation is highlighted in red. Pentagonal (pink) and heptagonal (blue) defects formed after rotation of a $-\text{O}-\text{Cu}-\text{O}-$ chain. 2) and 3) illustrate the propagation and rotation of the "5-7-7-5" defect within the lattice. Adapted from reference [22] **d)** Postulated formations of *phase II* from oxygen depletion of *phase I*. Legend: "29": "29" reconstruction, *hexagonal*: crystalline hexagonal Cu_2O -like structure, "5-7": "5–7" Cu_2O oxide, *metallic*: metallic $\text{Cu}(111)$, *red.*: reduction, and *ox.*: oxidation.

4.3 Adsorption of NHCs on Cu_xO/Cu(111)

DBZ NHC

Having confirmed the formation of the copper oxide and its structures, we proceeded to investigate the adsorption of NHCs onto its surface at 300 K. The investigated species were DM NHC and DISO NHC as in the previous chapter, with the new addition of DBZ NHC (Figure 4.4.a). Note that we did not conduct a full characterisation of DBZ NHC adsorption on Cu(111) beyond TPD and LEED experiments. However, desorption of DBZ NHC from Cu(111) bore many similarities with the TPD spectra obtained for DM and DET NHC. Mainly, marginal desorption yields of fragments $m/z = 27$ amu (HCN^+), $m/z = 39$ amu (C_3H_3^+), and $m/z = 65$ amu (C_5H_5^+) were detected irrespective of exposure, with a small peak discernible at $T_{\text{max.}} = 548$ K (Figure 4.4.b-d). This behaviour suggests that DBZ NHC, or its degradation products, remain adsorbed on the surface. Furthermore, a *flat-lying* geometry is presumed on the same basis as discussed for DM and DET NHC adsorption on Cu(111) in Chapter 2. Besides the hexagonal $p(1 \times 1)$ of the Cu(111), no other diffraction pattern was visible in LEED experiments for a range of exposures and temperatures.

Next, the oxide was prepared in a similar manner as detailed above, and the samples were inspected by LEED. The appearance of a diffraction pattern corresponding to the "29" reconstruction (*phase I*) was taken as a confirmation of oxide formation. Note that only *phase I* produces a diffraction pattern since the defective *phase II* is aperiodic. Given that the two phases exhibit different local oxygen coverage, the average oxygen coverage of the prepared samples was estimated as $\theta_{\text{O}} = (0.05 \times 0.586 \text{ ML} + 0.95 \times 0.376 \text{ ML}) = 0.387 \text{ ML}$; where 0.05 and 0.95 represent the percentage of *phase I* and *phase II* derived from a single STM image, respectively. The coverage of *Phase III* is negligible; therefore, it was not taken into account. It has also been assumed that each preparation produces the same phases in the same ratio. This is an important assumption; as the literature on copper oxides demonstrates, this system is particularly sensitive to subtle changes in the preparation conditions.^{21,23,24,26}

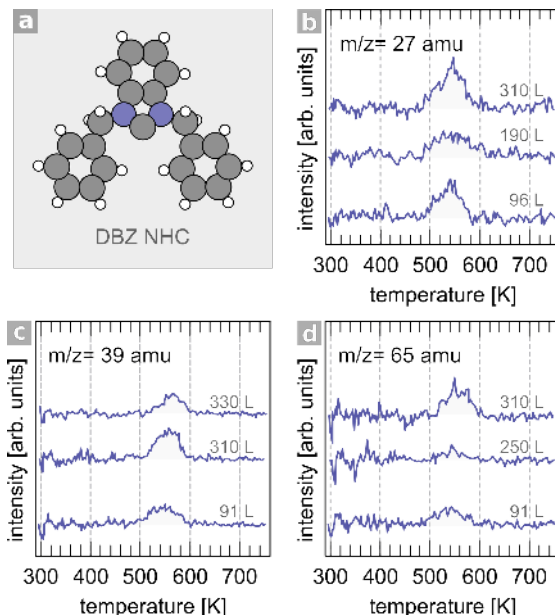


Figure 4.4 ■ TPD spectra of DBZ NHC adsorbed on Cu(111) a) Structural model of 1,3-Dibenzyl-benzimidazol-2-ylidene (DBZ NHC) derived from the thermolysis of 1,3-Dibenzyl-1H-benzo[d]imidazol-3-ium hydrogen carbonate salt precursor. Carbon (grey), Hydrogen (white), and Nitrogen (blue). b-d) TPD spectra of fragments $m/z = 27$ amu (HCN^+), $m/z = 39$ amu (C_3H_3^+), and $m/z = 65$ amu (C_5H_5^+) detected from DBZ NHC films on Cu(111) prepared at the indicated exposure, $\beta = 3.6 \text{ Ks}^{-1}$.

Figure 4.5.a,b shows a LEED pattern of the prepared oxide surface acquired at 38.3 eV before and after exposing the sample to DBZ NHC (150 L). The adsorption of DBZ NHC removed the diffraction pattern of the ordered "29" reconstruction, which is interpreted as the reduction of the oxide layer. This behaviour was observed for a range of investigated exposures up to 230 L, where the pattern was either significantly attenuated or disappeared entirely. After inspection by LEED, the samples were further examined by TPD (Figure 4.5.c). Fragments $m/z = 28$ amu and $m/z = 44$ amu were the predominant desorption products. The desorption trace of fragment $m/z = 44$ amu displayed a small peak centred at $T_{\text{max}1} = 451 \text{ K}$, and a larger one at $T_{\text{max}2} = 620 \pm 20 \text{ K}$, which showed some variability in the maximum desorption rate. This fragment is assigned to CO_2 generated from what can essentially be described as a thermally-activated combustion reaction between DBZ NHC, or its decomposition products, and the oxide layer. Neither CO_2 chemisorption on copper or on copper oxides is stable in the UHV regime; therefore, it is very

unlikely that these peaks arise from adventitious adsorption of background CO₂.^{39,40} The peaks are attributed to the sequential oxygen consumption and reduction of the oxide layer. The lower temperature peak T_{max1} is tentatively assigned to the removal of chemisorbed oxygen from *phase I*, and the higher temperature peak T_{max2} to the removal of lattice oxygen. This is postulated on the basis that chemisorbed oxygen constitutes the lowest local coverage ($\theta_O = 0.172$ ML) compared to lattice oxygen, giving rise to a low-intensity peak in the TPD spectra. Furthermore, Yang *et al.* established from their combined STM and DFT studies that copper oxide reduction by CO starts with the removal of chemisorbed oxygen, followed by upper lattice oxygen, and lower lattice oxygen of the buckled oxide framework; that is, ΔG of reduction follows the sequence $O_{chem.} < O_{upper} < O_{lower}$ (Figure 4.3.d).²⁶

Fragment $m/z = 28$ amu displayed a broad peak centred at $T_{max} = 624$ K, which may correspond to either CO ($m/z = 27.995$ amu), or the isobaric N₂ ($m/z = 28.006$ amu) or C₂H₄ ($m/z = 28.0532$ amu) species, which is indistinguishable by the resolution of the QMS employed in this study. Since the T_{max} of this fragment coincides with T_{max2} in the TPD spectra of CO₂ these two desorption events appear to be related. One possible interpretation is that, as oxygen coverage becomes depleted from the surface by the release of CO₂, the desorption of CO becomes kinetically more favourable over further oxidation to CO₂. This scenario resembles carbon-contaminated Pd(111) treated with O₂, where subsequent TPD produces CO and CO₂ with such peak profiles. An alternative interpretation is that N₂ is generated from the oxidation of surface-bound HCN,^{41–43} a known product formed from the thermal decomposition of NHCs. Neither scenario can be completely ruled out, yet, either case points to an oxidation reaction. A wide range of oxygenates and intermediates are likely to arise for such a complex reaction, which makes a comprehensive assignment based on TPD data alone unfeasible. However, the removal of oxygen is unequivocally associated with DBZ NHC adsorption and its thermally-activated combustion.

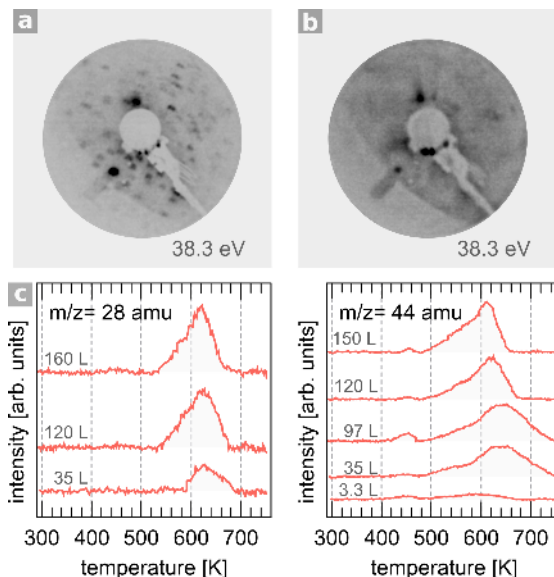


Figure 4.5 ■ Reduction of copper oxide by DBZ NHC. **a)** LEED collected at 38.3 eV of the prepared copper oxide featuring a pattern corresponding to a "29" reconstruction. **b)** LEED pattern collected at the same beam energy after exposing the copper oxide to 150 L of DBZ NHC **c)** TPD spectra of fragments $m/z = 28$ amu, and $m/z = 44$ amu (CO_2^+) acquired after sublimation of DBZ NHC at the indicated exposure onto the oxide, $\beta = 2.5 \text{ K s}^{-1}$.

DISO NHC

A similar set of experiments to those described for DBZ NHC were conducted for DISO NHC. Figure 4.6.a,b depicts the LEED pattern of the prepared oxide collected at 37.1 eV before and after exposure to DISO NHC (13 L). Essentially the same scenario observed for DBZ NHC manifested; the LEED pattern was lifted upon exposure of the oxide to DISO NHC. It is worth commenting that, in all cases, the lifting of the LEED pattern was confirmed to result from NHC adsorption, and not due to electron beam damage of the oxide layer. This was corroborated by examining the oxide layer using beam energies up to $E_0 = 55.7 \text{ eV}$ and extended beam illumination times ($\approx 1 \text{ h}$), after which the "29" reconstruction remained visible.

The TPD spectra were characterised by a high yield of CO_2 ($m/z = 44$ amu) as well as H_2O ($m/z = 18$ amu), another characteristic product of a combustion process (Figure 4.6.c). The reaction-limited desorption of H_2O displayed a

single broad peak at $T_{max} = 519$ K, whereas CO_2 desorption displayed two: a small peak at $T_{max1} = 446$ K and a larger one at $T_{max2} = 532$ K. A third peak emerged at $T_{max3} = 622$ K for DISO NHC exposures ≥ 15 L. These peaks can easily be related to those observed for DBZ NHC: the low-temperature T_{max1} is essentially the same for both molecules, whereas T_{max2} and T_{max3} in DISO NHC closely follow the broad T_{max2} in DBZ NHC. Hence, the same assignment is proposed for these peaks.

Notably, HCN ($m/z = 27$ amu) desorption was detected in a broad peak with a $T_{max} = 526$ K. In some instances, the peak was resolved into two peaks located at $T_{max1} = 526$ K and $T_{max2} = 562$ K. Interestingly, desorption of HCN occurred within a similar temperature range to NHC desorption from clean Cu(111). However, this does not necessarily mean that DISO NHC desorbs reversibly from the oxide. In fact, the yield of fragment $m/z = 41$ amu, a signature of isopropyl groups (C_3H_5^+), was virtually zero. The TPD data suggest altogether that the isopropyl groups do not prevent DISO NHC from oxidative degradation.

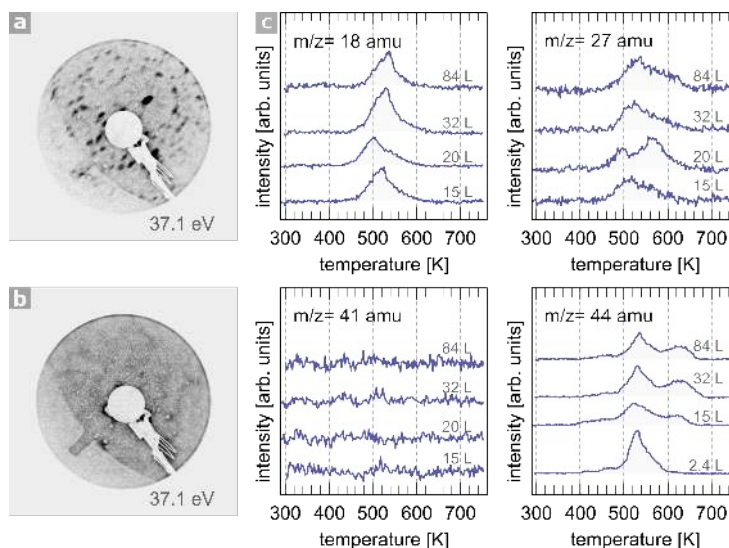


Figure 4.6 ■ Reduction of copper oxide by DISO NHC. a) LEED obtained at 37.1 eV of the prepared oxide featuring a pattern corresponding to the "29" reconstruction. b) LEED pattern collected at the same beam energy after exposing the copper oxide to 13 L of DISO NHC c) TPD spectra of fragments 18, 27, 41 and 44 amu acquired after DISO NHC sublimation onto the oxide.

DM NHC

The interaction of DM NHC with copper oxide was investigated by STM and HREELS. The HREEL spectra of the prepared oxide displayed a strong peak at 230 cm^{-1} and a smaller one at 410 cm^{-1} , wholly consistent with the reported by Dubois²⁰ (Figure 4.7.a). The former is assigned to a $\nu(\text{Cu-O})$ mode due to the oxide layer, and the latter to $\nu(\text{Cu-O})$ at defect sites. The absence of characteristic bulk cuprite phonons at 151 cm^{-1} and 650 cm^{-1} , and a bulk cupric oxide phonon at 550 cm^{-1} , confirms the formation of a surface oxide as opposed to a bulk oxide.^{20,44-46} After exposure to DM NHC, these peaks were massively attenuated and new peaks emerged at 3070 cm^{-1} , 1485 cm^{-1} , 1360 cm^{-1} , 1160 cm^{-1} , and 760 cm^{-1} , all of which can be readily associated with the adsorption of DM NHC or similar species (See Chapter 2 for assignment). However, the spectra differed from those obtained for DM NHC adsorption on clean Cu(111) in that most energy losses are substantially enhanced relative to the $\beta(\text{C-H})_{\text{o,p}}$ at 760 cm^{-1} . This behaviour is not unexpected, as not only different binding modes may arise on this heterogeneous surface, but also different chemical species. For instance, enetetramines and free carbenes react with oxygen to form ureas. Having said that, the spectra did not exhibit peaks that can be assigned to carbonyl species. Mainly, a strong energy loss at *ca* 1750 cm^{-1} would be expected due to a carbonyl $\nu(\text{C=O})$ mode for 1,1-dimethyl-benzimidazol-2-one species. Such species were detected by mass spectrometric analysis of the supernatant solution collected from NHC-treated copper foils.⁴⁷ However, this mode could become silent in HREELS if the carbonyl group binds parallel to the surface plane.

Upon deposition of DM NHC (90 L) onto the copper oxide held at 300 K, STM imaging revealed the development of new structures of a brighter contrast with respect to the oxide (Figure 4.7.b). Atomic resolution of these structures was occasionally obtained, as shown in the expanded region displayed in Figure 4.7.c. The periodicity of the hexagonal lattice was $\bar{a} = 0.256\text{ nm}$, consistent with the lattice constant of metallic Cu(111). Therefore, these newly formed structures unambiguously correspond to metallic fronts, generated from the reduction of the oxide layer by DM NHC. The metallic fronts were predominantly imaged at step edges, though Cu adislands were also detected. These observations bear many similarities with the reduction of copper oxide by CO

reported by Yang *et al.*²⁶ The authors proposed that the alternating oxide and metallic phases are evidence of the "5–7" structure reduction starting at the step edges. Removal of lattice oxygen from the "5–7" structure releases Cu atoms to the terrace, while simultaneously exposing the underlying metallic phase. The reduction mechanism is illustrated schematically in Figure 4.8, which we presume also applies to copper oxide reduction by DBZ and DISO NHCs.

Closer inspection at the metallic fronts revealed that molecular-sized features decorated the step edges (Figure 4.7.d). These species featured two bright lobes and an apparent length of $l = 1.38 \pm 0.14$ nm as measured along the long molecular axis. These dimensions are comparable to (DM NHC)₂Cu complexes obtained from DM NHC adsorption on a clean Cu(111) (See Chapter 2). Therefore, the tentative assignment of these features to such complexes based on apparent dimensions seems reasonable. This assignment is also supported by the spectrometric detection of coexisting benzimidazol-2-one species and (NHC)₂Cu complexes in NHC-treated Cu foils.⁴⁷

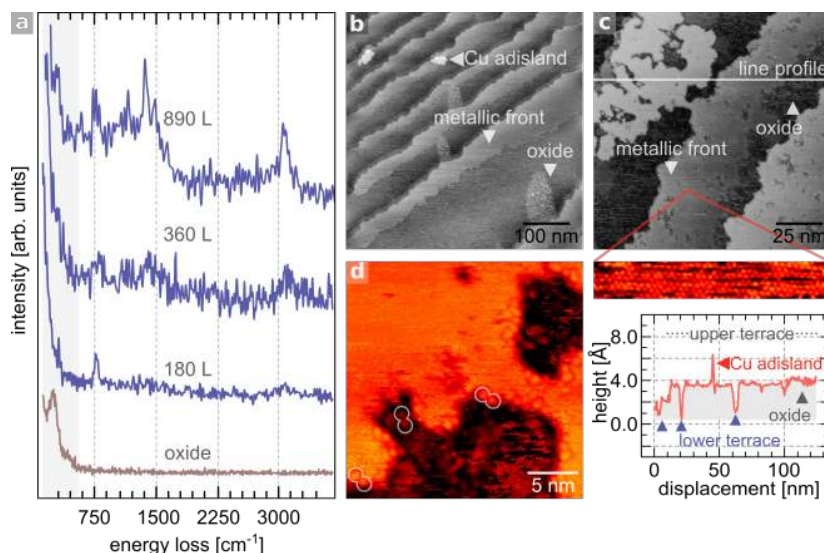


Figure 4.7 ■ Reduction of copper oxide by DM NHC. **a)** HREEL spectra of copper oxide followed by DM NHC sublimation at the indicated exposure. $E_0 = 5.0$ eV, FWHM = 40.8 cm^{-1} . **b)** STM image of copper oxide exposed to 90 L of DM NHC. Highlighted are the alternating oxide and metallic fronts formed at the step edges and as adislands, $V_t = 1.2$ V, $I_t = 600$ pA. **c)** close up of step edge, $V_t = -1.0$ V, $I_t = 500$ pA; (expanded region) atomic resolution of the metallic front. The measured periodicity is consistent with that of Cu(111), image size $10.39 \times 1.64 \text{ nm}^2$, $V_t = -1.2$ V, $I_t = 600$ pA. Line profile accompanying the image indicates position of topographic features. **d)** adsorbates at the step edges of metallic front. $n_{\text{features}} = 25$, $\bar{x} = 1.38 \text{ nm}$, $s = 0.14 \text{ nm}$, $Md = 1.41 \text{ nm}$, $\text{min.} = 1.15 \text{ nm}$, $\text{max.} = 1.61 \text{ nm}$; $V_t = -1.0$ V, $I_t = 500$ pA.

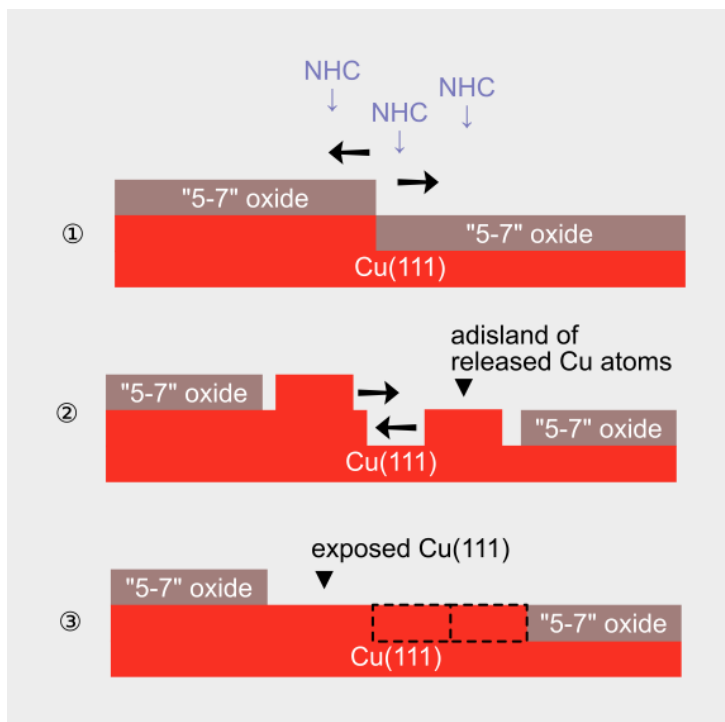


Figure 4.8 ■ Schematic of copper oxide reduction by NHCs. 1) Upon exposure of the oxide to NHCs, the reduction of the oxygen defective "5–7" structure starts at the step edges of upper and lower terraces. 2) The density of Cu atoms in Cu(111) is 1.86 higher than in the "5–7" oxide structure, hence the released Cu atoms occupy about half of the surface area of the oxide, exposing the underlying Cu(111). 3) The released Cu atoms follow a step-down path to extend the metallic front (dashed lines), as it represents the lowest Ehrlich-Schwoebel diffusion energy pathway. Adapted from reference [26].

4.4 NHC SAMs as Inhibitors against Oxidation

In this section, preliminary results are presented on the ability of NHCs to protect copper against oxidation. The samples under investigation were prepared by sublimation of DM, DISO, and DBZ NHCs onto a clean Cu(111) crystal using a range of exposures. The NHC-protected copper samples were then subjected to an oxygen-rich atmosphere ($P_{O_2} \simeq 1 \times 10^{-6}$ mbar) for $t = 20$ min at 300 K. After restoring UHV, the samples were characterised by monitoring the thermal desorption products. STM and HREELS were also employed in the characterisation of DM NHC-protected Cu(111).

TPD data of DM NHC-protected Cu(111) are shown in Figure 4.9.a. The spectra of fragments $m/z = 18$ amu (H_2O^+), $m/z = 27$ amu (HCN^+) and 44 amu (CO_2^+) exhibited a very complex desorption profile with several peaks that shifted down in temperature, and whose relative intensity fluctuated coverage. H_2O desorption displayed a peak at $T_{max} = 477$ K which shifted down to $T_{max} = 430$ K at higher DM NHC exposure. The desorption spectra of CO_2 contained two coalesced peaks at $T_{max1} = 493$ K and $T_{max2} = 554$ K. At higher DM NHC exposure (*e.g.*, 350 L), the peaks split, and T_{max1} shifted down to 427 K. As mentioned in the previous section, due to the complexity of the thermal reaction and the several oxygenate intermediates that may form, a comprehensive assignment of each desorption event is very challenging. Nevertheless, the detection of CO_2 and H_2O clearly confirms that oxygen adsorption onto the Cu(111) surface can still take place by diffusion through the DM NHC film. Oxidative degradation of the DM NHC monolayer readily takes place at temperatures $T_{onset} = 350$ K. Fragment $m/z = 27$ amu (HCN^+) displayed two major desorption events at $T_{max1} = 385$ K and $T_{max2} = 576$ K. Their position also shifted downwards with coverage, with the concomitant emergence of a shoulder for T_{max2} . Notably, T_{max2} resembles that of DM NHC SAM degradation on clean Cu(111) and may hint at this peak being related to DM NHC on metallic copper domains. This notion is further supported by examining the samples under STM as presented in Figure 4.9.b-d.

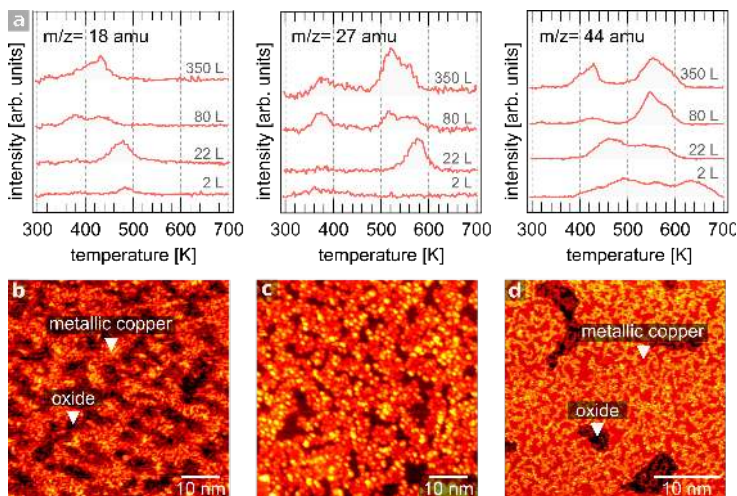


Figure 4.9 ■ Oxygen on DM NHC-protected Cu(111) a) TPD spectra of fragments $m/z = 18, 27$ and 44 amu for samples protected by DM NHC, after exposure to O_2 , $\beta = 3.6 \text{ Ks}^{-1}$ STM images of protected samples exposed to 2100 L of O_2 at b) 300 K c) 443 K and d) 522 K . Molecular-sized features were resolved which exhibited no long-range order. $n_{\text{features}} = 890$, $\bar{x} = 0.96 \text{ nm}$, $s = 0.45 \text{ nm}$, $Md = 0.92 \text{ nm}$, $min. = 0.08 \text{ nm}$, $max. = 2.68 \text{ nm}$. Image b) was acquired at $V_t = -1.0 \text{ V}$, $I_t = 300 \text{ pA}$, Images c) and d) were acquired at $V_t = -0.6 \text{ V}$, $I_t = 300 \text{ pA}$.

The samples examined under STM were prepared in a similar manner as described for TPD experiments: a clean Cu(111) was protected by exposing the clean crystal to 2300 L of DM NHC, followed to exposure to an oxygen-rich atmosphere. The surface topography was characterised by molecular-sized features ($\sigma = 0.92 \text{ nm}$) with no long-range order, on a background of bright and dark contrast areas. Previous reports have described how terrace oxide formed at 300 K manifest as dark patches on the Cu(111) surface. Therefore, the bright and dark areas were readily assigned to metallic copper and copper oxide domains as marked in the STM image.^{21,24,25,48} This assignment is also justified on the basis that, after heating the sample to higher temperatures, the darker areas diminished in size and the brighter ones dominated. This behaviour is also consistent with the surface oxygen consumption in the oxidative degradation of the DM NHC SAM observed in TPD experiments. Notably, heating the sample at 522 K produced a network of interconnected features that extended over the bright areas, similar to the degradation of DM NHC SAM on clean Cu(111) (See Chapter 2). This observation substantiates the assignment of $T_{\text{max}2}$ in TPD data corresponding to HCN evolution from metallic copper regions.

Changes in the appearance of the molecular-sized features with heating were evident from STM images; however, the chemical nature of these species is currently unknown. HREEL characterisation of the sample at the different heating stages is presented in Figure 4.10. After exposing the DM NHC-protected Cu(111) to O₂, the spectral features were significantly enhanced. In particular, enhancement was evident for the energy losses at 3050 cm⁻¹ due to a ring ν (C–H) and those within the 1240–1600 cm⁻¹ region due to ν (C–N) and ν (C=C) stretching, and C–H bending modes. The dominant energy loss at 735 cm⁻¹, assigned to the ring ν (C–H), blueshifted and split into two bands at 750 cm⁻¹ and 770 cm⁻¹. Besides these changes, there was no clear indication of new species forming. Mainly, the spectra were devoid of energy losses associated with carbonyl bearing species. More specifically, a strong absorption at *ca* 1750 cm⁻¹ would be expected for a carbonyl ν (C=O) mode. This is a similar case to DM NHC adsorption on Cu_xO/Cu(111) discussed in the previous section where, despite the dramatic changes in the topography, the presence of oxygenate species could not be resolved by HREELS. The intensity of the spectral features diminished for sample temperatures ≥ 425 K, in agreement with oxidative degradation of the monolayer to combustion products detected by TPD.

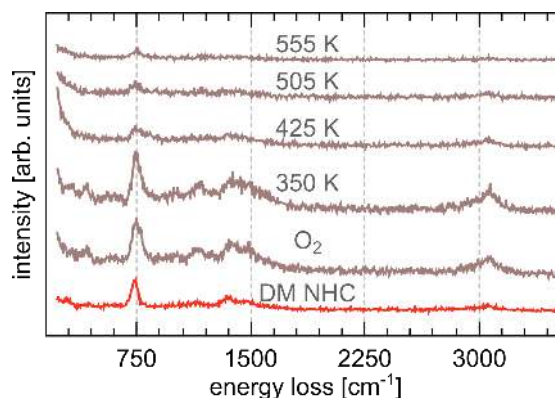


Figure 4.10 ■ HREELS of oxygen on DM NHC-protected Cu(111). A Cu(111) crystal was first exposed to DM NHC (710 L), followed by exposure to O₂ (2700 L). Sample heating and HREEL spectra collection were carried out under UHV. $E_0 = 5.0$ eV, FWHM = 26.9 cm⁻¹

Figure 4.11.a,b shows fragments $m/z = 28$ amu and $m/z = 44$ amu monitored after exposing a DBZ-NHC protected Cu(111) sample to an oxygen-rich atmosphere at 300 K. The assignment of these fragments is as before. The desorption spectra of fragment $m/z = 28$ amu displayed two peaks at $T_{max1} = 581$ K and $T_{max2} = 627$ K, whereas for $m/z = 44$ amu several peaks were distinguished at $T_{max1} = 413$ K, $T_{max2} = 504$ K, $T_{max3} = 575$ K and $T_{max4} = 630$ K. Notably, T_{max3} and T_{max4} coincide with T_{max1} and T_{max2} in TPD spectra of $m/z = 28$ amu, which implies that these desorption events are related. As in the case of DM NHC, the detection of these products is strong evidence of oxygen diffusion through the DBZ NHC SAM, and oxidative degradation of the layer. In all cases, the desorption of these products was detected for low DBZ NHC exposure (≤ 84 L). However, at higher exposure the yield of these products decreased dramatically, to the point where CO₂ desorption was totally quenched. One possible interpretation for these results is that a denser DBZ NHC SAM blocks oxygen adsorption, so that oxidative degradation of the SAM is inhibited. An alternative explanation is that the copper surface was not passivated in the first place. This notion was verified as follows: after collecting the TPD spectra for the 180 L sample, the same sample was re-exposed to O₂ at 300 K (Figure 4.11.c). This time, two peaks were visible at $T_{max1} = 468$ K and $T_{max2} = 660$ K, which likely represent the oxidation of carbonaceous species generated after the first TPD run. This signifies that an organic layer was indeed created in the first place. A second test was also performed to corroborate that the dosing conditions had not changed, Mainly, whether the dosing rate dropped, leading to lower DBZ NHC coverage, and subsequently to a low CO₂ yield (Figure 4.11.c). Soon after examining the 180 L sample, a second sample was prepared using a lower DBZ NHC exposure (41 L). The TPD spectra for this sample showed that CO₂ desorption was restored, confirming that changes in the dosing conditions did not cause the observed reduction of CO₂ yield for the high DBZ NHC exposure samples.

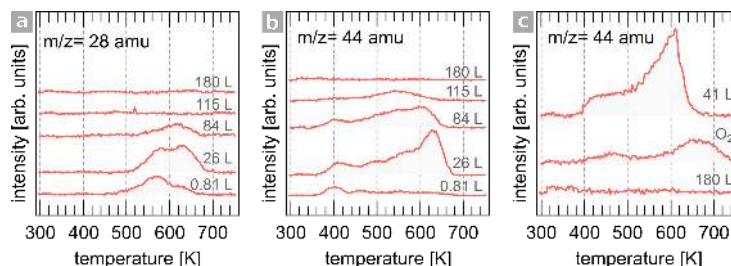


Figure 4.11 ■ Oxygen on DBZ NHC-protected Cu(111). TPD spectra of fragments **a)** $m/z = 28$ amu and **b)** $m/z = 44$ amu of samples protected by DBZ NHC at the indicated exposure. **c)** TPD spectra of fragment $m/z = 44$ amu comparing the high exposure DBZ NHC sample (180 L) as in b) before and after re-exposure to O_2 , as well as a low exposure sample (41 L) sample, $\beta = 3.6 \text{ K s}^{-1}$.

TPD spectra of fragments $m/z = 27, 41$ and 44 amu of DISO NHC-protected Cu(111), collected after exposure to an oxygen-rich atmosphere, are presented in Figure 4.12. Similarly to DBZ NHC-protected Cu(111), the spectra for fragment $m/z = 44$ amu displayed several peaks at $T_{max1} = 404 \text{ K}$, $T_{max2} = 474 \text{ K}$, $T_{max3} = 537 \text{ K}$, and $T_{max4} = 631 \text{ K}$ at low DISO NHC exposure. At high DISO NHC exposure (e.g., 49 L), CO_2 desorption was completely quenched. A similar interpretation is proposed, where a denser DISO NHC SAM inhibits oxygen chemisorption to some extent. Evidence of metallic copper remaining on the surface was derived indirectly from the TPD spectra of fragments $m/z = 27$ amu and $m/z = 41$ amu. The desorption profiles of these fragments mimicked each other and displayed a peak at $T_{max1} = 439 \text{ K}$ that shifted down for the higher DISO NHC exposure samples. A second peak also emerged at $T_{max2} = 568 \text{ K}$ whose position remained constant. Interestingly, the desorption profile of T_{max2} for both fragments resembled a first-order kinetic similar to that observed for DISO NHC desorption from clean Cu(111). Assuming that T_{max2} arises from the reversible desorption of DISO NHC, a Redhead analysis with a pre-exponential factor of $z = 1 \times 10^{13} \text{ s}^{-1}$ yields a comparable chemisorption energy of $E_{des} = 149 \pm 10 \text{ kJ mol}^{-1}$. Additionally, the increase of T_{max2} is accompanied by a decrease in intensity of $m/z = 44$ amu; which clearly suggests that the formation of the oxide phase is somewhat inhibited. It is worth noting that this behaviour is entirely different from the inverse system described in the previous section, where DISO NHC appeared to undergo complete oxidative degradation on the preformed oxide layer. However, the DISO NHC SAM does not completely block oxygen chemisorption, since T_{max1} remained visible for both fragments. This peak is tentatively assigned to the desorption of

oxygenate products of DISO NHC.

Overall, based on the TPD data alone, it appears that the functional group at the *N, N*-position not only plays a crucial role in the adsorption geometry of NHCs on Cu(111), but also in the degree of surface passivation. This effect was only apparent at high NHC exposure of DBZ and DISO NHC, which translates into denser NHC films. By comparison, CO₂ desorption was still detected for DM NHC-protected samples, even with high carbene exposure.

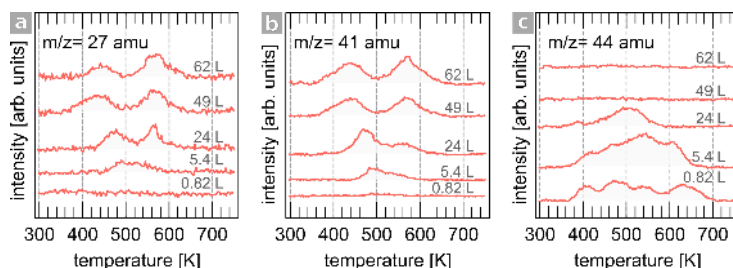


Figure 4.12 ■ Oxygen on DISO NHC-protected Cu(111). TPD spectra of fragments a) 27 amu, b) 41 amu, and c) 44 amu of samples protected by DISO NHC at the indicated exposure. $\beta = 3.6 \text{ K s}^{-1}$

4.5 Summary and Outlook

Previous investigations of alkanethiol SAMs of various chain length and functionalities have shown to be good candidates for corrosion inhibitors for copper surfaces. However, their inhibition ability is rapidly lost through oxidative degradation of the monolayer via the generation of sulfonates and formation of copper sulphide. The robustness of NHC films against chemical degradation, including oxidising conditions, encouraged our investigations of their passivating ability. In this chapter, a series of experiments were conducted to probe the interaction of NHCs with copper oxides, as well as the ability of NHC films to protect copper from oxidation.

The characterisation of a copper oxide thin layer was firstly described, followed by the interaction of DBZ, DISO and DM NHC with this surface. TPD spectra revealed the desorption products typical of a combustion reaction. However, a detailed mechanism of this very complicated process was beyond

the scope of this study. Nevertheless, reduction of the oxide layer was apparent from LEED and STM data. Metallic fronts developed from step edges upon adsorption of DM NHC on the oxide, which corroborated the reduction of the layer. The presence of features similar in size and shape to $(\text{DMNHC})_2\text{Cu}$ complexes seen on Cu(111) were also resolved by STM. However the presence of oxygenate species could not be detected by HREELS.

A second set of experiments were presented where a Cu(111) crystal was protected by DM, DBZ and DISO NHCs, and their blocking ability towards oxygen chemisorption evaluated. The blocking ability was qualitatively described by monitoring the thermal desorption products generated in TPD experiments. CO_2 , CO, and H_2O were predominantly detected, which confirmed oxygen diffusion through NHC films. Mixed metallic and oxide regions were also imaged under STM for DM NHC-protected Cu(111), and the consumption of the oxide was evident at high sample temperatures. The different wingtip substituents appeared to have various degrees of oxygen blocking ability at sufficient NHC exposure. In particular, isopropyl and benzyl substituted NHCs quenched CO_2 production. Similar positive effects arising from tailoring of substituent groups, mainly when comparing isopropyl versus methyl groups, have been reported in corrosion inhibition.¹³

Although subject to further investigations, one potential implication of the copper oxide etching observed by the studied NHCs is in the area of electronic manufacture. Solder is routinely used to form joints between electronic components and copper contacts on printed circuit boards. In order to improve wettability and adhesion of solder, copper contacts are treated with a chemical etchant to remove oxide layers and to expose the active metallic copper surface. Although established methods are efficient at etching copper oxide, standard preparation protocols involve the use of fluxes containing a mixture of solvents and acids. Substitution of fluxes for improved protocols is of interest not only from an environmental point of view but also from a processing perspective. The acid left over on the circuit board need to be thoroughly removed otherwise, it can lead to electromigration of material and electrical shorts in the device.⁴⁹ The envisaged application of NHCs in this area is two-fold. First, NHCs could serve as mild etchants that replace acid fluxes in the removal of copper oxide layers from copper contacts. Secondly, NHC can also serve as a

passive layer to inhibit further oxidation during processing, and may alleviate the use of special storage conditions.

There is ample scope for further investigation of the presented systems, both from a fundamental research point of view, as well as for prospective applications. The experiments detailed in this chapter were only exploratory and did not engage with a comprehensive mechanistic study of the reduction process. Future work will be required to develop a clear atomistic understanding of oxide reduction by NHCs. Some improvements on the experimental protocol may involve using well-defined, homogeneous oxide surfaces, *i.e.*, a full monolayer of "44", "29", or "5-7" structures. Also, characterisation of intermediate species generated during reduction, aided by theoretical models, would be required to gain a comprehensive understanding. How these model systems transfer to real conditions is undoubtedly of great interest in applied surface functionalisation. We trust that the initial investigation presented herein will encourage further developments in the field.

4.6 References

- [1] J. Cotton, I. Scholes, *Br. Corros. J.* **1967**, 2, 1–5.
- [2] F. Grillo, D. W. Tee, S. M. Francis, H. Früchtl, N. V. Richardson, *Nanoscale* **2013**, 5, 5269–5273.
- [3] F. Grillo, D. W. Tee, S. M. Francis, H. A. Fruchtl, N. V. Richardson, *J. Phys. Chem. C* **2014**, 118, 8667–8675.
- [4] C. Gattinoni, A. Michaelides, *Faraday Discuss.* **2015**, 180, 439–458.
- [5] P. E. Laibinis, G. M. Whitesides, *J. Am. Chem. Soc.* **1992**, 114, 9022–9028.
- [6] G. Fonder, F. Laffineur, J. Delhalle, Z. Mekhalif, *J. Colloid Interface Sci.* **2008**, 326, 333–338.
- [7] Z. Mekhalif, G. Fonder, F. Laffineur, J. Delhalle, *J. Electroanal. Chem.* **2008**, 621, 245–253.
- [8] Z. Mekhalif, G. Fonder, D. Auguste, F. Laffineur, J. Delhalle, *J. Electroanal. Chem.* **2008**, 618, 24–32.
- [9] T. Laiho, J. Leiro, *Appl. Surf. Sci.* **2006**, 252, 6304–6312.
- [10] Y. Feng, W.-K. Teo, K.-S. Siow, Z. Gao, K.-L. Tan, A.-K. Hsieh, *J. Electrochem. Soc.* **1997**, 144, 55–64.
- [11] H. Ron, H. Cohen, S. Matlis, M. Rappaport, I. Rubinstein, *J. Phys. Chem. B* **1998**, 102, 9861–9869.
- [12] D. A. Hutt, C. Liu, *Appl. Surf. Sci.* **2005**, 252, 400–411.
- [13] Y. Tan, M. Srinivasan, S. Pehkonen, S. Y. Chooi, *Corros. Sci.* **2006**, 48, 840–862.
- [14] R. Haneda, H. Nishihara, K. Aramaki, *J. Electrochem. Soc.* **1997**, 144, 1215–1221.
- [15] R. Haneda, K. Aramaki, *J. Electrochem. Soc.* **1998**, 145, 1856–1861.

- [16] R. Haneda, K. Aramaki, *J. Electrochem. Soc.* **1998**, *145*, 2786–2791.
- [17] L. Srisombat, A. C. Jamison, T. R. Lee, *Colloids Surf. A* **2011**, *390*, 1–19.
- [18] X. Ling, N. Schaeffer, S. Roland, M.-P. Pileni, *Langmuir* **2015**, *31*, 12873–12882.
- [19] C. M. Crudden, J. H. Horton, I. I. Ebraliidze, O. V. Zenkina, A. B. McLean, B. Drevniok, Z. She, H.-B. Kraatz, N. J. Mosey, T. Seki *et al.*, *Nat. Chem.* **2014**, *6*, 409.
- [20] L. Dubois, *Surf. Sci.* **1982**, *119*, 399–410.
- [21] F. Wiame, V. Maurice, P. Marcus, *Surf. Sci.* **2007**, *601*, 1193–1204.
- [22] F. Yang, Y. Choi, P. Liu, D. Stacchiola, J. Hrbek, J. A. Rodriguez, *J. Am. Chem. Soc.* **2011**, *133*, 11474–11477.
- [23] S. Matencio, E. Barrena, C. Ocal, *Phys. Chem. Chem. Phys.* **2016**, *18*, 33303–33309.
- [24] T. Matsumoto, R. Bennett, P. Stone, T. Yamada, K. Domen, M. Bowker, *Surf. Sci.* **2001**, *471*, 225–245.
- [25] T. J. Lawton, G. Kyriakou, A. E. Baber, E. C. H. Sykes, *ChemCatChem* **2013**, *5*, 2684–2690.
- [26] F. Yang, Y. Choi, P. Liu, J. Hrbek, J. A. Rodriguez, *J. Phys. Chem. C* **2010**, *114*, 17042–17050.
- [27] F. Jensen, F. Besenbacher, E. Lægsgaard, I. Stensgaard, *Surf. Sci.* **1991**, *259*, L774–L780.
- [28] A. Önsten, M. Göthelid, U. O. Karlsson, *Surf. Sci.* **2009**, *603*, 257–264.
- [29] S. M. Johnston, A. Mulligan, V. Dhanak, M. Kadodwala, *Surf. Sci.* **2002**, *519*, 57–63.
- [30] F. Besenbacher, J. K. Nørskov, *Prog. Surf. Sci.* **1993**, *44*, 5–66.
- [31] A. Soon, M. Todorova, B. Delley, C. Stampfl, *Phys. Rev. B: Condens. Matter* **2006**, *73*, 165424.
- [32] A. Soon, M. Todorova, B. Delley, C. Stampfl, *Surf. Sci.* **2007**, *601*, 5809–5813.

- [33] A. J. Therrien, R. Zhang, F. R. Lucci, M. D. Marcinkowski, A. Hensley, J.-S. McEwen, E. C. H. Sykes, *J. Phys. Chem. C* **2016**, *120*, 10879–10886.
- [34] F. Jensen, F. Besenbacher, I. Stensgaard, *Surf. Sci.* **1992**, *269*, 400–404.
- [35] C. P. León, C. Sürgers, H. v. Löhneysen, *Phys. Rev. B: Condens. Matter* **2012**, *85*, 035434.
- [36] A. J. Stone, D. J. Wales, *Chem. Phys. Lett.* **1986**, *128*, 501–503.
- [37] M. B. Nardelli, B. I. Yakobson, J. Bernholc, *Phys. Rev. B: Condens. Matter* **1998**, *57*, R4277.
- [38] H. F. Bettinger, T. Dumitrică, G. E. Scuseria, B. I. Yakobson, *Phys. Rev. B: Condens. Matter* **2002**, *65*, 041406.
- [39] J. Nakamura, J. A. Rodriguez, C. T. Campbell, *J. Phys.: Condens. Matter* **1989**, *1*, SB149.
- [40] M. W. Abee, PhD thesis, Virginia Polytechnic Institute and State University, **2001**.
- [41] F. Stone, T. Williams, *Stud. Surf. Sci. Catal.* **1981**, *7*, 1394–1395.
- [42] P. Dagaut, P. Glarborg, M. U. Alzueta, *Prog. Energy Combust. Sci.* **2008**, *34*, 1–46.
- [43] L. Wang, X. Wang, X. Jing, P. Ning, *RSC Adv.* **2016**, *6*, 113834–113843.
- [44] H. Y. H. Chan, C. G. Takoudis, M. J. Weaver, *J. Phys. Chem. B* **1999**, *103*, 357–365.
- [45] G. Niaura, *Electrochim. Acta* **2000**, *45*, 3507–3519.
- [46] A. Kudelski, *J. Raman Spectrosc.* **2003**, *34*, 853–862.
- [47] C. M. Crudden, J. H. a. Horton, s.
- [48] S. Ditze, M. Röckert, F. Buchner, E. Zillner, M. Stark, H.-P. Steinrück, H. Marbach, *Nanotechnology* **2013**, *24*, 115305.
- [49] C. Liu, D. A. Hutt, *Circuit World* **2003**, *29*, 19–23.

Chapter 5

Conclusion

The unifying theme throughout this thesis has been the exploitation of covalent bonding to achieve robust functionalised surfaces. Durability is an essential aspect of functional materials and is intimately linked to the choice of suitable chemical modification. Due to their intrinsic strength, supramolecular structures connected via covalent bonds frequently offer superior stability. Within the different types of possible covalent bonds, a range of chemical strengths also arise. Some of these bonds are reversible and constitute the field of dynamic covalent chemistry. Additionally, it is generally through covalent bond formation whereby tailoring of molecular properties is achieved effectively. Hence, the extension of covalent bonding beyond the molecule seems the natural next step towards the fabrication of synthetic secondary structures. This notion was experimentally investigated in two well-differentiated topics under UHV. Various surface science techniques were employed in this study: STM and LEED to examine the surface topography of the samples; and TPD, HREELS, and RAIRS for their spectroscopic characterisation.

Chapter 1 of this thesis engaged with the challenges and requirements that led to the fabrication of surface covalent organic frameworks on reactive metal surfaces. As discussed in the introduction, while functionalisation of inert substrates via self-assembly of molecules linked by hydrogen bonds and vdW forces is reasonably well understood and predictable; the fabrication

of covalent supramolecular structures pose a few challenges. Despite the remarkable advances in the synthesis of bulk covalent frameworks, the field of sCOFs is still in its infancy. Many solution-based chemical reactions have been successfully transferred onto the surfaces of gold, HOPG, silver and copper. However, only a few have been successful in producing long-range covalent architectures, especially under UHV conditions. The various considerations and limitations were outlined. To date, most examples of extended covalent architectures have been synthesised on inert substrates, which primarily act as a support for the reaction propagation in two dimensions. The main goal of this chapter was to develop a protocol that permitted the synthesis of a sCOF onto a reactive surface, which could be exploited as a robust chiral interface. The motivation was provided in the introduction, which pertains to the main disadvantages of current methods towards chiral heterogeneous catalysts.

Direct synthesis of sCOFs on reactive metals met with no success, as exemplified by the attempts at depositing melamine, TPA, TBPB, and BDBA onto Pd(111) at 300 K. The deposited monomers immediately underwent some type of dissociative reaction: dehydrogenation, dehalogenation, or dehydration. In the case of TPA, decarbonylation took place, which resulted in the degradation of the monomer and loss of functionality. Due to the many parameters that come into play, initial attempts at creating imine-based sCOFs under UHV were abandoned in favour of homomeric reactions; that is, Ullmann coupling and boronic acid self-condensation. Even in the cases where the monomers were activated and retained their integrity, the strong surface-molecule bond on pure palladium, and high diffusion activation barriers hampered extended polymerisation. These results confirmed that the role of mono-mer mobility is crucial for fabricating high quality, extended, covalent architectures. For this reason, the hypothesis of tuning the reactivity of palladium by alloying was evaluated.

The initial experiments involved depositing monomers onto AuPd alloys of various compositions. The composition of these alloys vary with temperature, therefore, various Au:Pd ratios were conveniently obtained by simply annealing. It was soon found that, the presence of palladium ensembles in AuPd alloys act as strong nucleation points for the deposited molecule. Thus, the local reactivity at these sites remained essentially palladium-like. In other

words, the ensemble effect dominates, similar to previous investigations on this alloy. These results encouraged us to formulate a different approach. We envisaged a stepwise protocol whereby the polymerisation takes place on a gold-rich palladium surface so that the surface chemistry mimics that observed on pure Au(111). After this, annealing of the sample could be used to induce palladium-enrichment. This protocol was demonstrated effective in sCOF synthesis through Ullmann coupling of TBPB. Similarly, evidence of polymerisation and palladium enrichment was found for this protocol implemented in the self-condensation of BDBA. However, the coverage was low, and the sCOF crystallinity very poor. The cause of this behaviour was attributed partly due to etching of gold by BDBA. Nevertheless, the devised protocol appears to be transferable to other surface reactions. In either case, CO titration experiments confirmed the presence of surface palladium atoms. Overall, Chapter 1 navigated through the main challenges of sCOF synthesis on reactive surfaces. A proof of concept for sCOF fabrication on a catalytically relevant surface was demonstrated. Further work will be required to establish if this very same approach is transferable to Pd@Au nanoparticles, since sCOF synthesis in ambient conditions offers greater flexibility regarding availability of building blocks, choice of chemical reactions, preparation conditions, and sCOF quality.

In Chapter 2 an entirely new topic was introduced: NHC-based SAMs. However, the underlying motivation remained the same, the search for robust surface functionalisation. The current SAM technology is based *de facto* on organosulphur chemistry with gold as the substrate. Indeed, the literature of organosulphur compounds is vast, and their self-assembly mechanism reasonably well understood. However, their limitations have also been acknowledged, which primarily concern the poor thermal and chemical stability. These limitations impact significantly on the lifetime of thiolate-based SAM in real application devices. More recently, NHCs have transcended the field of organometallic and homogeneous catalysis and proved suitable ligands for SAM fabrication. Chapter 2 addressed the binding, orientation, and surface chemistry of NHCs on model Au(111) and Cu(111) surfaces under UHV conditions. The use of NHC adducts as a simple method to liberate the free carbene was demonstrated. We found that the substituent groups at the *N, N* position play a critical role in NHC self-assembly. Methyl- and ethyl- substituted NHCs adsorb parallel to the surface plane, whereas NHCs bearing isopropyl groups

bind in an *upright* geometry, in agreement with theoretical predictions. *Upright* NHCs desorb cleanly, whereas *flat-lying* NHCs decompose leaving surface contamination. For DM NHC adsorption on Cu(111), however, the coexistence of a secondary *upright* phase was detected spectroscopically and by STM. Furthermore, the thermally-induced conversion into a SAM of (DMNHC)₂Cu was evident. The chemisorption energy of DISO NHC onto Au(111) and Cu(111) was experimentally determined to be essentially the same within error. This observation set NHCs apart from their organosulphur congeners, with the latter having a chemisorption energy to gold approximately 25 kJmol⁻¹ lower than the former, and rapidly decomposing on Cu(111) to form sulphides. Future work could involve the use of abnormal NHCs, as these species feature even a more σ -donation carbenic carbon (C2), which translates into even stronger bonds. Overall, Chapter 2 provided evidence of the facile formation of NHC monolayers under UHV, their thermal robustness, and for the first time, their formation on a copper substrate. The fact that appropriately designed NHCs bind to copper is a significant discovery and paves the way for future work on the practical applications in surface functionalisation.

Lastly, Chapter 3 of this thesis briefly delved into using NHC SAMs as protective films against corrosion. The experiments were conducted under controlled atmospheres in the high vacuum regime. These conditions are, of course, far from realistic. However, valuable information was gained in terms of the active role of substituents in passivation of copper, and the interaction of NHCs with copper oxide. The reduction of a model copper oxide by NHCs was demonstrated. LEED, TPD and STM data provided solid evidence of copper oxide removal, and the appearance of metallic fronts. In all cases, NHCs are oxidatively decomposed, with no indication of reversible adsorption from the oxide. Inhibition of oxygen adsorption on NHC-protected Cu(111) was qualitatively assessed. We found that in all the examined cases, oxygen can diffuse through the NHC film and chemisorb. However, the extent of oxygen adsorption seemed to depend on the type of NHC. DBZ and DISO NHC-protected copper samples completely quenched CO₂ desorption for the denser NHC layers. This observation was interpreted as an indication of oxygen blocking by the NHC SAM, which was not observed for DM NHC-protected Cu(111). Although the presence of oxygenate byproducts was presumed from the TPD products, the chemical nature of these species could not be determined.

Further work will be required for their unambiguous identification. Subject to further investigation, the observed copper oxide etching, and apparent passivation of copper, could potentially have practical implications in the passivation and cleaning of copper surfaces. Mainly, NHCs could serve as an elegant method to simultaneously remove copper oxide, and passivate the freshly exposed metallic copper surfaces.

Acknowledgments

I would like to express my gratitude to C. J. Baddeley for providing me with the opportunity of embarking on this project. Thanks for the encouragement and advice during my time at St Andrews. The Engineering and Physical Sciences Research Council (UK) is gratefully acknowledged for funding my Ph.D studentship (EP/M506631/1). I am indebted to Steve Francis, Federico Grillo, Brian Walker, and Bob Cathcart, who would assist me when technical difficulties cropped up. Thanks for keeping technology from 1960 running in 2017. I would like to acknowledge José Garrido and Renald Schaub, whom I had the pleasure of meeting. I am appreciative of the support I received from *mis chic@s guap@s* and my mum since day one. Special thanks to Grant Simpson, whom I was fortunate to share time with. I am, and always be, grateful to David Bain for his unconditional support and love during this journey. I could not have made it this far without you.

List of Contributions

Publications

- Cathleen M. Crudden, J. Hugh Horton, Abrar Al Rashed, Brian Mariampillai, Christian R. Larrea, and Christopher J. Baddeley. PCT/CA2017/050665, *Patent*, (2017).
- Larrea, Christian R., Christopher J. Baddeley, Mina R. Narouz, Nicholas J. Mosey, J. Hugh Horton, and Cathleen M. Crudden. "N-Heterocyclic Carbene Self-assembled Monolayers on Copper and Gold: Dramatic Effect of Wingtip Groups on Binding, Orientation and Assembly." *ChemPhysChem*, (2017).
- Crudden, Cathleen M., J. Hugh Horton, Mina R. Narouz, Zhijun Li, Christene A. Smith, Kim Munro, Christopher J. Baddeley et al. "Simple direct formation of self-assembled N-heterocyclic carbene monolayers on gold and their application in biosensing." *Nature communications*, 7, (2016).
- Grillo, Federico, JA Garrido Torres, M-J. Treanor, Christian R. Larrea, Jan Philipp Goetze, Paolo Lacovig, H. A. Früchtl, Renald Schaub, and Neville V. Richardson. "Two-dimensional selfassembly of benzotriazole on an inert substrate." *Nanoscale*, 8, (2016).
- Larrea, Christian R., and Christopher J. Baddeley. "Fabrication of a HighQuality, Porous, Surface-Confined Covalent Organic Framework on a Reactive Metal Surface." *ChemPhysChem*, 7 , (2016).

- Anderson, Amanda E., Federico Grillo, Christian R. Larrea, Riho T. Seljamäe-Green, Herbert A. Fruchtl, and Christopher J. Baddeley. "Metallo-supramolecular Assembly of Cr and p-Terphenyldinitrile by Dissociation of Metal Carbonyls on Au (111)." *The Journal of Physical Chemistry C*, 2, (2016).

Conferences

- "Fabrication of a porous sCOF on a reactive metal surface."
ECOSS-32, Grenoble, France, 2016.
- "Fabrication of a porous sCOF on a reactive metal surface."
SURCAT, Glasgow, UK, 2016.

List of Abbreviations

1D	one dimension
2D	two dimensions
3D	three dimensions
aNHC	abnormal N-heterocyclic carbene
BDBA	benzene-1,4-diboronic acid
BPBA	4-bromophenylboronic acid
COF	covalent organic framework
DBZ NHC	1,3-dibenzyl-benzimidazol-2-ylidene
DET NHC	1,3-diethyl-benzimidazol-2-ylidene
DFT	density functional theory
DISO NHC	1,3-Diisopropyl-benzimidazol-2-ylidene
DM NHC	1,3-Dimethyl-benzimidazol-2-ylidene
FFT	fast Fourier transform
FWHM	full width at half maximum
hBN	hexagonal boronitride
HOMO	highest occupied molecular orbital
HOPG	highly oriented pyrolytic graphite
HREELS	high-resolution electron energy loss spectroscopy
IAd	Arduengo's carbene
LDOS	local density of states
LEED	low energy electron diffraction
LUMO	lowest unoccupied molecular orbital
MEISS	medium energy ion scattering spectroscopy
MLE	monolayer equivalent
MOF	metal organic framework
MST	minimum spanning tree
NEXAFS	near edge X-ray absorption fine structure

NHC	N-heterocyclic carbene
PBE	Perdew-Burke-Enzerhof
Pd@Au	palladium at gold core-shell
PGM	platinum group metals
PTCDI	perylene-tetracarboxylic diimide
QMS	quadrupole mass spectrometer
RAIRS	reflection-absorption infrared spectroscopy
SAM	self-assembled monolayer
sCOF	surface-confined covalent organic framework
SERS	surface-enhanced Raman spectroscopy
SPR	surface plasmon resonance
STM	scanning tunnelling microscope (microscopy)
SURMOF	surface metal organic framework
TBPB	1,3,5-tris(4-bromophenyl)benzene
TEP	Tolman electronic parameter
THF	tetrahydrofuran
TPA	terephthalaldehyde
TPD	temperature programmed desorption
UHV	ultrahigh vacuum
VAM	vinyl acetate monomer
vdW	van der Waals
XPS	X-ray photoelectron spectroscopy

